Departmento de Física Aplicada y Electromagnetismo
UNIVERSIDAD DE VALENCIA

VNIVERSITAT DE VALÈNCIA

Optical characterization of nanowires for optoelectronic devices and energy harvesting

Tesis doctoral

By

CARLOS RODRÍGUEZ FERNÁNDEZ

Supervised by

ANDRÉS CANTARERO SÁEZ
MAURICIO MORAIS DE LIMA, JR.

PROGRAMA OFICIAL DE DOCTORADO EN FÍSICA
DE LA UNIVERSIDAD DE VALENCIA

MARCH 2019

When you have excluded the impossible, whatever remains, however improbable, must be the truth - Sir Arthur Conan Doyle

LIST OF PUBLICATIONS AND PRESENTATIONS

Publications directly related to this thesis

Carlos Rodríguez-Fernández, Mohammed Almokhtar, Wilfredo Ibarra-Hernandez, Mauricio Morais de Lima Jr., Aldo H Romero, Hajime Asahi, and Andrés Cantarero

ISOTOPIC HEFT ON THE B_{1l} SILENT MODE IN ULTRA-NARROW GALLIUM NITRIDE NANOWIRES

Nano Letters 2018 18 (8), 5091-5097

Carlos Rodríguez-Fernández, Cristina V. Manzano, Aldo H. Romero, Jaime Martín, Marisol Martín-González, Mauricio M. de Lima Jr and Andrés Cantarero

FINGERPRINT OF STOICHIOMETRIC Bi_2Te_3 NANOWIRES BY RAMAN SPECTROSCOPY

Nanotechnology 27 (2016) 075706 (8pp)

B. K. Barick, Carlos Rodríguez-Fernández , Andres Cantarero and S. Dhar

STRUCTURAL AND ELECTRONIC PROPERTIES OF INN NANOWIRE NETWORK GROWN BY VAPOR-LIQUID-SOLID METHOD

AIP Advances 5, 057162 (2015)

Shivesh Yadav, Carlos Rodríguez Fernández, Mauricio M de Lima, Jr., Andrés Cantarero, Subhabrata Dhar

STRUCTURAL AND LUMINESCENCE PROPERTIES OF GAN NANOWIRES GROWN USING COBALT PHTHALOCYANINE AS CATALYST

Journal of Applied Physics 118, 225703 (2015)

Further publications

Patricia Gómez-Claramunt, Samia Benmansour, Antonio Hernández-Paredes, Christian Cerezo-Navarrete, Carlos Rodríguez-Fernández, Josep Canet-Ferrer, Andrés Cantarero and Carlos J. Gómez-García

TUNING THE STRUCTURE AND PROPERTIES OF LANTHANOID COORDINATION POLYMERS WITH AN ASYMMETRIC ANILATO LIGAND

Magnetochemistry 2018, 4(1), 6

Mario Culebras, Ana María Igual-Muñoz, Carlos Rodríguez-Fernández, María Isabel Gómez-Gómez, Clara Gómez, and Andrés Cantarero

MANUFACTURING TE/PEDOT FILMS FOR THERMOELECTRIC APPLICATIONS

ACS Applied Materials and Interfaces 2017 9 (24), 20826-20832

Contributions at conferences, workshops and meetings related to this thesis (presenting author underlined)

- Talk at the Meeting of the American Physical Society, Boston (USA), March 2019.
  Andrés Cantarero, Carlos Rodríguez-Fernández, Mohammed Almokhtar, Wilfredo Ibarra-Hernandez, Mauricio Morais de Lima Jr., Aldo Romero, Hajime Asahi
  Crop up of the B_{1l} mode in high quality GaN nonowires due to isotopic disorder

- Poster presented in Reunión del Grupo Especializado de Física del Estado Sólido (GEFES2018) Valencia (Spain), January 2018

  Carlos Rodríguez-Fernández, Cristina V Manzano, Marisol Martín-González, Mauricio Morais de Lima Jr. and Andrés Cantarero
  "The characteristic Raman spectrum of stoichiometric and Te-rich Bi2Te3 nanowires"

- Seminar Talk at the Seminar of the Experimental Physics, University of Valencia, January 2017.

  Carlos Rodríguez-Fernández
  Optical characterization of semiconductors nanowires

- Seminar Talk at the Institute for Solid State Physics, University of Jena, July 2016.

  Carlos Rodríguez-Fernández
  Processing of hybrid solar cell using ZnO Nanowires

- Poster presented in Reunión del Grupo Especializado de Física del Estado Sólido (GEFES2014) Ciudad Real (Spain)

  Carlos Rodríguez-Fernández, Cristina V Manzano, Marisol Martín-Gonzaález, Mauricio Morais de Lima Jr. and Andrés Cantarero
  "Raman scattering in single Bi_2Te_3 nanowires: Effect of the nanowire diameter and anharmonicity"

  Carlos Rodríguez-Fernández, M. M. de Lima Jr., A. Cantarero and S. Dhar
  "Growth and optical characterization of extremely long GaN Nanowires"

Further contributions (not related to this thesis)

- Poster presented in the EMN Meeting on Polymer; Hong Kong (China), January 2016

  Mario Culebras, Ana M. Igual, Carlos Rodríguez-Fernández, Clara M. Gómez and

Andrés Cantarero
"PEDOT-Te films synthesized by electrochemical methods for the preparation of hybrid thermoelectric materials"

- Invited Talk at the University of Basel (Germany)
  Carlos Rodríguez-Fernández and Andrés Cantarero
  Magnetotransport properties of individual InAs nanowires

Research Projects as Participating Scientist

1. **GSD2010-0044 Consolider nanoTHERM**. Tailoring electronic and phononic properties of nanomaterials: towards ideal thermoelectricity. Economy and Competitiveness Ministry of Spain, 2013-2016.

2. **MAT2012-33483**. NANOHILOS SEMICONDUCTORES Y DE POLÍMEROS CON APLICACIONES EN ENERGÍA. Economy and Competitiveness Ministry of Spain, 2013-2016.

3. **MAT2016-63955-R**. NANOESTRUCTURAS SEMICONDUCTORAS Y NANOCOMPOSITES PARA LA RECUPERACIÓN ENERGÉTICA. Economy and Competitiveness Ministry of Spain, 2016-2018.

4. **CPI-18-26**. Termoelectricidad: nuevas teorías. Economy and Competitiveness Ministry of Spain, 2018-2019.

DEDICATION AND ACKNOWLEDGEMENTS

Quisiera agradecer a toda la gente que me ha apoyado durante mi doctorado así como los expertos evaluadores que han empleado su tiempo en leer y valorar detenidamente este trabajo. En especial, me gustaría agradecer a Andrés sus útiles consejos durante estos últimos años. Además, sin su confianza, enseñanzas e ideas no habría sido posible la realización de este trabajo. Seguramente sea imposible explicar con palabras mi agradecimiento por la oportunidad que me ha dado. Quiero remarcar también en los agradecimientos a Mauricio. Gracias a él he aprendido como encauzar los experimentos más complicados de este trabajo. Su predisposición así como su paciencia han sido claves para gestionar este gran proyecto de manera fructuosa y satisfactoria. Por supuesto, no todo ha sido trabajo, las largas charlas sobre la NBA, el Kárate, el fútbol y los deportes en general dan fe de ello así como las conversaciones relacionadas con la familia y la política.

Muchas gracias también a Núria y a Ana Cros por sus ayudas, charlas, atención e interés durante mi etapa como estudiante de doctorado. En esta dedicatoria no puedo excluir a Pascual. Quizás haya sido una de las personas con las que más tiempo, siendo sincero con la que más momentos he pasado en el trabajo. Gracias a todo este tiempo he podido conocer a una persona humilde y atenta la cual siempre ha estado dispuesta a ofrecer su ayuda en cualquier momento y sin ningún compromiso, y todo ello siempre sustentado con su gran sentido del humor y buen rollo.

Además no quiero prescindir esta vez de Julián, ¿creías que iba a olvidarme otra vez ? En la tesis del master no te nombré pero aquí no voy a dejar la oportunidad de agradecerte el tiempo que invertiste en mi, ni tampoco olvidaré tus conversaciones sobre el Kárate y Taekwondo. También me gustaría agradecer a las chicas de secretaría Maria Ángeles, Fina y Mayte que siempre me han ayudado con todas las dudas administrativas (que no son pocas).

Un apartado especial y cientos de líneas serían necesarias para mencionar a mis compañeros de trabajo y estudiantes. Especial mención a Maria José y la cantidad de risas que me ha proporcionado. Puede resultar un poco cansina y "pesada" pero desconectando el chip cuando toma la palabra es suficiente para pasar un buen rato. Siendo honesto muchas gracias por aguantar mis bromas pesadas y ser mi compañera favorita del "curro", eres una gran persona con un gran cuerpo (quiero decir corazón). Y por supuesto a Hannan Elsayed por compartir su cultura conmigo. A Antonio Crespo por su compañerismo y humildad. A Dominick y Andre por ser tan cordiales y agradables. También a varias personas que han pasado por el grupo como Maribel (ojalá en

un futuro podamos seguir colaborando), Michael Möller, Eleonora, Viviane y Kalu. A los "químicos" Mario, Jose, Ana y especialmente a Álvaro por ayudarme con las células solares. A los chicos de InteNanoMat Esther, Pedro y sobre todo a Sandra con la que he compartido varias comidas y almuerzos. A mis compañeros de máster Álex, Juan, Thais, Bernat, Cinthya, la Bandida, Carlos, Mohamed X, Dani, Blanca y Juanjo con los que he vivido tantas experiencias en tan poco tiempo. También no me quiero dejar en la palestra a Dani y Maarten dos de las últimas personas que han estado trabajando en el laboratorio de al lado. Y por supuesto a Josep con el que he podido colaborar estos últimos años y del que recuerdo las largas charlas sobre ciencia y futuro.

No me quiero olvidar de mi estancia en Jena. Por eso me gustaría agradecer a Carsten por acogerme allí. También a Cindy Buechner que se encargó de todo el papeleo. A los compañeros Philipp Schöppe que me introdujo en el magnífico grupo de Jiu-Jitsu brasileño, a Robert Röder, Yaser (siempre se acuerda de mi), Martin, Jura y por supuesto a Maximilian Zapf que me mostró todos los laboratorios y me enseñó a crecer las muestras.

Por último me gustaría agradecer a mi familia, mis tios, mis primas y mi abuela. A mi padre y a mi madre por el gran esfuerzo, dedicación y motivación que me han dado durante todos mis años de estudiante. Sin ellos no hubiera hecho ni la licenciatura de Física y se lo debo todo. A mi hermana que la he visto crecer de manera imparable y que seguro se convertirá en una gran científica. Y por supuesto a Aida que me ha compañado en todo momento durante toda mi etapa predoctoral y que se ha convertido en la mujer de mi vida. Muchas gracias a todos.

AUTHOR'S DECLARATION

I declare that the work in this dissertation was carried out in accordance with the requirements of the University's Regulations and Code of Practice for Research Degree Programmes and that it has not been submitted for any other academic award. Except where indicated by specific reference in the text, the work is the candidate's own work. Work done in collaboration with, or with the assistance of, others, is indicated as such. Any views expressed in the dissertation are those of the author.

SIGNED: ..... DATE: .....

TABLE OF CONTENTS

List of Tables

LIST OF FIGURES

FIGURE **Page**

CHAPTER 1

INTRODUCTION

In 1959, Richard Feynman gave a lecture at the annual American Physical Society meeting at Caltech entitled "There's Plenty of Room at the Bottom", where he considered the possibility of direct manipulation of individual atoms and molecules for designing new materials with extraordinary properties and characteristics never seen before. Some years later, this talk supposed a revolution in almost all scientific scopes (physics, chemistry, medicine, biotechnology, ...), with the consequent increase of publications and creations of specific magazines where these new properties and applications were investigated.

Thanks to this revolution, our daily life changed completely. The devices used nowadays are getting smaller and more powerful. The bulky mobile phones and computers of a few years ago have given way to smaller and lighter terminals with increasing advanced features. The environment and the energy sector are also being favoured by advances in the energy collection system (solar cells, thermoelectric devices, ...). However, the development of all these technologies require basic understanding of the properties of the materials employed for its technological use. In other words, it is necessary a perfect correlation between the basic knowledge and its implementation in a practical situation. For example, the basic research on the optical properties of a given material such as luminescence can be used for developing more efficient optical devices, leading to higher brightness and stability of display and lighting devices. In this way cases as Cree, Inc. can be found which was the first company to break 300 lm/W LED efficacy barrier for white LEDs using the basic luminescence properties.

Due to the great future prospects in the development of nanometric devices that make use of these new physical properties and phenomena there are more than enough reasons to work with nanostructured semiconductors (mainly nanowires). This work will provide a small contribution on the understanding and study of the new basic physical phenomena that occur at the nanometer scale.

The field of semiconductor nanowires has become one of the most important and active within the scientific community and like any other research area several subfields have emerged within the field of nanowires such as electronics, photonics, energy conversion and storage among others. Throughout this thesis known and unknown properties of several one-dimensional materials will be studied trying to solve the new challenges arising from the nanoscale contributing to the future development of photovoltaic, electrical and thermoelectric devices.

1.1 Nanostructured semiconductors - Nanowires

The traditional semiconductor industry has given rise to one of the technological revolutions in the 20th century. The discovery of the transistor, the research in light emitting devices (LED), the fabrication of solid state lasers and invention of silicon integrated circuits marked a breaking point in the industry. This made it possible to create new qualified jobs and the development of new professional careers. At the moment, there are far more chips on earth than people. Since the fabrication of the first semiconductor chip their manifold properties have been expanded enormously due to the shrinking of the structural sizes. Blue shift in the optical absorption, nonlinear optical effects and size dependent luminescence are some examples of the new interesting properties exhibited when the shrinking of the structural sizes goes down to the nanometer range. This allowed the development of new and smart products with less cost such as smartphones, solar panels and portable computers that have given a twist in the way of life for people around the world.

At the nanometer scale, the characteristics of the materials exhibits some unique and remarkable physical properties that enable new applications compared to their bulk counterparts. They become size-dependent in this range. For example, properties such as fluorescence, melting point, chemical reactivity, magnetic permeability and electrical conductivity are affected by the size, shape and aspect ratio of the nanomaterial [7–9]. In general, there are two basic approaches to the synthesis of nanomaterials and the fabrication of different kinds of nanostructures; bottom up and top-down approaches.

In one hand, the top-down method uses larger initial structures (bulk) to create nanodevices, while bottom up approaches include the miniaturization of materials components (up to atomic level) with further self assembly process leading to the formation of nanostructures. Moreover, the top down approach implies that the nanostructures are synthesized by etching out crystals planes which are already present on the initial material (bulk) which can lead significant crystallographic damage to the processed patterns, and the imperfection of surface structure. These imperfections leads to extra challenges in the device design and fabrication, increasing the development costs. In addition, they are not suitable for large scale production because initially uses larger structures where the building blocks are removed from the substrate to form the nanostructure. For these reasons, bottom up self-assembly methods offer the most realistic solution to overcame those limitations. Using self-assembly approach one can be able to produce nanostructures with less defects and more homogeneous chemical composition, being less expensive than top-down methods. Although bottom up is more favourable for the fabrication of next-generation functional materials and devices this approach could be overwhelmed as the size and complexity of the desired assembly increases.

A particular example of self-organized nanomaterials are semiconducting nanowires which are attracting considerable attention due to their encouraging potential as the future building-blocks for the next generation of high performance optoelectronic devices and systems. Nanowires can be defined as nanostructures with cylindrical symmetry with small diameters (in the nanoscale range) and several microns length. In many cases, they are described as quasi-one dimensional nanostructures. There are several reasons why this type of nanostructures are of great interest for the next generation of light-emitting diodes, solar cells and thermoelectric devices [10–12]. If the nanowire diameter is sufficiently small to be compared to the exciton Bohr radius (around ten nanometers in GaN for instance) the motion of the electrons becomes limited because they are quantum confined laterally. This confinement has an influence on the electronic and photonic properties and can, for example, affect the excited electronic states by blue shifting the energy, increasing the band gap [13, 14]. In addition, quantum confinement in elongated nanowires can be useful to increase the hole mobility that enhances the performance on field-effect transistors (FETs) [15].

Another peculiar characteristic of the nanowires are related to surface effects. The influence of the large surface-to-volume ratio allows to enhance light confinement and photosensitivity that makes nanowires ideal for wide range of optoelectronic devices such as solar cells, optical switches, photodetectors and interconnects [16–21].

1.2 Key challenges

A feature of the nanostructured materials is that many of their physical properties do not have the same behaviour as observed in their bulk counterparts. For example, in nanowires the characteristic diameters are less than a few hundred nanometers, and therefore they are below the characteristic lengths of many physical phenomena; e.g. wavelength of the photons, phonon mean free path, diffusion lengths of the excitons, size of the magnetic domains etc. Moreover, the defects present in the structure such as dislocations, impurities, surface roughness among others are more relevant on nanomaterials than in bulk solid materials [22]. That can also affect the development of nanoelectronic devices due to the high non-uniform heat dissipation density. Thermal conductivity of nanostructures (including nanowires) can be altered and reduced because of phonon scattering by interface roughness. Although the reduction in thermal conductivity does not involve a substantial loss in the electrical transport qualities of the nanowire[22–24].

It deserves mentioning the fact that the development of nanowire based electronic and thermoelectric devices depends on the ability to grow nanowires with strict control over properties such as crystal structure, optical properties, morphology and chemical composition. The lack of control on the dimensions can affect the behaviour of charge carriers in quantum electronic devices. Unintentional radial growth can be also problematic for performance of nanodevices because material is deposited on the nanowire sidewalls and produces a non-uniformity composition along the length of ternary nanowires, undesirable nanowire tapering and unintentional shell structures coating axial heterostructure nanowires. In addition it is worth to note that control over chemical composition (nanowires heteroestructures, intrinsic and doped nanowires,etc.) is relevant in the development of emerging based-nanowires devices. Unfortunately, it is quite hard to control the crystallographic phase purity of nanowires, in particular in III-V compounds such as GaAs and InP nanowires [25]. For instance, the crystallographic phase, whether cubic (zinc-blende) or hexagonal (wurtzite) has significant effects on the physical and optical properties (modification of bandgap) of the nanowires [26].

Another well-recognized challenge for the researchers is the difficulty to perform an appropriate characterization for reproducing and validating experimental measurements at the nanometer range scale. It is very common that some nanostructured materials present unique sample preparation, and not every research groups have access to the tools needed to characterized properly these samples. In most of the cases, the multi-

disciplinary nature of the Nanotechnology requires a knowledge beyond of the expertise of the research groups. In many cases, this lack of information on nanostructured materials may create a sense of helplessness by researchers, who would like to either use them for thermoelectrics, electronic, biomedical and energy applications, since their incomplete characterization are viewed in many cases as a significant failure on the wide part of the research community.

Finally, because nanowires and nanostructured materials in general offer such breathtaking results in optoelectronics and phonon behaviour, their optical properties are of great interest. Within the available tools provided in this work to characterize the samples, Raman spectroscopy is very suitable for studying the crystal structure, their purity, composition, phonon behaviour and temperature because of its non-destructive nature and micrometer resolution. This technique has been widely applied in the characterization of nanowires semiconductors as indicated along the thesis. But, since the nanowires present particular geometric characteristics in their shape and they can have a smaller size than the wavelength and illumination area of incident laser light (spot from the objective), the way of using this technique over them is still a challenge.

1.3 Scope and goals of the thesis

Optoelectronics has become an important part in modern life. For any device where light is used to transfer information semiconductor devices are often necessary to convert electrical current into optical signal and vice versa. Such devices include: photodetectors used in digital cameras and safety systems; light emitting diodes for general lighting and traffic signals; or laser diodes with a wide range of uses that include Blu-ray disc and fiber optics communications among others. Moreover, semiconductors nanodevices take advantage of their shrinking size to open new possibilities in modern optoelectronics devices. The goal of this work will be the understanding of the properties of some of the most commonly used semiconductor nanowires like GaN, InP and ZnO for their application in modern optoelectronics and providing fundamental optical knowledge about them.

Another key objective that will be studied in this thesis is related to basic knowledge of the characteristics of nanomaterials with applications in the field of energy harvesting. It is well-known the need to develop new technological products to contribute to environmental and climate protection by saving energy and raw materials, decreasing consumption of fossil fuels and making an efficient use of resources for reducing green-

house effect. Materials such as Bi_2Te_3 and ZnO are of the great interest because they can be employed for performing this kind of nanotechnological products and they are generally used to carry out thermoelectric (in the case of Bi_2Te_3 material) and photovoltaic (ZnO) devices. For this issue their understanding and characterization are vital for performing new energy harversting devices.

This thesis presents a detailed investigation of the optical properties of Bi_2Te_3, GaN, InN, InP and GaN/AlN nanowires grown by different techniques for their application on future optoelectronic and thermoelectric devices. The thesis also includes a prototype of hybrid solar cell. The outline of the thesis is organized as follows: Chapter 1 presents a bird's eye view of the content of the thesis. Chapter 2 reviews basic notions of epitaxial growth, fundamentals in the synthesis of the nanowires and experimental techniques used for characterization and their underlying theory. Although several characterization techniques are employed in this work, Raman spectroscopy is applied as the major research method for this thesis. Concepts of Raman scattering theory as well as the mainly used Raman setups are presented. The organization of the several chapters is based on how Raman spectroscopy is applied for characterizing the samples. This is reflected on Chapters 3, 4 and 5, where materials were studied in large part by non-resonant, resonant and Surface Enhanced Raman Spectroscopy (SERS), respectively.

Chapter 3 is divided into two parts. On one hand, Chapter 3 reports the growth and optical characterization of long single GaN nanowires. Surface modes characteristics of these nanostructures are identified by Raman spectroscopy. On the other hand, it explains the appearance of extra peaks on Bi_2Te_3 tiny nanowires, which are erroneously assigned in the literature as infrared (IR) activated forbidden Raman modes. Stochiometric and non-stochiometric Bi_2Te_3 nanowires ensembles are characterized. Optical phonon modes are identified and compared with density functional theory (DFT) calculations. The measurements on Bi_2Te_3 nanowires are supported with additional experiments on Bi_2Te_3 films.

Chapter 4 presents Resonance Raman Spectroscopy (RRS) of ultrathin GaN and GaN/AlN nanowires in order to obtain information of the electronic structure and polarity of the material. In the experimental characterization of the ensembles, anomalous results appears; e.g. supplementary peaks attributed to forbidden silent mode and huge Raman intensities. In order to shed some light into the physical origin of these observations DFT calculations of the lattice dynamics in GaN were discussed. A thorough analysis of the different physical mechanisms allowing the forbidden mode to appear is carried out for understanding the physics behind the experimental results.

Chapter 5 shows the optical characterization of individual InN and InP nanowires. In this chapter these nanowires are localized in a marked substrate and investigated by means of Raman and SERS. In order to increase the Raman signal from SERS measurements, gold nano-branched particles onto the nanowires are deposited. The signal enhancement in the Raman spectra plus the possibility of accessing to forbidden modes by SERS technique are discussed.

In Chapter 6, a novel prototype of hybrid solar cell using ZnO nanowires is performed. This Chapter shows the growth of ZnO nanowires by Chemical Vapour Deposition, their optical characterization and the fabrication of the photovoltaic cell.

Finally, the major results of this thesis are summarized in Chapter 7.

CHAPTER 2

EXPERIMENTAL DETAILS

The objective of this chapter is to provide a short summary of the basic concepts of epitaxial growth and fabrication techniques employed in this work. Parameters concerning growth processes will be described in next chapters depending upon the material grown. The second part of this Chapter is focused on the fundamentals of the experimental techniques used for characterization of the samples. In particular, basic notions on the interaction of light with matter will be detailed. That includes the theoretical background of the Raman effect, explaining the selection rules for the scattering process, resonant Raman spectroscopy and plasmonics on surface enhance Raman spectroscopy. Because these techniques are highly complex and cannot be explained in detail the discussion is restricted to the basic principles and issues relevant to this work. Fundamentals are based on the works of Cantarero, Yu and Cardona [27–29]. The setups and the experimental equipment used are also described.

2.1 Synthesis techniques

2.1.1 Epitaxial growth

Before introducing the growth methods employed for developing the nanomaterials, some fundamental concepts of epitaxial growth are presented. Epitaxy is described as the ordered growth of one crystalline material on top of a crystalline substrate with a similar lattice parameter [30]. This implies that the crystalline material grown will be

influenced by the crystalline substrate which acts as a seed. Because of this, the deposited material may lock into one or more crystallographic orientations with respect to the substrate crystal. When a crystal is grown epitaxially on a substrate of the same material, epitaxy is termed as homoepitaxy. By contrast, if the grown material is different to that of the substrate, as a silicon film grown on sapphire or gallium nitride grown on a silicon substrate, it is termed as heteroepitaxy. Nowadays, epitaxial growth techniques are employed for the fabrication of electronic circuits, replacing bulk growth techniques, such as massive semiconductors or wafers, since the devices are fabricated with a size of only a few microns (or even nanometers). One of the major advantages of epitaxy over bulk techniques is the accuracy to control the structure and composition which may be better than the single atomic monolayer and the purity of the crystal.

There are several epitaxial techniques used for the growth of III-V, II-VI compound semiconductors and other materials. The most common epitaxy techniques used for obtaining high crystalline nanowires, which is the main subject of the present work, are metal organic vapor phase epitaxy (MOVPE) and Molecular Beam Epitaxy (MBE). These growth techniques provide nano-sized semiconductors grown with excellent crystal quality, allowing mostly epitaxially determined orientations with respect to a template. In the next subsection the main growth techniques utilized in this thesis will be explained. In particular, it shall be described those techniques that were employed in the growth of the nanowires.

2.1.2 Nanowire growth techniques

Information about synthesis techniques have been taken, in part, from the works of Kimberly A. Dick and Jing-jing Feng et al. [30, 31].

The formation of nanostructured materials can be performed by a variety of techniques. In the particular case of the 1-dimensional structures, the growth depends on the suppression of the crystal growth rate in two dimensions. In general, there are two main categories of nanowire growth: the template-assisted and the free-standing one. Template-assisted growth limits the formed crystal to a predefined direction. This method uses, for instance, prefabricated cylindrical nanopores as templates [32]. Then nanopores are filled by the desirable material with a diameter predefined by the diameter of the nanopore [33]. Among all ways to fill nanopores, electrochemical deposition is a well-established, simple, versatile and low cost method, which has been successfully utilized for fabricating nanowires for thermoelectric applications [34–38].

In free-standing growth, nanowires are usually grown from a single nucleation point and shrinking is achieved due to the relative growth rates of the different dimensions. A large advantage of this method compared to the other one is the facility and versatility to grow nanowires on different substrates and transfer them to other surfaces after growth, which is useful for individual analysis and studies. In many cases, the growth of free-standing nanowires is achieved by the vapor-liquid-solid (VLS) mechanism first described by Wagner and Ellis for micrometer sized Si whiskers [39]. This process requires a catalyst, which forms an eutectic * with the growth material having lower melting point. The catalytic particles (typically, a metal as gold) are deposited onto a substrate. Then, it is heated to a temperature above the eutectic point of the system which is chosen between the catalytic particle and the target material †. Due to the elevated temperature the catalyst forms nanometer sized droplets. Then the sample supplied from the gas phase is brought in contact with the melted droplet and forms the eutectic solution. Finally, these liquid droplets supersaturates due to the continuous feeding of the catalyst particle leading to nucleation of the nanowire material. The material growth is assisted by the solid-liquid interface that acts as a sink causing the continued material incorporation of semiconductor in the lattice leading to axial crystal growth with the droplet riding on top as seen in Figure 2.1. The diameter and length of the nanowire can be controlled by the size of the catalyst droplet and the time of growth material vapour supply. The process can be visualized at Figure 2.1. This image is taken from [41] which illustrates the VLS process for Sb_2O_4 nanowire growth.

We will be briefly described below the synthesis techniques employed for growing semiconductors materials:

Electrodeposition is a process which a metal thin layer is deposited from a solution of ions onto an electrically conducting surface. This method is based on the principle of electrosynthesis and is analogous to a galvanic cell acting in reverse. It uses electrical current to reduce the cations of a desired material from an electrolyte and coat those materials as a thin film onto a conductive substrate surface [42]. This technique is quite versatile allowing its application to a wide range of potential uses in thermoelectrics due to its capability in fabricating one-dimensional nanostructures [36, 43]. So far, the most common electrodeposition used includes reaction deposition, co-deposition,

*An eutectic reaction is a three-phase reaction by which, on cooling (slowly) to the eutectic temperature, a liquid solution transforms into two solid phases at the same time that will remain stable as the temperature is lowered [40].

†The temperature chosen is selected according to the binary phase diagram which is a temperature-composition map that represents the equilibrium phases present at a given temperature and composition.

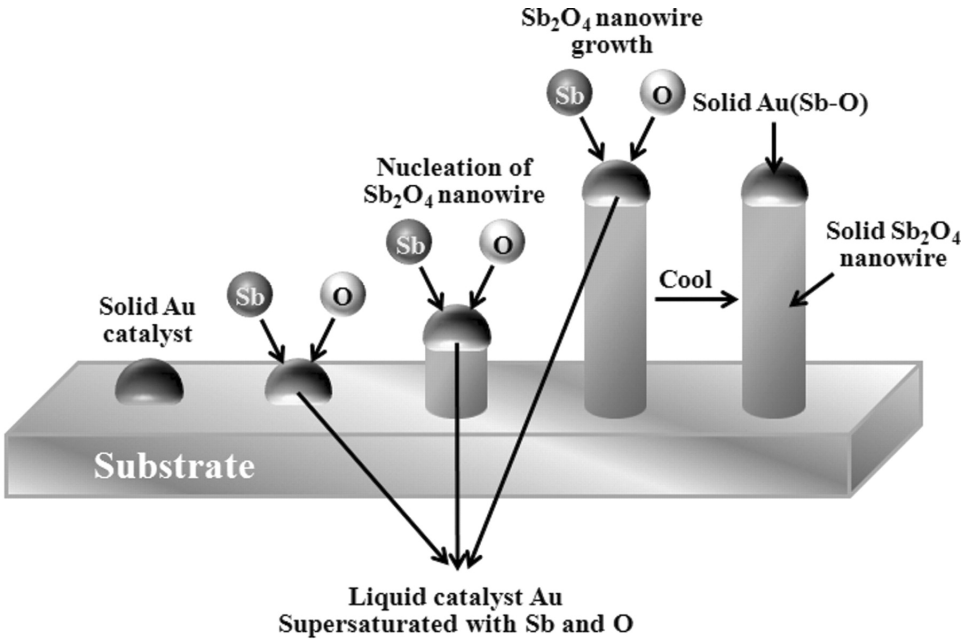

Figure 2.1: Schematic illustration of VLS process for Sb_2O_4 nanowire growth. This process can be divided into four main steps: First, catalytic particles are deposited on a substrate to initiate the growth process (it could be Gold, Nickel, Indium...). Then a gas that contains the growth material is brought in contact with the melted droplet, using techniques like Chemical Vapor Deposition (CVD), Chemical Beam Epitaxy (CBE), MBE, etc.. After that, nucleation occurs when supersaturation is reached. And finally, at the particle-wire interface, the nanowire grows.

and two-step deposition. For electrodeposition process current, voltage, temperature, solvent concentration and solution pH should be taken into account. However electrodeposition depends on additional factors such as the solution ionic strength and electrode surface state among other can complicate the process. In addition, it is relatively difficult to control the thickness and composition of films in complex compositions. Bi_2Te_3 nanowires (as well as Bi_2Te_3 films) were grown by electrodeposition.

Chemical vapor deposition (CVD) is a deposition method used especially in the semiconductor industry to produce high-quality and high performance solid materials. In this technique the wafer (substrate) is exposed to volatile precursors which react and decompose (or both) on the surface of the substrate, and then the deposition is produced on top of the wafer. Frequently, this is accompanied by the production of chemical by-products that are removed out of the chamber by unreacted precursor gases. Because of the wide range of applications and the large variety of materials deposited CVD can be implemented in a variety of formats such as metalorganic chemical vapor deposi-

tion (MOCVD), plasma enhanced chemical vapor deposition (PECVD), and low-pressure chemical vapor deposition (LPCVD), which are usually different in the initialization of the chemical reaction. GaN, InN and ZnO nanowires were synthesized in a CVD reactor.

Molecular Beam Epitaxy (MBE) is an ultra high vacuum (UHV) (low pressure ~ 10^{-8} - 10^{-10} Torr) based technique for producing high-purity nano-scale materials. The growth material is deposited on a heated substrate in UHV environment typically using one or more beams of atoms or molecules incident upon the substrate's surface. This technique has many advantages over similar deposition methods like vapor deposition e.g. arbitrarily sharp deposition resolution, significantly improved purity, and operation at low temperatures. In addition, reflection high energy electron diffraction (RHEED) is often used during operation for monitoring the growth of the crystal layers. However, the equipment involved is complex and very expensive because of the difficulty of achieving clean materials which are liquid or solid in high vacuum conditions. Ultrathin GaN nanowires were grown via Plasma-assisted MBE (PA-MBE) which involves the activation of molecular nitrogen in which active nitrogen is produced by catalytic decomposition of ammonia at the surface of the substrate.

Chemical Beam Epitaxy is described as a hybrid of MOCVD and MBE [44] that exploits the advantages of the beam nature of MBE and the control and use of an all-vapor source of MOCVD. Metal alkyls (e.g., triethylgallium), as group III sources, and hydrides (e.g., mine), as group V sources, are used to form the corresponding intermetallic crystalline compound in an UHV chamber [45]. InP nanowires were synthesized using this process.

2.2 Characterization techniques

2.2.1 Raman spectroscopy

Raman scattering is a standard non-destructive contactless characterization technique that provides access to the lattice dynamics and therewith delivers information on the crystal and electronic structures, strain, temperature, phonon-phonon, and electron-phonon interactions of the materials on an area spatially defined by the focal size of the optical beam. This technique consists of using a laser light source to irradiate a sample and generate Raman scattered light, which is usually detected through a charge-coupled device (CCD).

In addition, Raman spectroscopy has numerous advantages over other analysis tech-

niques because it requires no sample preparation and provides a high spatial resolution up to sub-micron scale. Using this technique one can measure both organic and inorganic substances, samples in various states (gas, liquid, solution, solid, crystal, emulsion) and transparent samples using a confocal optical system. Another significant advantage of Raman Spectroscopy is that it is a highly specific, like a chemical fingerprint of a material.

Raman spectroscopy is based on the Raman effect which was first reported by C. V. Raman and K. S. Krishnan [46], and independently by Grigory Landsberg and Leonid Mandelstam, on 21 February 1928 [47]; although the inelastic scattering of light was predicted by Adolf Smekal in 1923 [48].

2.2.1.1 Interaction of light with matter; the Raman effect

When light interacts with matter various processes can occur. In a semiconductor most of the incident light is either reflected, absorbed, or transmitted; only a small amount of incident light is scattered within a whole solid angle. The light scattered can be scattered either elastically (Rayleigh or Mie scattering) or inelastically (Raman or Brillouin scattering). The light scattered elastically from small particles such as atoms or molecules is named Rayleigh scattering*. The Rayleigh scattering is possible due to the existence of defects (dislocations, vacations, etc...) in the sample; in a high-quality crystalline material with translational symmetry, the elastic scattering is very low compared to a material with defects [49, 50]. In contrast, the inelastic scattered is caused by elemental excitations of the material; inelastic scattering by acoustic phonons is known as Brillouin scattering, while inelastic scattering by other dynamic inhomogeneities such as optical phonons in a lattice or molecular vibrations and plasmons is known as Raman scattering. This work will be focused on the analysis of Raman scattering by phonons†.

For spectroscopic Raman measurements the incident light must be monochromatic. In addition, much more than 99% of scattered light still has the same wavelength after scattering (Rayleigh scattering) and only a tiny amount of photons (several orders of magnitude smaller than that scattered elastically) are spectrally shifted with respect to the incident radiation due to inelastic scattering process (the outgoing photon has a different frequency of the incoming one); for this reason the design of special spectrom-

*Mia scattering is an elastic scattering mechanism that predominates for particle sizes larger than the incident radiation and the resulting scattered radiation is non-uniform.

†The scattering by electronic excitations or magnetic excitations are also Raman scattering [28].

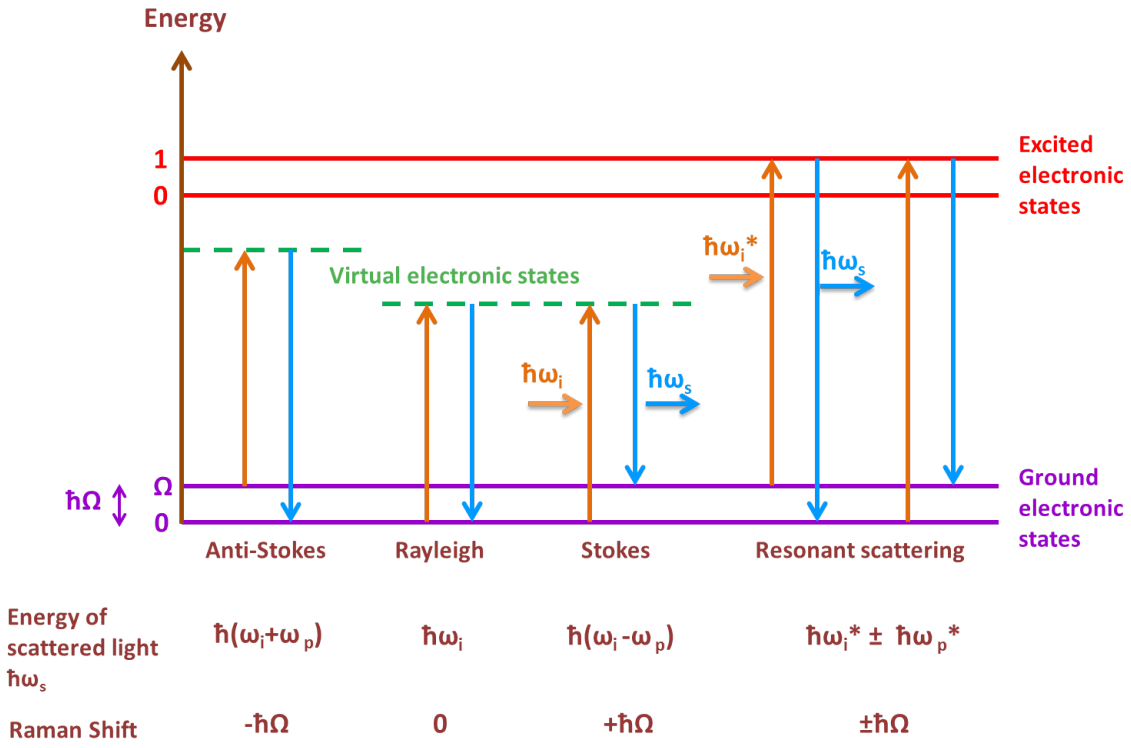

Figure 2.2: Jablonski energy diagram of the scattering processes of light with Rayleigh, Raman and Resonant Raman scattering (Stokes and anti-Stokes shifts). The vibrational or phonon energy is denoted by $\hbar_\Omega$.

eters that eliminates strong Rayleigh light are needed. In a typical Raman spectrum the intensity of the scattered light is plotted as a function of the scattered light (Raman shift), I=I(ω), where ω is typically given in cm^{-1}. Not all the vibrations can be observed in a Raman experiment since the observation depends on symmetry and polarizability of the molecule or phonon mode. The lower energy emission is called Stokes shift and it is represented at the right of the laser line in a I=I(ω) plot, while the phonon absorption is called anti-Stokes shift, represented at the negative x-axis. At low temperature the number of phonons present in the material is very low and usually nothing is observed in the anti-Stokes region, while at room and higher temperatures the anti-Stokes phonons are observed, although the intensity is lower, much lower at a larger frequency[‡]. In Figure 2.2 the elastic Rayleigh scattering and inelastic Raman scattering processes (Stokes and anti-Stokes) are illustrated in a Jablonski energy diagram. The Resonant Raman scattering process is also shown, in which the energy of the laser

[‡]There are other techniques like stimulated Raman scattering where the most important region is the anti-Stokes.

matches with a real electronic transition of the studied system, causing the transition between electronic states becomes real and the Raman signal increases orders of magnitude. More information about these processes are given in the next subsections.

2.2.1.2 Principles of Raman effect

The inelastic Raman scattering process is governed by the laws of conservation of energy and momentum. This means that the light is frequency shifted to lower energies (Stokes) or higher energies (anti-Stokes) with respect to the incoming light as a consequence of a scattering event; a quasi-particle (phonon,plasmon or magnon) is created or annihilated, respectively. The corresponding energies and momenta of a scattering process in a crystalline solid are defined by the following Equations:

$$\hbar\omega_s = \hbar\omega_i \pm \hbar\omega_p \tag{2.1}$$

$$\hbar k_s = \hbar k_i \pm \hbar k_p \tag{2.2}$$

The energy transfer between the incident photon of energy $\hbar\omega_i$ plus/minus (absorption/emission of a phonon, respectively) the phonon energy $\hbar\omega_p$ must coincide with the energy of the outgoing photon, $\hbar\omega_s$. However since the momentum of the incident and scattered photons $|\overline{k}_{max}| \leqslant 10^5 \mathrm{cm}^{-1}$ in the visible are rather small compared to the size of the first Brillouin zone $\pi/a_0 \sim 10^8 \mathrm{cm}^{-1}$, scattering mainly occurs close to the Γ point (the center of Brillouin zone) where the phonons participating in the scattering process are long wavelength phonons with $q \simeq 0$.

In a classical picture, the Raman scattering process can be explained using classic theory of the electromagnetism. When a plane electromagnetic wave with frequency ω_i (laser light)

$$\vec{E}(\vec{r},t) = \vec{E}_i(\vec{k}_i, r)e^{i(\vec{k}_i\vec{r}-\omega_i t)} \tag{2.3}$$

interacts with an infinite medium with electric susceptibility (χ), a sinusoidal polarization will be induced:

$$\vec{P}(\vec{r},t) = \epsilon_0 \overleftrightarrow{\chi}(\vec{k}_i,\omega_i)\vec{E}_i(\vec{k}_i,\omega_i)e^{i(\vec{k}_i\vec{r}-\omega_i t)}, \tag{2.4}$$

the electrons of the constituent molecules are perturbed periodically with the same frequency that the electric field of the incident wave. The electrical susceptibility can be modulated by different elementary excitations. In the case of phonons or molecule vibrations, i.e., normal modes of atomic vibrations in the crystal with wave vector $\vec{q}$ and frequency ω_p, these elementary excitations can be represented as:

$$\vec{Q}(\vec{r},t) = \vec{Q}(\vec{q},\omega_p)e^{i(\vec{q}\vec{r}-\omega_p t)}, \tag{2.5}$$

where Q represents the phonon displacement. These atomic displacements modify the electric susceptibility. If the characteristic frequencies ω_i, which determine χ, are much larger than ω_p, the electric susceptibility can be expanded in a power series of the phonon displacement $\vec{Q}(\vec{r},t)$. Keeping only the first-order terms and assuming a plane wave for $\vec{Q}(\vec{r},t)$, results in:

$$\overleftrightarrow{\chi}(\vec{k}_L,\omega_L,Q) = \overleftrightarrow{\chi}_0(\vec{k}_L,\omega_i) + \left.\frac{\partial\overleftrightarrow{\chi}(\vec{k}_L,\omega_L)}{\partial Q(\vec{r},t)}\right|_o Q(\vec{r},t) \tag{2.6}$$

If we replace the previous Equation in (2.4) the polarization of the medium can be expressed as:

$$\vec{P}(\vec{r},t,Q) = \vec{P}_0(\vec{r},t) + \vec{P}_{in}(\vec{r},t,Q) \tag{2.7}$$

where

$$\vec{P}_0(\vec{r},t) = \epsilon_0\overleftrightarrow{\chi}_0(\vec{k}_L,\omega_L)\vec{E}(\vec{k}_i,\omega_i)e^{i(\vec{k}_i\vec{r}-\omega_i t)}, \tag{2.8}$$

is the polarization vibrating in phase with the incident light, i.e. the term is responsible for elastic light scattering and the term

$$\vec{P}_{in}(\vec{r},t,Q) = \epsilon_o\left.\frac{\partial\overleftrightarrow{\chi}(\vec{k}_L,\omega_L)}{\partial Q(\vec{r},t)}\right|_o \vec{Q}(\vec{q},\omega_q)\vec{E}_i(\vec{k}_i,\omega_i)e^{i[(\vec{k}_i\pm\vec{q})\vec{r}-(\omega_i\pm\omega_p)t)} \tag{2.9}$$

denotes a polarization varying with $\omega_i \pm \omega_p$ [†], an induced oscillation which generates dipole radiation at the Stokes and anti-Stokes frequencies[‡].

The intensity of the scattered radiation can be calculated from the time-averaged power radiated by the induced polarizations ($\vec{P}_{in}(\vec{r},t,Q)$) into the solid angle,

[†]The frequency of the phonon involved in the dispersion is equal to the difference between the frequencies of the incident radiation $\omega_i = \omega_L$ and the scattered ω_S.

[‡]The expansion to higher terms in Eq. 2.6 induces polarizations at higher frequencies giving rise to second order Raman scattering or Raman overtones.

$$I_S \propto \omega_S^4 \left| \vec{e}_L \cdot \frac{\partial \overleftrightarrow{\chi}(\vec{k}_L, \omega_L)}{\partial Q(\vec{r}, t)} \bigg|_o \vec{Q}(\vec{q}, \omega_q) \cdot \vec{e}_S \right|^2, \tag{2.10}$$

where $\vec{e}_L$ and $\vec{e}_S$ represent the polarization of the incident and scattered radiation, respectively. Introducing the unit vector parallel to the phonon displacement (defined as $\widehat{Q} = \vec{Q}/|Q|$) the previous relationship can be rewritten as [29]:

$$I_S \propto \omega_S^4 \left| \vec{e}_L \cdot \frac{\partial \overleftrightarrow{\chi}(\vec{k}_L, \omega_L)}{\partial Q(\vec{r}, t)} \bigg|_o \widehat{Q} \cdot \vec{e}_S \right|^2, \tag{2.11}$$

where

$$\frac{\partial \overleftrightarrow{\chi}(\vec{k}_L, \omega_L)}{\partial Q(\vec{r}, t)} \bigg|_o \widehat{Q} = \Re, \tag{2.12}$$

is known as the Raman tensor. Since χ is a symmetric tensor, the Raman tensor is taken as a symmetric tensor (if we neglect the difference in frequency of the incoming and outgoing light)[||] and has the same symmetry as the corresponding phonon [51]. The phonons observed in a Raman process, called active modes, depend on the crystal symmetry. The active phonon modes observed in a Raman scattering experiment also depend on the incoming and outgoing polarizations. The geometry and polarization gives rise to the Raman selection rules. They will be given in detail for a couple of lattice structures analyzed in this work.

In a quantum-mechanical description, a Raman scattering process involves electronic excitations[§]. The energy of a photon scattered by a phonon is changed by a discrete value. In a Raman process, the coupling between the light and the phonon is via virtual electronic states [51]. This is not the case of infrared scattering, which it is based on the direct coupling of the electric field of the light and that of molecule or phonon vibrations. This can be illustrated by the Feynman diagrams corresponding to a first order Raman process, see Figure 2.3. Since the energy is conserved between the initial and final states (Fermi golden rule), the intermediate steps in the Raman process (virtual

[||] For this work magnetic semiconductors are excluded, which can introduce antisymmetric components in the Raman tensor

[§] Equations 2.10 and 2.11 must be multiplied by a factor $n_B + 1$ for the Stokes contribution and by n_B for the anti-Stokes term. The term n_B is the Bose-Einstein factor. These terms appear in a quantum mechanical treatment of the Raman scattering.

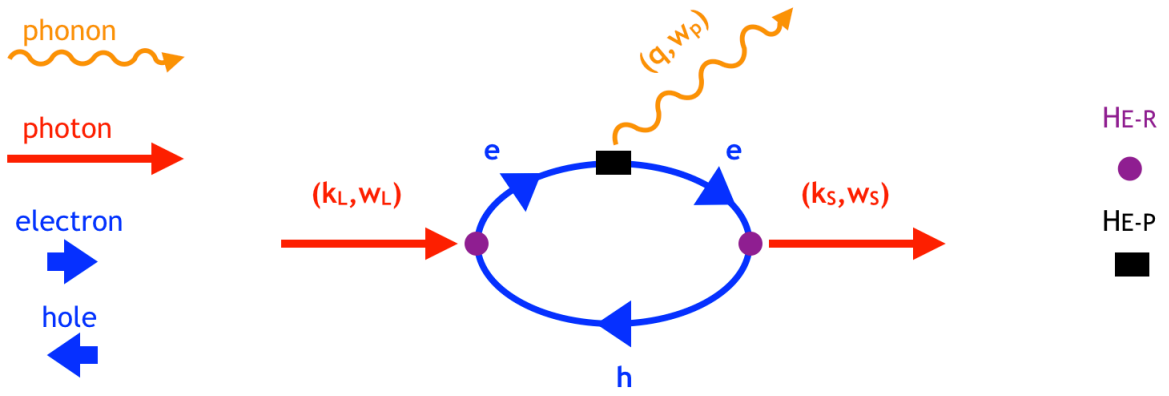

Figure 2.3: Feynman diagram for a first-order Raman scattering process in a semiconductor. A photon with energy $\hbar\omega_L$ creates an electron-hole pair. Then the electron emits or absorbs an optical phonon of energy $\hbar\omega_p$ and afterward the electron and hole recombine emitting a photon with energy $\hbar\omega_S$. H_{E-R} and H_{E-P} correspond to the electron-radiation and electron-phonon interaction Hamiltonians, respectively. In a complementary diagram the phonon can be emitted or absorbed by the hole.

electronic states) do not necessarily conserve energy, although the momentum is always conserved.

Following the Feynman diagrams, the Raman process happens in three steps. Firstly, an incident photon $\hbar\omega_i$ creates an electron-hole pair by excitation of the material from the ground state $|0\rangle$ to a virtual excited electronic state $|e\rangle$ (photon absorption). Secondly, the electron-hole pair at the electronic state $|e\rangle$ is scattered to a second intermediate virtual electronic state $|e'\rangle$ by the electron lattice interaction and a phonon with energy $\hbar\omega_q$ is created (Stokes) or annihilated (anti-Stokes). Finally, the electron-hole pair in the state $|e'\rangle$ decays into the electronic ground state $|0\rangle$ under the photon emission, $\hbar\omega_s$.

The Raman scattering probability corresponding to Figure 2.3 (only the Raman Stokes process is included) can be calculated with second-order perturbation theory [29]. The probability P_{ph} of scattering for a system from the initial state (in this case in the ground state$|0\rangle$) to the final state is then given according to Fermi's golden rule [52]:

(2.13)
$$P_{ph}[\omega_S] = \frac{2\pi}{\hbar}\left|\sum_{e,e'}\frac{\langle 0|H_{E-R}(\omega_S)|e'\rangle\langle e'|H_{E-P}(\omega_p)|e\rangle\langle e|H_{E-R}(\omega_L)|0\rangle}{[\hbar\omega_L-(E_e-E_0)]\left[\hbar\omega_L-\hbar\omega_p-(E_{e'}-E_0)\right]}\right|^2\delta\left[\hbar\omega_L-\hbar\omega_p-\hbar\omega_S\right],$$

where E_0, E_e, and $E_{e'}$ are the corresponding energies of the initial ($|0\rangle$) and intermediate

($|e\rangle$ and $|e'\rangle$) electronic states, respectively.

2.2.1.3 Raman Selection Rules

The intensity of the Raman process depends on the mode symmetry and the polarizations of the incident $\vec{e}_L$ and scattered light $\vec{e}_S$. From Equation 2.10 it follows that a phonon mode is Raman active if it induces a change of the Raman polarizability while is IR active (i.e. observable via infrared spectroscopy) if it induces a dipole moment. For systems with inversion symmetry the rule of mutual exclusion indicates that IR active vibrations are Raman inactive and vice versa. [53]. For a non centrosymetric crystal the normal modes can be both IR and Raman active. When these modes present a dipole moment are IR active and if the Raman polarizability is $\neq 0$ it is Raman active. Phonon modes which are neither Raman nor IR active are usually called silent modes.

Considering that the Raman tensor $\Re$ can be approximated by a symmetric tensor of rank two and using Eq. 2.11 one can calculate the polarization dependence of the scattered intensity, also referred to as Raman selection rules. Since most of the studied samples were grown in the zincblende (ZB) or wurtzite (WZ) structure, the discussion on the selection rules will be focused on these two special cases. The zone-center optical phonons in the zincblende structure correspond to a triply degenerate three dimensional representation, denoted in the literature as T_2 or F_2. The corresponding Raman tensor of the three modes can be defined as:

(2.14)

$$\Re(T_2(x)) = \begin{pmatrix} 0 & 0 & 0 \\ 0 & 0 & d \\ 0 & d & 0 \end{pmatrix}, \qquad \Re(T_2(y)) = \begin{pmatrix} 0 & 0 & d \\ 0 & 0 & 0 \\ d & 0 & 0 \end{pmatrix}, \qquad \Re(T_2(z)) = \begin{pmatrix} 0 & d & 0 \\ d & 0 & 0 \\ d & 0 & 0 \end{pmatrix}.$$

These tensors correspond to the phonon vibrations along the coordinate axes of the crystal x[100], y[010], and z[001] which form the $\{e_1, e_2, e_3\}$ basis. The triply degenerated zone-center optical phonon in the ZB structure splits for q$\neq$0 into a longitudinal optical (LO) (which pertains to the Raman tensor $\Re(T_2(x))$) and doubly degenerated transverse optical (TO) modes (related to the Raman tensors $\Re(T_2(y))$ and $\Re(T_2(z))$). Notice that the elements d in the Raman tensor $\Re$ are different for the LO and the TO modes due to the macroscopic longitudinal electric field. For WZ structure with C_{6v}^4 symmetry, the Raman tensors are given by [¶]:

[¶]The details of how to extract the Raman tensors for both structures can be found in reference [29].

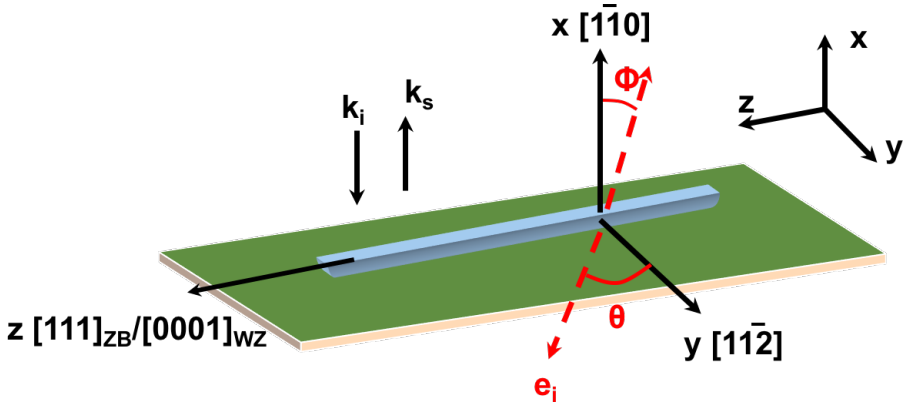

Figure 2.4: Backscattering geometry for lying nanowires. The angle between the incident light polarization and the nanowire z axis is defined as θ in the $z-y$ plane while ϕ corresponds to the rotation angle around the z axis with respect to the x axis in the $x-y$ plane. The principal axes of the nanowire are $x[1\bar{1}0]$,$y[11\bar{2}]$ and $z[111]$.

(2.15)
$$\Re(A_1(z)) = \begin{pmatrix} a & 0 & 0 \\ 0 & a & 0 \\ 0 & 0 & b \end{pmatrix}, \qquad \Re(E_1(x)) = \begin{pmatrix} 0 & 0 & c \\ 0 & 0 & 0 \\ c & 0 & 0 \end{pmatrix},$$

$$\Re(E_1(y)) = \begin{pmatrix} 0 & d & 0 \\ 0 & 0 & c \\ 0 & c & 0 \end{pmatrix}, \qquad \Re(E_2) = \begin{pmatrix} d & d & 0 \\ d & -d & 0 \\ 0 & 0 & 0 \end{pmatrix},$$

These tensors are used to calculate the scattering selection rules for the ZB and WZ structure. They are described using the Porto notation $\vec{k}_i(\vec{e}_i,\vec{e}_S)\vec{k}_S$, where $\vec{k}_{i,S}$ and $\vec{e}_{i,S}$ are the wave vector and the polarizations, respectively, of the incident i and scattered S photons (see Figure 2.4)[¶].

In the case of ZB structure, the selection rules of atomic displacements along the nanowire principal axes[‡] can be calculated transforming the Raman tensors of Equation 2.14. Firstly, the following transformation matrix is applied

[¶]The direction of the incoming and outgoing light gives us the geometry of the experiment (forward scattering). Depending on the geometry and polarization, a mode can be observed in the Raman experiment. All together is called Raman selection rules.

[‡]Notice that the principle axes of the nanowire are $x[1\bar{1}0]$,$y[11\bar{2}]$ and $z[111]$, forming the $\{ e'_1, e'_2, e'_3 \}$ basis.

$$\mathfrak{M} = \begin{pmatrix} \frac{1}{\sqrt{2}} & \frac{-1}{\sqrt{2}} & 0 \\ \frac{1}{\sqrt{6}} & \frac{1}{\sqrt{6}} & \frac{-2}{\sqrt{6}} \\ \frac{1}{\sqrt{3}} & \frac{1}{\sqrt{3}} & \frac{1}{\sqrt{3}} \end{pmatrix}, \tag{2.16}$$

in order to get the Raman tensors assigned for phonon displacements along the nanowire axes. Considering the facet $x[1\bar{1}0]$ as the upper surface of the nanowire (see Figure 2.4) the Raman tensors of atomic displacements along the x, y, and z axis in the $\{e_1, e_2, e_3\}$ basis can be estimated using:

$$\mathfrak{R}'_{e_i} = \sum_{j=1}^{3} \mathfrak{M}\mathfrak{R}_{e_j}, \qquad i = 1,2,3 \tag{2.17}$$

and the Raman tensors $\tilde{\mathfrak{R}}_{e'_i}$ in the $\{e'_1, e'_2, e'_3\}$ basis can be described by

$$\tilde{\mathfrak{R}}_{e'_i} = \mathfrak{M}\mathfrak{R}'_{e_i}\mathfrak{M}^T. \tag{2.18}$$

Implementing the Raman tensors 2.14 in Equation 2.17 and 2.18 one can calculate the Raman intensities of the zincblende structure for different configurations using Equation 2.11. It is worth mentioning that the scattering geometry determines the phonon wavevector $\vec{k}$ and the optical phonon modes are assigned to their tensors according to $\vec{k}$. For backscattering geometry, $\vec{k}$ is along $x[1\bar{1}0]$ in the laboratory coordinate system used in this work (Figure 2.4). Hence the selection rules for the LO phonon mode are determined using the relation $I_S \propto |\vec{e}_L \cdot \mathfrak{R}_{e'_i} \vec{e}_S|^2$. In the case of the TO phonon mode the selection rules are determined by the sum of the intensities obtained for the directions along y and z axis, respectively. The process to calculate them can be found in [28]. The polarization $\vec{e}_i$ of the incident radiation and the polarization $\vec{e}_S$ of the scattered light are expressed according to the z axis (which corresponds to the axis along the nanowire) in Figure 2.4 as

$$\vec{e}_i = \begin{pmatrix} 0 \\ \sin\theta \\ \cos\theta \end{pmatrix}, \qquad \vec{e}^{\perp} = \begin{pmatrix} 0 \\ 1 \\ 0 \end{pmatrix}, \qquad \vec{e}^{\parallel} = \begin{pmatrix} 0 \\ 0 \\ 1 \end{pmatrix} \tag{2.19}$$

where $\vec{e}^{\perp}$ and $\vec{e}^{\parallel}$ are the scattered radiation perpendicular and parallel to nanowire z axis. In this configuration, the LO phonon is forbidden in the case of a $x[1\bar{1}0]$ surface

in a ZB material for both parallel and perpendicular polarization. This does not apply, however, for a different surface facet. In order to examine the $[11\bar{2}]$ surface facet one needs to consider the upper surface of the nanowire as $x[1\bar{1}0]$. Then, the rotation of 90° of the nanowire along the growth direction $z[111]$ from the zincblende structure allows to get the selection rules for $x[11\bar{2}]$ surface. For this purpose, a rotation matrix $\mathfrak{S}$ is multiplied by $\mathfrak{M}$ as:

$$A = S \cdot (\phi)\mathfrak{M} \tag{2.20}$$

where ϕ (see Figure 2.4) is the rotation angle around the z axis and S the matrix rotation about the nanowire axis $z[111]$. S can be defined as:

$$S = \begin{pmatrix} \cos\phi & -\sin\phi & 0 \\ \sin\phi & \cos\phi & 0 \\ 0 & 0 & 1 \end{pmatrix} \quad . \tag{2.21}$$

Consequently, when A is implemented in equations 2.17 and 2.18, this rotation will affect the LO mode selection rules (the description of the polar intensity of the LO mode according to ϕ can be found at the references [25, 54–56]. One can notice that in this configuration the $x[11\bar{2}]$ and $x[1\bar{1}0]$ directions correspond to $\phi = 0$ and $\phi = 90°$, respectively. In the case of the $x[1\bar{1}0]$ direction, the LO is allowed for parallel and perpendicular polarization configuration, in backscattering. That has significant effects in a Raman spectrum as discussed in Chapter 5.

In the case of WZ structure, the transformation of the Raman tensors is not required because the scattered intensity for WZ nanowires grown in the [0001] direction[§] does not present any dependence on ϕ. Therefore, the allowed optical modes are represented by their respective tensors (Equation 2.15). The vibration of the atoms, polarity and selection rules for WZ structure are defined in Chapter 4 and 5 for GaN and InP nanowires. A special case of the activation of a silent mode non reported in the literature will be discussed in Chapter 4. The selection rules for different configurations and for ZB and WZ crystals are summarized in Chapter 5 (Table 5.1).

[§]The unit cell along [111] from ZB structure is equivalent to the [0001] direction of the WZ structure (Figure 2.4)and its unit cell length is double with respect to WZ along these direction.

2.2.1.4 Resonant Raman Spectroscopy

In Raman spectroscopy, the excited electronic states are virtual states while resonant Raman Spectroscopy (RRS) takes place if the energy of the excitation (or scattering) photons matches or is it very close to a real electronic transition (interband transition). Thus, the Raman scattering probability in Equation 2.13 diverges if actual electronic levels with energy E_e and $E_{e'}$ are real. In this case, the broadening or lifetime of the electronic states must be taken into account adding a factor Γ_e or $\Gamma_{e'}$ in the energy denominator of the Equation 2.13.

In general, at low temperatures the enhancement is larger because the broadenings are lower. In addition, the cases where the incident light $\hbar\omega_L$ or scattered light $\hbar\omega_S$ are close to $E_{e,e'}$ (energy of the real electronic states $|e\rangle$ and $|e'\rangle$, respectively) there will be an intensification of the Raman scattering due to resonance, which is known as incoming and outgoing resonances.

RRS has numerous advantages over the normal Raman Spectroscopy since it can give information on surfaces and interfaces with monolayer sensitivity, allows to study diluted nanostructures and it achieves higher material selectivity in multilayered structures. An important advantage is that some electronic properties of a sample can be inferred by its resonance effect. An example for these advantages is displayed in Chapter 4. By RRS, several effects as isotopic disorder on ultrathin GaN nanowires are analyzed and discussed in the course of this thesis, especially in section 4.1.5.

2.2.1.5 Experimental Raman setup

The essential parts of the Raman setup used in this work are: a laser to carry out the excitation of the sample (from UV to visible wavelengths), a spectrometer to separate the intensity of the light as a function of wavelength and a photodetector to measure their respective intensities. In particular, the laboratory components used for the Raman experiments were the triple Jobin Yvon T 64000 spectrometer (with the possibility to choose gratings among 900,1800 or 2400 grooves/mm), four different lasers for visible (Ar+/Kr+) and Ultra Violet (UV) wavelength, and a charge-coupled device (CCD) detection system with 1024 × 256 pixels cooled by liquid nitrogen. In addition, the system contains a confocal microscope and a $x-y-z$ microscope stage for micro-Raman experiments. The spectrometer has three fundamental operation modes, simple and triple, in this case in subtractive or additive. In simple mode only one grating (spectrograph) is used and the signal from the sample passes through an edge or Notch filter that consid-

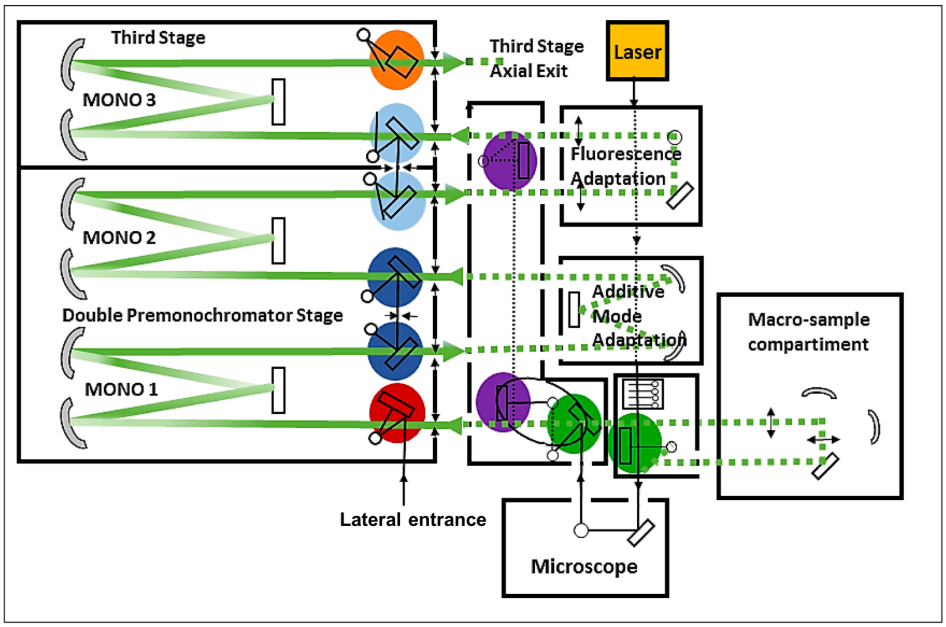

Figure 2.5: Schematic of a triple stage Raman spectrometer Horiba T64000 (adapted from Horiba).

erably reduces the Rayleigh scattering, coming from the laser line. In case of working in triple configuration in subtractive mode, the laser filtering is performed by the first two gratings (premono) of the monochromator system. The subtractive mode allows collecting spectra of low frequency bands very close to the laser line (typically down to 20 cm^{-1}) over a broad wavelength range and gives a high stray light rejection.

Since in many cases the Raman signal is very weak, the use of the lasers require the filtering of any emission that is different from the laser excitation chosen, as for example the spontaneous emission of the plasma lines. For this purpose specific holographic filters (or prism monochromators) are used for certain excitation lines. By selecting the appropriate filters, the laser is driven by the mirror combination to the objective of the microscope, which focuses a spot on the sample surface of the order of a few μm (for instance, using 514,5 nm laser line excitation and 100× objective the size of the spot will be around~ 1 μm). Then, the light scattered from the sample is collected in the microscope in backscattering configuration and orientated by mirrors to the triple monochromator. Finally, the spectrally dispersed light coming from the monochromator enters into the CCD detector and the signal on the computer is visualized. The complete process is controlled by the LabSpec software from Jobin-Yvon. To get a better understanding of the optical path and the different elements, the setup is illustrated in Figure

2.5. The specific requirements for each experiment are detailed in their corresponding subsection of the Chapter.

2.2.2 Surface Enhanced Raman Spectroscopy

Surface enhanced Raman spectroscopy (SERS) can be described as an extension of Raman spectroscopy where metallic nanostructures are used to enhance the intensity of Raman signal. Metal nanostrucutres (typically gold or silver) interacts with the light when the sample is illuminated with a laser. Laser excitation of these metallic structures resonantly drives the surface charges creating a highly localized (plasmonic) light field on the nearby molecules [57]. It should be taken into account that plasmonic properties of metallic nanostructures are strongly dependent on the geometrical parameters and the surrounding media of the nanostructures and thereby the extent of enhancement will depends on the shape and size of the metal nanoparticles. This technique has numerous advantages such as: positive identification of a molecule in situ, little sample preparation and present high levels of sensitivity compared with typical Raman spectroscopy.

2.2.2.1 Background of Surface Enhanced Raman Spectroscopy

Considering a single molecule the total Stokes Raman signal $P^{RS}(\omega_S)$ in absence of plasmonic nanoparticles can be approximated to

$$P^{RS}(\omega_S) = N\sigma^R_{free} I(\omega_L) \tag{2.22}$$

where N is the number of molecules in the probed volume [58], σ^R_{free} is the Raman cross section of the molecule and $I(\omega_S)$ is the excitation laser intensity. However, in the case the molecule is in the vicinity of the metal nanostructure, the Stokes Raman signal may be modified by two different effects, the enhancement of local electromagnetic fields and the chemical enhancement*.

If the electromagnetic enhancement factors $A(\omega_L)$ and $A(\omega_S)$ are defines as the enhancement for the laser and the Raman scattered field, N' is the number of molecules

*Although the exact mechanism for the enhancement in SERS experiments is not clearly understood, two sets of theory are accepted [59] by the scientific community; the electromagnetic and chemical theory. The electromagnetic mechanism relies on the excitation of the localized surface Plasmon (LSP) on metal surfaces, whereas the chemical theory proposes changes of the molecule electronic structure.

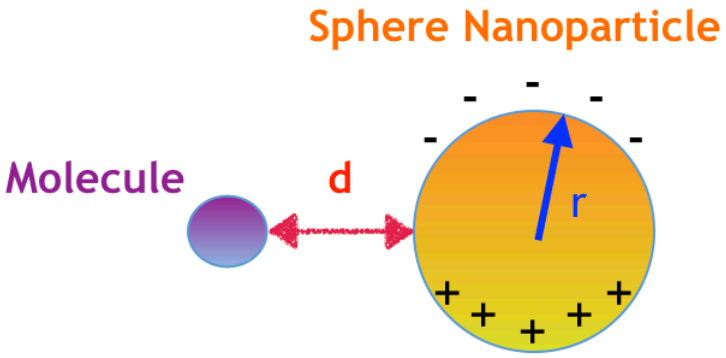

Figure 2.6: Schematic illustration of a molecule at a distance d from the surface of the metal sphere.

involved in the SERS process and σ^R_{ads} the new Raman cross-section after the chemical enhancement, the total SERS signal can be described as:

$$P^{SERS}(\omega_S) = N'\sigma^R_{ads}|A(\omega_L)|^2|A(\omega_S)|^2 I(\omega_L) \tag{2.23}$$

Considering a small nanoparticle in the quasi-static approximation, the distribution of the electric field E_{sp} of a point dipole in the centre of the metal sphere is defined by the following expression [†]

$$E_{sp} = \frac{\varepsilon_{metal}(\omega) - \varepsilon_{medium}}{\varepsilon_{metal}(\omega) + 2\varepsilon_{medium}} \frac{r^3}{(r+d)^3} E_0 \tag{2.24}$$

When a molecule is at a distance d from the surface of the metal nanoparticle (Figure 2.6) it experiences a field E_m ($E_m = E_0 + E_{sp}$), which is the sum of the incident field E_0 and the induced field E_{sp}. Then, the field enhancement factor $A(\omega)$ can be defined as the ratio of the total field at the position of the molecule to the incident field.

$$A(\omega) = \frac{E_m(\omega)}{E_0} \sim \frac{\varepsilon_1(\omega) - \varepsilon_2}{\varepsilon_1(\omega) + 2\varepsilon_2} \frac{r^3}{(r+d)^3} \tag{2.25}$$

Therefore, the total enhancement factor for the Stokes signal in the small particle approximation is given by

[†]Note that this equation is valid for the molecules oriented in the dipole orientation of the metal sphere.

$$G_{em}(\omega_S) = |A(\omega_L)|^2 |A(\omega_S)|^2 \sim \left|\frac{\varepsilon_1(\omega_L) - \varepsilon_2}{\varepsilon_1(\omega_L) + 2\varepsilon_2}\right|^2 \left|\frac{\varepsilon_1(\omega_S) - \varepsilon_2}{\varepsilon_1(\omega_S) + 2\varepsilon_2}\right|^2 \left(\frac{r}{r+d}\right)^{12} \tag{2.26}$$

where the overall enhancement scales as the fourth power of the local field of the nanoparticle and decreases with increasing distance by the factor $1/d^{12}$ (the decay of the field of a dipole over the distance $1/d^3$ to the fourth power). By checking this equation the possibility to obtain an enhancement of $\approx 10^{11}$ for the gap between two spherical particles separated by 1 nm distance can be observed [58].

2.2.3 Photoluminescence Spectroscopy

Photoluminescence (PL) spectroscopy is a powerful contactless nondestructive technique that allows the investigation of the band-structure of the semiconductors. This technique provides direct measurement of the bandgap energy and can be employed to determine the presence of impurities, dopants and structural defects. The technique is based on the radiative recombinations of photoexcited $e-h$ pairs. When an $e-h$ pair is created by the absorption of an incoming photon with energy higher than that of the band gap, the pair thermalizes quickly to the lower energy state and recombines radiatively by emitting a photon of lower energy [‡] (the emitted photon usually has an energy equal to the band gap energy). In case these pairs are located at different energy states, the photons emitted during their radiative recombination have distinct energies which correspond to different transitions in the semiconductor. The setup employed in most of the experiments is the same as for the Raman spectroscopy measurements. For μPL and Macro-PL measurements on ZnO nanowires the setup installed at Solid-State group of Carsten Roning at the University of Jena was employed, see Figure 2.7.

For macro-PL measurements the laser light is focused onto the surface of the sample by means of Beam Splitter 2 (BS2) and mirror 4 (M4) whose intensity can be adjusted using a variable neutral optical density filter (OD) and measured by the Si-power meter 2. The luminescence of the sample is collected with the lenses L1 and L2 and focused onto the monochromator. The laser light reflected from the sample is eliminated with the Ultraviolet blocking filter F1. For μPL measurements, the laser light is guided by BS3 and focused by a 50× objective onto the sample. The luminescence is collected in backscattering geometry, passes the BS3 and the long pass filter (F3) and is detected either by a TV camera or the CCD detector for spectral acquisition.

[‡] In fact, the recombination of electrons and holes can be caused by band-to-band transitions, excitonic transitions, free-to-bound transitions and donor-acceptor pair transitions. For more details, see Refs. [29].

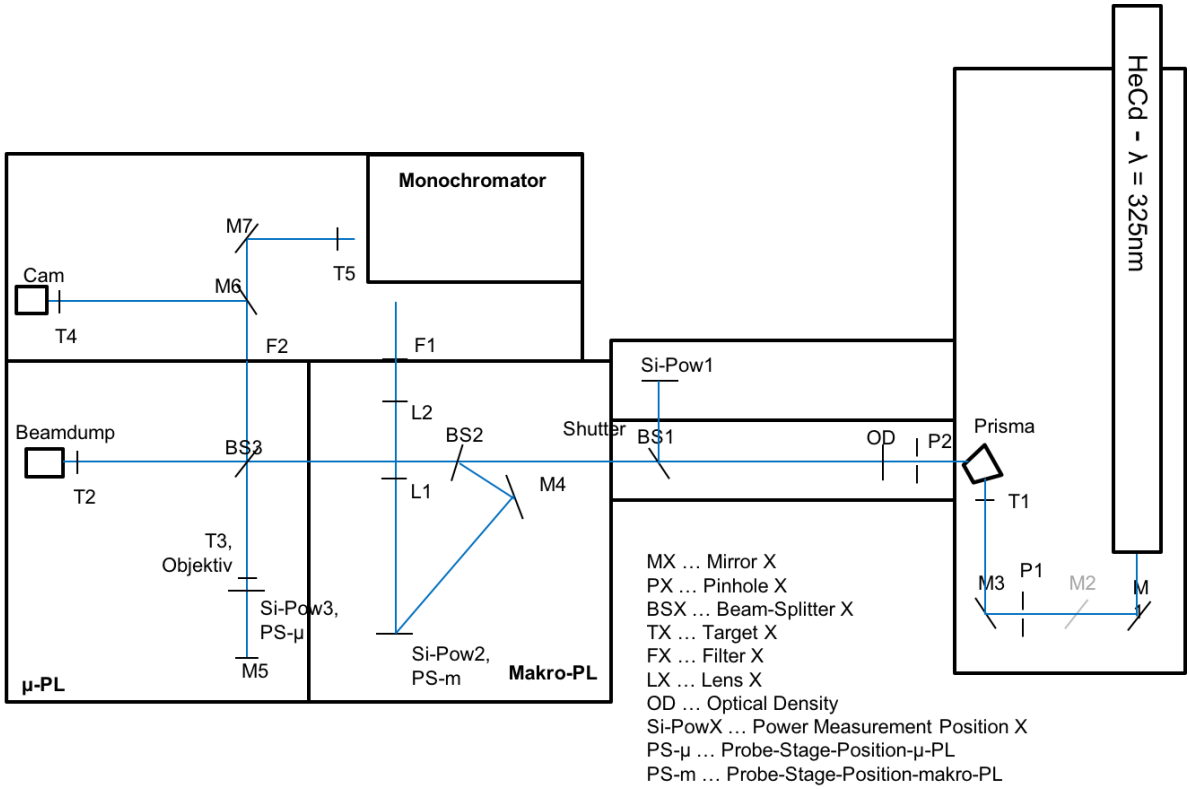

Figure 2.7: Scheme of the macro and μPL of Carsten group.

2.2.4 Atomic Force Microscope

Atomic Force Microscopy (AFM) is a type of Scanning Probe Microscopy (SPM) which provides topographical information down to the atomic scale and allows to measure local properties, such as height, friction, magnetism, with a mechanical probe. There are two primary modes of operation for an atomic force microscope, the so-called contact mode where the cantilever drags across the sample surface and it uses the deflection of the cantilever to measure the contours of the surface of the sample, and the non-contact mode where the tip does not contact the surface of the sample and vibrates slightly above its resonance frequency. The use of AFM during this work is only focused on the specific shape and dimensions of individual constituents. Furthermore, AFM combined with a Raman spectrometer by the AFM-Raman system (NTEGRA spectra PNL) was employed to measure simultaneously the topography and mapping phonon displacements of individual InP nanowires in the same sample area.

2.2.5 Scanning and Transmission Electron Microscopy

Morphology characterization and the study of surface properties of all samples were performed using Scanning electron microscopy (SEM). In many instances, the diameter of nanowires and SERS nanoparticles are typically below the Abbe resolution limit of light microscopes and the electron microscope allows the needed resolution for structural characterization at nanometer scale since it provides a resolution limit in the order of the DeBroglie wavelength of the electrons.

Electron microscope is a powerful magnification tool that utilizes focused high kinetic energy beam of electrons to generate a variety of signals at the surface of solid specimens in order to obtain information. The signals that derive from the electron-sample interactions provide topographical, morphological and compositional information. This signals include secondary electrons (SE), transmitted electrons, back-scattered electrons (BSE), specimen current, light and characteristic X-rays. For SEM characterization SE are collected by various detectors installed in the SEM chamber and used for surface imaging. More information about SEM technique are given in [60, 61]. SEM images were taken in different groups. Most of the SEM measurements for structural characterisation were performed with a JEOL JSM-6490 SEM equipped with a LaB6 thermal electron gun with a resolution down to 10 nm at the Jena University and S-4800 (HITACHI) with spotlight of field emission (FEG) with 1.5nm to 30kV resolution from the University of Valencia.

On the other side, for Transmission Electron Microscopy (TEM) a beam of high-energy electrons is transmitted through an ultra thin specimen to form an image. For this thesis, samples such as Bi_2Te_3 nanowires were transferred to a TEM subtrate (which is made up of a copper grid with a carbon foil) by imprint and placed in a TEM system. TEM investigations were at the performed Central Service for experimental research at the University of Valencia using a TECNAI G2 F20 (FEI) with 0.24nm resolution (point resolution). This equipment allows making HRTEM images, diffraction patterns of electrons and spectroscopic techniques such as EDS and mapping.

2.2.6 Energy dispersive X-ray scattering

Energy Dispersive X-Ray Analysis (EDX), also referred to as EDS or EDAX, is an analytical technique employed to identify the elemental composition of materials or chemical characterization of a sample. This technique was used in combination with Raman Spectroscopy and TEM studies in Chapter 3 to investigate the elements and their stoi-

chiometric composition (energy dispersive X-ray spectroscopy) in Bi_2Te_3 nanowires and films. The capabilities of the EDX system is based on the fundamental principle of spectroscopy where each element has a unique atomic structure which allows a unique set of peaks on its electromagnetic emission spectrum, in this case, through the analysis of X-rays emitted from the matter in response to the stimulus of a high-energy beam of charged particles. As a high-energy beam of electrons penetrates the samples, target atoms can be ionized leading to holes generated on the core shells. Then bound electrons of outer shells fill the holes and cause the emission of X-ray fluorescence lines whose energy is characteristic for each element and transition.

2.2.7 Reflection high energy electron diffraction

Reflection high energy electron diffraction (RHEED) was used to monitor in situ the surface of the ultrathin GaN nanowires samples during the growth. This system is based on the electron diffraction of the crystal structure of the sample. The high energy electrons beam is provided by an electron gun in a grazing angle (1-2°) with respect to the sample and images are captured by fluorescent screen installed at the opposite side of the electron gun. This technique only reflects the surface of the sample since the penetration of the electron beam is around one or two monolayers which is enough for studying nanowires with 10 nm of diameter.

CHAPTER 3

Optical characteristics of GaN nanowires and Bi_2Te_3 Nanowires and films

This chapter study analyzes the structural and optical properties of GaN nanowires and Bi_2Te_3 nanowires and films. For this purpose, the section is splitted into two different parts for each material. In the case of GaN, surface optical phonon modes related to surface effects were observed on individual nanowires. These nanowires were grown by VLS using cobalt phthalocyanine as catalyst. For ensembles of Bi_2Te_3 nanowires the signature of stoichiometric as well as Te-rich samples in bulk and in the form of nanowires are shown in the Subsection 2. Additionally Bi_2Te_3 films were also characterized. Although several techniques were used to characterized the samples structurally and morphologically, Non-Resonant Raman Spectroscopy was the main tool employed.

GaN nanowires were synthesized and characterized in collaboration with Shivesh Yadav and Subhabrata Dhar. The details of the synthesis and electrical characterization have been published in [62]. The synthesis of Bi_2Te_3 nanowires were performed by Cristina Vicente Manzano and Marisol Martín-González. Optical characterization was investigated in close collaboration with Cristina Vicente Manzano. Total energy calculations were performed by Aldo H Romero. The characterization of stoichiometric and non stoichiometric Bi_2Te_3 nanowires were published on [63].

3.1 Motivation

One hand, Gallium nitride (GaN) has revolutionize the optoelectronic industry in the last few years. The appearance of blue and violet light emitting diodes (LEDs) and lasers [64] in the market not many years ago permitted a huge increase in the capacity of digital versatile discs (DVDs) and to lay the foundation stone towards the future white illumination without Joule loses [65]. In addition, GaN in the nanowires form have attracted considerable attention because of their potential for developing nanoscale electronic and optoelectronic devices, which offer new functionalities as compared to their conventional bulk counterparts, as we have previously seen. For example, there are reports on GaN nanowire based blue lasers [66], photodetectors [67, 68] light emitting diodes (LEDs) [69, 70] high electron mobility transistors (HEMT) [71] and sensors [72] showing the capabilities of the GaN nanowires.

One of the most characteristic features of GaN is its wide band gap. It has also been demonstrated to have superior electrical performance and chemical stability at high temperatures. These characteristics make GaN-based materials very interesting for application in monolithic solar-thermoelectric energy cells. In addition, engineering band gap of materials by doping and alloying are effective approaches to reduce the high thermal conductivity and increase the electrical conductivity.

On the other hand, Bismuth telluride (Bi_2Te_3) is an exceptional material with a great potential for different applications, especially used in thermoelectricity [73]. Bi_2Te_3 and its alloys are the best bulk thermoelectric materials known today. An enhanced thermoelectric efficiency, usually measured by the dimensionless figure of merit ZT ($ZT = \alpha^2\sigma/k$, where α is the Seebeck coefficient, σ the electrical conductivity and k the thermal conductivity) can be increased when Bi_2Te_3 is combined with Sb_2Te_3 in the form of superlattices or nanocrystals [74] due to the decrease of the lattice thermal conductivity ($ZT \sim 2$). The growth of Bi_2Te_3 in the form of nanowires also allows to increase ZT due to the decrease of the thermal conductivity [75, 76]. On the other hand, in Bi_2Te_3/Te heterostructures and Bi_2Te_3 nanoplates with Te nanocrystals in between, a Seebeck coefficient 40 times larger than that shown in stoichiometric samples was obtained (replacing Bi by Sb provides similar results) [77]. However, excess of uncontrolled Te can lead to the degradation of the crystallinity of the material both −in nanowires and films− decreasing the electron mobility and therefore also lowering the thermoelectric power factor [78, 79]. A second interesting property of Bi_2Te_3 is the fact that its surface can be conducting while the bulk material is an insulator. Bismuth telluride is

actually a three-dimensional topological insulator [80, 81]. Other materials like Bi_2Se_3 [82] or Bi_2Se_3/Sb_2Se_3 heterostructures [79] are also well-known topological insulators. There is a huge amount of work on this topic nowadays because of the vision of novel applications, mainly in spintronics [83].

3.2 GaN nanowires

3.2.1 Growth and morphology of GaN Nanowires

It is reasonable that device based on nanowires should have high optical and transport qualities because defects in the lattice limit light emission, introduce signal noise, and lead to early device failure. In order to fully benefit from the advantages related to the dimension of nanowires in electronic and optolectronic nanodevices, nanowires should be grown with a good crystal quality and well-defined composition because a change in crystal structure has significant effects on the physical properties of the nanowire [26].

Most of GaN nanowires are often synthesized using VLS or vapor-solid-solid (VSS) mechanisms, where metal catalysts (Au, Ni, In...) are used for the nucleation and growth [84–86]. These techniques offer a cost-efficient solution with high quality for synthesis. Moreover, VLS growth can be carried out almost on any substrate. However, a drawback of VLS method is the risk of inclusion of the metal catalyst as impurity in the nanowires, which can affect their optical and electrical properties. Additionally, more metal complex materials have been employed as catalyst like ferrocene, iron phthalocyanine, nickel phthalocyanine, and cobalt phthalocyanine [87]. In the present work, GaN nanowires were synthesized using VLS technique with cobalt phthalocyanine as catalyst.

GaN nanowires were grown on Si (100) substrates using VLS in a chemical vapor deposition (CVD) reactor. High purity gallium (99.9995%) and ammonia (99.9995%) were used as precursors and cobalt phthalocyanine (Co-Ph) (β-form, dye content 97%) was used as catalyst [87]. Argon (99.999%) was used as the carrier gas. 100 mg of metallic gallium was kept on a Si wafer, which was then placed inside a cylindrical quartz reactor. 50 mg of cobalt phthalocyanine was dissolved in 1ml of toluene and casted on the Si substrate, which was then dried under infrared (IR) light and placed beside the gallium containing Si wafer. The reactor was purged with argon gas at a rate of 200 sccm for 20 min. The reactor temperature is then set to increase temperature. Ammonia flow was opened when temperature reaches 300 °C and kept at 20 sccm (cm^3/min in standard

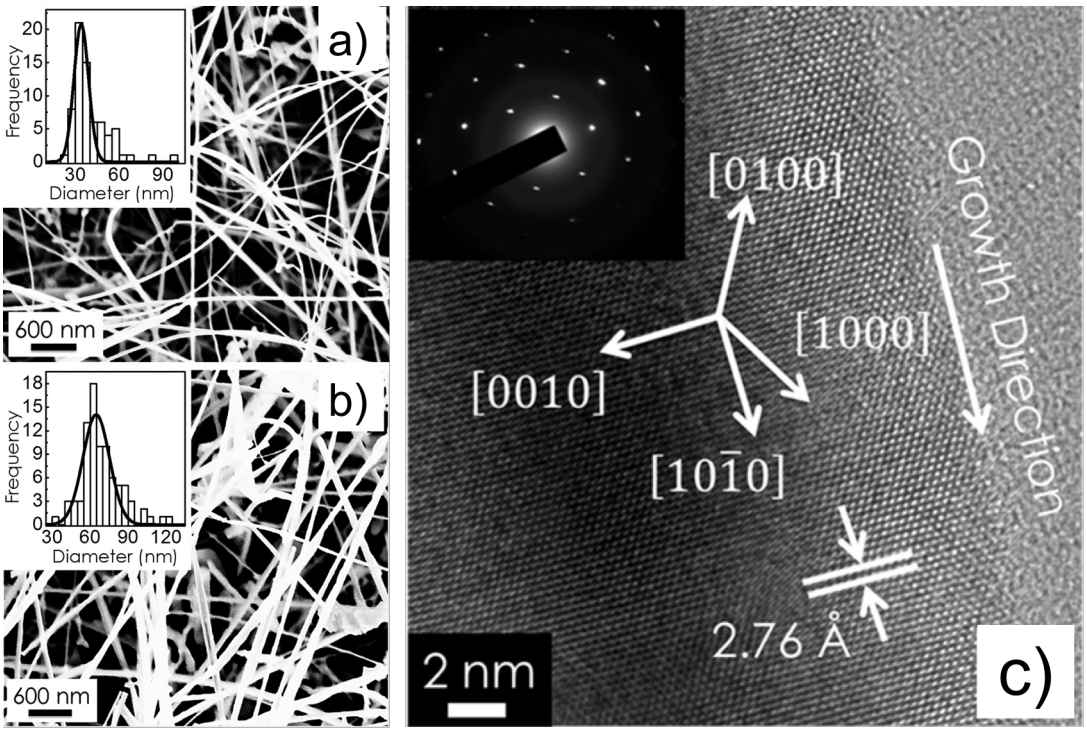

Figure 3.1: FE-SEM top view images for samples grown at 870 °C with ammonia flow rates of (a) 10 sccm and (b) 40 sccm. The inset (a) shows the histogram plot for the diameter distribution. Solid black lines represent fitting with a Gaussian function c) HRTEM image displaying a portion of a nanowire grown at 920 °C with ϕ_{NH_3} = 20 sccm. The inset of the Figure (c) represents the selective area electron diffraction (SAED) pattern recorded for the region with [0002] to be the zone axis.

conditions for temperature and pressure) throughout the growth. Several samples were grown with ammonia flow rate ϕ_{NH3} ranging from 5 to 50 sccm and growth temperature T_G ranging from 845 to 1010 °C. Growth was carried out for 5 h for all samples. The structural and morphological properties of the nanowires were investigated using HRTEM an field emission scanning electron microscopy (FE-SEM). Samples were dispersed in methanol and then drop casted on carbon coated TEM grids for the HRTEM study.

Figure 3.1 shows the FE-SEM top view images for samples grown at 870 °C with different ammonia flow rates. Several tens of micron long nanowires with diameter of a few tens of nanometer are evident for both samples. Noticeably, wires are narrower in sample grown with ϕ_{NH3} = 10 sccm. Diameter distribution is obtained from line scan analysis of various top view images recorded at different parts of these samples. Insets of the respective panels show the histogram plots of the distribution. The distribution

is shifted to smaller diameter (peaking at 34 nm) for the sample grown with ϕ_{NH_3} =10 sccm as compared to that (peaking at 65 nm) for the sample grown with ϕ_{NH_3} =40 sccm. It has to be noted that the wires with diameter smaller than 15 nm could be found in ϕ_{NH_3} =10 sccm sample [note that the size estimation through SEM becomes harder for the wires with diameter smaller than 10 nm]. However, small narrow wires are hardly observed in 40 sccm sample. In fact, the average diameter has been found to increase with ϕ_{NH_3}. It should be mentioned that nanowires are also grown at various temperatures ranging from 845 to 1010 °C, keeping ϕ_{NH_3} fixed at 20 sccm. It has been observed that the overall nanowire density decreases with T_G but the average diameter of the nanowires does not change.

Figure 3.1 (c) shows the HRTEM image displaying a portion of a nanowire grown at 920 °C with ϕ_{NH_3} = 20 sccm. The inset of the figure represents the selective area electron diffraction (SAED) pattern recorded with [0002] as the zone axis for the region. Interplanar distances, which are determined from the SAED pattern as well as directly from the micrograph, confirm the wurtzite phase for the wire. It is noticeable that the growth direction of the wire is $[10\bar{1}0]$ (non-polar m-plane).

3.2.2 Optical characterization of GaN nanowires

Photoluminescence spectroscopy was carried out at various temperatures ranging from 10 to 300 K. In PL, samples were excited with a 25 mW He-Cd laser (325 nm). Emission was sent through a 0.5m focal length monochromator and detected using a Peltier cooled CCD array from Andor. The Figure 3.2 (a) compares the normalized room temperature PL spectra for samples grown at various temperatures keeping the ammonia flow rate fixed at 20 sccm. All the spectra are featured by only a near band edge transition. Moreover, density of defects related to the yellow luminescence (YL) band (at 2.2 eV), which are quite common in GaN [88], have hardly been observed in any of these samples. This suggests that the density of defects related to yellow luminescence must be very low in these samples. In the inset of the Figure 3.2 (a), near band edge profiles are shown in an extended scale. Clearly, the peak shifts to higher energies as the growth temperature increases. When examined closely, the band edge feature is found to be comprising of two peaks. The near band edge feature is deconvoluted with two Gaussians for these samples, which returns two peaks centered at 3.28 and 3.40 eV. Figure 3.2 (b) shows the ratio of the integrated intensities of the high energy and low energy peaks R_{hl} as a function of growth temperature. Evidently, R_{hl} increases with the growth temperature. The apparent blue shift of the band edge feature is thus due to the enhancement of the

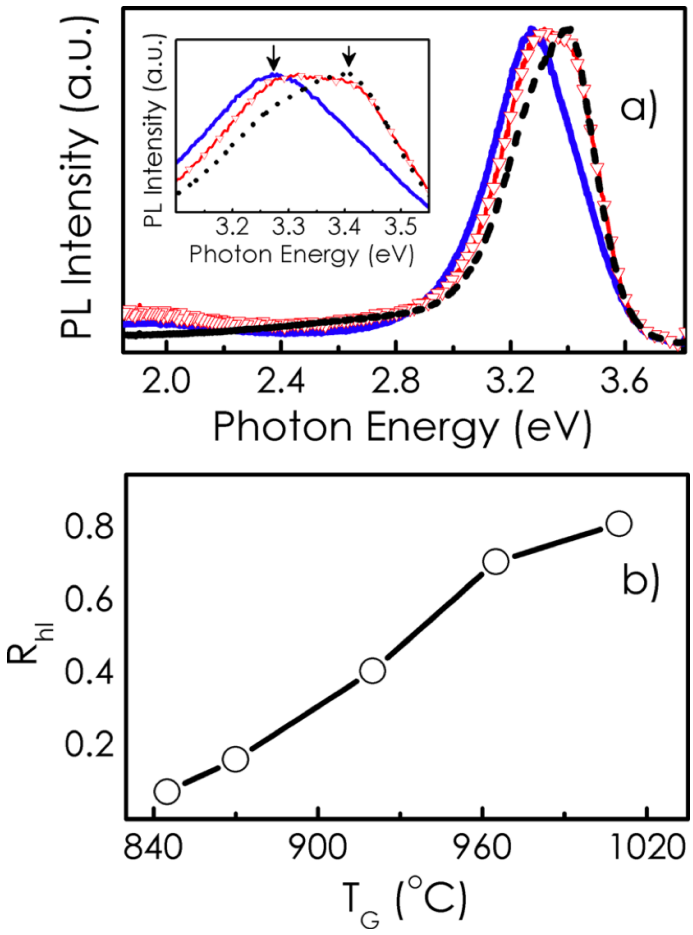

Figure 3.2: (a) Normalized room temperature PL spectra recorded for the samples grown at 845 °C (solid blue), 920 °C (red connected triangle), and 1010 °C (black dashed) with fixed ϕ_{NH_3} = 20 sccm. The inset shows the band edge part of the spectra in an extended scale. (b) The ratio of the integrated intensities of the high energy and low energy peaks R_{hl} as a function of growth temperature.

relative intensity of the higher energy peak with increasing T_G.

As can be observed, Figure 3.3 presents normalized PL spectra recorded at 10 [panel (a)] and 300 K [panel (b)] for samples grown at different flow rates at a fixed T_G of 870 °C . These measurements allow to study the role of the ammonia flux on the luminescence characteristics of the GaN nanowires. All of these samples were featured by the near band edge transitions both at 300 and 10K. Neither YL nor any other transition could be observed for these samples even down to the lowest photon energy of 1.85 eV explored here. Twin peak structure of the band edge feature, which has already been observed in Figure 3.2, is more prominently resolved at 10 K for 40 sccm sample [see panel (a)]. The sharper feature, which appears at 3.478 eV, can be attributed to free

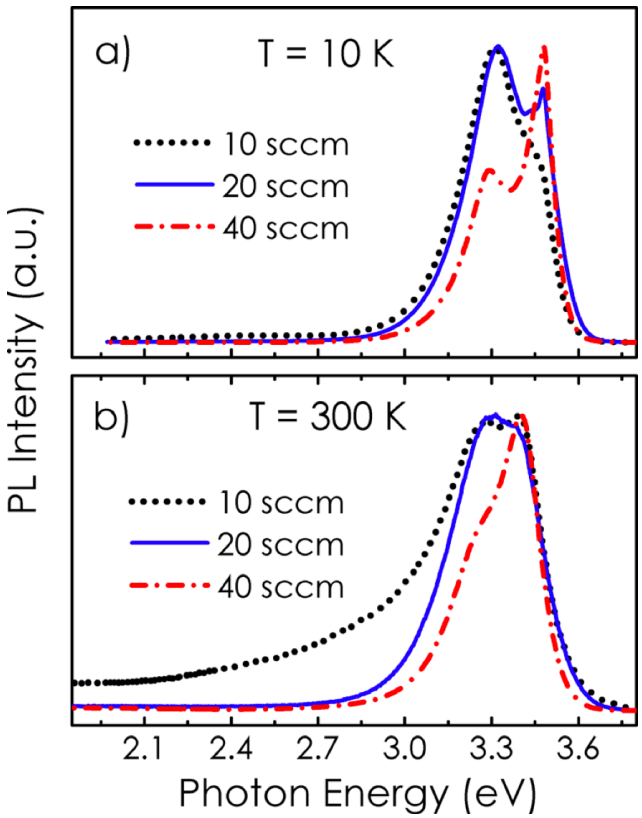

Figure 3.3: Normalized PL spectra recorded at (a) 10K and (b) 300K for samples grown at 870 °C with different flow rates.

excitons (FX) as its position matches very well with that reported for FX transition of GaN [88]. While the peak appearing at 3.29 eV can be attributed to certain type of defects (might be associated with the recombination of excitons trapped in certain defects [62]). It is interesting to notice that at both temperatures, the intensity of this defect feature (peak located at 3.29 eV) gradually decreases with respect to that of the FX transition as the ammonia flow rate increases. Furthermore, the defect feature becomes narrower with increasing the ammonia flow rate. These findings show that the density of the defects responsible for this transition must be decreasing with the increase in reactive nitrogen flux during growth. This in turn suggests that defects, which result from nitrogen deficiency, might be responsible for this transition. Note that in Figure 3.2, the ratio of the higher energy to lower energy peak intensities R_{hl} has been found to increase with increasing the growth temperature. This observation is in fact consistent with that of Figure 3.3 as the flux of reactive nitrogen is expected to increase due to higher dissociation rate of ammonia with increasing growth temperature.

Apart from photoluminescence studies, the samples were characterized by means

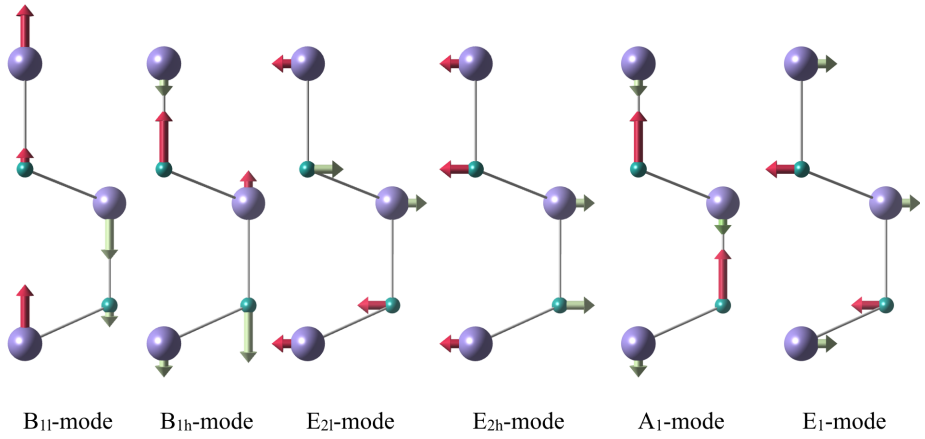

Figure 3.4: 9 Optical modes of the wurtzite structure. The arrows indicates the instantaneous movement (a picture in the time). Purple and cyan circles are represented by Ga and N respectively. There are two types of the E_2 and B_1 modes that are distinguished by superscripts L (low) and H (high).

non-resonant Microscope Raman Spectroscopy. In principle, a Raman scattering process give us information of the phonons at the Γ-point or zone center since the wave number of the exciting light is basically zero (in the dipole approximation). However, through the Raman scattering overtones more information can be extracted from Raman spectrum. Overtones are modes at the border of the BZ (zone of Brillouin), which can be accessed through two phonon process ($k \approx q_1 \pm q_2$) , where k is the wave number of the light and q_1 and q_2 the wave number of the phonons involved in the Raman process. Typically, there is a whole structure at the background of a Raman spectrum called two-phonon density of states (DOS) where many phonons can be involved (several examples of DOS will be presented in the next section and in Chapter 4 fot Bi_2Te_3 and GaN, respectively). As previously reported in the growth section GaN nanowires were obtained in the wurtzite phase, where the growth direction of the wires was along $[10\bar{1}0]$. Following group theory, the phonon modes in the wurtzite structure have the following decomposition [89]:

$$\Gamma = 2A_1 + 2B_1 + 2E_1 + 2E_2 \tag{3.1}$$

The three acoustic modes are $A_1 + E_2$, while the remaining 9 are optical. The $E_1 + A_1$ are polar modes, *i. e.* they split into TO and LO, while the E_2 modes are non polar.

For Raman characterization GaN nanowires were mechanically transferred from the

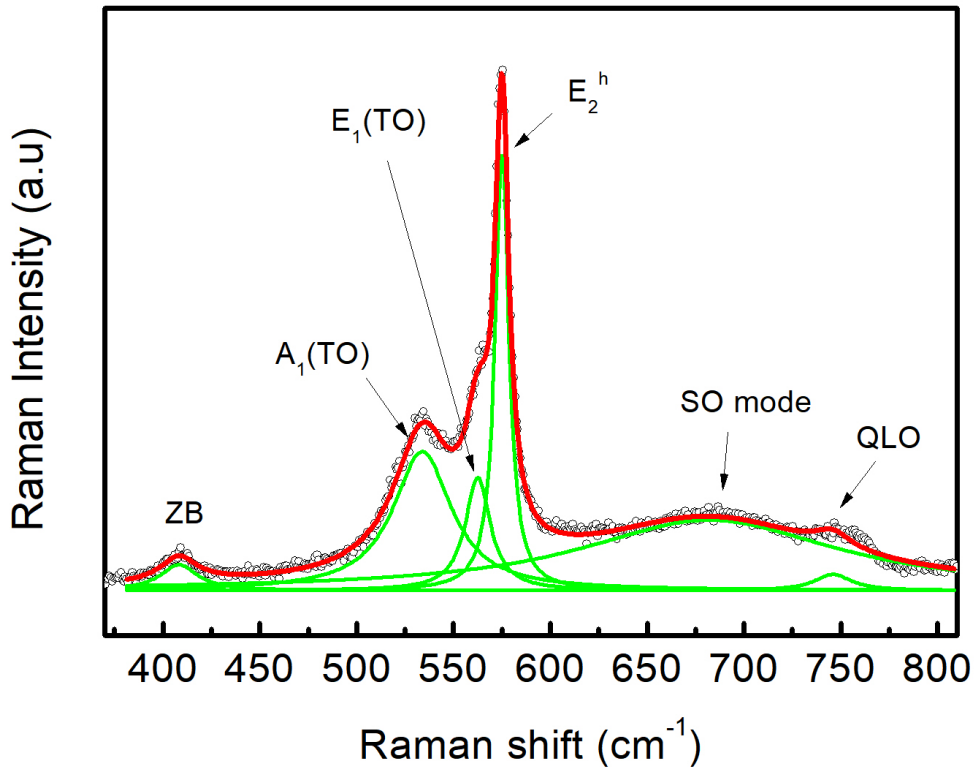

Figure 3.5: Raman spectra recorded on an individual GaN nanowire grown at 920 °C with ϕ_{NH_3} =20 sccm. The Raman spectra was fitted with Lorentzians from each individual modes. The cumulative peak is represented by red colour.

growth substrates to marked substrates by simply dragging and dropping, then individual nanowires break and fall onto the marked substrate (see Appendix A.1). Raman scattering measurements were carried out at room temperature in backscattering configuration using the setup described in Chapter 2 (subsection 2.2.1.5). Excitation line at 514.5nm was provided by an Ar/Kr laser focused onto the sample with a 100× microscope objective having a numerical aperture of 0.90. To avoid sample heating during the experiment a special care was taken. No polarizer was used in collecting the backscattered light. Analysis of the phonon modes of GaN are limited to the spectral range from 350 cm^{-1} to 800 cm^{-1} . Raman measurements were performed on single nanowires. Considering laser line excitation, x-direction, is set perpendicular to the nanowire axis (nanowires are in lying position), LO modes are forbidden (more information about selection rules in Chapter 2 and 5).

Table 3.1: Optical phonon modes of the Raman spectrum compared with the reported biography.

Phonon mode	GaN NW (cm^{-1}) [a] (data reported)	GaN NW(cm^{-1}) [b] (data reported)	GaN NW(cm^{-1}) (this work)	Bulk GaN (cm^{-1}) [c] (data reported)
ZB	252	254	−−	−−
ZB	421	421	410	−−
$A_1(TO)$	537	533	534	533
$E_1(TO)$	562	560	562	561
E_2^h	569	569	573	569
$A_1(LO)$	728	725	−−	735
$SO(A_1)$	−−	652	687	−−
$SO(E_1)$	−−	691	−−	−−

[a] Reference [87]
[b] Reference [90]
[c] Reference [91]

Figure 3.5 shows a typical Raman spectrum recorded at room temperature in backscattering geometry for single nanowire. E_2^h , A_1^{TO} , and E_1^{TO} Raman modes are located at 573, 534 and 562 cm^{-1} respectively, which are associated with the wurtzite phase of GaN, in agreement with the literature [90, 92, 93].

When the phonon modes in the Table 3.1 are carefully examined, these peaks are found to be similar to that of bulk crystals. However, three additional modes are observed at 410, 687 and 746 cm^{-1}, all of which are not identified by the C_{6v}^4 ($P6_3mc$) space group in first-order Raman scattering at the zone centre. Possible mechanisms that could bring these peaks are discussed below. It is worth mentioning that these peaks were observed at different spots and places of the individual GaN nanowire samples. Thus, the possibility of any impurity contaminant effect is highly implausible in the present analysis. The peak at 410 cm^{-1} was assigned by Sahoo to a zone boundary (ZB) [90]. The peak centered at 746 cm^{-1} is described at the literature as a forbidden $E_1(LO)$ Raman mode induced by the Fröhlich interaction or quasi-LO mode (QLO) [94, 95]. However, no resonance measurements were performed on these samples because the laser excitation of 2.41 eV (514.5 nm) was far below the GaN band gap of 3.47 eV. Therefore, this mode mode was assigned as a quasi-LO mode which originate from the interaction of phonons belonging to the A1 and E1 symmetry groups [94–96]. Finally, the broad feature appearing at 687 cm^{-1} had already been previously reported as a surface optical (SO) phonon modes [71, 97]. The elongated shape of nanowires gives rise to a large surface-to-volume ratio, resulting in the appearance of new vibrational modes related to the oscillation of surface atoms which are characteristic vibrations of

the free surface of polar semiconductors, as GaN. The characteristics of SO modes will be explained in the next subsection.

3.2.2.1 Surface optical phonon modes

In a crystal, the number of phonon modes depends on the number of atoms in the unit cell. Very thin nanowires have translational symmetry only along the nanowire axis. We can suspect the presence of confined modes in the plane perpendicular to the nanowire. But, as it has been previously shown, phonon confinement is produced if the dimensions are below 3-4nm. Otherwise the confine modes overlap an finally they contribute to the asymmetry of the Raman peak. Nanowires of the order of several tens of nanometers could be considered a bulk material. The only difference from bulk will be the appearance of a surface or an interface (core/shell nanowires) mode which are called in the literature surface optical (SO) modes.

The concept of surface phonon is similar to the ordinary lattice vibrations in bulk. However, surface phonons are exclusively related to lattice vibrations of a solid surface and the atoms involved in their propagation are confined to the near-surface region of the material. Since the atomic amplitudes of SO decay exponentially with the distance from the surface they could not be observed in bulk materials. The contribution to the intensity of bulk phonons masks the possible existence of SO modes. They are only observable in very thin films or other kind of nanostructures. As is well known, lattice vibrations depends on the symmetry of the crystal structure, while surface vibrations arise from the abrupt termination of the crystal. This causes surface vibrations be of interest in semiconductor nanomaterials (such as two-dimensional or one-dimensional nanostructures), because they can couple with electrons and thereby affect the electrical and optical properties of semiconductor devices. There are numerous studies that reveals that these modes are influenced by the shape, roughness or any perturbation on the surface potential (defect density, surrounding medium...) capable of absorbing the phonon momentum [87, 98–100].

Although many techniques have been proposed to analyze SO phonons, such as high resolution electron energy loss spectroscopy and He-atom scattering (Ibach and Mills, 1982; Benedek and Toennies, 1994), Raman scattering spectroscopy is also an effective tool for the investigation of SO modes. The resolution and sensitivity of modern Raman equipments allow the observation of Raman signals generated by SO phonons as can be appreciated in Figure 3.5. In general, since the signal is very weak as compare to other phonon modes, these phonons are difficult to observe. There are only a few reports

available where SO phonons are studied by Raman in GaN nanowires[94, 101–103].

SO phonons are generated and propagated along the interface and depend on the dielectric function of the semiconductor as well as on the material, e.g. air, oxide, or any liquid in contact with the surface and their frequency depend on the wave vector q measured along the surface. The SO frequency corresponds to wave numbers in between the TO and LO phonon modes.

Considering a single cylindrical semiconductor nanowire with a radius r, the calculated SO mode frequency for $r \to 0$ can be obtained by the expression:

$$\omega_{SO}^2 = \frac{\varepsilon_0 + \varepsilon_m}{\varepsilon_\infty + \varepsilon_m}\omega_{TO}^2 \tag{3.2}$$

where ω_{TO} is the frequency of the TO phonon which is connected with the LO phonon frequency by the Lyddane-Sachs-Teller relation: $\omega_{LO}^2/\omega_{TO}^2 = \varepsilon_0/\varepsilon_\infty$. Details about this expression are well-described on Ref. [28]. In order to estimate the frequency of the surface optical modes in GaN, the high frequency dielectric constant ε_∞ is taken to be isotropic and equal to 5.35 [104], the dielectric constant of the surrounding medium (air) is taken as 1 and the frequency of the longitudinal modes are taken from the Ref. [90]. The LO-TO splitting of E_1 and A_1 mode gives a static dielectric constant ε_0 of $9,55$ and $9,9$, respectively. The theoretical SO phonon gives a value of $\omega_{SO}(A_1) = 698$ cm^{-1} and $\omega_{SO}(E_1) = 722$ cm^{-1}. However, the calculated surface phonon modes are far from the experimental measurements for small radius of the GaN nanowires. The Lorentzian fit of the peak gives a shift of 11 cm^{-1} respect to the result presented in Table 3.1. The atribution to a surface mode in a Raman spectrum is still ambiguous due to the challenges in measuring individual and isolated nanowires with $r \to 0$ (very small radius), which is limited by the optical resolution of the objective. In Appendix A.1, a Raman spectrum of a single nanowire with largest diameter (around 400nm) is presented where the SO modes are located at 641 and 684 cm^{-1} for A_1 and E_1 respectively, which are more comparable to the reported values given in Table 3.1 [90]. That corrobates the fact that SO modes strongly depend on the diameter [28]. Furthermore, Equation 3.2 establishes that the position of the SO phonon mode is related with the dielectric constant of the surrounding medium. An interesting experiment would be to measure SERS or Tip-Enhance-Raman Spectroscopy (TERS) on isolated nanowires surrounded by different dielectric media and distinct radius (from 10 to 200nm).

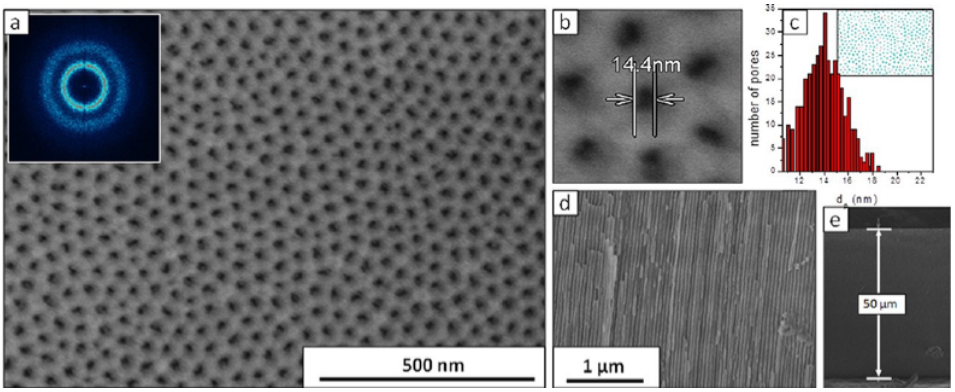

Figure 3.6: Image taken from the Ref. [3]. SEM micrographs of the AAO anodized in the presence of 50 wt % of ethylene glycol. (a) Large view where the polydomain structure can be observed (magnification: 100 000×); the inset corresponds to the Fourier transform (FT) of an image taken at 50 000×. (b) High-magnification SEM micrograph of the hexagonal cell from which the pore diameter has been directly measured. (c) Pore diameter distribution diagram obtained from the digitally analyzed image shown in the inset. (d) Detailed view of the cross section where the parallel pore walls can be clearly seen. (e) Total thickness of one of the templates (~50 μm).

3.3 Bi_2Te_3 Nanowires and films

3.3.1 Growth of Bi_2Te_3 Nanowires

Bi_2Te_3 nanowires were grown by pulse electrodeposition according to a previously published work from Marisol Martín González and Cristina Vicente-Manzano [36]. A conventional three vertical electrode cell and a potentiostat-galvanostat (Eco Chemie, Model AUT302.0) were used to perform the electrodeposition process. Pt wire, an Ag/AgCl electrode, and anodic alumina oxide (AAO) templates were introduced in the cell as a counter electrode, a reference electrode, and a working electrode. These AAO templates were made by a two-step anodization process in 10 wt. % sulfuric acid, it was also described in previous works by Cristina et al. [3, 105]. Different concentrations of Bi (99.999% from Aldrich Co.) and Te (99.99% from Alfa Aesar) were dissolved in 1M HNO_3 aqueous solution in order to obtain different composition in the nanowires from stoichiometric Bi_2Te_3 to Te-rich Bi_2Te_3 . Te film was also prepared at constant potential by electrodeposition for comparison reasons. In this case, the working electrode was changed by 150 nm of Au on top of 5 nm of Cr above Si. The solution used was 10^{-2}M Te in 1M HNO_3 aqueous solution.

3.3.2 Structural and optical characteristics of stoichiometric and Te-rich Bi_2Te_3 nanowires

Bi_2Te_3 belongs to the $R\bar{3}m$ space group with rhombohedral symmetry, like Bi_2Se_3 [106] (Bi_2Se_3 belongs to the Pnma space group [107]). It contains a formula unit inside the primitive cell (the structure is shown in Figure 3.7). There are two non-equivalent Te atoms (Te_1 and Te_2), drawn in different colors in the figure. The Te_1 is bonding two Bi atoms, while the Te_2 planes are limiting the layers, i.e. they are bonded by van der Waals forces. This compound has 12 optical modes, which split, due to the center of inversion, into gerade (even) and ungerade (odd) modes. The gerade modes do not show a dipole moment while they present a change in the polarizability, i.e. they are Raman active phonons, and the ungerade modes, where a dipole moment is present, are infrared (IR) active phonons. Thus, the Raman active modes are six, $2A_g$ + $2E_g$ (the A_g modes are one-dimensional, with the atoms vibrating along the [111] direction in the rhombohedral cell, and the E_g modes are two-dimensional, vibrating in the plane perpendicular to the [111] direction), while the IR active are the remaining six, $2A_u$ + $2E_u$. In a center-symmetric crystal the Raman and IR modes are exclusive, i.e. if a mode is Raman active, this mode cannot appear in an IR spectrum and the other way round. Nevertheless, there are many works where the mode located around $117cm^{-1}$ is assumed to be an IR mode which appear due to the lack of symmetry and the authors claim that the appearance of this mode is the fingerprint of one or two quintuple layers of (Te_2-Bi-Te_1-Bi-Te_2) [108–111]. However a Raman spectrum shows the one-phonon DOS when the translational invariance is lost. Thus the existence of well defined peaks in a Raman spectrum is a proof of the existence of translational invariance.

Figure 3.8 shows the total DOS corresponding to Bi_2Te_3 (solid, black line), the partial DOS corresponding to Te (dotted line-blue online) and Bi (dashed line-red online). The contribution of Bi, with a mass approximately twice as that of Te is larger at lower frequencies, while the opposite happens for Te. Bismuth telluride can be grown as BiTe (in a cubic and hexagonal phase), as Bi_2Te_3 (the rhombohedral phase), or even in more complex phases richer in Bi [112]. Probably, this is the reason why it is not so simple to grow Bi_2Te_3 in a stoichiometric way.

The Bi_2Te_3 structure is similar to that of many other layered materials like Bi_2Se_3 [113], InSe, GaSe and GaTe [114], In_3Se_3 [115] or MoS_2 and WS_2 [116], where the group VI elements are bonded through van der Waals forces giving rise to the layered structure. Recently, Zhang et al. [117] have shown the existence of Te clusters in Bi_2Te_3

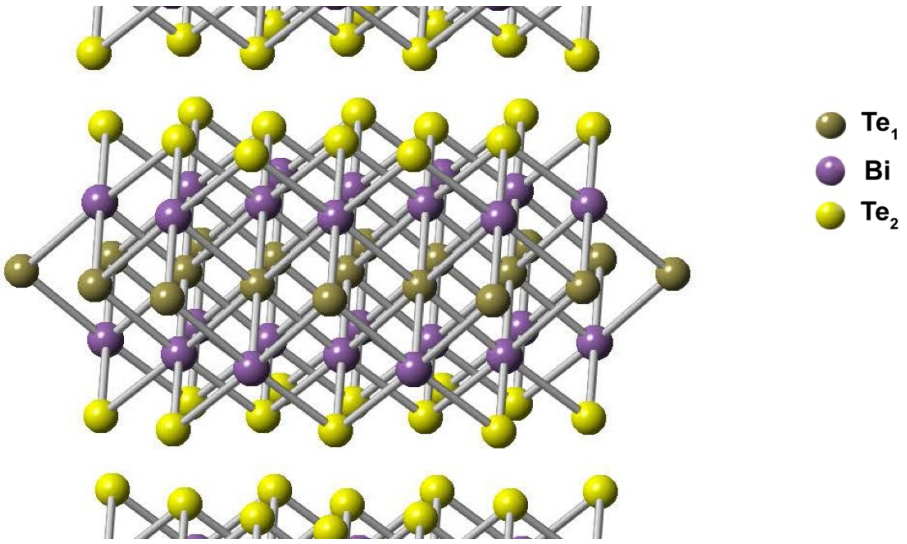

Figure 3.7: A quintuple layer from the rhombohedral Bi_2Te_3. The Te_1 atoms are bonded with two Bi atoms, while the Te_2 are bonded with a Bi on one side. They are limiting the layers.

nanowires. In fact, the authors claim that the figure of merit of their samples is increased because of the presence of Bi_2Te_3/Te nanowires heterostructures. Unfortunately, they did not present the Raman scattering data of their samples. In this work, the Raman data of stoichiometric Bi_2Te_3 and Te-rich nanowires are presented. The spectra of the stoichiometric samples contain several Raman peaks corresponding to bulk Bi_2Te_3, while that of the non-stoichiometric (Te-rich) samples show additional Raman peaks, related to the Te clusters. HRTEM measurements reveal the absence of clusters in the stoichiometric samples, while in the Te-rich samples one can found clusters of different sizes corresponding to the bulk Te-Te interatomic distance, confirming the results presented by Raman Spectroscopy.

The chemical composition and structural characterization of the Bi_2Te_3 nanowires embedded in the alumina matrix were performed by TEM combined with EDX. These measurements were carried out on a Tecnai G2 F20 (FEI) operating at 200 kV. In order to quantify the Te content within the Bi_2Te_3 nanowires the parameter δ is defined in such a way that $\delta = 0$ corresponds to the stoichiometric material. As a function of δ, the chemical formula can be expressed as $Bi_2Te_{3(1+\delta)}$. δ has been obtained experimentally through TEM-EDX measurements with low magnification, which provide the average of the Te content in the different samples of Bi_2Te_3 nanowires embedded in the alumina template. Figure 3.9 shows a HRTEM image of a Te-rich Bi_2Te_3 nanowire (a), as well as its Fast Fourier Transform (FFT) (b). A piece of nanowire was removed from the

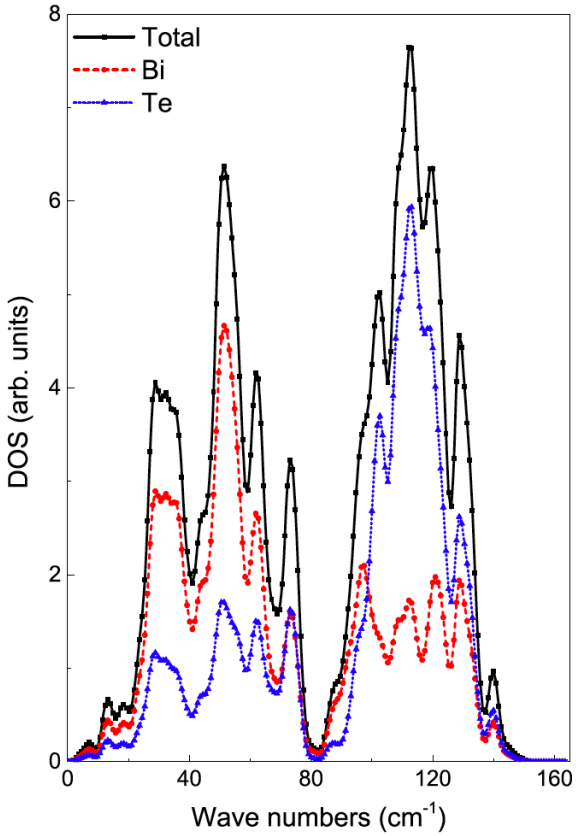

Figure 3.8: Total (solid line) and partial phonon DOS corresponding to Te (dotted line, blue online) and Bi (dashed line, red online) calculated for stoichiometric Bi_2Te_3. The symbols are the values obtained from the *ab initio* calculations, as explained in Appendix A.2 , while the lines are a β-spline to show a curve.

sample quantified previously with $\delta = 0.71$. The bright spots in Figure 3.9 (b) correspond to the diffraction planes in Figure 3.9 (a). The green arrows indicate spots that can clearly be attributed to planes belonging to Te clusters ($d = 1.93 \pm 0.01$ Å) [1]. The region corresponding to the Te cluster [green over-layer in Figure 3.9 (a)] can be inferred by performing an inverse Fast Fourier Transform (IFFT) using a mask to select only the relevant peaks.

The local elemental composition was further studied by EDX as shown in Figure 3.10. The regions probed by the electron beam are represented by the thin lines in the left-hand side panels (Figures 3.10(a)-(c)) for the nanowires brunches (embedded in the alumina) with different stoichiometry while the measured Bi and Te content profiles are shown in the respective right-hand side panels (Figures 3.10(d)-(f)). The profile of Figure 3.10 (d) for the stoichiometric sample shows a homogeneous content distribution

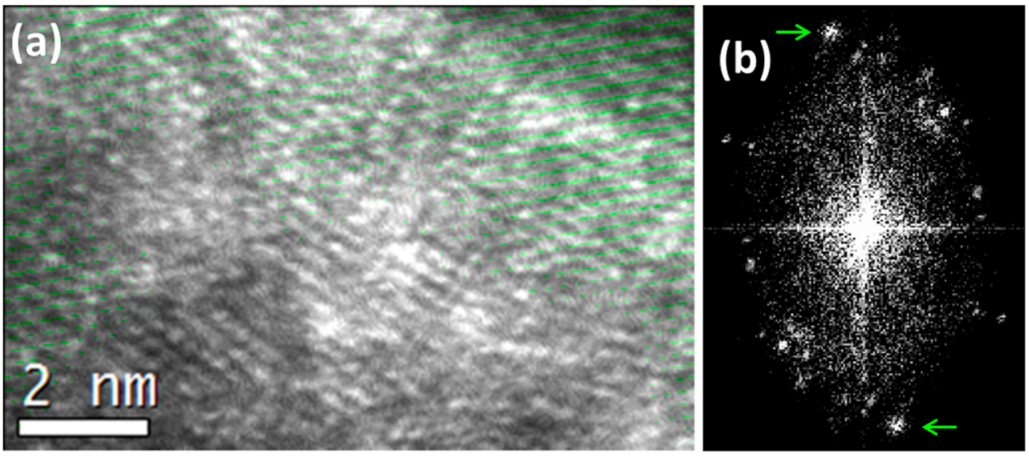

Figure 3.9: (a) HRTEM of a single nanowire sample of $Bi_2Te_{3(1+\delta)}$, with $\delta = 0.71$. The dashed lines (green colored online) areas illustrate the planes reconstructed via the inverse fast Fourier transform of the bright spots indicated in (b) by the arrows. (b) The fast Fourier transform of the image shown in (a).

close to the expected values (indicated by the horizontal dotted and dashed lines) of molar percentages for Bi≈ 40% and Te ≈ 60%. When the Te regions appear, the profile becomes inhomogeneous (Figure 3.10 (e)-(f)). The regions with clusters correspond to the Te content equal to 1 (see Figure 3.10 (f)). As can be visualized, the clusters are of a few nanometers (10-30 nm) in size.

The Raman scattering measurements were carried out at room temperature in a backscattering configuration in the Jobin Yvon T64000 spectrometer (previously detailed in Chapter 2). The excitation line (647.1 nm) was provided by an Ar/Kr laser focused onto the sample with the 100 × microscope objective. The experiment was performed in the subtractive mode, in order to go below 80 cm^{-1}. To avoid the sample heating during the experiment, special care was taken, limiting the power down to a few μW, focused on a $\sim 1\mu m$ spot. Previous to all measurements a Si sample was measured and the phonon was checked to be at 519.5 cm^{-1} [118]. After measuring the Si phonon, the spectrometer was not moved from its position, thus the experimental values have an uncertainty smaller than 0.5 cm^{-1}.

Figure 3.11 shows the Raman spectra of several samples with different Te content as measured by HRTEM-EDX. From the upper to the lower panel, the Raman spectrum of a stoichiometric sample, of a sample with $\delta = 0.42, \delta = 0.56, \delta = 0.71$ and a Te thin film are presented. In the sample with higher Te content three additional peaks can be visualized at 88, 117 and 137 cm^{-1}, corresponding to the E_1, A_1, and E_2 optical modes, respectively, of Te. The position of these additional Raman peaks can be compared with

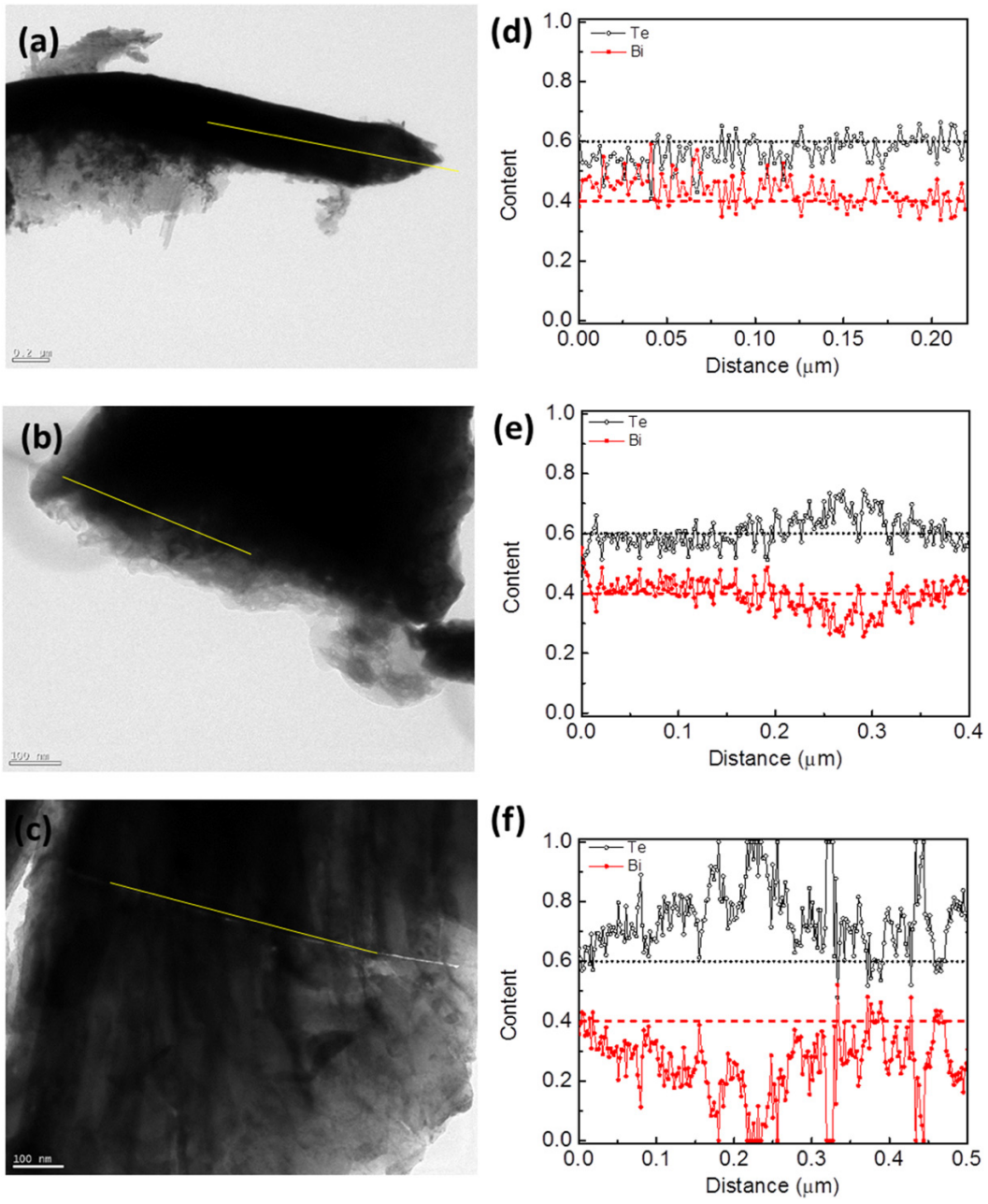

Figure 3.10: (a)-(c) TEM images of Bi_2Te_3 nanowires ensembles embedded in alumina with (a) stoichiometric Te content, (b) 29% Te excess, and (c) 36% Te excess. (d)-(f) Results of the EDX line scan profiles taken at the regions indicated by the thin lines in their respective left-hand side panels. The data showing a Te content of 1 correspond to the nano-sized clusters.

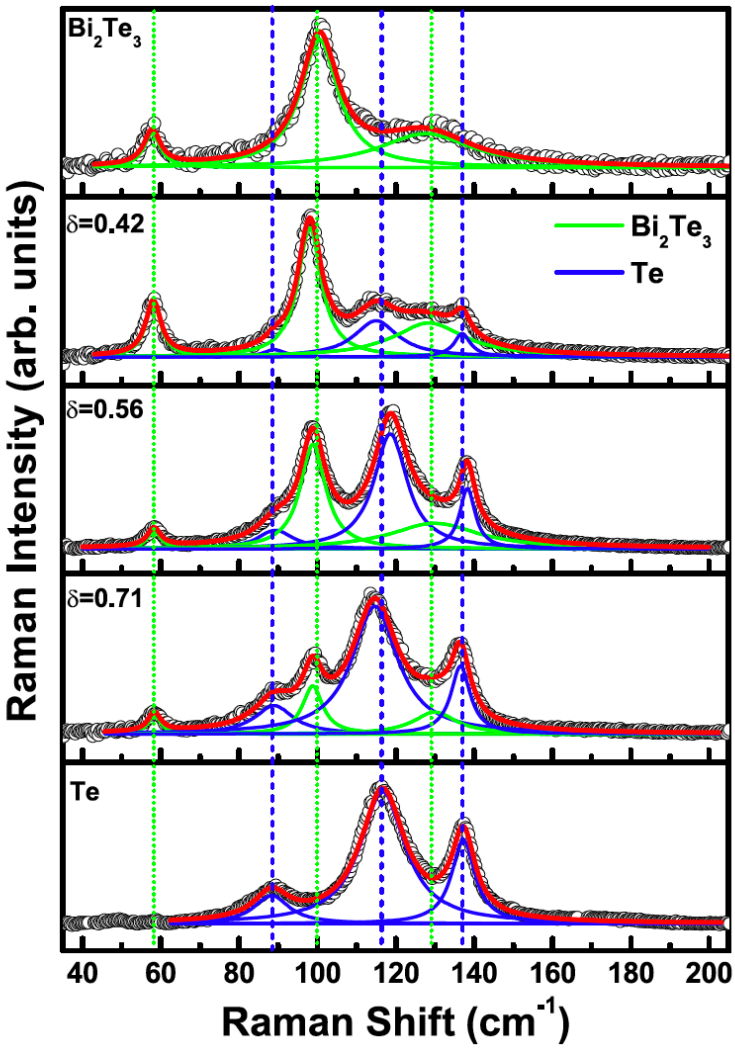

Figure 3.11: Room-temperature Raman-scattering spectra of Bi_2Te_3 nanowires for samples with different Te content. Measurements on stoichiometric Bi_2Te_3 nanowires as well as a pure Te film are also included for comparison. The amount of Te in excess (δ) as measured by EDX is indicated in the panels. The best Lorentzian fit for the individual peaks are shown. The vertical dashed and dotted lines correspond to the peak positions for the Te and Bi_2Te_3, respectively.

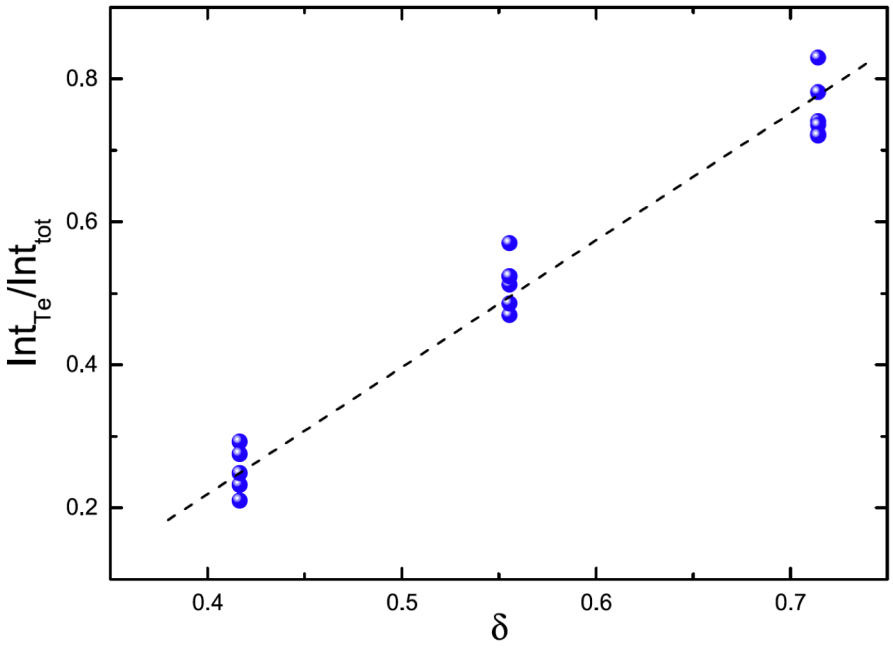

Figure 3.12: Integrated area of the Te peaks measured by Raman spectroscopy normalized by the total integrated area as a function of Te excess (δ). The dotted line is a guide to the eye.

that of the Te film (bottom panel). Clearly, these peaks cannot be attributed to the IR active modes of Bi_2Te_3 as demonstrated here and also because of the physical reasons given before. The Raman spectrum, even in the sample with a higher Te content, cannot be compared with that of a disordered sample (without translational invariance), since there is no similarity with the graph shown in Figure 3.8.

Because of the clear increase of the Raman intensity of the additional peaks in the samples with a higher Te content the correlation of the Te content with the area of the peaks was performed. The y-axis of Figure 3.12 represents the ratio between the area of the additional peaks related to the excess of Te divided by the total area of the Raman spectra, in order to normalize them. This ratio has been represented as a function of δ. Although they have been measured with two laser lines, 514.5 and 647 nm only the spectra measured with the 647 nm line has been selected. The dashed line is a guide to the eye. In this range of Te contents, and within the experimental variations, the correlation is clearly linear, although in a broader range of Te content there is no reason for the linearity. The Raman efficiency of the Te film is clearly larger (at this wavelength) than that of Bi_2Te_3.

Table 3.2: Comparison of vibrational modes corresponding to Bi_2Te_3 with different values published in the literature (cm^{-1}). The first row shows the phonon values provided by the *ab initio* calculations (see methods in Appendix A.2), the second row indicates the experimental data. Other values published in the literature are supplied for comparison. The last row of data corresponds to the phonon modes of the Te film measured as a sample control.

Bismuth telluride								
E^1_{1g}	A^1_{1g}	E^1_{1u}	E^2_{1u}	A^1_{2u}	E^2_{1g}	A^2_{2u}	A^2_{1g}	Ref
44.29	69.96	73.26	101.57	107.56	114.89	131.54	144.52	[a]
	57.8± 0.2				100.5 ± 0.2		127.6 ± 0.4	[b]
40.7					102.3		132.4	[111]
40.2	60.2				100.8		133.2	[119]
	60				101		133	[120]
	62.5	50	95	94	103	120	134	[121]
37	62				102		135	[122]
34.4	62.1				101.7		134	[123]
Tellurium film								
E	A_1	E						
88	117	137						

[a] Phonon frequencies calculated in the present work
[b] Data measured in the present work

Table 3.2 shows the optical modes of Bi_2Te_3 and Te. The upper part of the table shows the Bi_2Te_3 data while in the lower part, the data measured in the Te film are supplied. The first row of Bi_2Te_3 data corresponds to the phonon frequencies calculated in the present work (see Appendix A.2), while the second are the Raman modes observed experimentally (the E^1_{1g} is at very low frequency and it mixes with the Raman coming from the air, a typical problem of the Jobin Yvon T 64000). The remaining data have been extracted from the literature for comparasion. There are important discrepancies in the literature, as can be observed in the Table 3.2. As previously commented, the Raman shift of the Si phonon was used to calibrate the data. The uncertainty extracted from the curve fitting was smaller for the A^1_{1g} and E^1_{1g} modes and larger for the A^2_{1g} mode due to the larger broadening. The position of the A^2_{1g} is around up to 4 cm^{-1} smaller than other literature data. There is a smaller discrepancy in the case of the E^1_{1g} mode, only 2 cm^{-1} lower. These discrepancies may be sample dependent, probably due to defects, impurities, vacancies, etc. The calculated values (see Appendix A.2) are systematically higher, of the order of 10%, than that measured by Raman. In the case of the IR data obtained by Richter et al [121], the errors can be attributed to the sample quality; probably the sample were highly doped. Doped Bi_2Te_3 used to have a high

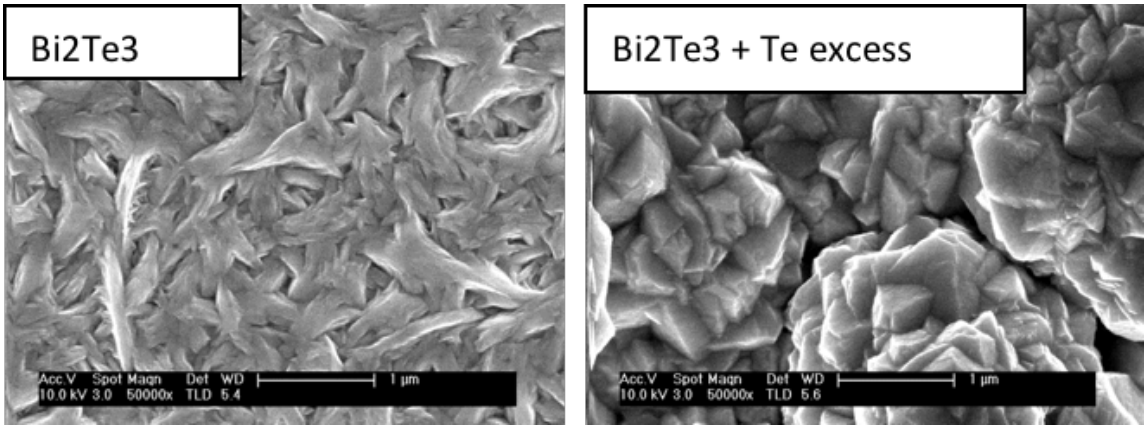

Figure 3.13: SEM of the Bi_2Te_3 stoichoimetric and with excess of Tellurium.

electron concentration either due to residual impurities or vacancies [124]. The Te film has been measured in order to compare the phonon modes with that which appear in the Te-rich samples. The modes are both Raman and IR active. There is no LO-TO splitting, since the Tellurium is covalent.

3.3.3 Growth and morphology of Bi_2Te_3 films

Bi_2Te_3 films were grown by electrodeposition due to its capability to inexpensively yield thermoelectric materials at room temperature, which can potentially be advantageous for scalable manufacturing. The growth process was performed with pulsed electrodeposition at a constant potential over 0.1 s and zero current density over 0.01 s. The applied potential was + 0.05 V relative to a Ag/AgCl reference electrode [125].

3.3.4 Structural and optical characteristics of stoichiometric and Te-rich Bi_2Te_3 films

For the identification of Te excess on the Bi_2Te_3 films, different techniques have been employed. The chemical composition and structural characterization of the samples were performed by TEM. An advantage of TEM over other techniques such as SEM is the possibility to obtain diffraction patterns from the sample under observation. Diffraction patterns give information of the separations of crystallographic planes which is important to identify the crystal structure. In addition, it also provides structural details enabling the localization of defects in the crystals. This technique is an excellent complement to energy dispersive X-ray spectroscopy (EDS).

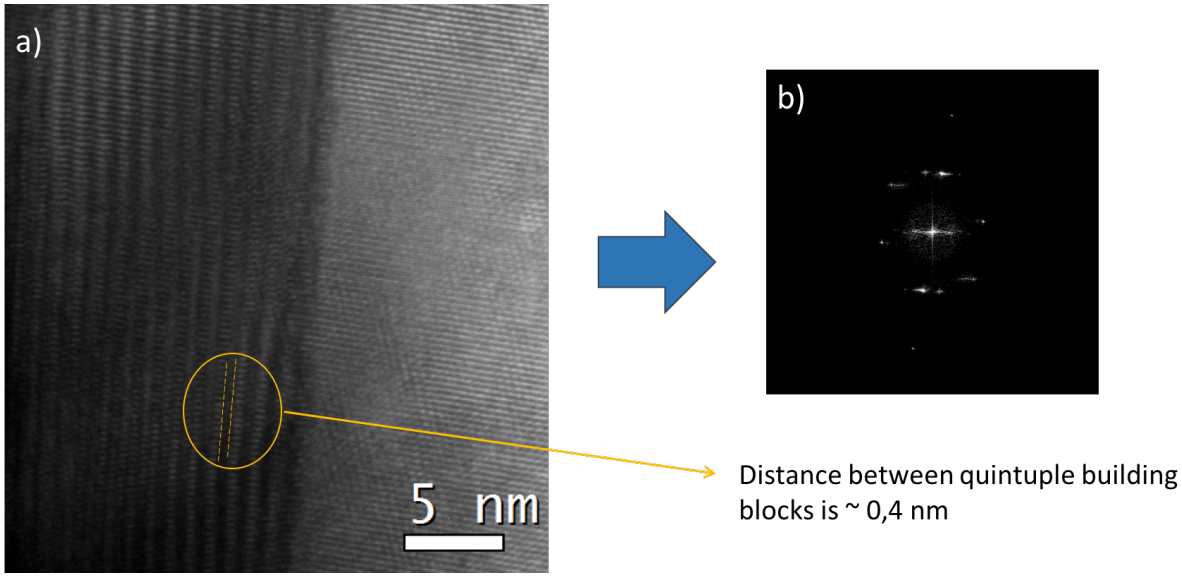

Figure 3.14: a) HRTEM of Bi_2Te_3 and b) Fast Fourier Transform of image (a), which shows interatomic distances.

TEM measurements were carried out on a Tecnai G2 F20 (FEI) operating at 200 kV. Modification and analysis of HRTEM images, FFT, Fourier mask filtering and IFFT calculation were performed using the software program Digital Micrograph^{TM}. As can be observed in Figure 3.14, a high quality Bi_2Te_3 crystal was characterized in order to compare its diffraction pattern with that of a sample with a high Te content.

The resolution of the HRTEM image allows discerning the lattice spacing between the well-known and characteristic quintuple building blocks of Te_2-Bi-Te_1-Bi-Te_2 which are separated by Van de Waals forces. The separation between layers is approximately of $d \sim 0.4$ nm and it is caused by the weak Te_2-Te_2 bond between the quintuple layers of Bi_2Te_3. As can be appreciated, no observation of Te clusters are present in Figure 3.14, indicating the morphology of a high quality crystal of Bi_2Te_3. That can be corroborated taking the FFT of Figure 3.14 (a) and measuring the planes distances along the [111] direction (see Figure 3.14 b). Interatomic distances of Bi_2Te_3 extracted from the literature are presented for comparison in the Table 3.3.

However, the diffraction patterns in the case of the Bi_2Te_3 with high Te content have substantive differences compared to the stoichiometric Bi_2Te_3 (see Table 3.3). For a detailed analysis an exhaustive study in different forms (films and nanowires) of the material is performed with the purpose of extend the defects identification for any crystalline structure. Figure 3.15 (a) presents the HRTEM image of Bi_2Te_3 film with the presence of Te-defects. Unlike diffraction pattern of pure Bi_2Te_3 of Figure 3.14 (b), this

Table 3.3: Bi_2Te_3 with experimental and reported d-values.

d-value experimental (Å)	**d-value literature *(Å)**
5.048	5.0733
1.9022	1.8994
1.879	1.884
1.6201	1.6202
1.607	1.6137
1.57034	1.5681

Table 3.4: Experimental and reported values of interplanar distances on Bi_2Te_3 and Te material for different form of the structure (films and nanowires). For comparing with the literature additional d-values are presented in the Table for Te [1] and Bi_2Te_3 [2].

Powder pattern of Bi_2Te_3 with excess of Te									
Films					**Nanowires**				
Selected points	d-value Å (this work)	error	Material	d-value Å (literature)	Selected points	d-value Å (this work)	error	Material	d-value Å (literature)
1-1	1.94	0.03	Te	1.93	1-1	1.93	0.01	Te	1.93
2-2	3.87	0.03	Te	3.86	2-2	2.35	0.03	Bi_2Te_3 Te	2.38 2.35
3-3	3.26	0.03	Te	3.23	3-3	3.21	0.03	Bi_2Te_3 Te	3.23 3.23
4-4	2.25	0.02	Bi_2Te_3	2.24	4-4	2.70	0.02	Bi_2Te_3	2.69

image shows a combination of planes belonging to Bi_2Te_3 structure and Te clusters. These d-values are marked with red arrows (see Figure 3.15 (b)) and are gathered in the Table 3.4. Superposing images of the reconstruction from image b) via IFFT and Figure 3.15) (a) one can observe the presence of Te in the films in the Figure 3.14 (c), where the green color indicates the presence of Te clusters.

A similar characterization by HRTEM was previously reported in "similar" NWs. But, in this case, additional measurements (see Figure 3.16) in order to compare the interplanar distances of the films and nanowires is presented. In the case of nanowires many of the Bi_2Te_3 d-values are closed to the reported distances of Te, which can lead to misunderstanding. As can be observed in the Table 3.4, the unique interatomic distance that can be unambiguously assigned to Te is the value $d \sim 1.93$ (see Table 3.4) which has the same value as the previously reported d-space published by Carlos Rodríguez-Fernández and et. al. [63]. In both cases the presence of Te clusters can be identified, nevertheless, segregation of Tellurium is more evident between the layers of Bi_2Te_3 (see Table 3.4).

On the other hand, the observations of Te clusters were supported by Raman spec-

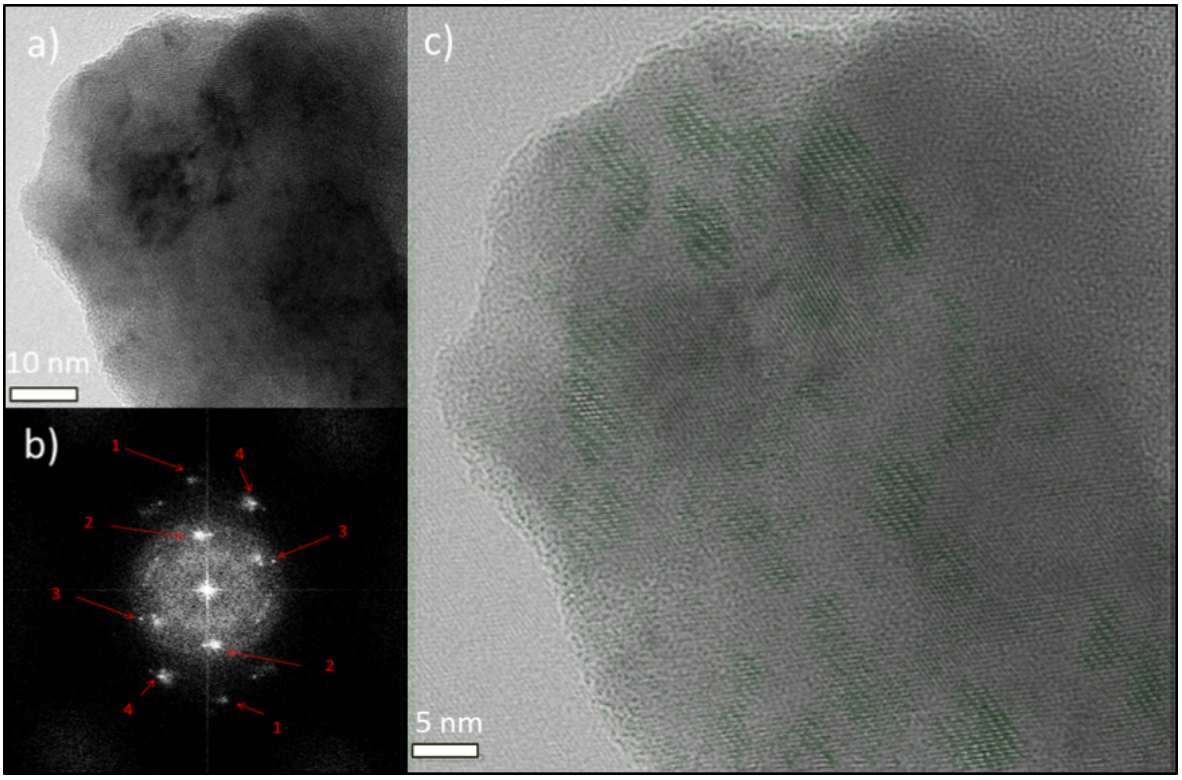

Figure 3.15: a) HRTEM of Bi_2Te_3 film with the presence of Te-defects b) FFT of the image (a) whose bright sports represents a combination of d-values of Bi_2Te_3 structure and Te clusters c) Combination of (a) and IFFT from b) where green colour represents the reconstruction for d-values corresponding to Te.

troscopy measurements. Figure 3.17 displays Bi_2Te_3 samples (nanowires and films) with excess of Te. The Raman spectrum of the nanowires was taken from the Section 3.3.2. The Te film was grown with the purpose of comparing with Te clusters. In thin films well defined peaks centered at 88, 118 and 137 cm^{-1} were assigned to the phonon modes E_1, A_1 and E_2 respectively of Te crystal whose lorentzian fits are representative lattice vibrations, while three peaks located to 59, 98 and 130 cm^{-1} were assigned to optical modes A^1_{1g}, E^2_{1g} and A^2_{1g} of Bi_2Te_3. If we compared films and nanowires one can observe that the peak located at 118 cm^{-1} from the films is shifted approximately ~1.4 cm^{-1} respect to the nanowires ,which could suffer stress due to the shape and size of the nanowire (diameter average around 40-60 nm).

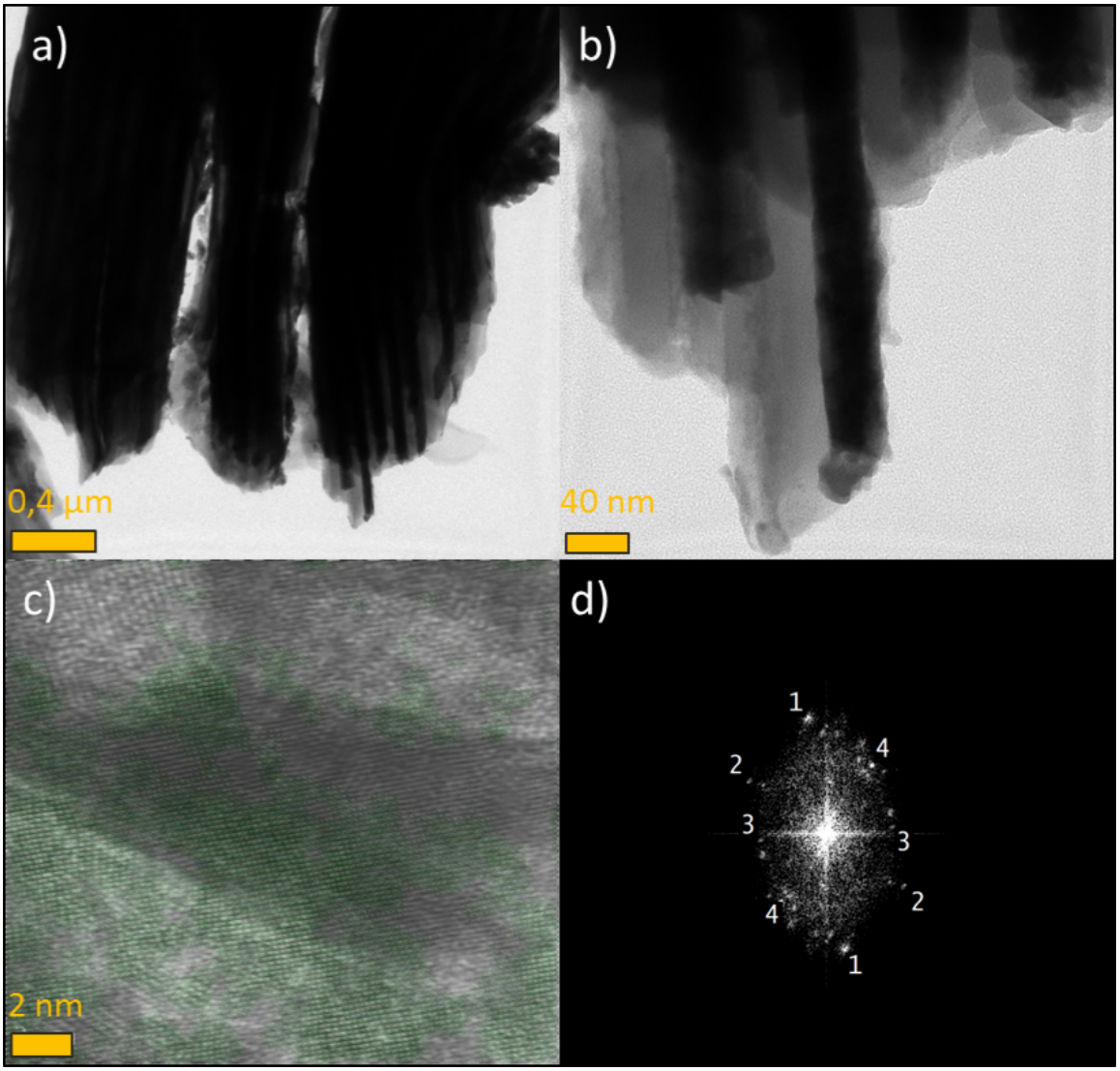

Figure 3.16: a) and b) TEM images of Bi_2Te_3 nanowires embedded in the alumina template c) HRTEM of a selected area from nanowires where green colour illustrates Te clusters. Image has been reconstructed by performing an IFFT using a mask to select only the points 1-1, which pertain to interatomic distance of Te (see Table 3.4).

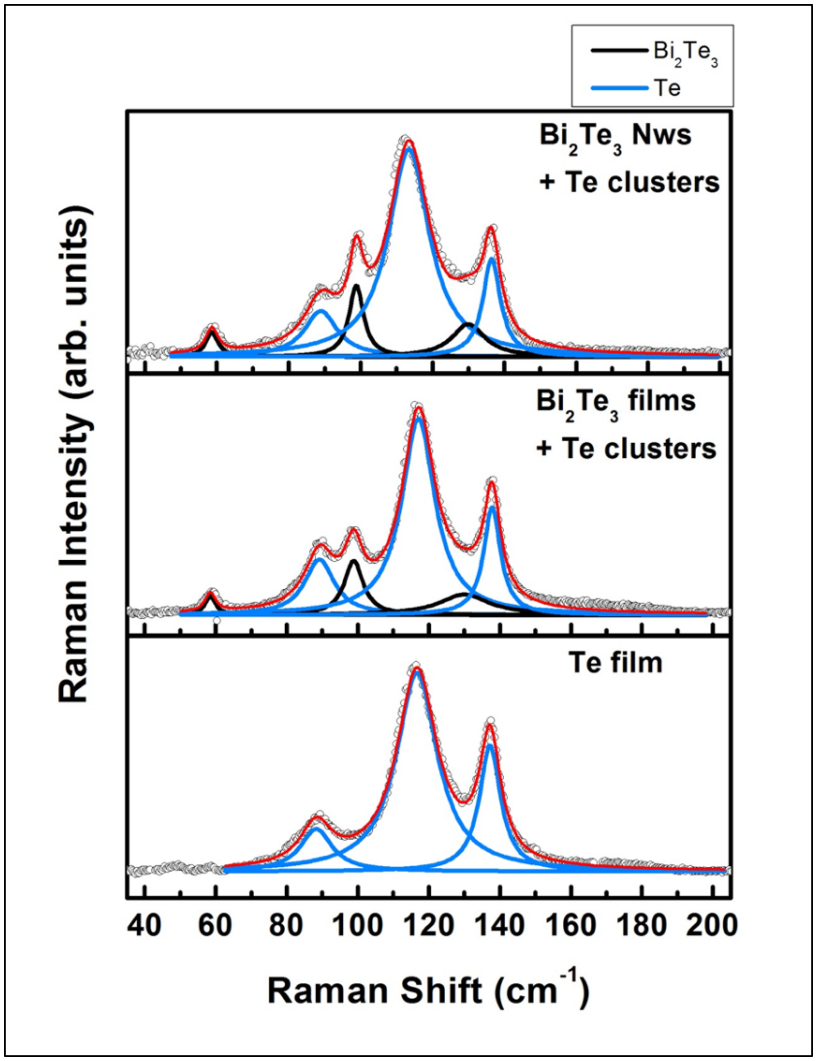

Figure 3.17: Upper and middle panel show room temperature Raman scattering spectra of Bi_2Te_3 (with approximately 36% excess of Te in both cases) for nanowires and films respectively. Bottom spectrum includes pure Te film for comparison.

3.4 Summary

In this chapter, PL and Raman scattering results have been presented for GaN nanowires, which were synthesized using the VLS technique with cobalt phthalocyanine as catalyst. Normalized PL measured at different positions revealed the value of the near band edge transitions for GaN nanowires, which was deconvoluted with two Gaussian peaks centered at 3.28 and 3.40 eV. The PL spectra do not present the typical yellow band, showing the high crystal quality of the nanowires. In Raman, the spectra from GaN, four modes appeared in agreement with literature values [90, 92, 93]: the allowed QLO,

E_2^h, $E_1(TO)$ and $A_1(TO)$ modes were observed at 746 cm^{-1}, 573 cm^{-1}, 562 cm^{-1}, 534 cm^{-1} respectively. An extra peak seen at 410 cm^{-1} in GaN nanowires were attributed to the zone boundary phonons, as previously reported [90]. These peaks were observed at different spots of GaN nanowires. Additionally a peak centered at 687 cm^{-1} was assigned to the SO mode which is exclusive for nanomaterials and thin films with large surface-to-volume ratio. Effects related to the shape of the nanomaterial can become significant compared with their bulk counterparts. In nanowires, in particular GaN, the surface represents a mechanical boundary where the atoms experience a different local field than that from the bulk. This has consequences in the Raman spectrum since is possible to observe the propagation of an optical phonon related to surface vibrations. Additionally, surface optical phonon can be tuned within the frequency gap between the TO and LO phonons by modifying the shape, size, and the dielectric constant of the surrounding medium, introducing new opportunities in the design of GaN-based optical phonon devices.

In addition, a throughout Raman characterization in stoichiometric and non-stoichiometric Bi_2Te_3 nanowires and films was performed. The Raman signal in the range of 116-120 cm^{-1} has been attributed to a forbidden A_u mode (IR active) of Bi_2Te_3, which would become allowed due to the lack of translational symmetry when there are only a few layers of this material. Thus, the presence of this mode is considered as a signature of the reduced number of layers. However, in this section were shown that the appearance of extra peaks located at 88, 117 and 137 cm^{-1} in the Raman spectrum of Te-rich Bi_2Te_3 is clearly related to the existence of Te clusters. In order to show this relation, stoichiometric Bi_2Te_3 nanowires as well as Te-rich nanowires were grown. The absence of these peaks in stoichiometric nanowires, even in those with the smallest diameter, shows that they are not related to confinement effects or the lack of inversion symmetry, as stated in the literature, but to the existence of Te clusters. This is because the lack of translational invariance instead of allowing the appearance of IR phonons in the Raman spectrum, would give rise to a spectrum similar to that given by the one-phonon DOS. After an accurate analysis, Te clusters were found in non-stoichiometric samples by HRTEM, while they were absent in stoichiometric samples. Additionally, a linear correlation between the Raman intensity and the excess of Te in the Bi_2Te_3 samples was found, (see Figure 3.11). Finally, the experimental data and *ab initio* calculations of the phonon values obtained in this section for Bi_2Te_3 nanowires were compared with other data from the literature. In conclusion, the existence of peaks in a Raman scattering experiment is a proof of the existence of translational invariance. Thus, in a Raman

spectrum consisting of well-defined peaks corresponding to lattice vibrations, the selection rules are satisfied. In any case, an IR active mode cannot appear in a Raman scattering experiment because the physical mechanisms are different.

The results obtained in nanowires were further complemented with the characterization of Bi_2Te_3 bulk films. In this case, for the quantification of Te excess on Bi_2Te_3 similar characterization techniques were employed. The chemical composition and structural characterization of the Bi_2Te_3 films were performed by TEM. TEM images were analysed by a software from Digital Micrograph^{TM}. Performing FFT of the TEM images it was possible to obtain interplanar distances for Te as well as Bi_2Te_3 indicating the presence of isolated Te clusters. These results were corroborated with Raman spectroscopy experiments for the identification of Raman peaks corresponding to excess of Tellurium, as made before for the characterization of nanowires. The presence of Te clusters in bulk and nanowires could be complemented in the future with an optical characterization of flakes with few quintuple layers of stoichiometric and non-stoichiometric Bi_2Te_3.

CHAPTER 4

OPTICAL CHARACTERIZATION OF III-V NANOSTRUCTURES BY MEANS OF RESONANT MICRO-RAMAN SPECTROSCOPY

In the previous chapter, semiconductor nanowires were analyzed by means of non-resonant Raman spectroscopy. This technique was employed to study the stoichiometry of the material and analyzed surface effects on different nanowires. Throughout this chapter, new features in nitride nanostructures will be studied by RRS technique.

For this purpose, ultrathin GaN nanowires and nitride-based nanostructures were grown on a silicon substrate by plasma assisted molecular beam epitaxy (PA-MBE) and monitored in-situ by Reflection High Energy Electron Diffraction (RHEED). High-resolution field emission scanning electron microscopy (HR-FE-SEM) and HRTEM were used for the morphological characterization of the sample. Structural and optical analysis were performed by X-ray diffraction (XRD) patterns and Raman spectroscopy.

The novelty of this chapter compared with the previous one is the fact that the observation of the silent mode, namely the B_{1l} mode, was possible by means of RRS in the ultraviolet, where the 325 nm laser light is in resonance with the electronic states of the GaN crystal. But the B_{1l} modes are forbidden in Raman scattering and IR reflectivity, and therefore, these modes cannot be observed in a Raman spectra. The most impressive fact is that the reason of the appearance of the B_{1l} mode in Raman scattering is not a dimensionality effect, or surface effect, but the crystalline perfection and isotopic

disorder. In addition, due to the breaking of the symmetry rules, or the mixing of the symmetry of degenerate modes, the B_{1l} mode is not silent anymore, while the B_{1h} mode is.

GaN and nitride-based nanostructures were synthesized by M. Almokhtar and H. Asahi. W. Ibarra-Hernández and A. H. Romero did the theoretical model of lattice dynamics using DFT. The optical characterization was performed in close collaboration with M. Almokhtar. This work was published in Nano Letters [126].

4.1 Ultrathin nitride Nanowires

4.1.1 Motivation

As indicated already in the preceding chapter the interest in nitride semiconductors has been kept during the last years due to the appearance of new physical phenomena and applications [127–130]. In particular, semiconductor nanostructures based on GaN, AlN and their alloys are highly attractive for the next generation of advanced electronic and photonic nanodevices due to their potential application in short-wavelength optoelectronics and high-temperature electronics [131–134]. Especially, quasi-one dimensional nanostructures called nanowires can offer new advantages as compared to bulk or thin film, which suffer of the lattice mismatch due to the lack of a suitable substrate. The first advantage is the phenomenon called self-purification. It appears due to the diffusion or segregation of point defects to the nanowires surface, which disappear during growth from the nanowire core [135]. This phenomenon is obviously more important in thin nanowires. In addition, the free surface of the nanowires permits the elastic relaxation of the strain and, therefore, dislocations are expected to be confined at the interface between the substrate and the nanowires basis [136].

As seen in Chapter 2, RRS is a non-destructive optical characterization technique that enable to extract information on the electronic structure when the electronic transitions are close or below the laser excitation energy [54, 137–140]. Under resonant conditions, the Raman spectra of polar optical phonons are dominated by Fröhlich electron-phonon interaction, associated with the electrostatic interaction between the polar phonons and the virtual electron present in the Raman process as an intermediate state [138]. Fröhlich interaction is inversely proportional to the wave vector, which is close to zero in first order Raman scattering and, in resonance, it becomes dominant when compared to the mechanical deformation potential (DP) electron-phonon interaction. The DP is a

short distance interaction, but since the Fröhlich electron-interaction depends on the electrostatic potential (it goes as $1/r$), it is a long distance interaction and it is thus more effective when there is a perfectly aligned crystal with translational symmetry (high crystalline perfection). In RRS experiments, new features have been observed in nitride nanowires, some of them not well explained [141], and some others clearly related to the surface (surface optical modes), like those shown by Prasana *et al*[142] or to the phonon density of states (DOS) [143].

4.1.2 Growth of ultrathin GaN Nanowires

GaN nanowires with designed diameter and length of 12 and 100 nm, respectively, have been grown on Si(111) substrates by PA-MBE. Prior to the GaN growth, the substrates were cleaned by a solution of SPM (Sulfuric Acid Peroxide Mixture). The Si substrates with native oxides were thermally outgassed at 750 °C for 10-15 min without plasma-enhanced nitrogen irradiation in the PA-MBE growth chamber. Elemental Ga, Al and RF plasma-enhanced N_2 were used as sources. The Ga flux was fixed at 5.2×10^{-8} Torr, the N_2 flow rate was fixed at 1.0 sccm and the RF plasma power at 300 W. The growth is started with a GaN buffer layer grown for 40 sec at 450 ~ °C followed by a thermal annealing at 800 °C for 10 min in a plasma-enhanced N_2 atmosphere to produce GaN nanoclusters. RHEED patterns show a reconstructed surface pattern (7×7) for the Si substrates. Then, GaN NRs were grown at 800 °C for 30 min under N-rich conditions with a Ga/N ratio of 1/3. The maximum growth rate was fixed at 200 nm/h.

4.1.3 Structural and microscopy analysis of GaN

In-situ monitoring of the growing GaN nanowires by RHEED patterns is shown in Fig 4.1 a). The RHEED shows broken-ring patterns indicating that hexagonal-GaN nanowires were grown with the *c*-axis (0001) perpendicular to the substrate surfaces. In addition, the XRD patterns image in Fig 4.1 b) were recorded using θ-2θ scans for the structural identification. No peaks other than the diffraction peaks from GaN (0002) and Si (111) are detected, proving again that the GaN nanowires are grown along the *c*-axis direction. HR-FE-SEM and HRTEM were used for the morphological characterization of the sample, see Fig 4.1 c) and d) respectively. TEM images were taken for the GaN nanowires separated from the substrate in ethyl alcohol. The SEM image clearly depicts the vertical *c*-oriented nanowires grow perpendicular to the SiO_2/Si substrates. Ultrathin GaN nanowires present a small size with an average diameter of 12 nm and

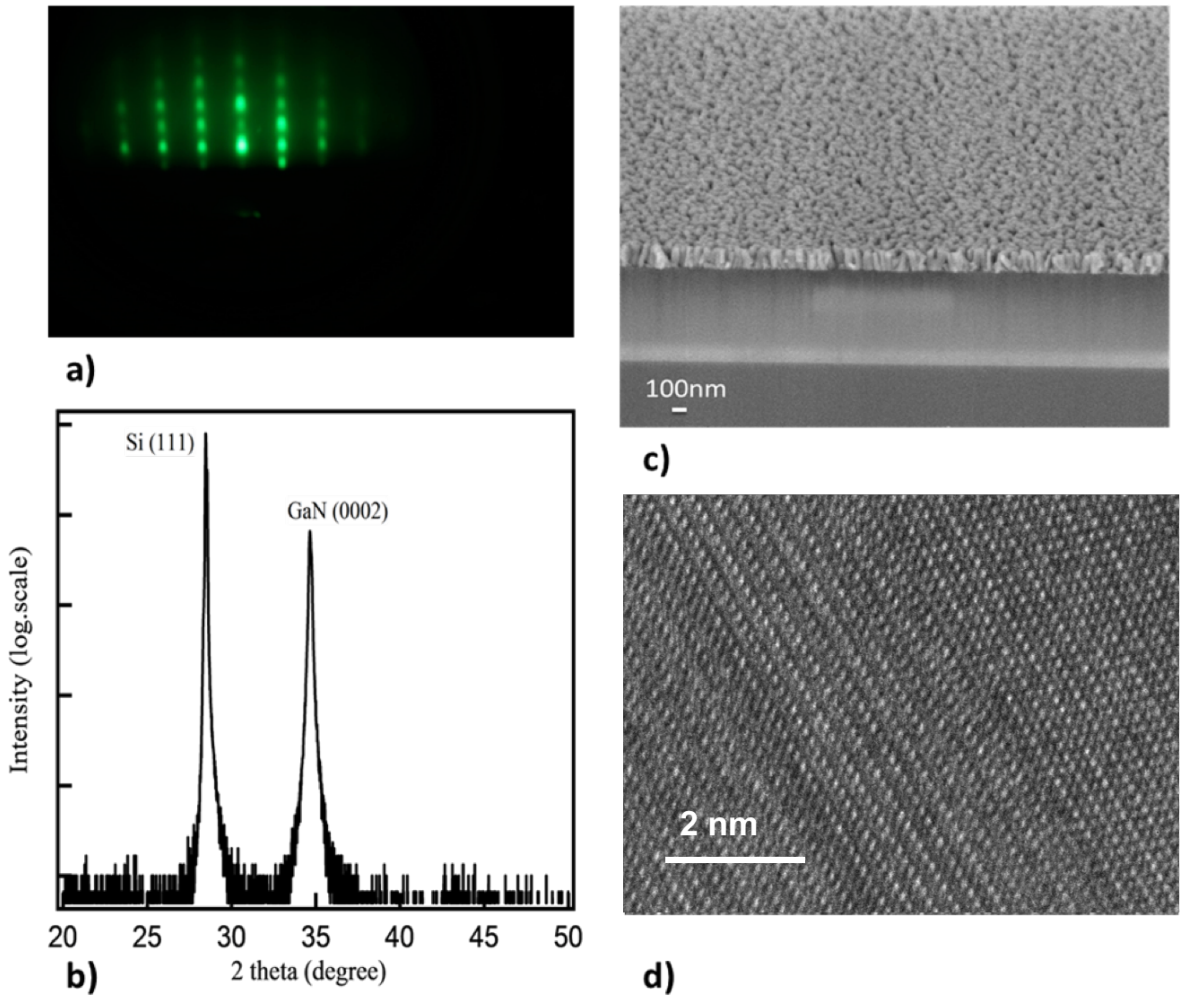

Figure 4.1: a) The RHEED pattern shows the GaN nanowires grown along the *c*-axis. b) XRD scans of the GaN nanowires grown on Si(111). c) SEM image of GaN nanowires grown on a Si substrate. d) HRTEM image showing the single crystalline structure of the GaN nanowires.

a length of 120 nm. Due to the small size, defects energetically prefer to migrate to the nanowires surface and disappear during growth (self-purification). Furthermore the HRTEM image confirms the high quality single crystalline structure of the nanowires.

4.1.4 Resonant Raman Spectroscopy and Fröhlich interaction on ultra-thin GaN nanowires

Gallium nitride, AlN and their alloys belong to the C_{6v}^4 ($P6_3mc$) space group, with two formula units per primitive cell and all atoms occupying C_{3v} sites. As discussed in Chapter 3 (Equation 3.1) the wurtzite structure presents three acoustic modes (a one dimensional A_1 and a two dimensional E_1 mode) and nine optical modes (the polar modes $E_1 + A_1$, the non polar E_2 and the two silent B_1). Since the $P6_3mc$ space group does not have a center of inversion, the polar modes ($E_1 + A_1$) are both Raman and infrared active. The E_2 mode has a change in the Raman polarizability but it does not carry dipole moment [27], it is thus only Raman active. On the other hand, the B_1 modes are silent (nor Raman nor IR active), they can be observed, in principle, by means of hyper-Raman scattering; however as far as we know they have never been clearly observed [144]. There are a few publications where B_1 modes are supposed to be observed in several wurtzite materials, but there are several discrepancies between them (they appear at different frequencies) and the reported spectra show a very broad signal around or close to the predicted modes, resembling more a maximum in the DOS than a phonon at the $\Gamma-$point [145]. Nevertheless, reviewing the literature, the clearest example of the observation of the silent B_1 mode, in wurtzite GaN, was given by T. Ruf *et al* [6] using Synchrotron inelastic x-ray scattering. These measurements indicate that these phonons are rather important input parameters for the comparison with theoretical models. Additionally, there are discussions in the literature where the indication of a broad peak can be also related to vacancies or impurities that can fall in the region around the expected phonon frequency. In that respect, there should be a systematic dependence study of the phonon line-width or even the peak position with respect to temperature, impurity density, etc [146].

The Raman back-scattering spectra of these nanowires were thoroughly studied using different laser lines excitations at room temperature (Figure 4.2). The setup was similar to that shown in Chapter 3, using Jobin Yvon T64000 spectrometer equipped with a liquid-nitrogen cooled charge-coupled device (CCD camera). The excitation line of 325 nm was provided by a He/Cd laser focused onto the sample using a 40× objec-

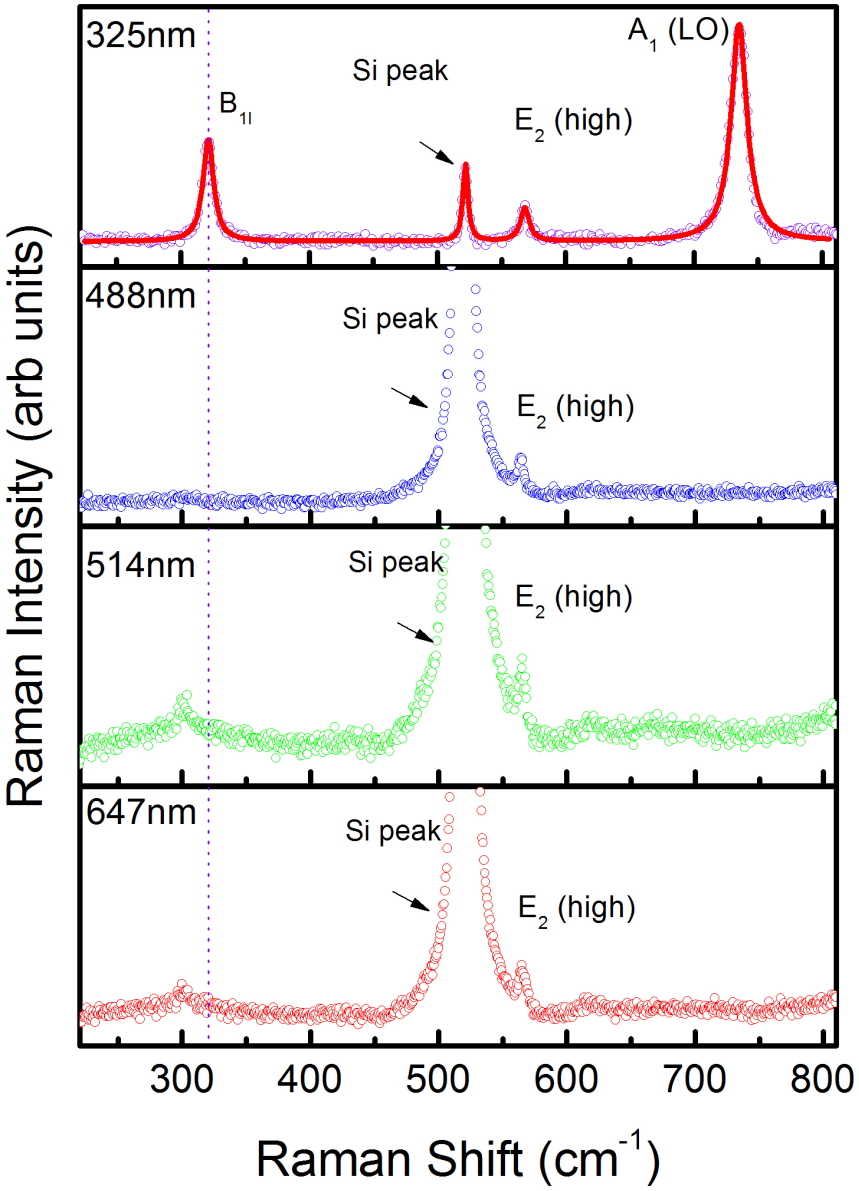

Figure 4.2: From the upper to the lower panel, the Raman spectrum of GaN nanowires covering the wide range of interest are shown, using the laser lines excitations 325, 488, 514 and 647 nm for comparison.

tive microscope with a numerical aperture (NA) of 0.50 while laser lines of 488, 514 and 647 nm were supplied by an Ar/Kr ion laser focused onto the sample with a 100× objective having a NA of 0.90. This setup focuses the light on an area around 1.5-2 μm for laser line of 325 nm and $\sim 1\mu$m for the Ar/Kr laser on top of the nanowire ensembles. The optical characterization was performed either using the triple spectrometer in subtractive mode (325 nm) or in single mode (visible lines with an edge filter). All measurements were calibrated with a silicon and diamond sample using the characteristic phonon peaks at 520 and 1332 cm^{-1} respectively. The Raman peaks were fitted with Lorentzians in order to find the contributions from individual modes with accuracy. The solid line (red online) is the cumulative fit of the Raman spectra. In backscattering geometry with the light along the nanowire $c-$axis, $\bar{z}(-,-)z$, only the $A_1(LO)$ and E_2 modes can be observed [27, 54, 147]. The E_1 mode is observed only in crossed polarization geometry or 90° scattering [27].

Figure 4.2 shows the Raman scattering spectra measured with different laser lines, from the red to the ultraviolet. The peak at 520.0 ± 0.5 cm^{-1} corresponds to the Si substrate, which has the maximum strength at the green (514 nm). The E_{2h} phonon mode of GaN appears at 567.1 ± 0.5 cm^{-1}, indicating that the nanowires are unstressed. The reference position to consider the GaN unstressed is 567.5 cm^{-1}.[148] The non-existence of stress confirms the high crystalline quality of the nanowires. Only in the upper spectrum, obtained with a laser excitation of 325 nm (3.8 eV, above the GaN gap), under resonance conditions, there are two additional peaks. The first one is the $A_1(LO)$ mode located at 734.1 ± 0.5 cm^{-1}, while the second is the B_{1l} mode, in principle forbidden, but observed due to its small dipole moment and resonance effects (Fröhlich electron-phonon interaction). The B_{1l} mode appears at 320.4 ± 0.5 cm^{-1}, close to the value measured by inelastic x-ray scattering [6], 329 cm^{-1} and the theoretical calculations (334 cm^{-1}). The theoretical calculations of Ref. [6] gives a value of 339.2 cm^{-1} for the B_{1l} mode and it was multiplied by 0.97 in order to be coincident with the experimental value. The resonance conditions are demonstrated through the enhancement of the $A_1(LO)$ mode. As it is known, the $A_1(LO)$ mode is strongly coupled to the electrons via the electron-phonon Fröhlich interaction (the Fröhlich Hamiltonian is diagonal).

The B_{1l} and B_{1h} mode activation is usually ascribed in the literature to a naive and uncorroborated argument: the relaxation of the translational invariance due to the presence of defects, impurities and structural disorder caused by ion implantation or mechanical damage [143, 146, 148–152]. This argument is controversial since in the case of lack of translational invariance the one phonon DOS must be observed instead

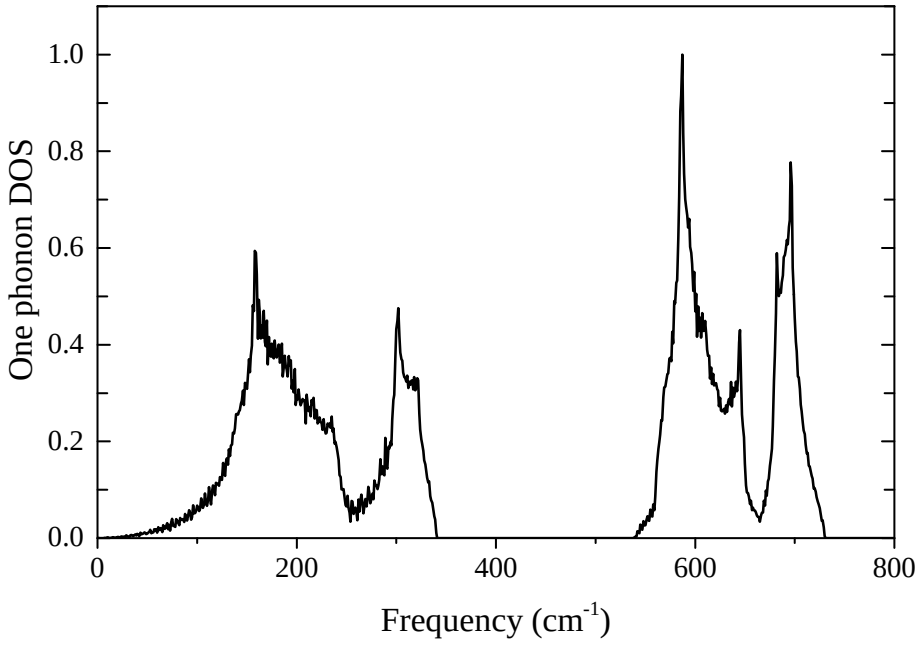

Figure 4.3: One phonon density of states ($\sum_{\mathbf{q}} \delta(\omega - \omega(\mathbf{q}))$). The area has been normalized to the number of phonons.

of the phonons at the Γ−point [63], i.e. some structure similar to that shown in Figure 4.5. Since this is not the case, the origin of the broad structures shown in Refs. [143, 146, 148–152] must be found in the two phonon DOS (see Appendix B).

In the present work, GaN nanowires were grown by PA-MBE which is known to be a clean method to grow high purity structures with very good crystalline quality [153–156], thus the existence of any phonon mode associated with lattice disorder, breakdown of the translational symmetry or defects can be excluded. Since the B_{1l} mode appears only under resonant conditions, this mode may be attributed to a Fröhlich allowed resonant mode, although group theory indicates that this is a silent mode. The reason why this silent mode becomes Raman allowed due to Fröhlich electron-phonon interaction will be given below. First, possible interpretations to explain the appearance of this mode in Raman will be analyzed and the reasons why they are not plausible will be given.

4.1.5 Activation of B_{1l} by Fröhlich interaction on high quality GaN nanowires

To address with some detail the observed vibrational response, theoretical calculations were performed within the framework of density functional theory (DFT)[157, 158] and density functional perturbation theory (DFPT) [159] as implemented in the Abinit code [160–162]. The calculations were performed by W. Ibarra-Hernández and A. H. Romero. They used the generalized gradient approximation to describe the exchange-correlation energy with the Perdew-Burke-Ernzerhof (PBE) formalism [163, 164]. The reciprocal space is discretized with a regular $k-$point mesh of $12\times12\times6$, while a cut-off energy for the expansion of plane-waves of 50 Ha (1360 eV) has been selected. This optimization ensures that the system is fully relaxed with forces between atoms no larger than 10^{-4} Ha/bohr and that the stress of the crystal cell is as low as 10^{-2} GPa. For the calculation of the dynamical properties (phonons), DFPT with a regular $q-$point mesh of $4\times4\times2$ was used. The *anaddb* postproccessing utility provided with the Abinit code allowed to extract the two phonon density of states (DOS), which is a histogram of all possible phonon events with $q_1\pm q_2=0$, from a Fourier interpolated phonon grid of $40\times40\times20$. The diagonalization of the interatomic force constants provides also the eigenvectors which are then analyzed within the symmetry utilities present in the Abinit code, in particular, for the center zone phonon modes.

First of all, the possibility of the appearance of a dipole moment due to the well known mixing between the B_1 modes will be discussed. By examining the eigenvector of the B_{1h} mode,

$$e(B_{1h})=\begin{pmatrix}0.03951459\\-0.03951459\\-0.70600167\\0.70600167\end{pmatrix}\approx\begin{pmatrix}0.00000000\\0.00000000\\-0.70710678\\0.70710678\end{pmatrix} \tag{4.1}$$

it can observed that the value is very close to what group theory predicts. Actually, the relative displacements of Ga and N are, respectively, 0.330 and 2.642 arb. units (the actual values are temperature dependent[165]). The N planes move one against the other, while the Ga planes move out of phase in comparison with the Ga planes, suppressing any possible dipole moment.

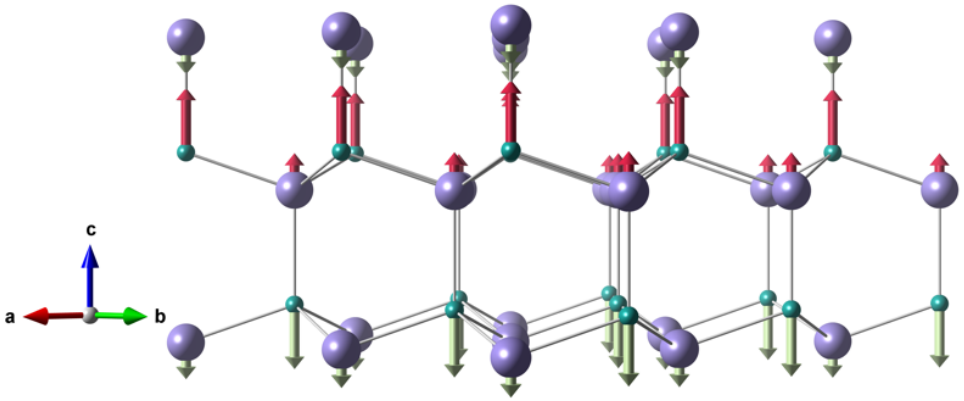

Figure 4.4: Several atomic layers showing the propagation of the B_{1h} phonon along the z-axis.

In the case of B_{1l} mode a similar result can be observed.

$$e(B_{1l}) = \begin{pmatrix} 0.70600167 \\ -0.70600167 \\ 0.03951459 \\ -0.03951459 \end{pmatrix} \approx \begin{pmatrix} 0.70710678 \\ -0.70710678 \\ 0.00000000 \\ 0.00000000 \end{pmatrix}, \tag{4.2}$$

which is also close to what group theory predicts. Taking into account the calculated eigenvectors, the relative displacements of the Ga planes are one against the other, like the N planes, but in that case, the Ga and the N planes within the unit cell move in phase. The result gives again the absense of dipole moment. The B_{1l} mode, even when the small N displacement is include, is still a silent mode. The combination of the silent modes gives rise to two new silent modes.

A second possible explanation for the existence of a dipole moment is the lack of translational symmetry due to the existence of a surface. Clearly, the asymmetry of the atomic movements in the surface gives rise to a small dipole moment. The problem of this explanation is that the contribution of the surface to the Raman signal is very small, even in very thin nanowires, as it is the case. If the diameter of these nanowires is 12 nm, the perimeter is $12 \times \pi \approx 37.7$ nm. If the bond lengh is around 0.15 nm, the number of atoms along the surface is roughly 250. However, the area of the circle is $\pi d^2/2 \approx 113$ nm^2. The number of atoms in the circle is around 5000. Thus, the contribution of the surface, as compare to the bulk, is very small, even in very thin nanowires. Thus the

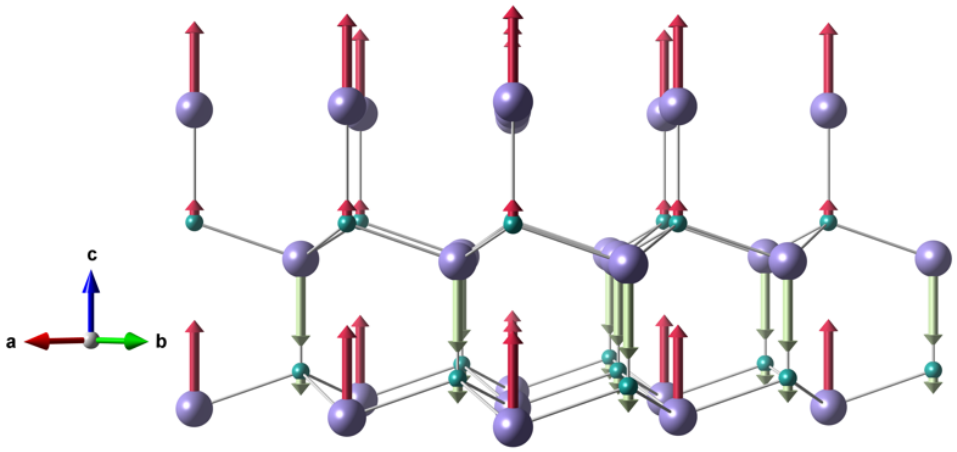

Figure 4.5: Several atomic layers showing the propagation of the B_{1l} phonon along the z-axis.

dipole moment is small and the contribution to the surface is small, concluding that the effect of the surface is negligible.

The third possibility is the breakdown of the selection rules due to the lack of translational symmetry produced by the existence of a impurity. Impurity-induced Raman scattering has been studied in the past [140] and it is obviously proportional to the impurity concentration. In these high purity nanowires this option must be discarded. In heavily doped crystals impurity-induce scattering is effective, but the peak must become very broad. However, the effect would be the same for the two B_1 modes.

A fourth possibility is that the observed peak is due to the density of two phonon states. From the lattice dynamics calculations the two phonon DOS is obtained (see Appendix B), for both the sum and the difference of energy between the phonon branches, and in any of them appears a peak around the frequency of the B_{1l} mode.

However, there is a peak at 320 cm^{-1}, only observable at resonance, i.e. due to Fröhlich interaction, which means that this phonon must have, compulsorily, a dipole moment. Where this dipole moment comes from? If one looks at the periodic table of elements and pays attention to the isotopic composition of Ga and N the following data are found: Ga has two stable isotopes, ^{69}Ga, with a mass of 68.925580(3) a.m.u. and a natural abundance of 60.108(9)%, and a second one, ^{71}Ga with 70.9247005(25) a.m.u. and 39.892(9)% of natural abundance[§]. The atomic displacement is proportional to the

[§]Data are taken directly from webofelements.com

eigenvector times the square root of the mass. There will be displacements where two ^{69}Ga atoms are involved, two ^{71}Ga or one of each one (isotopic disorder). This difference in the displacements produce a lack of symmetry in the vibrations and the appearance of a small randomly distributed dipole moment. Although the dipole moment is small, due to the large abundance of the isotopes, most of the lattice contribute to the dipole moment and since Fröhlich is a long distance interaction, in a high quality crystal the mode can be observed. Now, can be checked if this explanation would be consistent with the absence of the B_{1h} mode in the Raman spectra. Looking again at the periodic table, N has also two stable isotopes, ^{14}N with 14.0030740052(9) a.m.u. and a 99.632(7)% of atomic abundance, and ^{15}N, with 15.0001088984(9) a.m.u. and 0.368(7)% of natural abundance. The small isotopic disorder in the N, responsible for the movement in the B_{1h} mode, makes the contribution due to isotopic disorder negligible. It is worth comment the effect of isotopic disorder on the broadening. In a work of J. M. Zhang et al.[166] there is a careful study of the peak position and broadening of several Ge isotopes, natural Ge and a superlattice made by $^{70/76}$Ge. The broadening is very similar in all the cases, i.e. the isotopic disorder does not contribute much to the broadening.

The activation of the B_{1l} mode for high-quality GaN nanowires could be extrapolated to other highly crystalline polar materials, like ZnO (Zn has 5 stable isotopes but three of them have 49, 28 and 19% natural abundances). This is not the case of InP, since natural In is composed in a 95% by ^{115}In.

4.1.6 Ultrathin GaN/AlN nanowires

As seen before, one feature of the highly crystalline polar materials is the appearance of the silent B_{1l} mode under resonance conditions. The growth of "perfect crystal" could be employed for the design of more complicated nitride-based nanostructures, e.g the growth of Aluminum Nitride (AlN) on top of high quality ultrathin GaN nanowires. AlN is an important material for optoelectronic devices and has many attractive characteristics due to its large room temperature direct band gap of 6.2 eV which is the largest band gap among III-nitride compounds [167]. Due to its wide direct bandgap, AlN and Al-rich AlGaN alloy materials are suitable for deep ultraviolet (DUV) optoelectronic devices [168]. Besides, AlN shows high piezoelectric response [169] for applications in surface acoustic waves (SAW) devices [170] for instance, and present excellent thermal conductivity [171].

As noted throughout the thesis, the growth of nanowires can reduce drastically the dislocation/defect density with respect to bulk counterparts. However, AlN nanowires

usually exhibit extremely poor structural and optical properties. In addition, it is well-known that the optical quality (or the intensity ratio of the band-edge to the deep level impurity transitions) is strongly correlated with the growth conditions.

In order to overcome defect density on AlN structures, GaN nanowire arrays were first grown by PA-MBE, as described before. GaN nanowire arrays serve as a template to promote the formation of AlN nanowires, providing a better control of the AlN nanowire size, quality and density compared with the direct nucleation of AlN on top of Si or dielectric layer SiO_x [172]. Furthermore, this heterostructure is compatible with processes for achieving DUV devices on a Si-platform. [173]. In this case, the growth conditions for the AlN nanowires included a nitrogen flow rate of 1 sccm, a plasma power of 350 W, a growth temperature around of ~ 860 ^{o}C and an Al flux of 6×10^{-8} Torr.

Raman measurements were performed using the same setup and conditions given in Section 4.1.4, where the micro-Raman spectra of ultrathin nanowires (see Figure 4.6) were recorded along the c-plane of the wurtzite samples. No significant broadening, peak shift, or decrease in intensity was observed during data acquisition, indicating that thermal heating effect can be excluded. As the incident laser polarization is set parallel to the nanowires axis, only the E_2 phonon peaks and the polar $A_1(LO)$ are allowed by selection rules. Furthermore, in the same spectrum it is possible to visualize the Si peak at 520 cm^{-1} which is related to the substrate of the sample. Regarding ultrathin GaN/AlN nanowires non-polar E_{2h} modes of wurtzite GaN and AlN can be located at 569 cm^{-1} and 649 cm^{-1} respectively. This vibrational non-polar mode refers mainly to the vibration of N atoms in plane, perpendicular to the c-axis and it is known to be a good indicator of the strain in the samples. The E_{2h} phonon mode corresponding to GaN is in accordance with reported values of unstrained wurtzite GaN [91]. In the case of AlN it is possible to note a small shift compared with literature [148, 174]. This is due to AlN has smaller unit cell than GaN. Thus, when AlN is grown on top of GaN, it will experience a strain which affect the Raman peak corresponding to the non-polar E_{2h} mode.

Additionally, the longitudinal $A_1(LO)$ modes from GaN and AlN can be observed at 735 and 889 cm^{-1} respectively. As it can be discerned, Raman spectra is dominated by the polar $A_1(LO)$ mode of wurtzite-GaN. The reason for this is that GaN is under resonance (it was explained before) when the 325nm laser excitation is used. Nevertheless, the most important contribution to the Raman effect at resonance is the Fröhlich electron-phonon interaction produced by the interaction between the polar mode and the virtual electron created by the photon in the Raman process at long distances. As

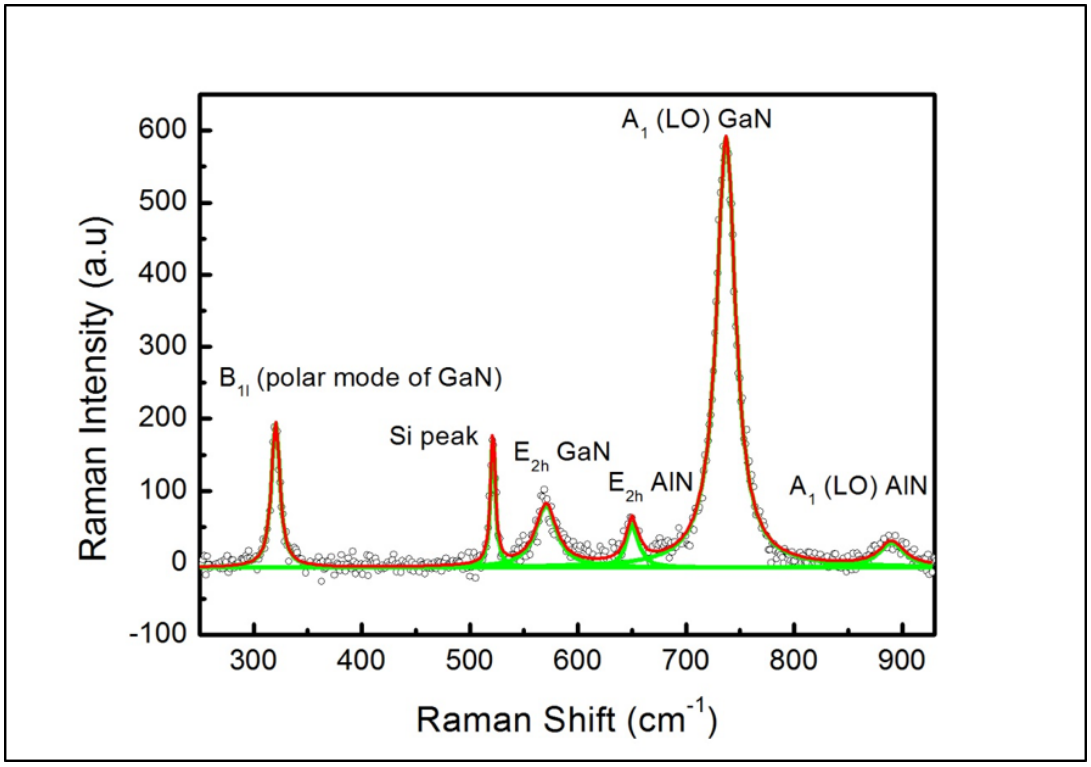

Figure 4.6: Raman spectrum of AlN/GaN nanowires at 325 nm laser line.

mentioned before, the electron-phonon Fröhlich Hamiltonian is inversely proportional to $q_{ph} = k_l - k_s$ (the wave number of the laser light minus the wave number of the scattered light) and the phonon wave number is nearly zero. In resonance, this interaction produces a huge enhancement in the Raman polarizability in the case of polar materials as can be appreciated in the strong signal of the longitudinal $A_1(LO)$ phonon mode of GaN. This is not the case of AlN. Finally, the high crystal perfection combined with resonant conditions allows to visualize the B_{1l} mode at the Raman spectrum for GaN. The B_{1l} mode is a clear peak, with more intensity than the E_{2h} mode and with less broadening than that of the $A_1(LO)$. As it was previously discussed, the B_{1l} mode presents a dipole moment due to isotopic disorder which is enhanced due to Fröhlich interaction.

4.2 Summary

Wurtzite semiconductor compounds have two silent modes, the B_{1l} and B_{1h}. A silent mode is a vibrational mode that does not carry neither dipole moment nor Raman polarizability. Thus, they are forbidden in both infrared reflectivity and Raman spectroscopy.

However, an additional well defined peak at 320 cm^{-1} was observed in the resonant Raman spectrum of high quality ultrathin GaN nanowires, corresponding to the frequency of the B_{1l} mode. The observation of this phonon mode is usually ascribed to the appearance of defects, impurities or even to disorder activated Raman scattering. But in all those cases a broader and not well-defined peak was shown in the Raman spectrum which probably was related to the DOS. Defects and impurities in thin diameter GaN nanowires (of 12 ~nm) were unfavourable due to the self-purification mechanism. Unshifted E_{2h} mode indicated that GaN nanowires were free of strain and confirmed with other structural and optical characterization techniques the high crystalline perfection of the GaN nanowires.

The Raman experiments were performed using several laser lines, from the red to the UV, a wavelength where Raman becomes resonant on GaN. The B_{1l}-mode was observed only in resonance, indicating that the appearance of this mode is related to Fröhlich electron-phonon interaction, i.e. a dipole moment emerges in the B_{1l} silent-mode. On the other hand, the B_{1h} mode does not appears, i.e., it remains silent since either no dipole moment is present in this mode or it is negligible when compared to that of the B_{1l} mode. The resonant interaction of the Raman scattering was demonstrated by the enhancement of the $A_1(LO)$ phonon mode.

To shed light onto the physical origin of these observations, DFT calculations of the lattice dynamics in GaN and analysis of the phonon eigenvectors were discussed. Furthermore, a careful analysis of the different physical mechanisms that allow the forbidden mode to appear to explain the physics underlying the nonzero dipole moment in the B_{1l} mode was performed, and the reason why this dipole moment is not present in the B_{1h} mode. After a thorough analysis, it was explained that the appearance of a visible silent mode under resonant conditions is because of isotopic disorder causes a lack of symmetry on the atomic vibrations of this mode. The difference in the atomic displacements due to isotopic disorder produce a small dipole moment, which is enhanced due to Fröhlich electron-phonon interaction. In short, the high crystalline quality of the nanowires and the appearance of a small dipole moment due to isotopic disorder makes the B_{1l} silent mode to appear as a Raman allowed mode due to Fröhlich electron-phonon interaction. The existence of the B_{1l} mode is vital in developing new measurement methodologies to perform a better characterization of polar materials that contribute to improvement of the phenomenological lattice-dynamical models.

Additionally, PA-MBE technique was employed to growth more complexed nitride-based nanostructures such as AlN/GaN nanowires. The high crystal quality of GaN

nanowires achieved during the growth process served as template to grow AlN on top of GaN nanowires arrays. Optical characterization were performed on AlN/GaN nanowires by means of RRS .The quality was preserved for GaN allowing to visualize the B_{1l} under resonant conditions. Raman measurements showed the AlN could suffer strain by the small shift present in the non-polar E_{2h}.

CHAPTER 5

SURFACE ENHANCED RAMAN SPECTROSCOPY ON INDIVIDUAL INP AND INN NANOWIRES

The previous chapters has been primarily concerned with the fundamental characterization of the electronic, structural and optical properties of nanowires by means of Resonant and Non-resonant Raman spectroscopy. The present chapter focuses on the characterization of single InP and InN nanowires by Surface enhanced Raman Spectroscopy using branched gold nanoparticles surface plasmons, also known as nanostars (NSs), multipods or nanoflowers.

This technique provides the same information that traditional Raman spectroscopy does but with a greatly enhanced signal. Although the spectra of most SERS experiments are similar to the non-surface enhanced spectra, there are often differences in the number of optical modes present. Additional modes not allowed by selection rules for InP nanowires are presented in the SERS spectrum. In addition, throughout the chapter it will be possible to discern the observation of the enhanced signal of surface optical (SO) phonon in InN nanowires. Another point of interest that will be covered in detail along this chapter will be the characteristic and well-known WZ/ZB polytypism along InP nanowires. The different phases of the material are observed more easily because of the enhancement of the intensity in the Raman signal when branched gold NPs are used.

InN and InP nanowires were growth by Subharata Dhar and Monica Cotta, respectively. Recio synthesized branched gold nanoparticles. Josep Canet Ferrer did the the-

oretical simulation of the the nanoparticle polarizability considering the excitation of its plasmonic modes (details are explained in Appendix C). The samples were optically characterized in close collaboration with Viviane Almeida.

5.1 Motivation

Surface-enhanced Raman scattering (SERS) spectroscopy is a highly sensitive method to obtain vibrational and chemical information from materials, whose enhancement is produced when nanometer sized nanoparticles are attached. The research on SERS has progressed from bulk samples studies to more complex and challenging analysis such as the detection of a single molecule [58, 175]. These highly sophisticated studies are possible by the amplification of electromagnetic fields generated by the excitation of localized surface plasmons (LSP). This permit overcoming the limitations of traditional Raman spectroscopy which consists of the inelastic scattering of the light where only one photon out of 10^7 is actually inelastically scattered. Normal Raman scattering does not supply enough signal in the case of small nanostructures like semiconductor nanowires where long acquisition times are necessary to avoid sample heating or any other alteration of the material by thermal or photochemical effect, leading to severe problems in obtaining reproducible spectra. For this reason, during the last decade a large number of works have been published based on the development of functional SERS substrates that produce extremely strong Raman signal even at low concentration of matter, in particular nanostructured materials as it is the case of nanowires. However, only a few number of works has investigated the SERS approach for non-resonant Raman characterization on isolated nanowires [176, 177].

An important challenge in a SERS experiment is the choice of substrates providing reproducible results. Currently, great efforts have been focused on developing different architectures using metal nanoparticles (typically, silver or gold) [178–181]. The advantages of these types of SERS substrates are well known and include stability, high reproducibility, tailoring of the substrates with various shapes and sizes of the particles in any geometry, easy fabrication and good detection of analytes, besides of covering most of the visible and near infrared wavelength range where most Raman measurements take place. Among gold nanostructures the synthesis of highly branched nanoparticles (NPs), also called nanoflowers, multipods or nanostars (when tips are symmetric), are particularly singular because are formed by a central body and arms or tips protruding from it. Because of this, the have a broader plasmons band than others NPs such as

gold nanorods due to the plasmon modes that are formed by hybridization of plasmons associated with the core and the tips [182]. In addition, this type of NPs displays higher enhancement factors (EFs) at the resonance wavelength than those for sphere or rod NPs [183].

Group III-V semiconductors such as GaAs, InP, InAs, or III-nitrides are in the focus of attention for their applications in optoelectronics, including light emitting diodes [187], lasers [188], solar cells [189] and photodetectors [190]. Among all III-V compounds, InP and InN nanowires are of special interest because their excellent electronic and optical properties. In the case of InN, it has the smallest direct bandgap among all nitrides (around ~0.7 eV) [184], which can be varied up to 6.2 eV by changing chemical composition of InGaAlN alloy, at the same time that addition of Al reduce the stress of the nitrides with the substrates [185]. The quaternary compound is a very interesting (suitable) material for the production of efficient solar cells because it covers almost the entire solar spectrum. Furthermore InN is an interesting material for high speed electronics because It possesses the lowest electron effective mass among all group III-nitrides [186]. On the other hand, InP nanowires are one of the most attractive materials because of its low gap (1.4 eV) suitable for infrared detectors, excellent carrier mobility, relatively efficient optical emission and wave-guiding characteristics [191–193]. InP, as many other zincblende semiconductors, grows in the wurtzite instead of the zincblende phase when they form nanowires. They can also present a mixture of both crystal phases which actually can be controlled to form homojunction quantum wells in a wire [194].

5.2 Branched Nanoparticles (NPs)

The synthesis and functionalization of NPs have aroused the interest of researchers due to their particular optical properties that can be manipulated by modifying size and shape of the NPs. In particular, gold NPs with sharp features generated strong electric fields at their tips upon absorption of incident light in the visible-near IR region [195, 196]. Their characteristic morphology makes branched NPs ideal towards applications such as LSPR and SERS sensing. Besides these nanostructures have generated attention because of their sharp edges and the correspondingly high localization of any surface plasmon modes. The electromagnetic spectrum of these NPs (see Figure 5.1) typically displays a plasmon band in the 600-1200 nm region, corresponding to plasmon modes confined at the tips. Furthermore a smaller band around 500-600 nm can

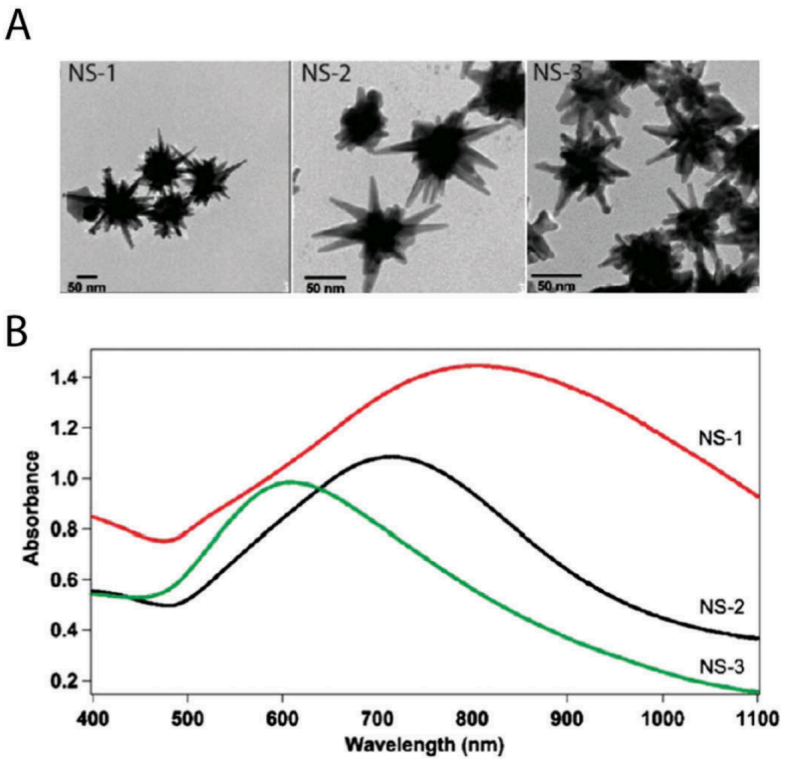

Figure 5.1: Image taken from [4] where is shown (A) TEM image of AuNSs synthesized with three different sizes. (B) Absorbance spectra of the corresponding NSs of (A) tested in SERS detection

visualized which is related to a mode localized at the central body [4].

Therefore, LSPR in AuNSs can be adapted by changing aspect ratio between tips and central body as can be observed at the reference paper of Reguera et.al. [4]. In addition, this work revealed theoretically and experimentally an extremely high electromagnetic field enhancement at the tips, corresponding to a low energy dipolar plasmon mode. That could have an influence at the near field and polarization of the incident light over the nanowire.

Typically, branched Au NPs have been successfully synthesized through the growth of Au seeds with the help of several directing agents including a surfactant [197], vapor phase polymerization [198], electrochemical method [199], hydrothermal technique [200] and seedless in situ growth method [201]. The NPs used in this work were synthesized by María José Recio Carretero as is described in her thesis [203].

5.2.1 Synthesis PVP Gold Nanostars (PVP-NSs).

Synthesized starting from a Au seed (the seeded growth process). Gold seeds and PVP coated seeds were prepared for SERS experiments.

Gold seed nanoparticles were prepared by adding 12.5 ml of 1% citrate solution to 2.5 ml of boiling 50 mM $HAuCl_4$ solution under vigorous stirring. After 15 min boiling the solution was cooled down to room temperature and then stored at 4°C for long-term storage [202].

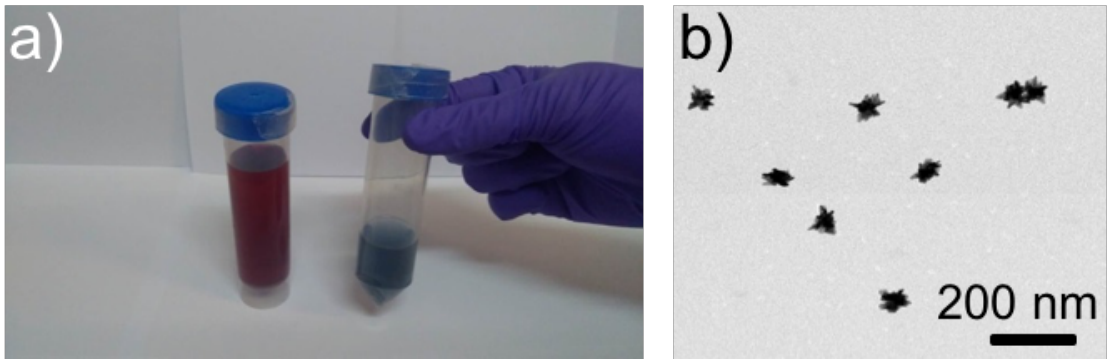

Figure 5.2: a) The red tube shows 13 nm gold seeds synthesized by standard citrate reduction and blue tube 55 nm Au-NSs synthesized through the reduction of $HAuCl_4$. b) Representative TEM image of Au NSs synthesized through reduction of $HAuCl_4$ in a PVP/DMF mixture, in the presence of preformed Au seeds,

Gold PVP coated seeds NPs were prepared by adding 0.122 g of PVP in 6 mL of water. After 15 min sonicating 50 mL of citrate seeds were added and was stirred at room temperature during 24 h. After that, it was centrifugated during 90 min at 6000 rpm and redispersed in EtOH. In a typical synthesis, 54.6 μL of an aqueous solution of 50 mM $HAuCl_4$ was mixed with 1.0 mL of 10 mM poly(vinylpyrrolidone) (PVP) (MW 10000) solution in 10 mL of N,N-dimethylformamide (DMF). After complete disappearance of the Au^{+3} 28.6 μL of the PVP coated seeds were added to the solution. In order to obtain middle size (mAuNS~ 50nm) of PVP-NSs, 500 μL were added to the solution with LSPR bands at 790 nm. It must be cleaned at least five times to eliminate the excess of PVP for Raman measurements (more details can be found in Ref. [203].)

5.3 InP nanowires

5.3.1 Growth and morphology of InP nanowires

InP nanowires were grown by the VLS method in a CBE system using 25 nm size Au nanoparticles as catalyst. The nanowires were grown on (001) GaAs substrates. After approximately ~12 minutes the substrate was cleaned with deionized water. Nanowires were grown at 420 °C using as growth precursors three different trimethyl-indium (TMIn) fluxes, 0.15, 0.3 and 0.45 sccm. All nanowires were grown along the [111] (zinc-blende) and [0001] (wurtzite) direction, respectively.

Figure 5.3: SEM image of a typical as-grown InP nanowire ensemble.

To characterize the nanowires, SEM measurements using a S-4800 (HITACHI) at operating voltages of 5 kV were performed. In Figure 5.3 a high density of random ensembles InP nanowires can be observed. SEM image of a typical as-grown InP nanowire ensemble at side view shows the homogeneous coverage with nanowires up to 20 μm length. In addition, InP nanowires exhibits a larger diameter than InN nanowires allowing the coupling of the NPs over nanowire. For SERS experiments InP nanowires were transferred mechanically from the as-grown substrate by imprint onto a pre-patterned Si/SiO_2 substrate as is indicated in Appendix A.1.

5.3.2 Surface Enhanced Raman Spectroscopy on isolated InP nanowires

Different concentrations of gold NPs over nanowires were deposited by drop-cast method (Figure 5.4 c) and d)). As can be appreciated in the case b), branched NPs can stick together coating completely the nanowire. After deposition morphology of the NPs is preserved in shape and size (see 5.4 d) where Nanoparticle's tips are randomly oriented. However, the nanowires that showed the best conditions for SERS experiments were those which had been entirely and uniformly surrounded by branched NPs. That can be appreciated through image manipulation using DigitalMicrograph^{TM} program where branched NPs over the single nanowire were remarked. A wide perspective of an individual nanowire with branched NPs can be visualized on Figure 5.4 c). AFM image

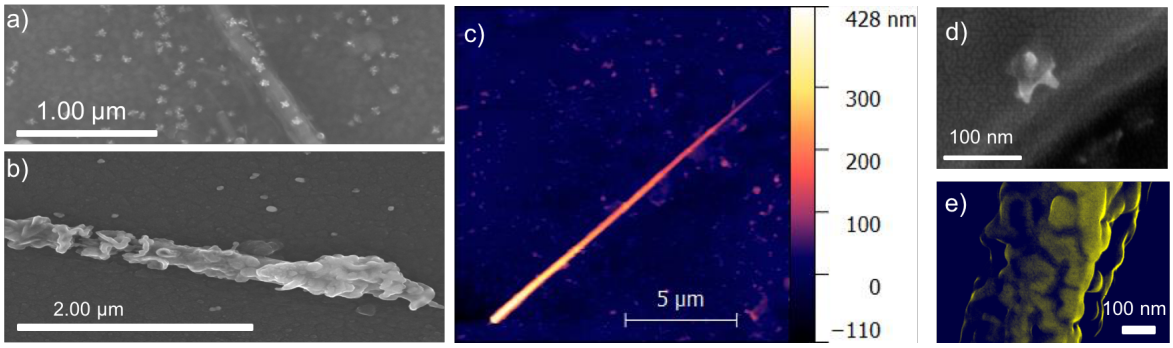

Figure 5.4: a) and b) Different kind of coating where a) is partially coated and b) is completely coated c) Atomic force microscope topographical image of a well isolated InP nanowire deposited on a patterned substrate covered with branched NPs e) Single NP over individual nanowire showing the shape and tips are conserved d) SEM image manipulated with DigitalMicrograph^{TM} program to remark the zone of interaction among branched NPs over isolated nanowires.

shows that the individual nanowires are monodisperse and well separated from one another on the substrate. Figure 5.4 also reveals that the diameter of the surrounded InP nanowires is approximately of 370 nm and has a length greater than 10 μm. Additional NPs around the wire can also affect on SERS experiments since near field region is in the order of λ (more details about the interaction of the nanowires with the electromagnetic field of NPs are given in the Appendix C).

All Raman measurements were carried out in back-scattering configuration (i.e. parallel wave vectors of the incident and the scattered light) with a triple-grating Jobin Yvon T64000 spectrometer equipped with a liquid-nitrogen-cooled charge-coupled device. The excitation line at 647.1nm was provided by an Ar/Kr laser focused onto the sample with a 100× microscope. In order to assure the system is not undergoing a resonance Raman effect and avoid any enhancement of the Raman scattering caused by photon energies closed to the electronic transition of InP, SERS spectra were collected for non-resonant excitation. That allows to distinguish the "real" enhancement provided for by the NPs whose unique resonance is closed to the LSP. The silicon peak was used as reference for calibration of the Raman measurements. Prior to the Raman measurements, the nanowires were located on a pre-patterned Si/SiO_2 substrate by imaging the surface with a charge-coupled device.

Figure 5.5 a) depicts the typical Raman spectrum of the measured samples for an isolated InP nanowire with branched NPs (at the upper panel) and without NPs (bottom panel). As can be observed significant differences can be appreciated at the two

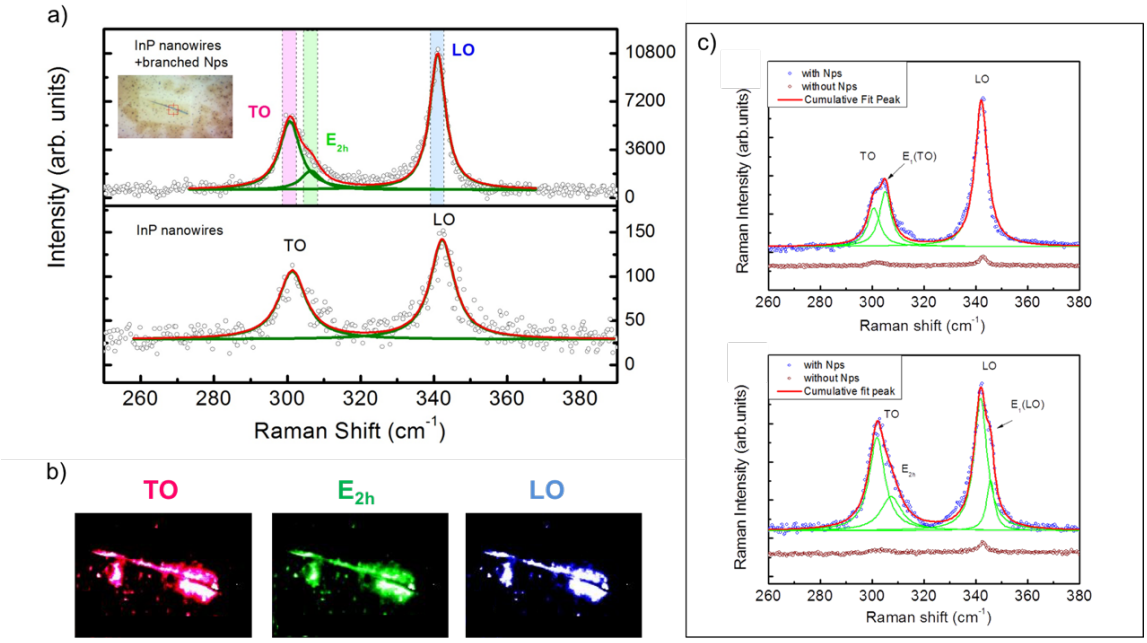

Figure 5.5: a) Non-Resonant Raman spectroscopy of individual nanowires with and without branched gold NPs where the colored range is represented by the Raman mapping of the phonon modes selected in the a) panel. c) Non-Resonant Raman scattering spectra of two isolated nanowires where is possible to identify at upper panel the $E_1(TO)$ phonon mode which is forbidden for parallel polarized configuration and lower pannel the $E_1(LO)$ mode which is not allowed for backscattering configuration.

spectra in using or not NPs. At the lower panel, two clear peaks were assigned to the transverse-optical (TO) mode and the longitudinal-optical (LO) mode at 301.9 and 341.9 cm^{-1}, respectively, in agreement with literature [204]. These optical phonon modes are related to the [111] of the zinc-blende structure. However, by means of SERS measurement an additional peak located at 307 cm^{-1} is shown at the upper panel. This mode does not pertain to the optical mode of the InP zinc-blende structure, but to the E_{2h} of the wurtzite structure. In general, arsenide and phosphide compounds can crystallize in both hexagonal and cubic crystal structures, being the zinc-blende structure the most stable in the bulk form. Nevertheless, these compounds can also crystallize in a hexagonal structure in the form of nanowires due to the lack of strain, i.e. because of surface relaxation [205], or even both phases can coexist depending on the grown conditions of the nanowires as in the present research, as previously commented. This lead to the appearance of extra peaks in the Raman spectra related to the optical phonon modes of wurtzite structure. It has been already reported that these additional modes can be

depicted by simply folding the Γ-L path of the Brillouin zone of the zinc-blende phase along the [111] direction to the to the phonon dispersion (Γ-A path) of the wurtzite structure along [0001] since unit cell length of the zinc-blende structure along the [111] axis is double with respect to the wurtzite along the [0001]. Therefore a combination of the phonon modes of zinc-blende and wurtzite structures should be visualized at the Raman spectra [25, 56]. In Table 5.1, the experimental values of the wurtzite and zinc-blende modes at the $\Gamma-$point are given. The uniqueness of the SERS measurement lies in the fact that wurtzite structure of a single InP nanowire can be easily identified because of the enhancement factor (with a higher intensity of up to two orders of magnitude compared to current Raman scattering experiment) avoiding long data acquisition times and sample heating.

Considering that the laser line excitation along the x-direction is set perpendicular to the nanowire axes only phonon modes corresponding to $x(y,y)\overline{x}$ and $x(z,z)\overline{x}$ polarization configuration from wurtzite structure are allowed (see Table 5.1) as no polarizer was used in collecting the back-scattered light. In the case of zinc-blende structure LO and TO are clearly visible in the Raman spectrum (Fig. 5.5). However, selection rules indicate that the LO mode is only allowed in crossed polarizations $x(y,z)\overline{x}$ in backscattering configuration [28]. The appearance of the LO phonon mode for parallel configuration is explained by the presence of high density of stacking faults. This occurs during growth since it is very frequent alternations between the $ABCABC...$ sequence for the zinc-blende phase along the [111] axis to the $ABAB...$ stacking sequence for the wurtzite phase along the [0001] axis [206, 207]. Thus the nanowires presents different facets groups which can be rotated atomic layers and induce the appearance of the forbidden LO mode [25]. In contrast TO mode is allowed for all backscattering configurations when the axis of the nanowire is perpendicular to the laser line excitation, i.e. the x-direction. The combination of the respective modes from different structures were characterized by SERS mapping.

AFM-Raman mapping measurements were taken using an AFM-Raman system (NTEGRA spectra PNL) with a 633 nm laser. Uncoated silicon tips with a force constant between 25N/m to 95N/m and a resonance frequency of 200-400kHz were used to check the profile and shape of the isolated surrounded nanowires in semi-contact mode (tapping mode). AFM scan was performed on a 15×15 μm area, with a scan resolution of 256×256 points, a rate of 0.5 Hz, gain constant of 1.45 and a Setpoint of 5.000 nA. Mapping of the nanowires was performed in an area of 300 μm^2 by recording step-spectra at every 150 nm with an integration time of 1 s using a 200× Mitutoyo objective. AFM

and mapping data were processed by Gwyddion software. By intensity integration of the [298-303 cm^{-1}] and [304-309 cm^{-1}] spectral domain around the TO (301.9 cm^{-1}) and LO (341.9 cm^{-1}) mode respectively, the intensity of the Raman signals over the full nanowire is investigated for zinc-blende structure (colored region bands selected in Fig. 5.5 a) are represented by Raman mapping in b)). The images show a lateral resolution better than 200nm, with an acquisition time of about 4 hours per image. The middle image (Fig. 5.5 b)) is obtained by integration of the E_2^h mode at 307.3 cm^{-1} [304-309 cm^{-1}] which corresponds to the phonon mode of wurtzite structure. For the TO, LO and E_2^h, the Raman signal is maximum where nanobranched particles are close to the nanowire.

Table 5.1: Phonon modes in wurtzite and zinc-blende. The polarization configurations for which Raman measurements are possible is indicated for wurtzite InP.

Wurtzite Structure			
Modes	ω (cm^{-1})	ω (cm^{-1})[a]	Pol. configurations
$A_1(TO)$	$--$	$302,1$	$x(y,y)\overline{x}$, $x(z,z)\overline{x}$
$E_1(TO)$	$304,3$	$302,4$	$x(z,y)\overline{x}$, $x(y,z)y$
E_{2h}	$307,3$	$306,4$	$x(y,y)\overline{x}$, $x(z,z)\overline{x}$, $z(y,x)\overline{z}$, $z(y,y)\overline{z}$
$A_1(LO)$	$--$	$341,9$	$z(y,y)\overline{z}$
$E_1(LO)$	$346,1$	$347,3$ [b]	$x(y,z)y$
Zinc-blende structure			
Modes	ω (cm^{-1})	ω (cm^{-1})[c]	Pol. configurations
TO	$301,9$	$303,7$	$x(-,-)\overline{x}$
LO	$341,9$	345	$x(y,z)\overline{x}$

[a] Experimental values of the optical phonon modes of wurtzite structure [208]
[b] Calculated phonon mode [208]
[c] Experimental values of the optical phonon modes of zinc-blende structure [204]

Apart from those modes, extra peaks have appeared on various Raman spectra (see in Figure 5.5 c)). These peaks were deconvoluted by Lorentzian fits for each one in order to extract the best position with accuracy. The peaks are located at 304.3 and 346.1 cm^{-1}. The peak at 304.3 cm^{-1} can be erroneously assigned to E_2^h phonon mode. Nevertheless, this peak is shifted 3 cm^{-1} respect to the E_2^h mode [208]. The E_2^h mode was located at 307.3 cm^{-1} in many individual nanowires with an accuracy of $\approx$ 0.5 cm^{-1}. For this reason, we exclude this peak corresponds to E_2^h mode. We could attributed this phonon to $A_1(TO)$ mode but it is shifted 2.2 cm^{-1} compared with reported values. At the literature, the closest value is attributed to the $E_1(TO)$ mode (see Table 5.1) which is forbidden for both $x(y,y)\bar{x}$ and $x(z,z)\bar{x}$ polarization configuration from wurtzite structure.

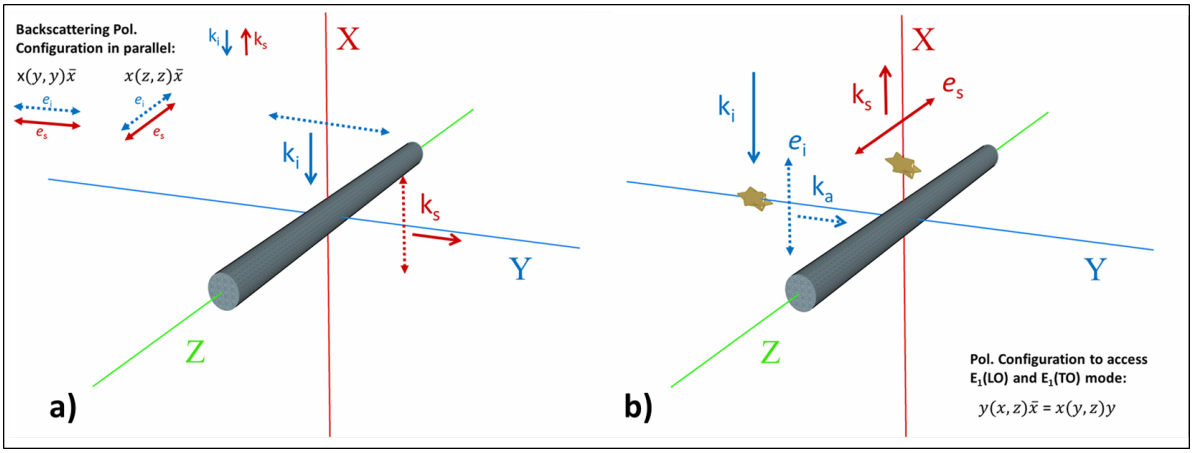

Figure 5.6: a) The configuration needed to activate both $E_1(LO)$ and $E_1(TO)$ phonon modes corresponds to $x(y,z)y$.The corresponding light polarizations are denoted e_i and e_s, respectively. The wave vector of the incident and scattering light is represented by k_i and k_s. For backscattering measurements the only configurations allowed are those where the incident and scattered light are parallel to each other since no polarized is used to rotate the polarization of the light b) Non-backscattering pol. configuration to access to forbidden modes that are not allowed for backscattering configuration. The wave vector of the electric field generated from the NP, k_a, is propagated along Y axis and is polarized perpendicular to the nanowire. Scattered light is amplified by the branched NPs and collected by the microscope with a polarization configuration parallel to the nanowire. This configuration is equivalent to $x(y,z)y$.

In the same way, it is possible to appreciate a big shoulder of the LO mode in Figure 5.5 c). The deconvolution of the spectrum shows a clearly visible peak at 346.1 cm^{-1}. This peak matches with the previosly calculated $E_1(LO)$ phonon mode [208]. However, no reported experimental values are given at the literature in nanowires since this phonon mode is completely forbidden for any backscattering polarization configuration (Table 5.1). But why this phonon mode is activated when the nanowires with gold branched NPs are measured? In order to explain this phenomenon in a simple way we performed an approximation considering the excitation of plasmonic modes in a NP as the result of electrical dipole in a sphere (see Appendix C). Note that the plasmon electric field at the location of the absorbed molecule could be greater considering more complex NPs shapes (with edges and tips) such as our branched NPs [209]. Therefore NPs can generate an electric field dipole at near field along the y or z axis, i.e. they can propagate the wave vector of the incident light along the y and z direction. For example, if we consider that the wave vector of the incident light (k_i) is propagated along y-direction with light polarized along x-axis through electric field generated at the NP (k_i will now

be perpendicular to both the nanowire and the microscope, i.e. the z and x-direction, respectively) and the wave vector of the scattering light is collected at the microscope we could measure Raman modes that are only allowed for $x(y,z)y$ which is equivalent to $y(x,z)\overline{x}$ polarization configuration as we can observed in Figure 5.6. It is important to notice that the wave vector of the scattered light must be polarized parallel to the axis of the nanowire in such a way that surrounded nanowires by NPs will have more probabilities to access to this polarization configuration. Thus forbidden phonon modes such as $E_1(LO)$ and $E_1(TO)$ which are not accessible under our current excitation configuration could be allowed through the near-field excitation of electric dipolar modes in different conditions. This case only represents an extra polarization configuration but different extra backscattering and non-backscattering polarization configurations could be achieved by positioning the NPs at the desired configuration.

5.4 InN nanowires

5.4.1 Growth and morphology of InN nanowires

InN nanowires were grown on Au coated quartz substrates by CVD method using VLS technique. The investigation of the growth parameter and their optimization for different thicknesses of gold layer substrates is described in the Appendix (chapter B.1). Gold layers were deposited by four target electron beam evaporator. These coated substrates were placed side wise along with high-purity indium metal (99.99%) in a quartz boat. The boat was then kept at the centre of a quartz tube furnace. Argon (purity 99.999%) and ammonia (purity 99.999%) were introduced into the reactor through mass flow controllers (MFCs). Samples were grown at different temperatures ranging from 500 to 650 °C for a fixed time of 8 h (see Appendix). The argon and ammonia flow rates were adjusted to 20 and 40 sccm during the growth process. Prior to the growth, quartz tube was purged with argon for 20 minutes.The morphology and structural properties of these nanowires are investigated using SEM (JSM-7600F JEOL) and HRTEM (JEM-2100F JEOL). Wires were thoroughly dispersed in methanol and casted on the carbon coated copper grid for HRTEM study.

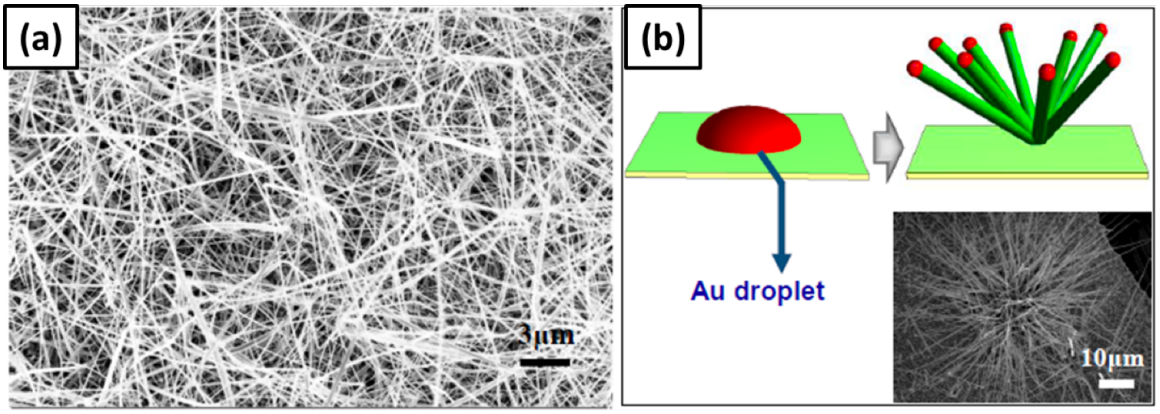

Figure 5.7: a) SEM micrograph of InN grown on 15 nm Au coated quartz substrate at 550 °C and b) schematic diagram of multiple nucleation of nanowires.

Fig. 5.7 (a) shows the SEM micrographs of InN grown on 15 nm Au coated substrate at 550 °C. It shows a high density of InN nanowires grown throughout the substrate. The nanowires have an average diameter of 20 nm and lengths of a few tens of microns. Interestingly, in this case, most of the nucleation sites have been found to act as the origin of several nanowires. This is termed as multi-nucleation growth mode [210]. Upon heating at 550 °C, 15 nm thick Au catalyst layer form bigger droplets as compare to 3 nm Au catalyst case. These droplets result in the formation of bunches of nanowires as shown schematically in Figure 5.7 (b). Inset of Figure 5.7 (b) shows the SEM image of a portion of the sample where the growth of a bunch of nanowires from a single nucleation center is clearly visible. Additionally, in Fig 5.8 can be observed TEM micrographs of InN nanowires grown on 15 nm Au coated substrate at 550 °C. The width of these nanowires are found to be ≈20 nm. Note that the excitonic bohr radius of InN is ~ 10 nm [1], which could mean that quantum confinement of carriers is in principle possible in these wires. Color contrast at the wire tips represents Au droplets. Inset of Figure 5.8 (a) shows a selected area electron diffraction (SAED) pattern along the [0002] zone axis for a wire. Hexagonal symmetry of the spotty diffraction pattern suggests that these nanowires are single crystalline in nature. Figure 5.8 (b) represents the bright field high resolution transmission microscope image of a wire, showing clear lattice fringes. (0002) and $(11\bar{2}0)$ planes of wurtzite InN can be identified from corresponding interplaner spacing of 2.8 and 1.7 Å (as indicated in the figure). These results suggest that InN nanowires are grown along the $[11\bar{2}0]$ direction (a-plane).

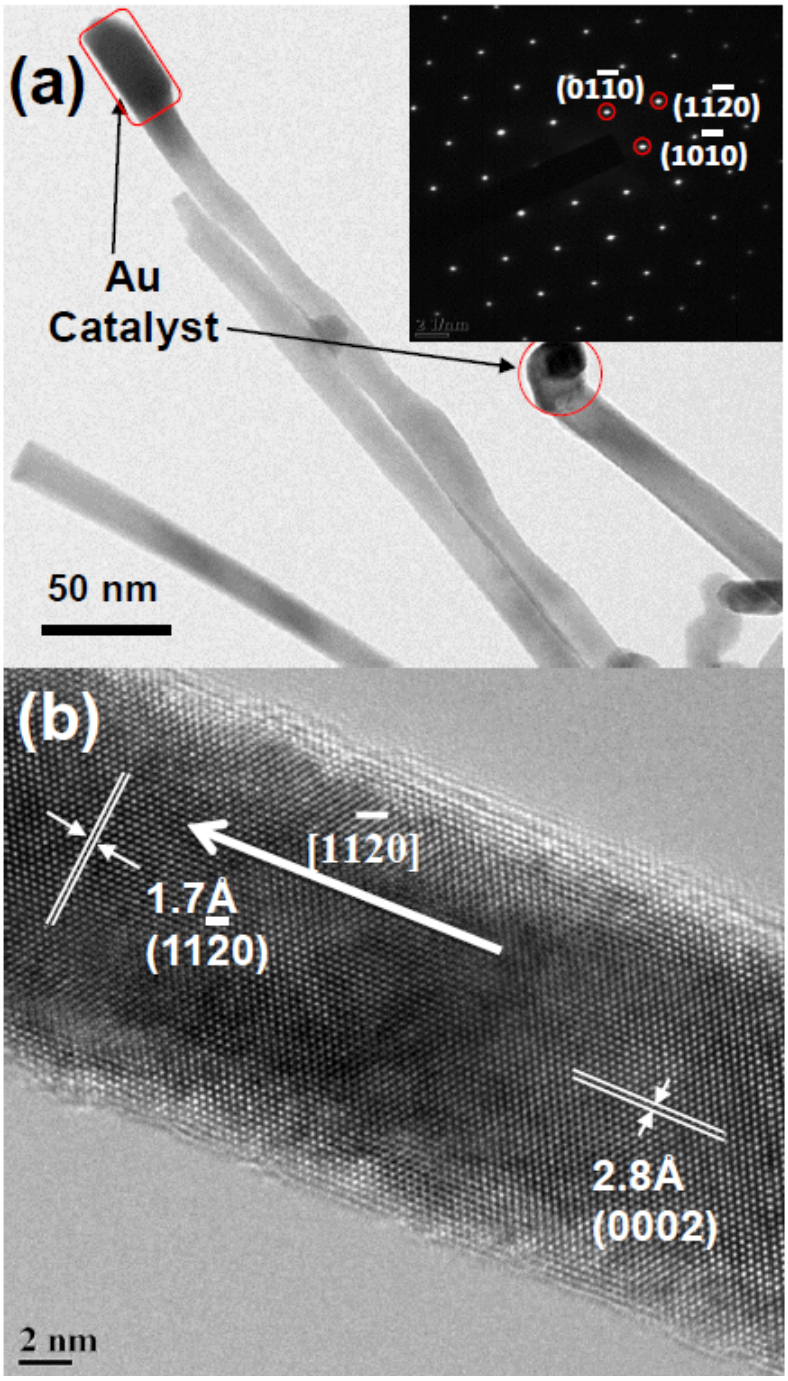

Figure 5.8: (a) High-resolution transmission electron micrograph of a few InN nanowires grown on 15 nm Au coated quartz substrate at 550 °C. Inset: selected area electron diffraction pattern of one of the nanowires and (b) High-resolution TEM image showing lattice planes.

5.4.2 XPS measurements

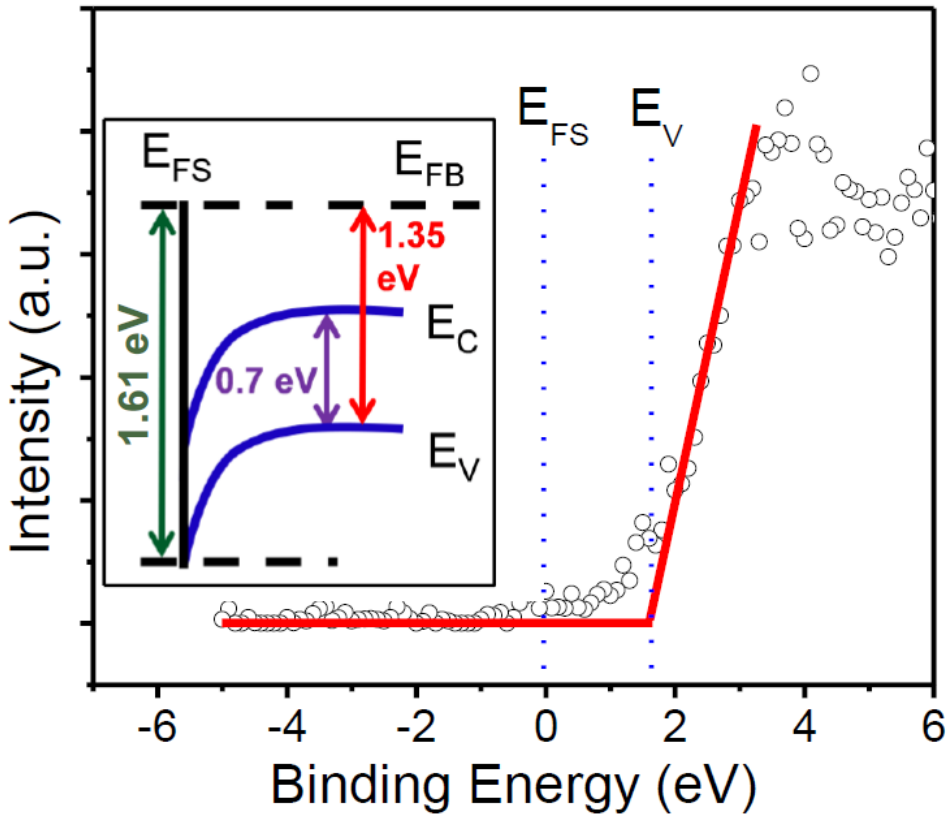

Figure 5.9: XPS profiles recorded at the valence band edge for InN nanowires grown on 15 nm Au coated quartz substrate at 550 °C, Inset: schematic representation of the band bending at the surface of a wire.

Figure 5.9 shows XPS spectra recorded at the valence band edge for the InN nanowires grown on 15 nm Au coated quartz substrate at 550 °C. Note that the zero energy of the spectra represents the position of the surface Fermi energy. The position of the valence band maximum (E_V) is estimated to be 1.61 eV below the surface Fermi level (E_FS). InN has a band gap of 0.7 eV at room temperature [211], which means that the surface Fermi level is located 0.91 eV above the conduction band minimum (E_C) in these samples as shown schematically in inset of Fig 5.9. This in turn implies that the electrons are the majority carriers in the sample. This surface pinning of fermi level above conduction band suggests accumulation of electron on the surface of nanowires which has also been reported earlier in InN thin films [212].

5.4.3 Surfaced enhanced Raman Spectroscopy on single InN nanowires

For SERS analysis InN nanowires were transferred to the substrate with the technique described in Appendix A.1, and branched NPs were deposited onto nanowires by drop casting. Unlike InP nanowires, InN nanowires are not completely surrounded (see Figure 5.10) since the small diameter does not enable gold NPs cover the whole width (in many occasions the diameter of the nanowire is around the size of the NP). However, in this case the shape of tips from the NPs are clearly more visible over the sample.

Raman measurements on single nanowires located at the mark substrate before to deposit NPs were performed. After deposition the nanowires were measured at the same power intensity and same polarization configuration in order to obtain an enhanced Raman spectrum without any additional effects provided by the configuration of the system, as in the case mentioned above for InP nanowires. The Raman setup employed was the same as InP nanowires (see subsection 5.3.2).

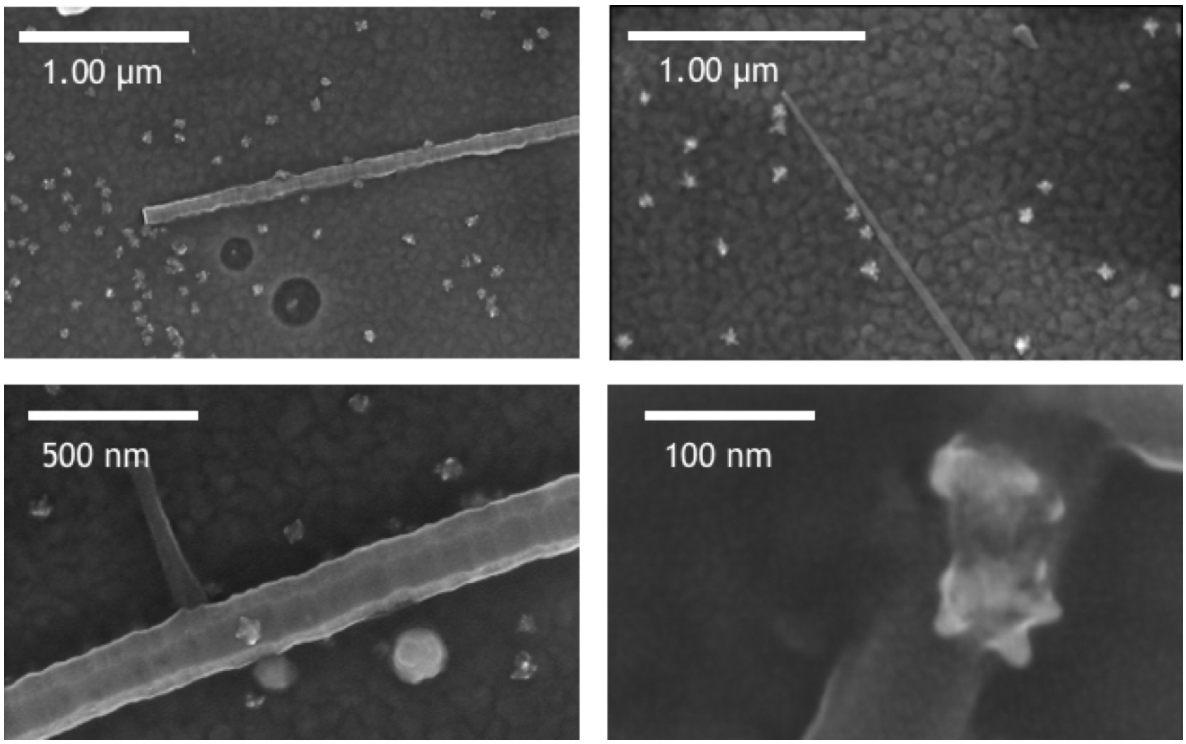

Figure 5.10: SEM images of InN nanowires coated with Au branched NPs where can be observed surface roughness of the nanowire and the shape of the NPs.

In Figure 5.11 two Raman spectra of an individual InN nanowire can be visualized.

The bottom/upper spectrum pertains to InN before/after depositing Au NPs. For this material, the enhancement is not so strong as InP nanowires due to low number of NPs adhered to the sample. Nevertheless, there is a significant evidence of improvement of the Raman signal (× 6 respect to the original spectrum). No additional modes in the enhanced Raman spectrum for the different samples measured were found. As InN belongs to C_{6v} group symmetry, as GaN, AlN and their alloys, the wurtzite InN structure presents the polar A_1 and E_1 modes which split into LO and TO optic components resulting a total of six Raman active modes. The configuration polarization used in these measurements is the same as the InP nanowires characterization. Therefore, only $A_1(TO)$ and E_{2h} phonon modes are allowed in the spectra range from 400 to 650 cm^{-1}. These modes are located at 449 ($A_1(TO)$) and 490 (E_{2h}) cm^{-1} in agreement with the literature [213, 214]. However, the broad spectrum presents additional modes with different intensities. In order to analyzed this spectrum, the peaks were fitted by Lorentzians as is reported throughout this work. Two unclear peaks at the position of 577 and 588 cm^{-1} were located. These Raman peaks were attributed at $E_1(LO)$ and $A_1(LO)$ by comparing the observed frequencies with those of reported Raman data for InN. In addition these modes appear at lower frequencies, than those of bulk InN [213, 214] due to confinement effect [215]. But these assignments are ambiguous since selection rules predict these modes are forbidden for the configurations used $x(y,y)\overline{x}$ and $x(z,z)\overline{x}$. In many cases these modes are assigned to longitudinal modes due to the relaxation of the selection rules in the lower quality m-face. Unlike InP nanowires, these nanowires were grown by CVD technique which is known to present inferior crystal quality of the grown samples compared to MBE, as can be observed by the comparison of the band-edge emission of PL spectra from a sample grown by both methods [216]. Therefore, InN material grown by CVD may contains an abundance of defects and impurities or even indium oxide in some cases and they can affect the InN electronic transitions. For instance, an enhancement of the Raman instensity of the polar $A_1(LO)$ phonon mode in InN under 830 nm (1.49 eV) excitation has been reported [217] due to electronic transitions related to defects and impurities, which are present in many of the current InN nanowires. That opens the possibility of the appearance of forbidden modes in the Raman spectra under resonant condition as for example is observed in InAs nanowires [54]. Although the analysis of the Raman spectrum is not straightforward and further analysis are needed.

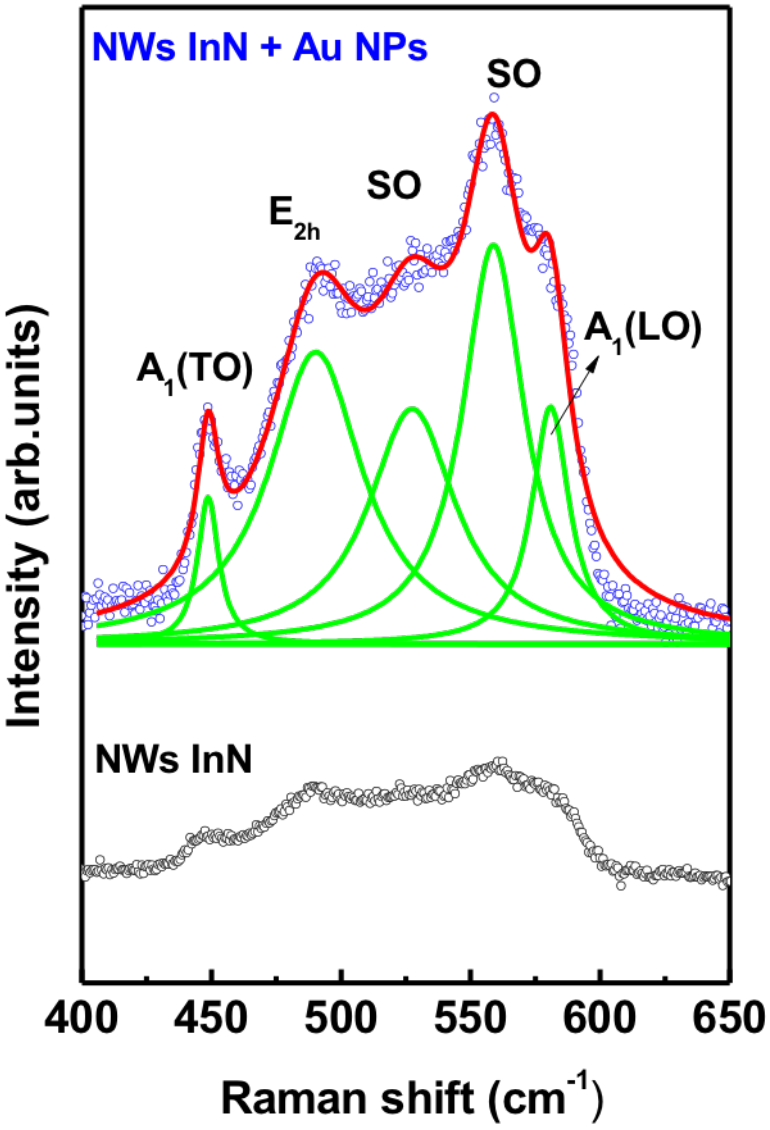

Figure 5.11: Raman spectroscopy of individual nanowires with and without Au branched NPs. The roughness of the nanowire allows to observe clearly the SO modes related to the surface of the sample which intensity is enhanced by the excitation of plasmonic modes in a NP as the resulting electrical dipole.

Additionally two intense peaks are observed at 528 and 560 cm^{-1} which may be attributed to surface optical modes. It has already been reported in a few cases that

when phonon is confined to the surface of the nanowire, the nanowire presents a clear evidence of the roughness and has small diameter oscillations of the nanowire (as can be displayed in Figure 5.10) the Raman spectra can exhibit high intensities of surface optical phonons in polar semiconductor nanostructures [213]. In addition, this becomes more evident when the signal is enhanced by SERS substrate. The high intensities of the SO modes arise due to a substantial fraction of atoms of InN nanowires reside on the surface in comparison with the interior of the nanowire.

5.5 Summary

In this chapter, branched gold NPs were synthesized and deposited onto nanowires. SERS measurements on InN and InP nanowires with an enhancement up to two orders of magnitude were performed. For InP nanowires the resolution of the Raman spectra allowed distinguish between the known polytipic structure of InP. Additionally, extra phonon modes were accessible by means SERS experiments which are forbidden for backscattering or perpendicular configuration. This analysis opens up the possibility to a new field of study where Raman polarization is analyzed with controlled SERS substrate. In the case of InN nanowires, an enhancement of all phonon modes visible at Raman spectrum was observed, specially SO phonon modes related to surface vibrations. These nanowires presented a visible roughness confirmed by SEM measurements that allowed to observe high intensities of the SO modes, whose Raman intensity was enhanced by SERS substrates. However, in this case no additional modes respect to the original Raman spectrum were found. Further studies would be needed to clarify electronic transitions in InN material due to defects and impurities. A solution might be to measure Raman scattering intensities of doped InN nanowires as a function of laser excitation wavelength in order to find InN samples that are under resonant conditions close to LSP from the SERS substrate. That would allow to distinguish clearly the electronic transitions by RRS whose signal is enhanced by SERS on individual nanowires.

In short, the simple approach for the fabrication of highly efficient branched gold NPs is expected to have numerous opportunities in integrating SERS with other nanostructure materials. One of the important future challenges in the efficient application of SERS in nanowires is the study of the polarizability of the NPs-dipoles that open new chances for developing SERS substrates that enable to access to specific polarization configurations.

CHAPTER 6

DEVICES FOR HARVESTING APPLICATIONS

In this Chapter, a proof of concept Hybrid Solar Cell made of ZnO nanowires with PEDOT:PSS [Poly(3,4 -ethylenedioxythiophene)-poly(styrenesulfonate)] is presented. The main objective is to go beyond of theoretical and experimental characterization of the samples and obtain a real application for energy harvesting.

In photovoltaics, nanostructured materials are being used to develop high efficiency solar cells due to their capabilities to improve light trapping. With this purpose, high-quality n-type ZnO nanowires were synthesized on Silicon substrates. The selection of ZnO, instead of a semiconductor with the gap in the visible range, was due to the facilities to grow high quality n-type ZnO nanowires in an n-doped substrate (Si). These nanowires were growth upstanding to process a hybrid solar cell using PEDOT:PSS as p-type material.

Synthesis and optical characterization of the nanowires were performed at the Friedrich-Schiller-University Jena, in close collaboration with the group of Prof. Dr. Carsten Ronning. Additional polymerization experiments were carried out in collaboration with Álvaro Seijas. Since it is only a proof of concept, if the resulting n-p type solar cell has a good $I(V)$ characteristics under illumination, this would be an excellent result.

6.1 Hybrid Solar Cell using ZnO nanowires

6.1.1 Motivation

One of the most important efforts has been devoted to the development of new materials or semiconductors nanostructures for the production of low cost and highly efficient solar cells. In particular, nanowire-based solar cells are currently being investigated for next-generation of photovoltaics (PV) architectures and for powering devices at nanometer scale [218, 219] as a means of lowering cost [220] through the fabrication of nanowires arrays [221]. One-dimensional nanostructures as nanowires have multiple benefits for PV applications due to their geometrical structure which provide direct electrical pathways that allows to ensure the rapid collection of carriers generated throughout the device.

ZnO is one of the most popular materials that could be incorporated in solar cell devices due to its excellent properties and numerous advantages such as non-toxicity, easy synthesis, good electrical properties, high exciton binding energy (60 meV), high room temperature mobility (115-155 $cm^2V^{-1}s^{-1}$) and high breakdown strength, in addition to being one of the hardest materials among II-VI group semiconductors. However, ZnO has a direct band gap of 3.3 eV, which makes it insensitive to visible light with absorption only in the UV range. Typically, most of ZnO materials present n-type [222] characteristics and its work function energy is very suitable for forming heterojunctions with organic materials. In addition, they can be grown as nanowire arrays with the appropriate dimensions for development efficient hybrid solar cells.

6.1.2 Background

A simple solar cell can be considered as a p-n junction diode where the current will flow only in one direction in forward biased conditions . The schematic of this device has been depicted in Figure 6.1. When a p-type material is placed in contact with a n-type, the electrons in the Conduction Band (CB) from the n-side migrate to the p-side while in the Valence Band (VB) the holes from the p-region move to the n-region. Close to the boundary of the p-n junction these charges recombine (electrons diffuse across to combine with holes) creating a "depletion zone", also called space charge layer or depletion layer, where no mobile charge carriers are present. This depletion layer acts like a wall (Coulomb barrier) between the p-type and n-type semiconductor that opposes the flow of free electrons and holes. In order to overcome this barrier potential,

the application of enough voltage that allow to move freely the charge carriers across the p-n junction is needed.

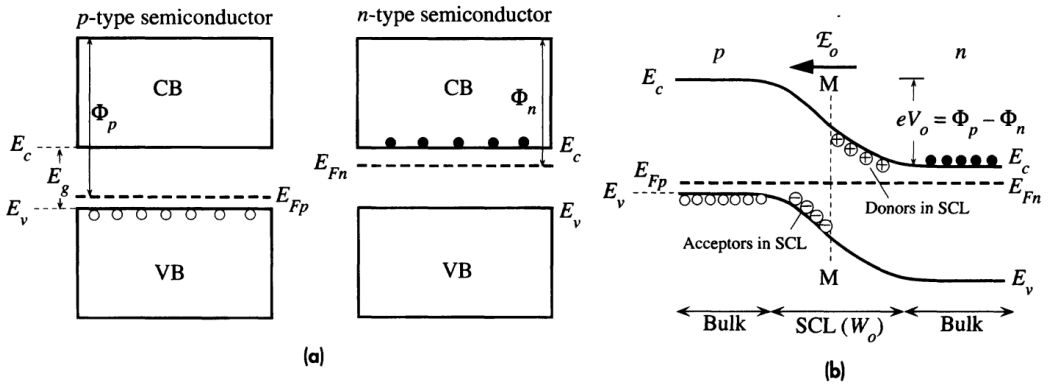

Figure 6.1: Image taken from Principles of Electronic Materials - S.O. Kasap. [5] a) Two separated n- and p-type semiconducors of the same bulk material b) p-n junction with no external bias. Radiation is absorbed in the space charge layer (SCL) and produce electron and holes. The Fermi level is uniform and in equilibrium.

In order to characterized the performance of solar cells some fundamentals are needed. The basic principles are extracted from the book of "Principles of Electronic Materials" from S.O. Kasap [5]. More detailed informations can be found elsewhere [223].

The behaviour of a diode can be defined by the Shockley ideal diode equation:

$$I = I_0 \left(e^{\frac{qV}{\eta k_B T}} - 1 \right) \tag{6.1}$$

Where I is the total current through the diode, I_0 is the "reverse saturation current", also called the dark saturated current, V is the applied bias voltage, T is the temperature and η is the ideality factor which is equal to 1 in an ideal diode. Actually, η determines the quality of the diode. In a solar cell the total current is defined by the following equation:

$$I = I_0 \left(e^{\frac{qV}{\eta k_B T}} - 1 \right) - I_{ph} \tag{6.2}$$

where I_{ph} is photocurrent, which is generated due the separation of charge carriers through photon absorption within the volume enclosing the SCL and is opposite to the

short circuit current I_{SC}. The short circuit solar cell current in light is given by $I_{SC} = -I_{ph} = KI_L$, where I_{SC} is the current of a circuit when the external load resistance is zero i.e. the current through the device without any applied bias voltage, K is a constant that depends on the particular device and I_L is the light intensity. The shift of the current in Equation 6.2 gives rise to another important parameter to characterize the performance of a solar cell, the open circuit voltage V_{OC}. It is defined as the value of the bias voltage when the net current in the circuit is zero and can be calculated approx using the Equation 6.2.

$$I_{ph} = I_0\left(e^{\frac{qV_{OC}}{k_BT}} - 1\right), \qquad I = 0$$

$$V_{OC} \approx \frac{k_BT}{q} ln\left[\frac{I_{ph}}{I_0}\right] \tag{6.3}$$

In order to better characterized the solar cells the short-circuit density current J_{SC} rather than I_{SC} is used in this work. This parameter defines the current density at zero bias. The product of $J_{SC} \times V_{OC}$ gives the theoretical power at short-circuit current and open-circuit voltage and represents the desirable goal in power delivery for a given solar cell [5]. Since the real maximum power of a solar cell is $P_m = J_m \times V_m$ which is the rectangular area under the curve corresponding to J_m and V_m (see Figure 6.2), the figure of merit for the solar cell can be defined as:

$$FF = \frac{P_m}{J_{SC} \times V_{OC}} \tag{6.4}$$

where FF is the filling factor and allows to compare the maximum power with the desirable goal in power delivery. From this value it is possible to appreciate that, as the quality of the solar cell increase, the FF approaches 1 although the exponential $I-V$ curve characteristics of a p-n junctions prevent that (this can be observed in Figure 6.2). By combining of the main parameters the power conversion efficiency $\eta_{photovoltaic}$ of a solar cell device can be calculated, which is defined as the ratio of generated electricity (output electric power density) to incoming light energy (input light power density P_{light}). In this work, a solar simulator has been used to control the input light power density.

$$\eta_{photovoltaic} = \frac{J_{SC} V_{OC} FF}{P_{light}} \tag{6.5}$$

Finally, a parameter widely used for characterizing solar cells is the external quantum efficiency EQE, which gives the ratio between the number of charge carriers collected by the solar cell and the number of all the incident photons on the device active area at a given wavelength. In other words, it indicates the amount of current that the cell produces when irradiated by photons of a particular energy. Note that the quantum efficiency of photons with energy below the band gap of the involved materials of the processed solar cells will be zero.

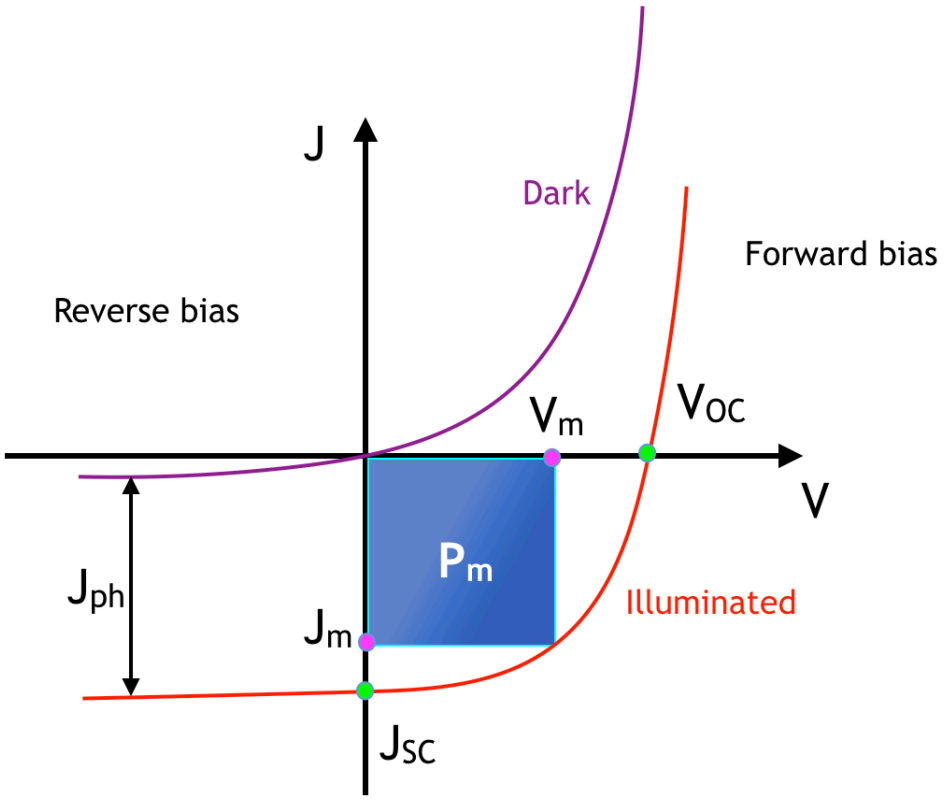

Figure 6.2: $J-V$ curve for a solar cell. The maximum power output corresponds to highest power density of solar cell. Adapted from Principles of electronic materials [5].

6.1.3 Growth,morphology and optical characterization of upstanding ZnO nanowires

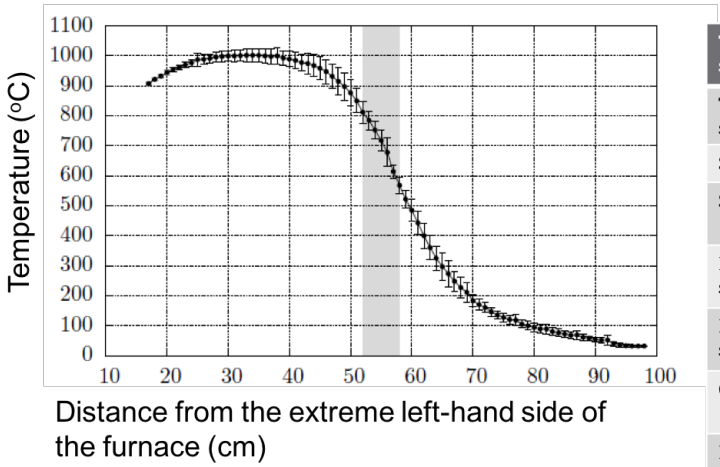

Conditions 3ZJ

Temperature source material	1050 °C
Temperature samples	≈750-930 °C
Source material	2g ZnO + C
Substrate	500nm AZO onto n-type Si
Position of the source material	36 cm
Position of the Si substrates	46 cm
Gas flow	10 sccm Ar, 10sccm O_2
Pressure	5 mbar

Figure 6.3: Temperature profile in the 3-zone furnace.

Relatively dense ZnO nanowires were synthesized using thermal transport technique in Jena in a three-zone-furnace (3ZJ). Close to the hottest point of the 3ZJ, the source material is placed and vaporized (see Figure 6.3). The temperature at this point was around 1050 °C. The source material consisting of a mixture (1 : 1 molar) of ZnO and carbon (Alfa Aesar: 99.99%) powder for carbonassisted growth (CAG) within an alumina boat. The aim of CAG is to reduce the sublimation point by the reduction of ZnO (it sublimes at 1800 °C) to Zn (Boiling point at 907 °C):

$$(1)\quad ZnO + C \Rightarrow ZnO + CO, \qquad (2)\quad ZnO + CO \Rightarrow ZnO + CO_2, \qquad (3)\quad CO_2 + C \Rightarrow CO$$

The source material was transported downstream to a colder point of the tube by Ar carrier gas (Ar and O_2 flow 10 sccm each and the base pressure was 5 mbar). Then, the nanowires grow upstanding onto a Si substrate with a ≈ 500 nm layer of sputtered Al doped ZnO (AZO) on top. The substrates are placed at 10-12 cm from the source. The nanowires were characterized by SEM, some representative images are shown in Figure 6.4. The growth condition in the 3ZJ provides ZnO nanowire batches with nanowire diameters between 100-400 nm and several μm length.

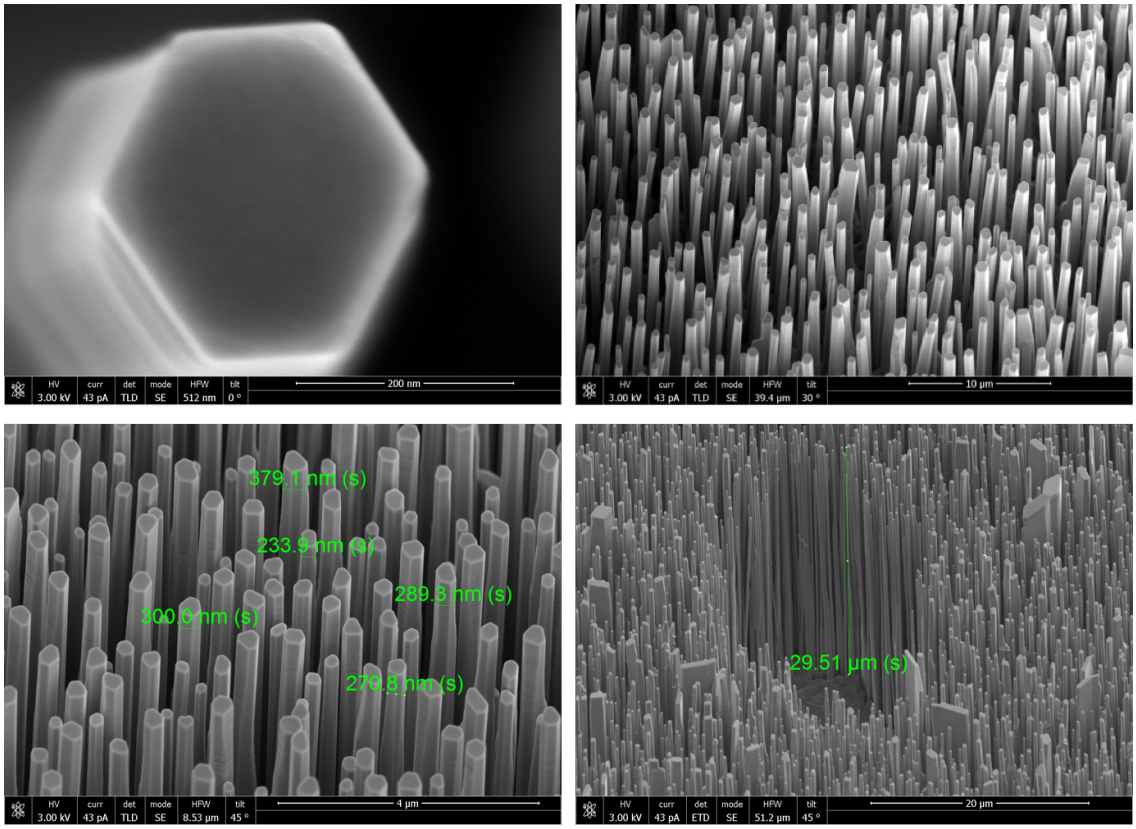

Figure 6.4: SEM images of the samples where the hexagonal structure of a single nanowire, diameter, length and density of the ZnO nanowires can be visualized.

For the macro and μ-PL measurements at room temperature, the setup installed at the Solid-State group of Prof. Carsten Roning at the University of Jena has been used (see section 2.2.3). The excitation line of 325 nm was supplied by a He-Cd laser with a maximum output power of 50 mW for macro PL measurements. Using this laser line, one can excites the ZnO nanowires with a photon energy above the band gap. The macro PL configuration provides a fast characterization of as-grown nanowire ensembles (see Figure 6.5 a)). This spectrum shows the survey luminescence spectrum of the ZnO nanowires and the underlying ZnO background structures which enclose a sharp peak corresponding to the near band edge emission (NBE) centered at 3.28 eV in the UV region and a broad structure centered at 2.32 eV related to the deep level emission (DLE). The origin of the DLE band are recombination processes via deep levels in the band gap of ZnO and can be related to the nanostructures below of the nanowires, however it is often explained as a consequence of oxygen vacancies and Cu-related impurities during the growth of the material [224–226].

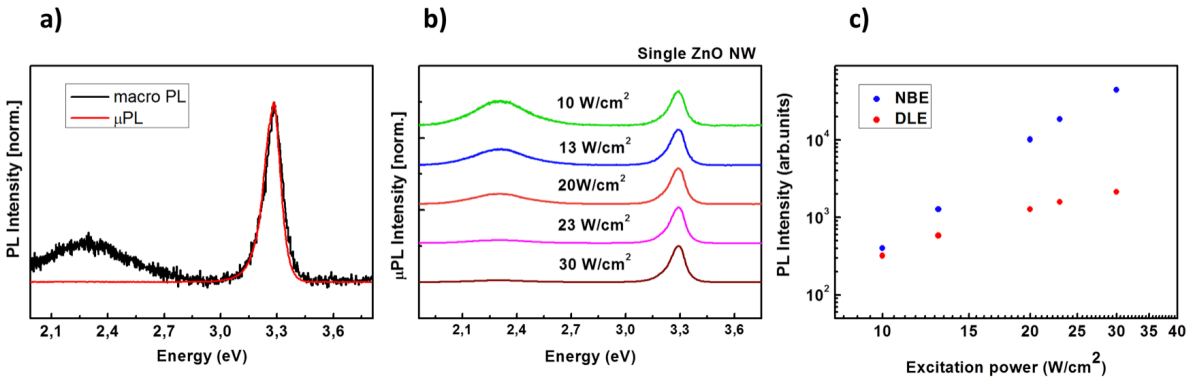

Figure 6.5: a) Macro andμ-PL spectra of as-grown ZnO nanowire ensembles compared to single nanowire transferred in a Si-substrate. b) Normalized PL spectra of a single ZnO nanowires measured under different excitation intensities. c) NBE and DLE intensities of ZnO nanowires as a function of the excitation power intensity.

The luminescence of individual ZnO nanowires transferred to a clean Si substrate (similar to the transferred technique explained in Appendix A.1) was studied in Jena using μPL under different excitation power (Figure 6.5 b)). For power intensity dependence measurements, the laser excitation intensity was progressively increased and the PL spectra of the ZnO nanowires were collected by the CCD. The spectra show that the defect emission at low power intensity is comparable to the NBE, while the NBE becomes more relevant at higher excitation power. Nevertheless, the presence of the strong DLE at low excitation conditions and the sharp peak related to the NBE of ZnO nanowires at higher excitation power intensities should not be taken as a reliable indicator of the crystalline quality since the absolute PL intensities under calibrated excitation conditions should be compared [227]. In Figure 6.5 c) the NBE and DLE intensities are compared, which gives a linear dependence with excitation power for the excitonic emission, while the DLE scales sublinear. Therefore, it is reasonably safe to conclude that ZnO nanowires were grown by VLS process with a good crystal quality.

Once I return to Valencia, a Raman characterization has also been performed. As GaN, ZnO with wurtzite structure belongs to the C_{6v}^4 ($P6_3mc$) space group. In backscattering geometry only the E_2 and $A_1(LO)$ are allowed when the incident light is parallel to the c-axis (more details can be found in Chapter 4). In Figure 6.6 we can see the Raman spectrum of an ensemble of as-grown ZnO nanowires on a Si/SiO_2 substrate illuminated with an excitation wavelength of 532 nm using a 20 × objective. Beside the peak at 519.5 cm^{-1}, which is assigned to the optical Raman mode of the Si substrate, an intense sharp peak is observed at 438 cm^{-1} corresponding to E_{2h} high non-polar optical

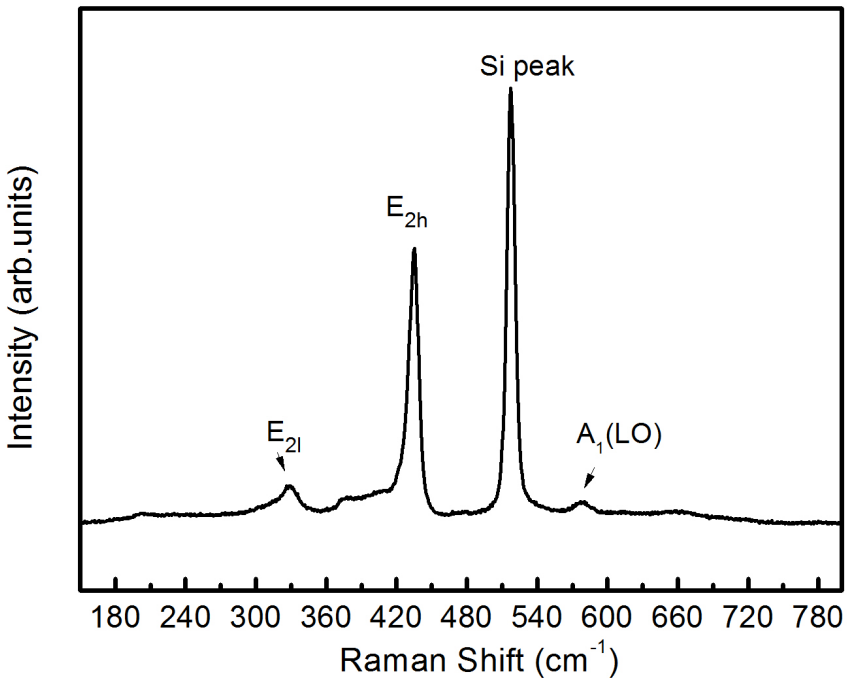

Figure 6.6: Raman spectra of ZnO nanowires ensembles.

phonon mode of the ZnO. The observation of this prominent peak indicates that the sample has a high crystal quality (existence of defects would result in a broadening of the E_{2h} mode). Moreover, the peaks which are assigned to E_{2l} and $A_1(LO)$ were observed at 331 and 575 cm^{-1}, respectively.

6.1.4 Processing of hybrid nanowire solar cell devices

After obtaining uniform arrays of ZnO nanowires on Si, a hybrid solar cell using PEDOT:PSS as p-type hole-transporting donor material and ZnO nanowires as n-type electron-transporting channels ihave been processed. PEDOT:PSS (Sigma-Aldrich) was spin coated in air on the ZnO nanowire arrays at 4000 rpm for 40 s to form a homogeneous layer. This film was heated at 100^o during 10 min, immediately after spin coating, for trapped solvent removal. For the front contact a gold thin film of around ≈ 7-10 nm of thickness was deposited by means of fine coater (JFC-1200). In the case of back contact an InGa alloy was employed in contact with the Si substrate of the sample over a copper path. In Figure 6.7 d), the cross-section SEM micrograph of a typical hybrid solar cell

structure without back contact is shown.

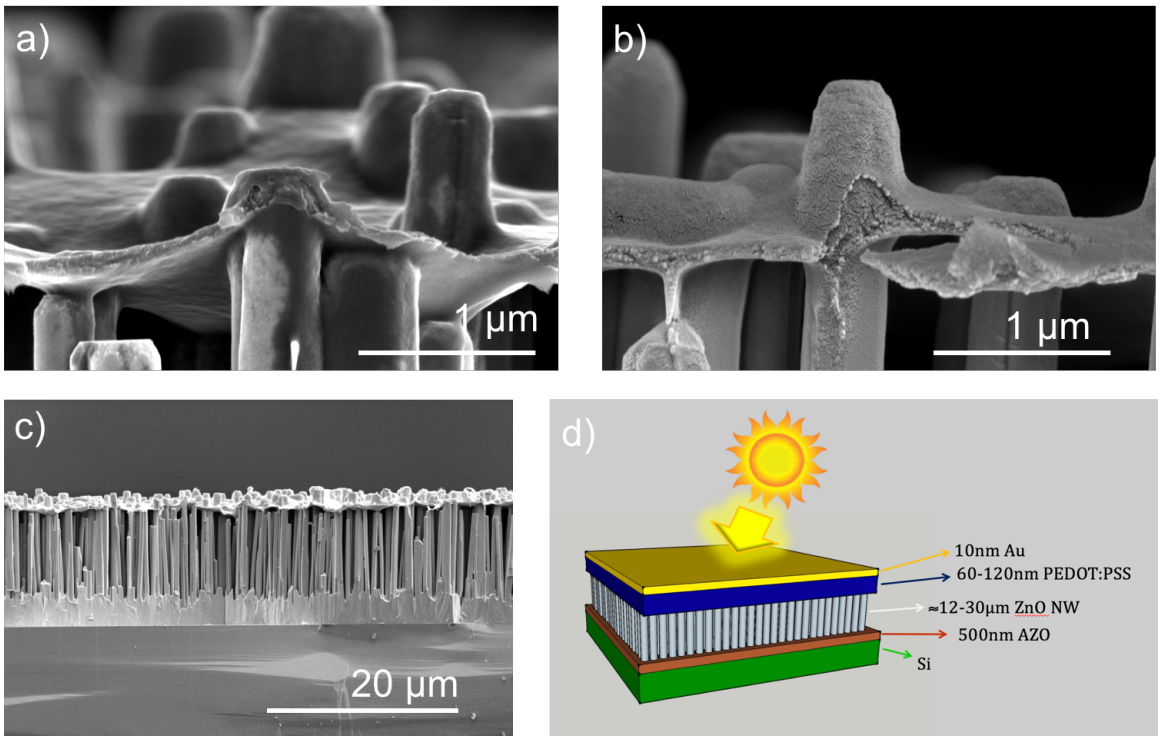

Figure 6.7: a) Morphology after coating with the PEDOT:PSS solution; b) Gold sputter coating; c) and d) Resulting ZnO nanowire/PEDOT:PSS hybrid solar cell.

Current-voltage characteristics of the hybrid solar cell devices were recorded by two and four-point probe configuration (see Figure 6.8 a)) using a computer-controlled Keithley 6487 picoammeter. A 150-W solar simulator with an Air Mass (AM) 1.5 global filter was used as a light source for providing 100 mW/cm^2 onto the hybrid solar cells in standard conditions.

The results show a diode behaviour in the processed solar cells. In Figure 6.8 b) and c) the $J-V$ characteristics and EQE measurements of the hybrid solar cells are depicted. With a FF of around 0.52, a small current under illumination is generated. However the maximum power conversion efficiency of the hybrid solar cell achieved was around $\eta_{photovoltaic} = 0,4\%$ which is far from the reported solar cells based on nanowires [228–230]. Promising results were found in measuring the EQE. Figure 6.8 c) presents the EQE response of two different solar cells processed by spin-coating.

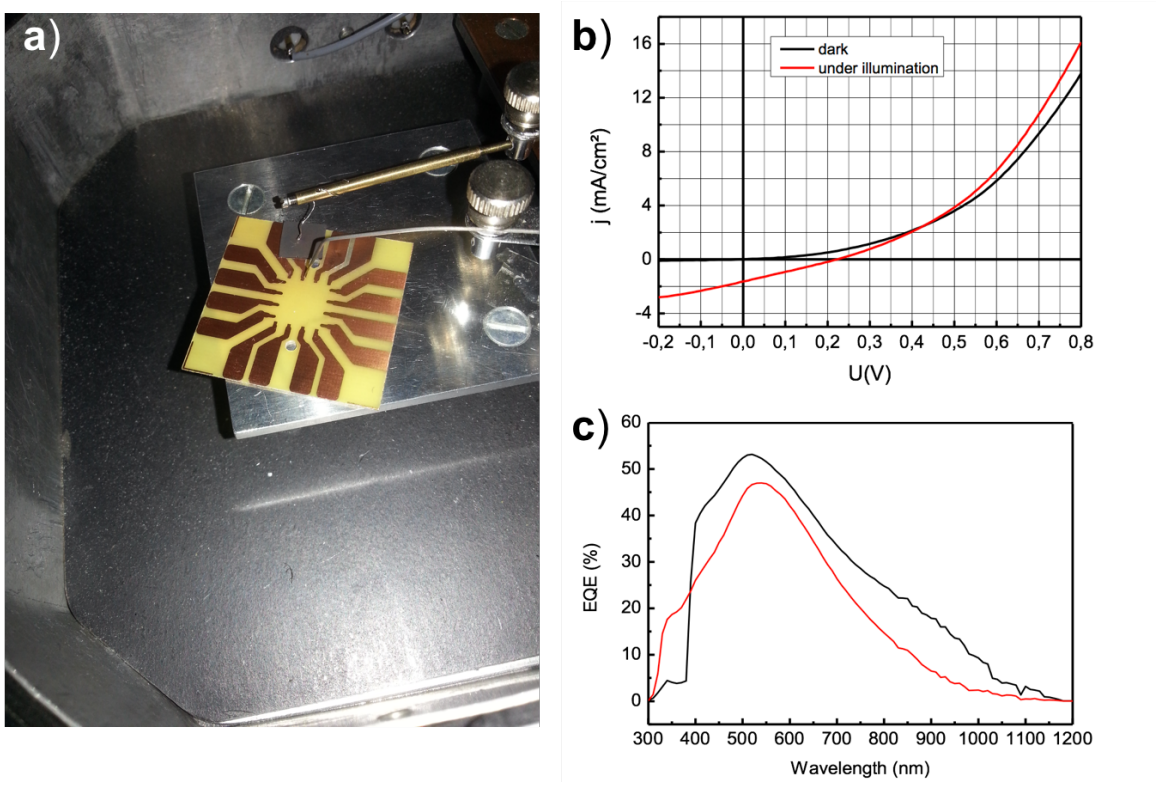

Figure 6.8: a) Setup for measuring $J-V$ characteristics. b) Photovoltaic $J-V$ curves and c) EQE response of the hybrid solar cell based on ZnO nanowire.

It shows a sharp change in the curve at around ~ 380 nm corresponding to the previous measured band gap from the ZnO nanowires (3.28 eV). In this point, the device starts to collect the photons with a quantum efficiency of 35%. Nevertheless, it should be underlined that the maximum absorbance were found in the green zone (≈ 500-550 nm) with a maximum efficiency of 54% which matches with the DLE as a consequence of oxygen vacancies and impurities during growth [224–226] .

One of the problems of the hybrid solar cells is that the PEDOT film only covers the upper part of the nanowires (Figure 6.7). Once the film has been made, the space between the nanowires cannot filled in and the total efficiency is very low. Since the rougher and poorer contacts of the nanowire/polymer confine the recombination of the devices they decrease their efficiency. In a recent work [230], Ruiyuan Liu et.al. reported a processed hybrid silicon nanowire/PEDOT:PSS heterojunction solar cell with high performance by precise control of the nanowire parameters via metal-assisted chemical etching with nanosphere lithography and modification of the wire surface by a solution-based passivation process which lead to better penetration of the polymer

over the nanowires and has therefore better contact between nanowires and polymer. In order to improve the nanowire/PEDOT:PSS contact (with no-Methylation Process and no-nanowire-surface modification) electrochemical polymerization of EDOT over ZnO nanowires based in the technique reported by Mario Culebras et.al is being investigated. [231]. These experiments are in progress. The first results obtained are highly promising.

Poly(3,4-ethylene dioxythiophene) [PEDOT] was synthesized electrochemically over the nanowires by constant density current and different constants potential methods under the following electrolytic condition: Working electrode, Zinc oxide nanowire substrate; counter electrode; platinum plate (2×2 cm^2); reference electrode, Ag/AgCl; electrochemical cell, undivided glass beaker cell; temperature, 25±2 °C; EDOT monomer and electrolytes variable as a function of potential method[§]. In the first method a solution of 0.01 M EDOT and 0.1 M $LiClO_4$ was prepared in acetonitrile at 1,5 mA/cm^2. The results of the electrochemical polymerization by this technique are shown at Figure 6.9 a). Although the nanowires were fully covered by PEDOT, due to the oxidation during the electrochemical process PEDOT becomes opaque (with a strong dark blue color) for the Sun radiation which leads to a non transparent photo-active layer.

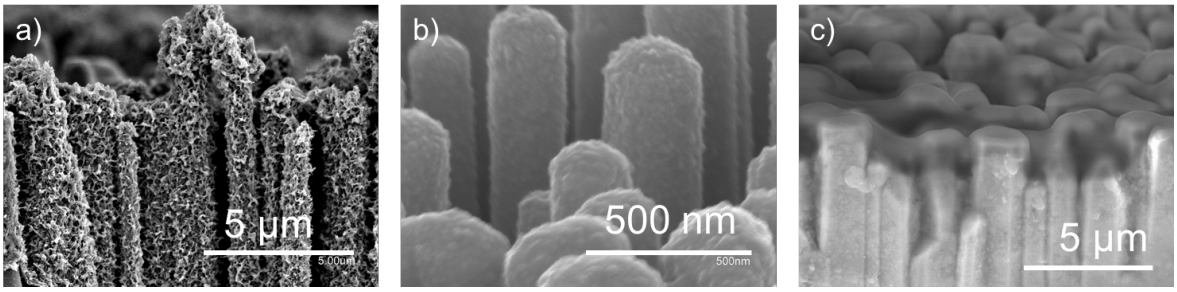

Figure 6.9: a), b) and c) SEM images of ZnO nanowires polymerized with the monomer EDOT at different conditions.

In order to solve these inconvenient, different electrodeposition processes at different conditions have been tasted. The results are shown in Figures 6.8 b) and 6.8 c). Both processes were performed using a 1 M solution of $LiClO_4$ in acetonitrile (100 mL). First case (Figure 6.8 b)) was carried out with the following conditions: EDOT monomer 2 mM, 90 cycles of 50 second at +1,44 V vs Ag/AgCl (reference electrode) and 5 second at 0 V vs Ag/AgCl. Although the film was transparent, only the nanowire surface was

[§]3,4- Ethylenedioxythiophene [EDOT] and Lithium perchlorate (LiClO4) were purchased from Alfa Aesar. Acetonitrile was purchased form VWR chemicals, it was used as a solvent for the electropolymerization.

coated. Another trial using a 5.6 mM solution of EDOT,24 cycles of 45 second at +1,44 V vs Ag/AgCl and 5 second at 0 V vs Ag/AgCl. The result is shown in Figure 6.8 c). A transparent PEDOT film introduced in the space between the nanowires can be observed in the SEM image. However, these conditions are still unreliable since the electrochemical process cause several damage on the sample. A further optimization process is in progress in order to improve the polymerization over nanowires and provide a more efficient ZnO nanowires hybrid solar cells.

CHAPTER 7

SUMMARY AND CONCLUSIONS

This section includes the main results and major accomplishments reached in the PhD thesis entitled "Optical characterization of nanostructures for optoelectronic devices and energy harvesting".

Along this work a wide spectrum of measurements using different techniques for characterizing the unique properties that exhibit the nanostructures have been performed. In particular the nanomaterials have been studied by means of Raman scattering and, in particular, resonant Raman scattering and SERS. The nanostructures characterized (particulary 1-D nanostructures such as nanowires) are materials widely employed for developing thermoelectric, photovoltaic and optoelectronic nano-devices as reported along the dissertation. The following highlights the important aspects and results of this work:

Systematic characterization of nitride nanowires which show Surface modes related to surface-to-volume ratio by Raman and SERS

Structural, electronic and optical properties of GaN and InN nanowires were systematic studied using HRTEM, FESEM, PL, Raman and XPS techniques. These nanowires were grown by the group of Prof. Subhabrata Dhar along the $[10\bar{1}0]$ and $[11\bar{2}0]$ direction, respectively, which is a non-polar direction.

In GaN samples the average wire width is found to decrease from 65 nm to 34 nm when III/V ratio increases. In the PL measured in this work the typical yellow band of GaN is not present, confirming the high quality of the samples. The InN nanowires,

however, were found to be several tens of micrometer long and as small as 20 nm wide. In addition, they were found to be degenerate n-type semiconductor. This was reflected in the observation of the blue shift of the band edge in photo-absorption spectroscopy. Investigation of the surface Fermi level position in these wires using XPS suggests the accumulation of electron on the surface of the nanowires. Furthermore, nitride-materials were characterized by Raman spectroscopy. The special feature of both materials was that they presented SO modes, which couldn't be observed in bulk since they are related to structures with large surface-to-volume ratio. The SO phonons are confined to the near-surface region of the material and their amplitudes decay exponentially with distance from sample surface of the nanostructure. Moreover, as seen in Chapter 3 they are strongly influenced by the diameter, surrounding medium, roughness and the defect density, whereupon can affect to the optical and electrical properties of the materials [98–100].

The fingerprint of the stoichiometric and non-stoichiometric Te-rich Bi_2Te_3 nanowires and films.

The optical properties and the structural and chemical composition of stoichiometric and non-stoichiometric Te-rich Bi_2Te_3 nanowires and films were investigated by HRTEM, EDS and Raman Spectroscopy techniques. Chapter 3 shows that the appearance of extra peaks in the Raman spectrum of Te-rich Bi_2Te_3 is clearly related to the existence of Te clusters, rather than because of IR phonon modes become allowed when translational symmetry is lost (when there are only a few layers of Bi_2Te_3). In addition, this Chapter presents a linear correlation between the Raman intensity and the excess of Te in the Bi_2Te_3 samples which confirms the findings of this study. The results were further discussed with *ab initio* calculations and with other data supplied in the literature.

Appearance of the silent B_{1l} mode in a Raman spectrum under resonant conditions due to isotopic heft presented in ultrathin high quality GaN nanowires and GaN heterostructures.

An extra peak with a small linewidth appeared in the Raman scattering spectra under resonant conditions. This peak was identified as a vibrational silent B_{1l} mode. However, the silent modes cannot appear neither in Raman nor in infra-red spectroscopies. Furthermore, no presence of the B_{1h} mode was found in any spectra. The simulltaneous appearance of the A_1(LO) and B_{1l} in the UV region indicates: a) that the B mode

is related to a resonance effect, i. e. Fröhlich interaction plays a role and b) the mechanism allowing the appearance of the B_{1l} does not allow the observation of the B_{1h}. After performing density functional theory calculations and discarding several options we concluded that the only difference between both modes is the Ga isotopic disorder. While Ga, which contributes to the B_{1l} mode, has mainly two isotopes, ^{69}Ga and ^{71}Ga, N, the main contributor to the high frequency mode, has basically one isotope, ^{14}N, i.e. it is isotopically ordered. The isotopic disorder generates a small dipole moment due to the lack of symmetry on the atomic vibration of this mode and the intensity of Raman peak is enhanced and clearly visible on the spectra because of Fröhlich electron-phonon interaction when the sample is measured by means of RRS.

SERS characterization of In-nanowires and identification of E_1(LO) forbidden mode in backscattering configuration

Multipod Au NPs with single crystalline tips were deposited onto InP and InN nanowires. These nanowires were characterized by Raman Spectroscopy technique before and after deposition of the SERS substrate. A strong enhancement of the Raman signal was found in both materials allowing the identification of the SO modes for InN nanowires and new extra peaks on InP materials.

In the case of InP the Raman spectra enhanced by SERS NPs enabled to distinguish between the polytype structure of InP (wurtzite and zinc-blende structure) through the identification of the E_{2h} (wurtzite) and TO and LO phonon mode (zinc-blende). Furthermore, extra peaks were assigned to $E_1(TO)$ and $E_1(LO)$ modes. These modes are forbidden for the polarization configuration used in the experiments. The case of $E_1(LO)$ is specially remarkable since this mode is not allowed for backscattering or perpendicular configuration. However the specific orientation of the NPs allowed to obtain additional polarized configurations that provided access to these forbidden phonons.

Development of a photovoltaic device based on nanowires

Last Chapter presents the developing of a photovoltaic device based on ZnO nanowires. Firstly, n-type nanowires with high crystalline quality were grown by CVD at the University of Jena. These nanowires were used for processing hybrid solar cells in combination with p-type PEDOT:PSS. The deposition of PEDOT over nanowires was performed by spin-coating. But no commercial performance was achieved. However, the polymerization of p-type PEDOT over intrinsic n-type ZnO nanowires by electrochemical de-

position open new opportunities to exploit surface-to-volume ratio of the upstanding nanowires.

In conclusion, an exhaustive optical characterization in nanostructured materials such as 1-D systems of Bi_2Te_3, InP, GaN and InN has been performed, whose electrical and optical properties are suitable for future design of nanodevices with thermoelectrical, optical and electrical applications. In addition, Raman Spectroscopy and some specific techniques (RRS and SERS) have proved to be powerful tools for studying the properties of the semiconductors nanomaterials. This has enabled to extend their applications for future researches on the characteristics, stoichiometry and qualities of the structures at the nanometer scale. The processing solar cell opens new possibilities in the fabrication of new photovoltaic devices for harvesting energy. Finally, with the work in ultra-thin GaN nanowires, an important step towards the understanding of the Raman scattering interactions in isotopic disorder with wurtzite structure in polar materials has been achieved, which can be extrapolated to a other highly crystalline polar materials with isotopic disorder like ZnO and used on improvement the phenomenological lattice-dynamical models.

APPENDIX A

APPENDIX A

A.1 Localization and measure of individual nanowires

For many experiments performed on single nanowires (Chapter 3 and 5) the nanowires were transferred to a marked substrate via imprint. The nanowire growth substrate is carefully slid in one direction over a pre-patterned Si/SiO_2 substrate in order to achieve a preferential orientation of the transferred nanowires. Pattern was made using Ti/Au (20/200nm) or Al-coating squire marks by optical lithography. SEM, Raman and PL experiments were carried out using these marked substrates. That allows working without charging the nanowires on SEM measurements. Furthermore, the marked substrate has been used to black the background signal of the growth substrate (Sapphire or Silicon) in order to prevent the appearance of the Raman modes that overlaps the weakest signals of phonon modes from the individual nanowire.

An example is shown on Figure A.1. GaN nanowires were growth on a Si (100) substrate (see section 3.2.1). The Raman signal from Si substrate, which may overlaps to the transverse $A_1(TO)$ and $E_1(TO)$ phonon modes, is completely removed from the Raman spectrum. This allows to ensure that the Raman signal is only originated from the individual nanowire. In this case, two additional modes located at 641 and 684 $cm-1$ were attributed to the SO phonon modes [90]. The nanowire can be observed by optical microscope due to the its long shape.

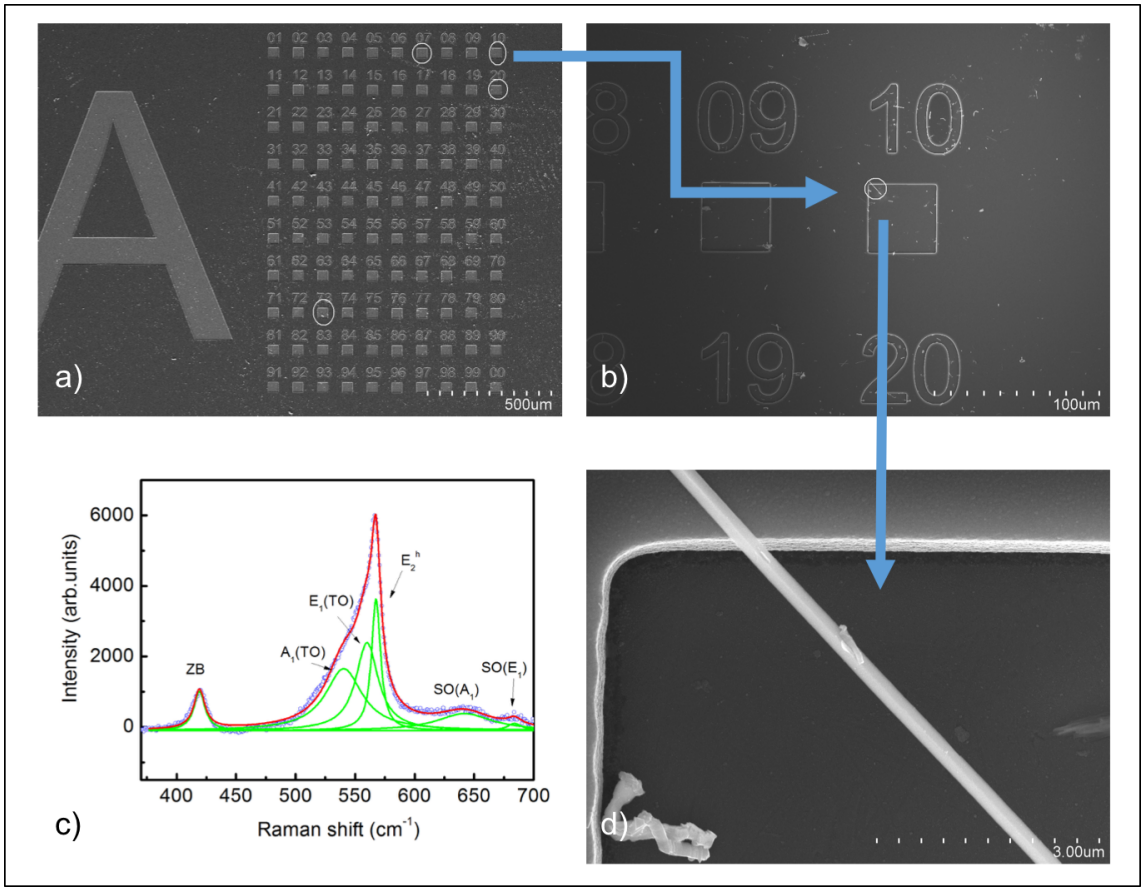

Figure A.1: a) b) and d) Localization of a single GaN nanowires with about 300nm of diameter in a marked substrate by SEM images d) Raman spectroscopy of the individual Nanowire.

A.2 Total energy calculations

Total energy calculations were performed within the framework of the density functional theory and the projector-augmented wave (PAW) [232, 233], method as implemented in the Vienna *ab initio* simulation package (VASP) [234, 235]. The used electronic configurations in the PAW pseudopotentials for each atom are as follows: fifteen valence electrons for Bi ($5d^{1}06s^{2}$ $6p^{3}$) and six electrons for Te ($5s^{2}5p^{4}$). The reciprocal space has been discretized by a Monkhorst-Pack k-point mesh [236] of ($9 \times 9 \times 9$) for the rhombohedral unit cell and the plane wave expansion has been limited by an energy cut-off of 520 eV. These convergence parameters were needed in order to have a resolution on the force smaller than 10-4 eV/ and an energy resolution smaller than 0.1 meV. The exchange and correlation energy was described within the generalized gradient approximation in the Perdew-Burke-Ernzerhof functional [163].

Due to the presence of layers with very weak interaction for this crystal structure, has been considered a non-local correlation functional as proposed by Dion et al [237] to correct the basic exchange correlation functional and that approximately accounts for dispersion interactions. The implementation in VASP has been reported in [238] and in particular the exchange functional version used in this work corresponds to the one reported by Klimes et al [238]. Vibrational properties were computed through the formalism of the density functional perturbation theory with a $3 \times 3 \times 3$ supercell as implemented in VASP and post-processed with the Phonopy code [239].

APPENDIX B

APPENDIX B

B.1 The calculated Phonon dispersion curve and two phonon DOS of GaN

In Figure B.1, the calculated phonon dispersion curve of the wurtzite phase of GaN is shown along several high-symmetry lines in the Brillouin zone together with available experimental data. Is needed to remark that, is also calculated the phonon dispersions and the eigendisplacements with other *ab-initio* codes as the Quantum Espresso package [240] and the Vienna Ab-Initio Simulation Package (VASP) [234, 235, 241, 242]. Was obtained very similar results with the three different codes, with small differences that can be attributed to the pseudopotential choice or the flavor of the approximation to the exchange-correlation energy. For practical purposes, here just report the results obtained with the Abinit package. In the work of Ref. [6] they used a scale factor of 0.97 to have a better fit with the experiment, which is not needed.

In Figure B.2 in Chapter 4 is shown the two phonon DOS calculated using the *anaddb* post-processing code coming with the Abinit package. Since one phonon can emit two phonons in an anharmonic process, the two phonon DOS is related to the phonon population, actually[243]

$$\Gamma(\omega) \propto \rho(\omega)[n(\omega_1) + n(\omega_2) + 1] \tag{B.1}$$

is giving us the contribution of the anharmonicity to the different phonons which appear in a single Raman spectrum. If a phonon is close to a maximum of the 2 phonon

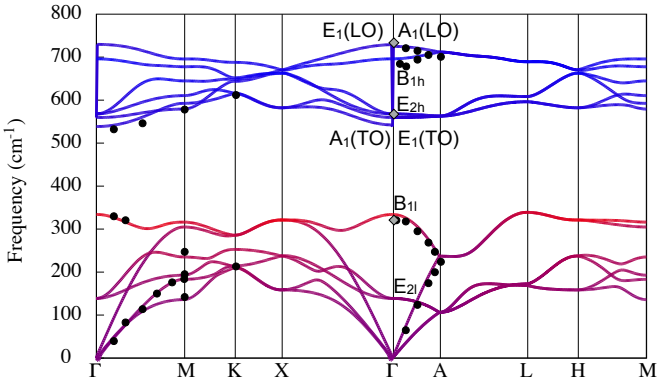

Figure B.1: Phonon dispersion relation of GaN along the most important symmetry directions. Black dots are experimental measurements of X-ray scattering extracted from Ref. [6], while gray diamonds at Γ are Raman experimental measurements of this work. Red and blue bands correspond to displacements dominated by Ga and N atoms, respectively.

DOS, the phonon broadening will be large. If there are no states at the phonon position, the broadening will be the spectral broadening. Of course we have additionally to the anharmonicity the elastic scattering due to isotopes or impurities. All these processes are temperature dependent through the phonon occupation.

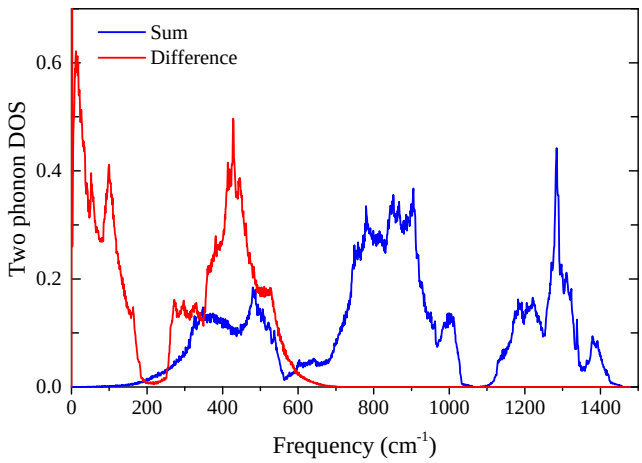

Figure B.2: Two phonon density of states, $\Sigma_{q_1}\Sigma_{q_2}\delta(\omega-\omega(q_1)\pm\omega(q_2))$, of GaN calculated as explained in the Chapter 4. The area of the curve has been normalized to $N(N-1)$, N being the number of phonons.

APPENDIX C

APPENDIX C

C.1 Near-field from an electric dipolar resonance.

The electric field around a resonant nano-structure can be decomposed in a range of electric and magnetic dipoles. However, in the case of plasmonic nano-antennas the magnetic dipolar contribution is just observed in few particular geometries, and hence, it can be neglected in most cases. Based on this, and for the sake of generality, we can consider the excitation of plasmonic modes in a NP as the resulting electrical dipole. A clear relation is found in the case of nano-rod NPs which elongated symmetry since it enables different electric dipolar resonances: one along the longitudinal (low energy mode) and another one along the transversal axe (high energy mode), as illustrated in Figure C.1. As well in the case of spherical NPs cross-polarized electrical dipoles can be distinguished by means of y- and z-polarized light excitation, respectively.

In the case of the nano-stars (NSs) the description would be qualitatively similar with quantitative differences among the different kinds of star-like geometries that can be synthesized. In general, the nano-star size tends to be the more relevant parameter since it clearly determines the energy of the localized surface plasmon resonance (LSPR). It is also well-known that the geometries with narrower peaks would lead to higher field enhancements, as suggested in few theoretical works [244]. More experimental and theoretical details about the influence of the shape, size, tip sharpness and number of peaks on the enhancement can be found in Refs. [182, 245]

By the hybridization of plasmon modes associated with the central body and the

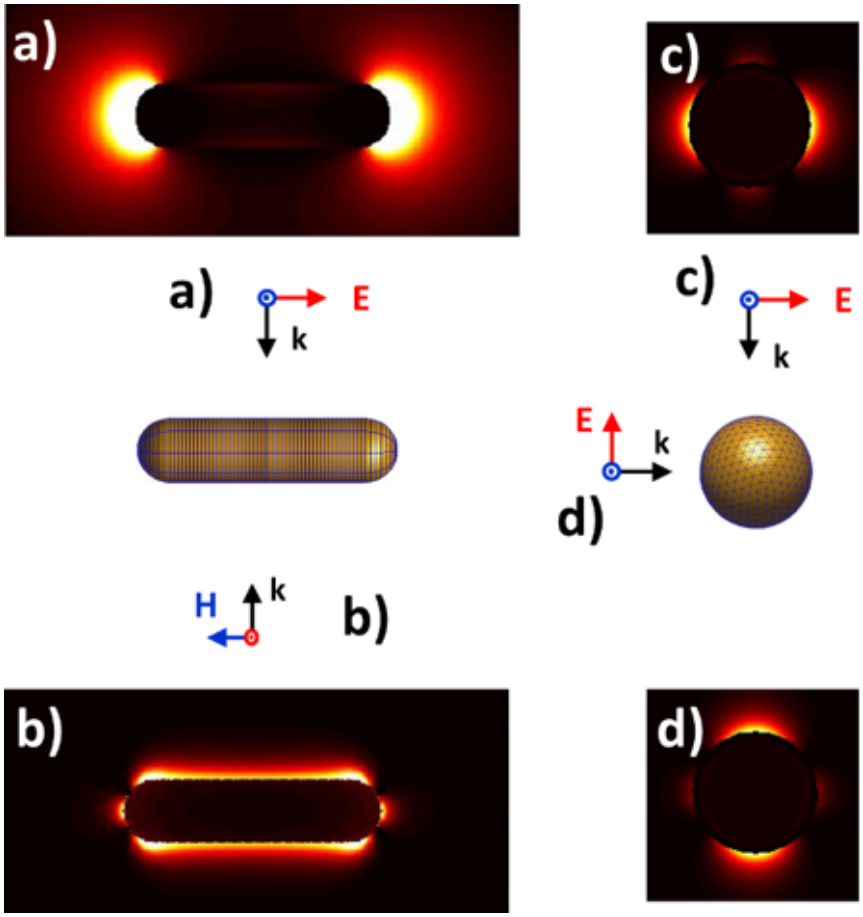

Figure C.1: Longitudinal a) and transversal b) modes in a nanorod. Y- c) and X-polarized d) resonances in a nanosphere.

tips of the NPs they are able to generate an electric field dipole along x, y, or z-direction (is just a question of statistic). It would depend on the number of NPs per unit area to find a properly aligned one. In the case studied in Chapter 5, may be interested on those NSs with a sharp tip pointing to the center of a nanowire, in parallel to the y-axis (based on the description of the axis represented in Figure 5.6). In the far-field the polarization response of light scattered by those particular NSs would not differ from a common y-polarized excitation light source. However, in this work we demonstrated that the high intensity from the samples measured is due to surface enhanced Raman scattering which occurs in the near-field of the NSs.

To discuss about this, in Figure C.2 the field square distribution of a y-polarized electric dipole was plotted. It turns out that the near-field considered clearly breaks with the constraints attributed to far-field sources in terms of polarization. Accordingly,

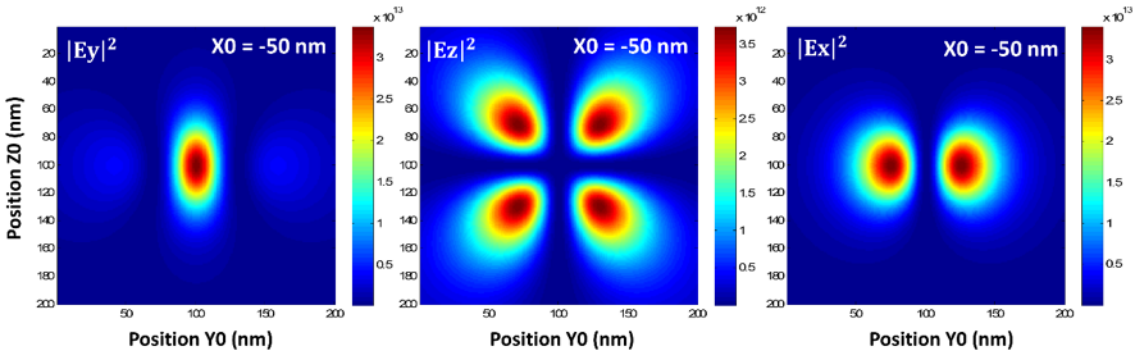

Figure C.2: Electric field square at the origin generated by an electric dipole at 632 nm wavelength located on the plane $X_o = -50nm$

the nominally forbidden phonon modes which are not accessible under our current excitation configuration are enabled through the near-field excitation of electric dipolar modes in different conditions. This is illustrated in Figure C.3 which shows the electric and magnetic field generated by an electric dipole P_y= -$P_o\hat{u}_y$ (= 632nm) when located in different points of the space, i.e. x_o ϵ [-100] 100 nm, y_o ϵ [-100] 100 nm and z_o = -50 nm with important contributions in all the directions of the space. This fits to the scheme of Figure 5.6 from the main text, with the origin (0,0,0) at the nanowire surface (of 300 nm diameter) and because of the different height (consider NSs of about 55 nm diameter) the electric dipoles attributed to the NSs would be laying in the z_o= -50 nm plane. In this situation, we can identify a point of high relevance for our discussion which is labelled as P1. When the electric dipole is located at P1 (y_o = 30 nm and z_o=0) the electric field in the origin is polarized in the x-direction E=-$E_o\hat{u}_x$ with the magnetic field pointing to H=-$H_o\hat{u}_z$. This is equivalent to excite from the far-field with a x-polarized plane wave traveling along the y-direction. This enables the nominally forbidden modes $E_1(TO)$ and $E_1(LO)$ in our current far-field configuration. Notice that we focus in P1 since we thought the it offers a clear picture of the issue since the electric and magnetic are aligned with the reference axes. However, there is a range of locations where an electric dipole would efficiently excite the nanowire in similar conditions. For example, at y_0 = 80 nm and z_0 = 50 nm the electric dipole would also produce a strong x-polarized component as required to excite those phonons.

Finally, in Figure C.4 E_x is plotted for three different x_o planes. The evolution of the E_x with x_o illustrates the patterns in Figure C.3 are expanded or compressed as x_o increases or decreases, and hence, counterparts of P1 can be found at any plane for x_o < 0. Importantly, at the planes closer to the dipole position (low x_o values) the near

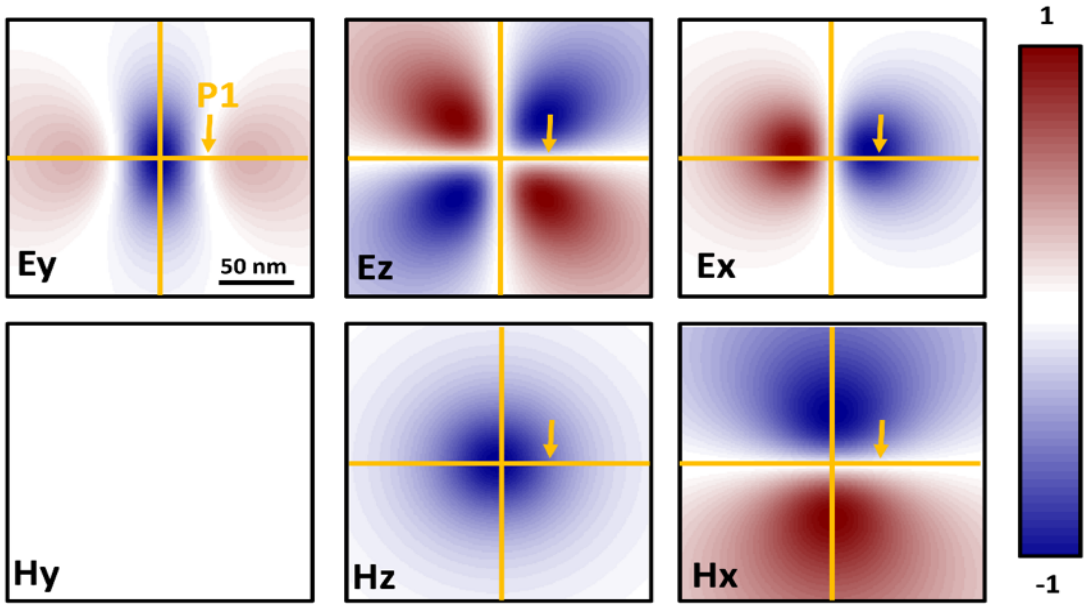

Figure C.3: Electric and magnetic fields at the origin generated by an electric dipole located at 632 nm wavelength located on the plane $x_o = -50nm$, each component is normalilzed to its maximum. At the point P1 $[(y_o = 30nm),(z_o = 0),(x_o = -50nm)]$ the electric field is polarized along the x-direction ($E = E_x\hat{u}_x$) with the magnetic field in parallel to the z-axis ($H = H_z\hat{u}_z$).

field is enhanced into a small volume. Roughly speaking, close to electric dipoles all the excitation configurations are allowed. This means that in SERS measurements where the excitation occurs at the very near-field, e.g. the dipole in touch with the nanowire surface, the vibrational modes are allowed.

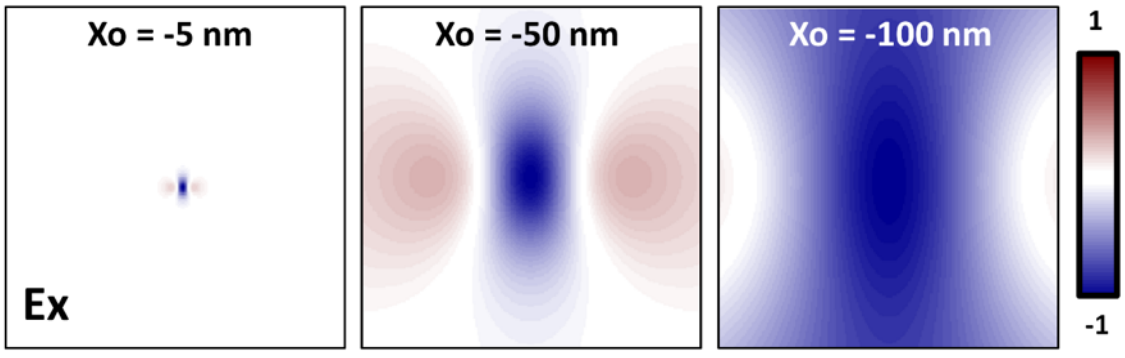

Figure C.4: Electric field at the origin considereing a Y-polarized electric dipole at three different planes: (a) x_o-5nm, (b) x_o-50nm and (c) x_o-100nm

To sum up, not only the modes $E_1(TO)$ and $E_1(LO)$ will be excited by means of y-polarized dipoles but also by means of any dipole with a relevant y-component. Moreover, is has not discussed about the possibilities of Z-polarized dipoles which may also enable additional excitation possibilities. It is also worth to note is has not considered the influence of the nanowire on the electric field distribution around the nano-star. Firstly, should not be expected a huge effect from the due to the dielectric character and size of the nanowire. In general terms, LSPR just redshifts after being attached to a surface with refractive index higher than air. Secondly, an accurate structural characterization of the nanowire and NSs would be required in order to identify particular conditions such as additional polarizability resonances, new modes on the semiconductor, hot spot, etc. This study would be out of the scope of this work and the situations described would not be representative of the measurements presented in the thesis. The last but not the less reason is that the above considerations will make more difficult to point out the phenomenon under discussion: the excitation at near-field of nominally forbidden modes.

Resumen en español

Cuando en 1959 Richard Feynman dio una charla en la reunión anual de la "American Physical Society" sobre la posibilidad de poder manipular moléculas y átomos de manera individual para el diseño de nuevos materiales con extraordinarias propiedades, nadie podía imaginar que esta primera verbalización pública de los principios teóricos de la nanociencia supondría una revolución en los campos de la física, la medicina, la química y la biotecnología en la década de los 90 con el auge de la nanotecnología. Gracias a esta revolución nuestro estilo de vida cambió. Los dispositivos que usamos ahora son más pequeños y potentes. Por ejemplo, los teléfonos y ordenadores de hace unos años han dado paso a terminales más pequeños y livianos con mayores características y funcionalidades. También el medio ambiente y el sector energético se han visto favorecidos en los sistemas de recolección de energía como las células solares y los dispositivos termoeléctricos.

Si esto le sumamos la tradicional industria de semiconductores, que en el siglo XX dio lugar a una de las mayores revoluciones tecnológicas con el descubrimiento del transistor, los LEDs, la fabricación de láseres de estado sólido y la invención de circuitos integrados de silicio, tenemos como resultado una mejora de las características y propiedades de estos dispositivos al poder incorporar mayor tecnología en un espacio mucho más reducido. Desde la fabricación del primer chip semiconductor, sus múltiples propiedades se han ampliado enormemente debido a la reducción de los tamaños estructurales. Entre algunos de los ejemplos claros de las propiedades que exhiben estos materiales cuando se reduce los tamaños en el rango del nanómetro podemos encontrar el desplazamiento al azul en la absorción óptica, efectos ópticos no lineales del material y luminiscencia dependiente del tamaño entre otros. Además propiedades como la fluorescencia, el punto de fusión, la reactividad química, la permeabilidad magnética y la conductividad eléctrica del material se ven afectadas por el tamaño, la forma y la relación de aspecto del nanomaterial (por ejemplo en un nanohilo con una mayor longitud que diámetro) [7–9]. Esto permite el desarrollo de nuevos productos inteligentes con un menor coste de producción como los teléfonos inteligentes, los paneles solares o los ordenadores portátiles que han dado un giro en la vida diaria de la gente.

Uno de los nanomateriales más prometedores y que está atrayendo una atención considerable son los nanohilos semiconductores debido a su potencial como futuros componentes para la próxima generación de dispositivos y sistemas optoelectrónicos de alto rendimiento. Los nanohilos se pueden definir como nanoestructuras con simetría cilíndrica de diámetros pequeños (en el rango de nanoescala) y varias micras de longitud.

Hay varias razones por las que este tipo de nanoestructuras son de gran interés para el desarrollo de diodos emisores de luz, células solares y dispositivos termoeléctricos, pero la más importante reside en su particular simetría y tamaño [10–12]. Especialmente son atrayentes los nanohilos semiconductores del grupo III-V tales como los nanohilos de InN, GaN y AlN (y en general nitruros del grupo III). La alta calidad cristalina alcanzada gracias al desarrollo de las técnicas de crecimiento como la epitaxia de haces moleculares, ha dado lugar a un interés creciente en la investigación de sus propiedades físicas, debido a su potencial uso en aplicaciones de optoelectrónica (LEDs, diodos lásers, transistores...). En concreto, los nanohilos de materiales InN, GaN y AlN revisten especial interés por sus variados gaps, del infrarrojo lejano (0.67 eV para el InN), pasando por el ultavioleta cercano (3.5 eV para el GaN), hasta el ultravioleta lejano (6.2 eV para el AlN), que combinados apropiadamente pueden, por ejemplo, cubrir totalmente el espectro de energía del sol. Asimismo, si el diámetro de la nanohilo es lo suficientemente pequeño como para compararlo con el radio de Bohr del excitón (alrededor de diez nanómetros en GaN, por ejemplo), el movimiento de los electrones entonces estará limitado ya que estos se encuentran confinados lateralmente. Este confinamiento tiene una influencia directa en las propiedades electrónicas y fotónicas y puede, por ejemplo, afectar a los estados electrónicos excitados mediante el desplazamiento hacia el azul de la energía, incrementando con ello el band gap del material [13, 14]. Además el confinamiento cuántico en nanohilos largos puede ser útil para incrementar la mobilidad de huecos que mejora el rendimiento en FETs [15].

Otra peculiar característica de estas nanoestructuras es aquella relacionada con los efectos de superficie. La influencia de una mayor superficie en relación con su volumen permite mejorar el confinamiento de la luz y la fotosensibilidad, lo que hace que los nanohilos sean ideales, como hemos comentado, para una amplia gama de dispositivos optoelectrónicos, como células solares, interruptores ópticos y fotodetectores [16–21].

Por otra parte los defectos presentes en las estructuras en los nanohilos como las impurezas, las dislocaciones y la rugosidad de la superficie tienen un mayor impacto y son más relevantes que sus contrapartes más voluminosos [22]. Eso también puede afectar al desarrollo de dispositivos electrónicos debido a la no-uniformidad en la disipación del calor. Por ejemplo, la conductividad térmica en un nanohilo que se use en la fabricación de un dispositivo electrónico se puede alterar y reducir modificando la rugosidad del material. Esto influye sobre la dispersión fonónica y, aunque su conductividad térmica varíe, esto no implica una pérdida sustancial en las cualidades de transporte eléctrico del material [22–24].

El objetivo de este trabajo será comprender las propiedades de algunos de los nanohilos de los semiconductores más utilizados, como el GaN, el InP y el ZnO, para su aplicación en dispositivos optoelectrónicos, además de proporcionar un estudio óptico completo sobre ellos. Otro objetivo clave que se ha desarrollado en esta tesis está relacionado con el estudio de las características de los nanomateriales con aplicaciones en el campo de la recolección de energía. Materiales tales como el Bi_2Te_3 y el ZnO acaparan una emorme atención en la comunidad científica porque pueden emplearse para realizar este tipo de productos nanotecnológicos. Por ejemplo los nanohilos de Bi_2Te_3 son los materiales nanoestructurados más prometedores para el desarrollo de nanodispositivos

termoeléctricos con alta eficiencia termoeléctrica. Así como los nanohilos de ZnO están siendo investigados para el diseño y fabricación de dospositivos fotovoltaicos. Su estudio y comprensión serán vitales para el desarrollo de este tipo de productos.

La parte más extensa de la tesis está centrada en la investigación de las propiedades de los nanohilos mediante espectroscopía Raman y las distintas variantes de esta técnica como por ejemplo la espectroscopía Raman Resonante (RRS) y la amplificación Raman por plasmones superficiales (SERS). La dispersión Raman consiste en la dispersión inelástica de la luz por fluctuaciones dependientes del tiempo de las propiedades del material (como los modos vibracionales), proporcionando así, información química y estructural de casi cualquier muestra mediante el estudio de la energía y polarizabilidad de la luz dispersada. Esto permite diferenciar estructuras químicas, incluso si están formadas por los mismos átomos con estructuras diferentes. Asimismo, al dar acceso a la dinámica vibracional del material, o dinámica de red, se puede obtener información sobre las estructuras electrónicas, la tensión del cristal, la temperatura del material y las interacciones electrón-fonón y fonón-fonón de un material en una área cuya resolución vendrá dada por el tamaño del spot del haz de luz (suele ser de varias micras usando micro-Raman). Además, la espectroscopia Raman tiene numerosas ventajas sobre otras técnicas de análisis, ya que normalmente no requiere preparación de la muestra (excepto SERS), es una técnica de no-contacto y no daña las muestras.

En el Capítulo 3 se estudiaron nanohilos de GaN crecidos mediante el método vapor-liquid-solid (VLS) a través del proceso de Deposición Química de Vapor o CVD (de sus siglas en inglés Chemical Vapor Deposition) usando ftalocianina de cobalto (Co-Ph) como catalizador del proceso. Se crecieron varias muestras variando el flujo de ammonia y la temperatura de crecimiento. Para la caracterización de las propiedades estructurales y morfológicas de estos nanohilos se realizaron medidas mediante microscopía electrónica de alta resolución (HRTEM) y microscopía electrónica de barrido (SEM). En la Figura C.5 se puede observar las imágenes obtenidas mediante ambas técnicas. Como puede verse en las imágenes SEM, los nanohilos presentan diámetros en torno a unas decenas de nanómetros. Además su tamaño permanece prácticamente inalterado cuando se varía la temperatura de crecimiento (aunque sí que está influenciado por el flujo de ϕ_{NH_3}, incrementando el diámetro cuando este lo hace). Sin embargo, la temperatura de crecimiento sí que influye en la densidad de hilos presentes en las muestras. Estas muestras fueron dispersadas, además, en metanol para facilitar el traspaso de los nanohilos a una cuadrícula-plantilla cubierta de carbono que permitiera la localización de los hilos mediante HRTEM. Como se puedo observar en la imagen C.5 c) los nanohilos fueron crecidos con una alta calidad cristalina con estructura wurtzita en la dirección $[10\bar{1}0]$ (non-polar m-plane).

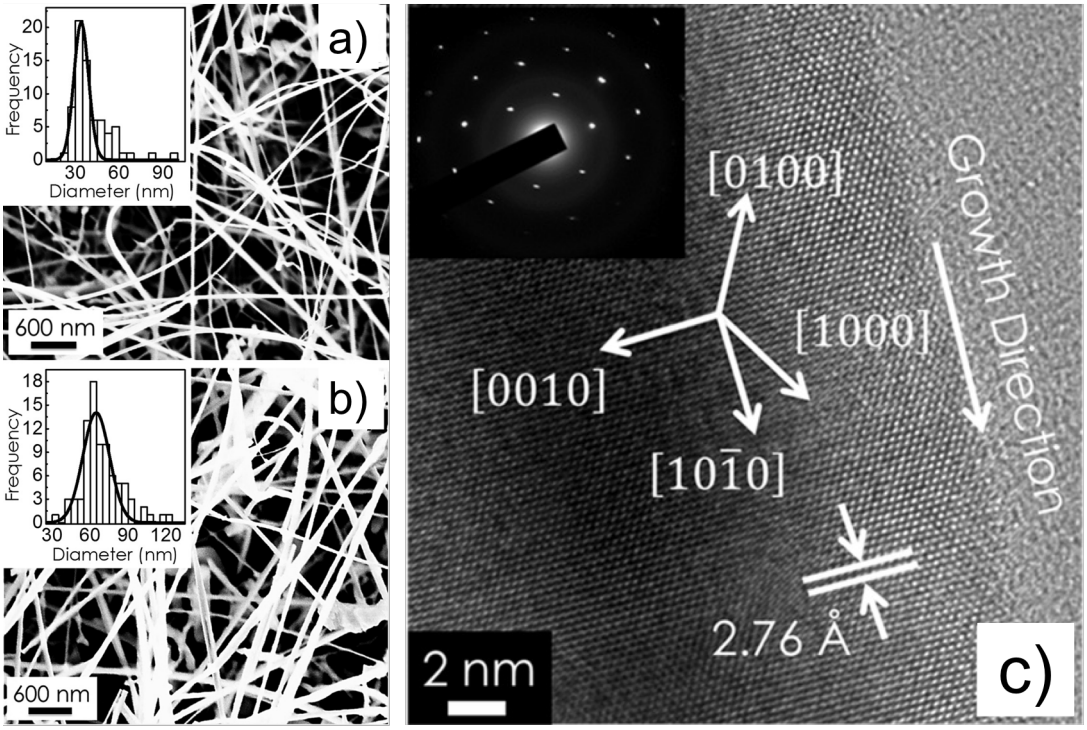

Figure C.5: Imágenes SEM de los nanohilos crecidos a una temperatura de 870 °C con flujos de amoniaco de (a) 10 sccm and (b) 40 sccm. El inset de las imágenes muestra la distribución del diámetro siendo la línea negra el ajuste Gaussiano del histograma b) Imagen de HRTEM donde se representa una porción del nanohilo. El inset de esta imagen muestra el patrón difracción de electrones del área selecta (SAED).

Estas muestras fueron caracterizadas ópticamente mediante fotoluminiscencia (PL) y espectroscopía Raman. Los diversos estudios de PL fueron llevados a cabo variando la temperatura de crecimiento con un flujo constante de ϕ_{NH_3} = 20 sccm (Figura C.6 a) y b)) y manteniendo la temperatura de crecimiento a 870 °C con distintos flujos (Figura C.6 c) y d) variando la temperatura de 10K a 300K. Como puede verse los nanohilos apenas presentan algún pico amplio en la región amarilla relacionado con la sub-banda prohibida correspondiente a los defectos típicos producidos durante el crecimiento en GaN. En todas las temperaturas se encuentra que el espectro de PL está dominada por el pico de emisión característico (ajustado mediante dos Gaussianas centradas en 3.28 eV y 3.40 eV). Sí que puede observarse que la proporción entre los picos de alta y baja energía R_{hl} aumenta conforme aumenta el crecimiento de la temperatura.

Por otra parte el espectro Raman medido en varios nanohilos individuales a temperatura ambiente y en configuración de retrodispersión muestra los picos característicos correspondientes a los fonones de la estructura wurtzita de GaN (ver Figura C.7). Estos picos están localizados en 573, 534 y 562 cm^{-1} y corresponden a los modos Raman vibracionales E_2^h , A_1^{TO} , and E_1^{TO}, respectivamente, de acuerdo con la literatura [90, 92, 93]. Además de estos modos es posible apreciar nuevos picos en el espectro Raman localiza-

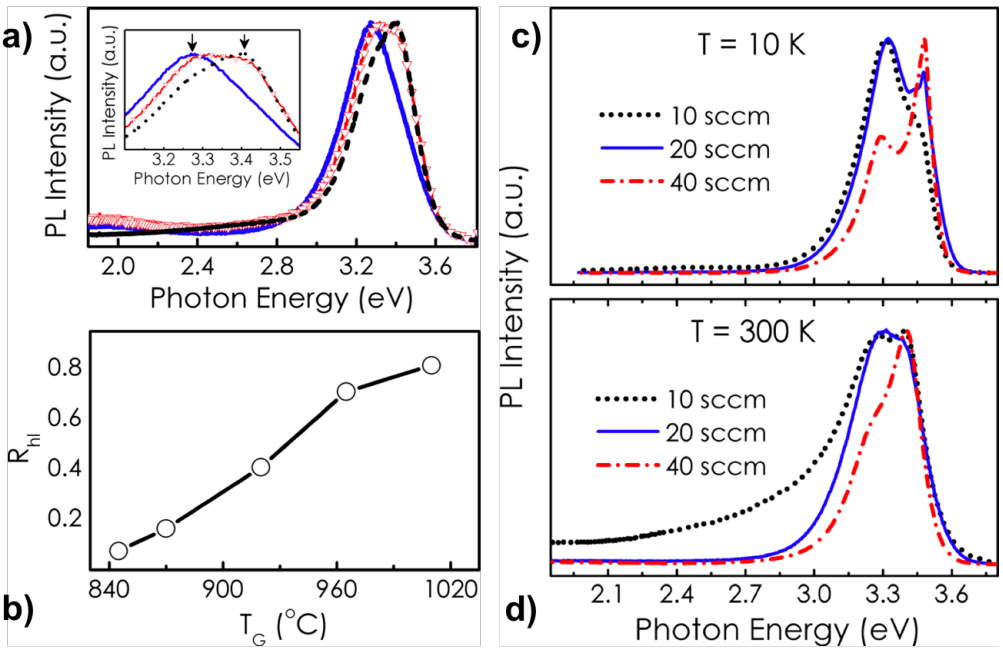

Figure C.6: (a) Espectro de PL normalizado a temperatura ambiente de muestras crecidas a 845 °C (línea sólida azul), 920 °C (triángulos rojos), and 1010 °C (línea intermitente negra) a un flujo constante de ϕ_{NH_3} = 20 sccm. El recuadro muestra la banda de emisión del espectro ampliada (b) Muestra la proporción de las intensidades integradas de los picos de energía alta (banda de emisión del GaN) y baja energía (banda de emisión relacionada a los defectos) como función de la temperatura de crecimiento c) Espectro de PL normalizado tomado a 10 K y d) 300 K para muestras crecidas a una temperatura de 870 °C con diferentes caudales de amoniaco.

dos en 410, 687 and 746 cm^{-1}, los cuales no están permitidos en el grupo espacial C_{6v}^4 ($P6_3mc$) del proceso de dispersión Raman de primer orden de la zona central.

El pico situado en 410 cm^{-1} fue asignado anteriormente por Sahoo [90] al límite de zona de GaN, mientras que el pico en 746 cm^{-1} es descrito en la literatura como un quasi-modo LO cuyo origen está asociado a la interacción de los fononnes pertenecientes a la simetría de grupo de los modos A_1 y E_1 [94–96]. Respecto al pico ancho que aparece centrado en 687 cm^{-1} ha sido asignado a un modo óptico de superficie (SO) [71, 97]. Estos modos superficiales son exclusivos de materiales con mayor relación de superfice que de volumen y están ligados a las oscilaciones de los átomos de la superficie de los materiales semiconductores polares. Por esa razón no pueden ser observados en materiales bulk. Por lo tanto, la superficie del nanohilo representa un nuevo límite mecánico donde los átomos de la superficie están menos unidos y experimentan un campo local diferente al de un material bulk.

Además en este Capítulo se estudiaron también nanohilos estequiométricos y no estequimétricos de Bi_2Te_3 crecidos mediante electrodeposición por Cristina Vicente Manzano y Marisol Martín González. Estos nanohilos fueron caracterizados mediante EDS,

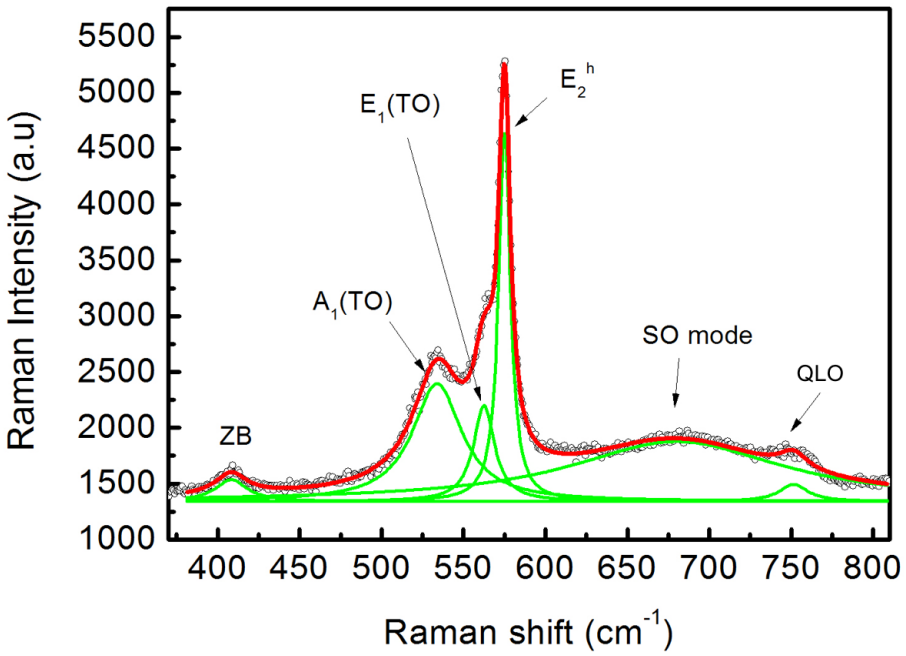

Figure C.7: Espectro Raman de un nanohilo individual de GaN. Los picos están ajustados mediante Lorentzianas para mostrar con la mayor precisión posible su posición en el rango de medida.

TEM y dispersión Raman. La peculiaridad de este trabajo reside en la aparición de nuevos modos ópticos con el exceso de Teluro, los cuales habían sido erróneamente asignados a modos prohibidos infrarrojo cuando existe ruptura de simetría en estructuras nanométricas de Bi_2Te_3. Las muestras no estequiométricas fueron crecidas con exceso de Teluro en diferentes concentraciones. Como puede observarse en la imagen C.8 se realizó mediante EDS un perfil del exceso de Teluro en los diferentes conjuntos de nanohilos de las muestras localizadas por TEM. Estos conjuntos de nanohilos fueron posteriormente caracterizados por espectroscopía Raman (ver Figura C.9). Como se puede apreciar en el espectro Raman correspondiente a las muestras estequiométricas se puede visualizar los modos ópticos A^1_{1g}, E^2_{1g} y A^2_{1g} de Bi_2Te_3 localizados en 57.8, 100.5 y 127.6 cm^{-1}, respectivamente, de acuerdo con la literatura [119, 120, 122], mientras que las no estequiométricas contenían tres modos adicionales localizados en 88, 117 and 137 cm^{-1} correspondientes a los clusters de Teluro.

La señal Raman que aparece en el rango de 116-120 cm^{-1} ha sido atribuida constantemente al modo A_u (IR activo) del Bi_2Te_3 como una seña de identidad de este material cuando hay solamente una pocas capas atómicas de Bi_2Te_3. Sin embargo el Bi_2Te_3 pertenece al espacio $R\bar{3}m$ con simetría romboédrica. Al poseer centro de simetría sus 12 modos ópticos átomos se dividen en modos pares e impares según si presentan un cambio en la polarizabilidad o tienen momento dipolar, respectivamente. Los modos

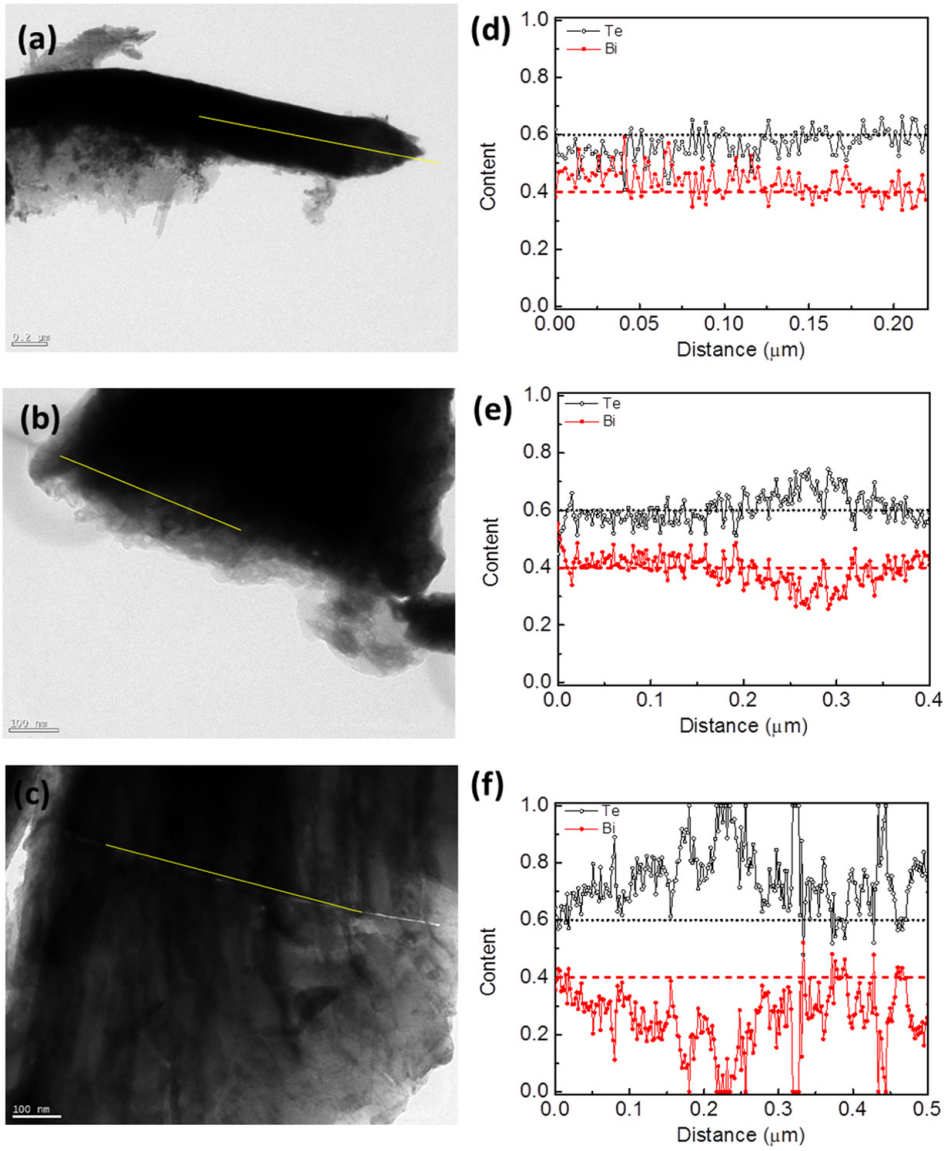

Figure C.8: (a)(c) Imágenes TEM de conjuntos de nanohilos de Bi_2Te_3 encajados en una plantilla de aluminio con (a) contenido de Teluro estequiométrico, (b) 29% de exceso de Teluro, y (c) 36% de exceso de Te. (d)(f) Representa los resultados del perfil del scan EDS correspondientes a las regiones medidas del lado izquierdo. Los datos que muestran un contenido de Teluro de 1 corresponden a clusters de Teluro de tamaño nanométrico.

pares son Raman activos mientras que los impares son IR activos y son excluyentes entre sí, es decir, los Raman activos son IR activos y al revés. Por lo tanto, este modo es prohibido según las reglas de selección. Además la ausencia de este modo en los nanohilos estequiométricos, incluso en aquellos con el diámetro más pequeño, muestra que no están relacionados ni con los efectos de confinamiento, ni tampoco aparecen debido la falta de simetría de inversión, como se indica mayoritariamente en la literatura, sino

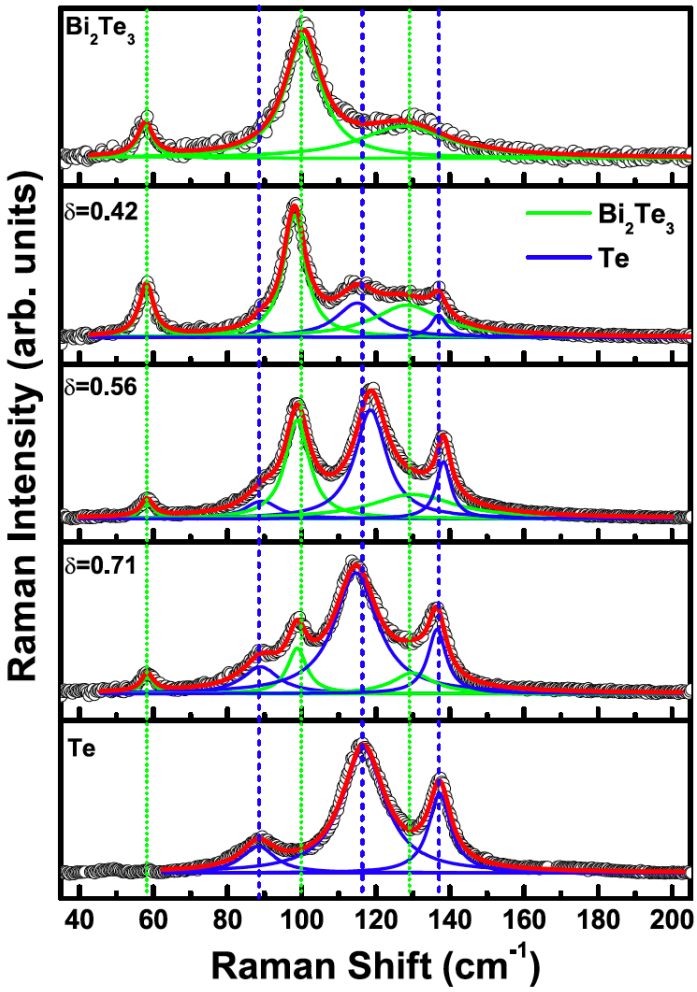

Figure C.9: Espectros Raman de nanohilos de Bi_2Te_3 con diferentes concentraciones de Teluro. Las medidas en nanohilos estequiométricos de Bi_2Te_3 y Teluro puro también fueron incluidas para comparar con las no estequiométricas. El valor de δ corresponde a la cantidad de Te en exceso respecto a la muestra estequiométrica y fue medida por EDS. Las líneas discontinuas verticales y punteadas corresponden a las posiciones de los picos del Te y del Bi_2Te_3, respectivamente.

que su apararición está ligada a la existencia de clusters de Teluro como puede apreciarse en la imagen C.9. Estos resultados fueron corroborados con medidas en películas de Bi_2Te_3 con diferentes estequiometrías.

En el Capítulo 4 fueron caracterizados nanohilos ultrafinos de GaN mediante espectroscopía Raman resonante. En la espectroscopia Raman, los estados electrónicos excitados son estados virtuales mientras que la espectroscopia Raman resonante tiene lugar si la energía de los fotones de excitación (o dispersión) coincide o está muy cerca de una transición electrónica real (transición entre bandas), aumentando, de esta manera la intensidad de la señal Raman. Esta variante de la espectroscopía Raman tiene

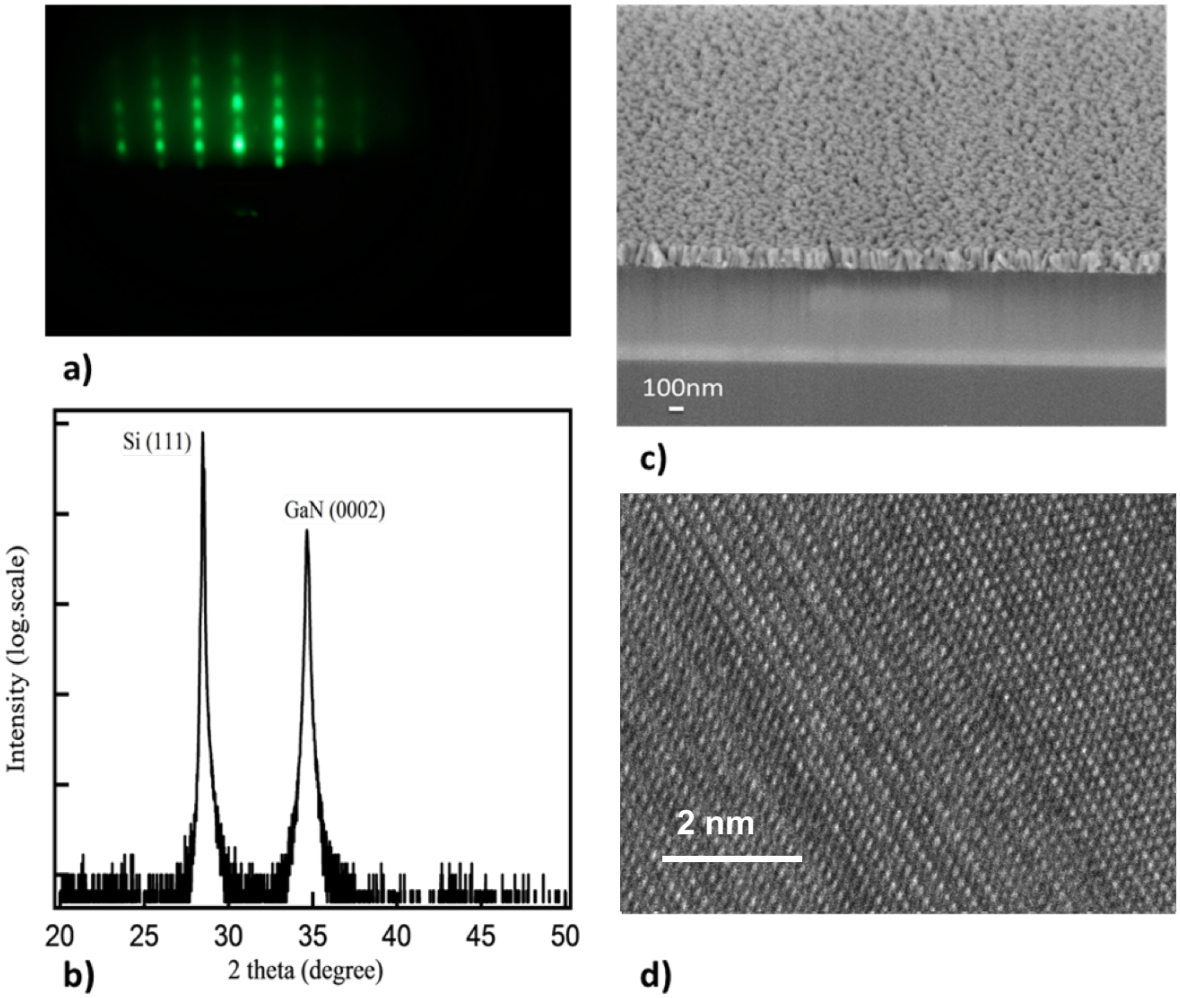

Figure C.10: a) El patrón de las imágenes mediante RHEED muestra que los nanohilos de GaN fueron crecidos a lo largo del eje *c* (0001) perpendiculares a las superficies del sustrato. b) Scan de la muestra mediante XRD. c) Imagen SEM de los nanohilos de GaN crecidos sobre el sustrato de silicio. d) Imagen mediante HRTEM donde se muestra la estructura cristalina de los nanohilos de GaN.

numerosas ventajas respecta al Raman "normal". Por ejemplo, puede proporcionar información sobre superficies de materiales con una sensibilidad de una o unas pocos monocapas, permite estudiar nanoestructuras diluidas y se puede conseguir una mayor selectividad en materiales con múltiples capas de diferentes estructuras. Una ventaja importante de la espectroscopía Raman resonante es que algunas de las propiedades electrónicas de las muestras pueden inferirse por su efecto de resonancia.

Bajo condiciones de resonancia los espectros Raman de los modos ópticos polares como el GaN están dominados por la interacción de Fröhlich entre el electrón y el fonón. La interacción de Fröhlich es inversamente proporcional al vector de onda, el cual es cercano a cero en la dispersión Raman de primer orden y que, en resonancia, se vuelve dominate cuando lo comparamos con la interacción mecánica electron-fonón del potencial de deformación (DP). La DP es una interacción a corta distancia, pero como la interacción de Fröhlich depende del potencial electrostático (con $1/r$), se trata de una interacción de larga distancia y, por lo tanto, es más efectiva cuando se tiene materiales con una alta simetría cristalina.

Los nanohilos ultrafinos de GaN fueron crecidos en un sustrato de silicio mediante PA-MBE (epitaxia de haces moleculares asistido por plasma) y monitorizado in-situ mediante RHEED (difracción de electrones de alta energía con reflexión) como puede verse en la imagen C.10. Además fueron analizados estructuralmente y morfológicamente mediante XRD, SEM y HRTEM.

En la imagen C.10 b) mediante XRD la posición de los picos expresada en valores de θ-2θ. Los nanohilos de GaN no presentaron picos distintos a los picos de difracción de GaN (0002) y Si (111) (ver imagen C.10). En las imágenes SEM se puede apreciar que los nanohilos fueron crecidos perpendicularmente a la superficie del sustrato. Estos nanohilos presentaron un tamaño de alrededor de 120 nm de largo y 12 nm de diámetro. Debido a su reducido tamaño, los defectos se suelen situar en la superficie de los nanohilos y desaparecer durante el crecimiento, un fenómeno conocido como autopurificación (los cristales con menor número de átomos son más estables cuanto mayor sea su pureza y la difusión de la impureza es menor en el material semiconductor). Además, la imagen HRTEM confirma la alta cristalinidad de los nanohilos de GaN.

El espectro Raman resonante mostraba variaciones respecto al espectro Raman normal (ver imagen C.11). Un pico extra de pequeña anchura aparecía en el espectro Raman bajo condiciones de resonancia (con la línea láser de 325nm). Este pico fue identificado como el modo vibracional silencioso B_{1l}. Sin embargo, los modos silenciosos no pueden aparecer mediante espectroscopía Raman ni IR. Además, no se encontró el modo silencioso B_{1h} en ninguno de los espectros. La simultánea aparición de los modos $A_1(LO)$ y B_{1l} en la región UV indica por una parte que el modo silencioso está relacionado con un efecto de resonancia y por lo tanto la interacción de Fröhlich tiene un rol importante en su aparición, y por otra parte, que el mecanismo físico o químico que activa su aparición no permite la observación del B_{1h}. Después de discutir varias opciones que explicaran estos resultados se concluyó que la única diferencia entre ambos modos silenciosos era la composición isotópica. Mientras que en el modo B_{1l} contribuye principalmente el Galio, el cual tiene dos isótopos ^{69}Ga y ^{71}Ga, el Nitrógeno es el principal contribuyente al modo B_{1h}, el cual tiene básicamente un isótopo, ^{14}N, es decir, este

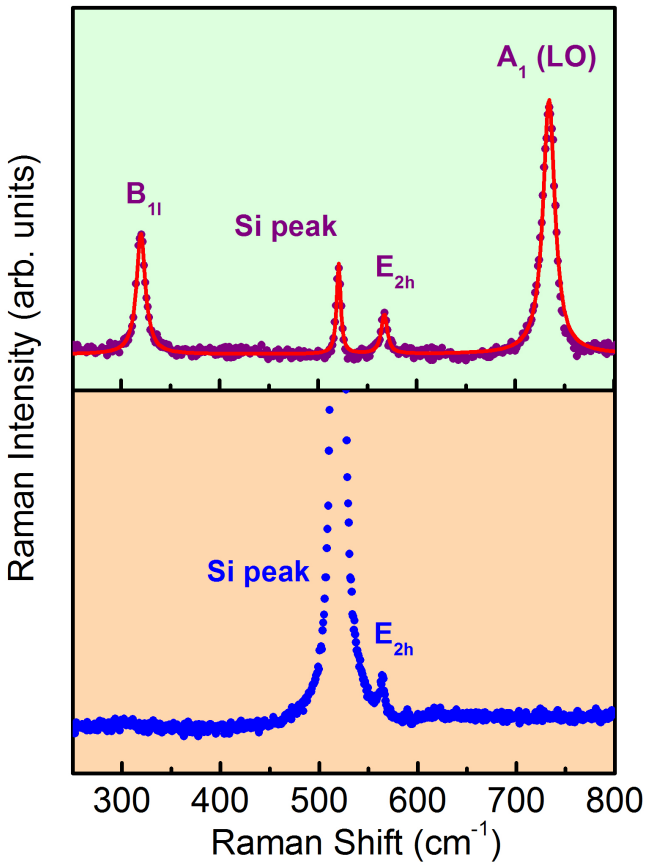

Figure C.11: En el panel superior se muestra el espectro Raman resonante medido con la línea de láser de 325 nm, la cual está en condiciones energéticamente resonante con los nanohilos de GaN. En el panel inferior se muestra el espectro Raman de los nanohilos de GaN con la línea de láser de 488 nm para comparar.

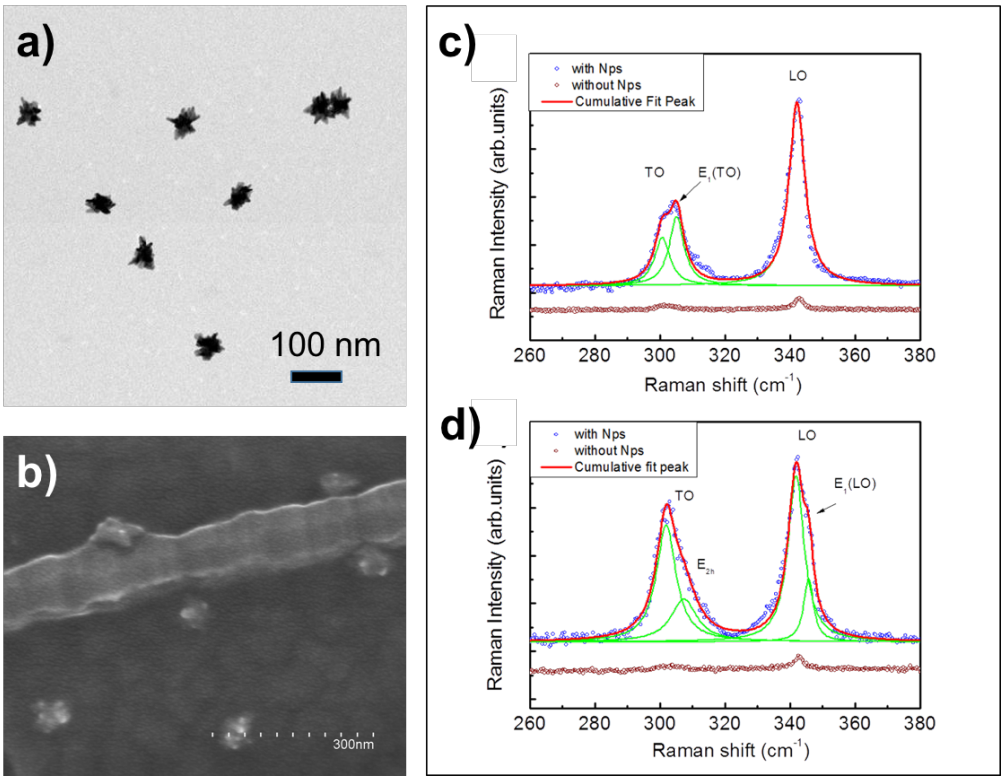

Figure C.12: a) Imágen TEM de las nanoestrellas de oro. b) Imágen SEM de las NPs sobre el nanohilo de InN, c) y d) espectros Raman de nanohilos individuales de InP con y sin NPs de oro.

modo está isotópicamente ordenado. En conclusión la aparación del modo silencioso B_{1l} se debe a que el desorden isotópico genera un pequeño momento dipolar debido a una pérdida de simetría en la vibración atómica de este modo y cuya intensidad es aumentada en el espectro Raman debido a la interacción de Fröhlich de electrón-fonón cuando la muestra es medida bajo condiciones de resonancia (RRS).

En el Capítulo 5 se sintetizaron y depositaron nanopartículas (NPs) de oro con forma de estrellas sobre nanohilos de InP y InN (ver imagen C.12). Estos nanohilos fueron caracterizados mediante espectroscopía Raman antes y después de la deposición de las NPs lo que permitió observar un aumento significativo en la señal de los espectros debido a los plasmones de superficie que están cerca de la resonancia de la energía del láser de excitación. Esta variante de la técnica Raman se conoce como SERS. El fuerte aumento de la señal mediante SERS propició la identificación de los modos ópticos de superficie en los nanohilos de InN y la aparición de nuevos modos ópticos en los nanohilos de InP.

Particularmente, en el caso de los nanohilos de InP, el aumento de la señal permitió distinguir entre las estructuras wurtzita y zinc-blenda del material a través de la identificación de los modos E_{2h} (wurtzita) y los modos fonónicos TO y LO (correspondientes a la estructura zinc-blenda), las cuales se forman durante el crecimiento de la muestra

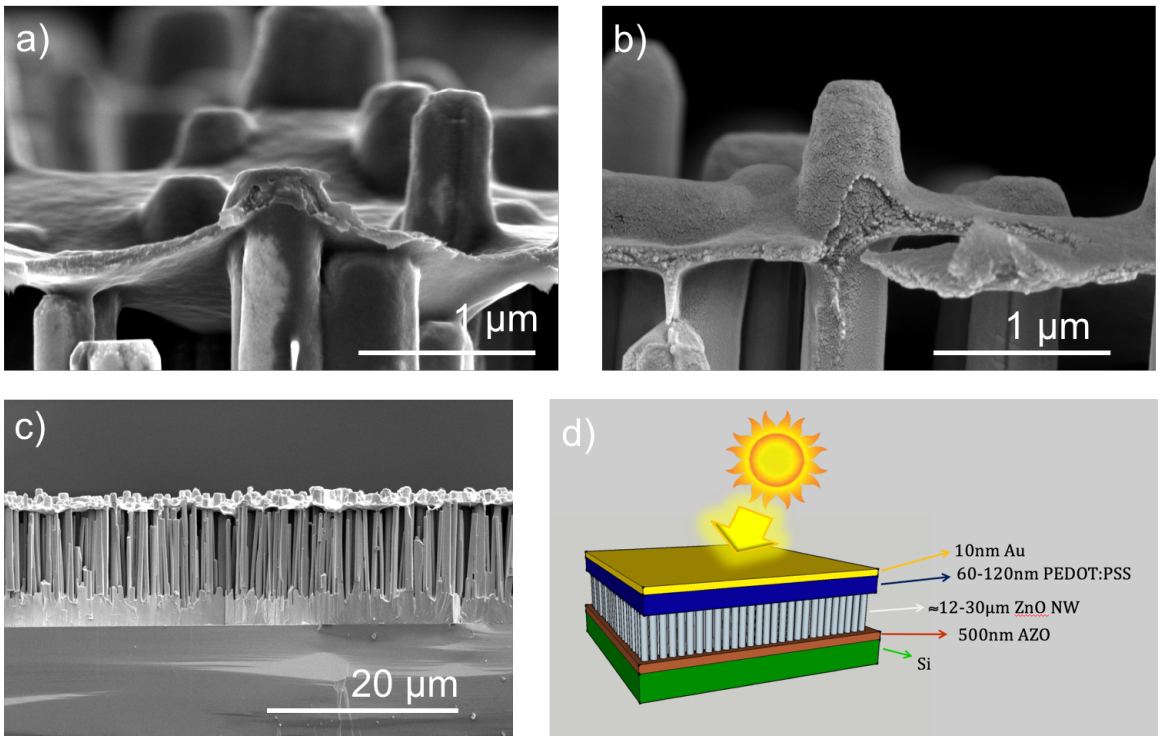

Figure C.13: a) Morfología de los nanohilos después de depositar el polímero PEDOT:PSS b) Recubrimiento de oro sobre la heterounión p-n c) y d) Resultante de la célula solar híbrida usando ZnO con el polímero PEDOT:PSS.

[25, 208].

Además, fue posible acceder a modos prohibidos usando las NPs ramificadas (como por ejemplo el modo $E_1(LO)$ que es prohibido Raman según las reglas de selección para un nanohilo tumbado en configuración de retrodispersión) gracias a la posibilidad de obtener configuraciones de polarización adicionales a las permitidas para un nanohilo individual cuando mides mediante espectroscopía Raman normal.

Por último en el Capítulo 6 se intentó desarrollar un nuevo dispositivo fotovoltaico basado en nanohilos de ZnO de tipo n. Estos nanohilos fueron crecidos en la Universidad de Jena y presentaron estructura hexagonal. Para la fabricación de la célula solar los nanohilos de ZnO fueron crecidos perpendicularmente a la superficie del sustrato. Para que crecieran completamente verticales se depositó una capa de Aluminio dopado con ZnO sobre la oblea de Silicio. Después los nanohilos se sintetizaron mediante deposición del vapor en un horno de tres zonas (3ZJ) usando como material fuente ZnO mezclado con C. Los nanohilos crecidos tenían un diámetro de entre 200 y 400 nm y más de 10 μm de longitud.

Estos nanohilos de tipo n fueron recubiertos mediante spin coating usando el polímero Poly(3,4-ethylenedioxythiophene)-poly(stryrensesulfonate) como capa de tipo p (aceptor), formando así el resultante de una heterounión p-n. Para los contactos frontales se depositó una capa de 10 nm de oro sobre la resultante heterounión. Todo ello se puede vi-

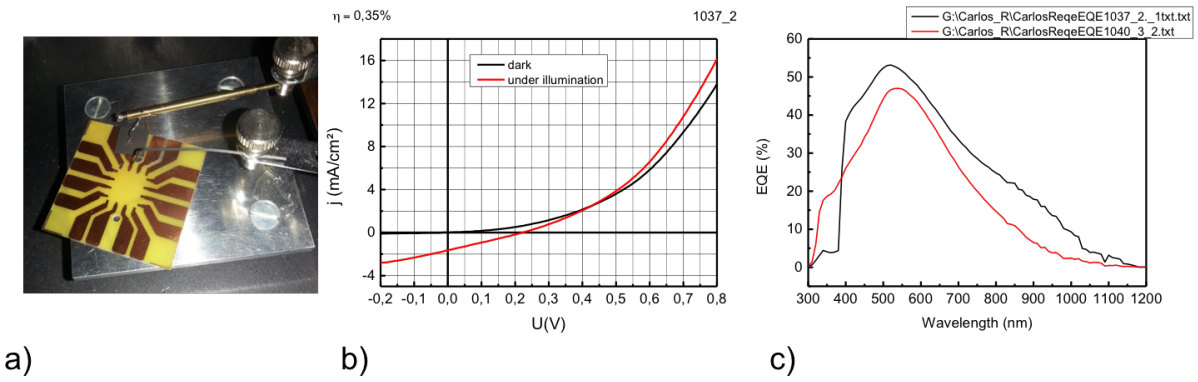

Figure C.14: a) Dispositivo para medir las curvas características J-V. b) Diagrama que representa las curvas carácterísticas de la célula solar fotovoltaica medida c) Medidas de eficiencia quántica externa de la célula solar procesada.

sualizar en la imagen C.13. Sin embargo y a pesar de presentar comportamiento diódico, no mostraron el suficiente rendimiento para su implementación en un futuro desarrollo comercial (ver imagen C.14).

Uno de los inconvenientes de depositar el polímero mediante spin coating es la dificultad de recubrir completamente la superficie de los hilos. Por lo que resulta complicado beneficiarse de las propiedades que estos poseen a escala nanométrica, como por ejemplo la mayor relación de superficie con relación al volumen de estas estructuras y el consiguiente aumento de captación de luz respecto a materiales con mayor volumen. Por ello se siguen investigando nuevas maneras de depositar el polímero sobre los hilos (por ejemplo mediante electrodeposición o polimerización del PEDOT directamente sobre los nanohilos de ZnO) de tal manera que puedan recubrirlos completamente sin opacarlos.

Finalmente, es necesario puntualizar que este trabajo ha permitido entender algunas de las características más importantes de los nanohilos para el desarrollo de sistemas optoelectrónicos y sistemas de recolección de energía (y que se pueden aplicar también en otras nanoestructuras como nanorods, nanotubes, nanoflakes e incluso películas delgadas). Se han caracterizado nanohilos de nitruro que presentaron modos superficiales mediante Raman y SERS. Se estudió la estequiometría de nanohilos de Bi_2Te_3 estequiométricos y no estequiométricos con mayor composición de Teluro (también en películas delgadas) y cuáles son sus características más relevantes a través de la espectroscopía Raman. También se observó por primera vez que el desorden isotópico en materiales con una elevada calidad cristalina influye en las vibraciones atómicas de este, provocando que aparezca un pequeño momento dipolar en un modo silencioso bajo condiciones de resonancia. Y por último se desarrolló un dispositivo fotovoltaico basado en nanohilos de ZnO.

BIBLIOGRAPHY

[1] C. Adenis, V. Langer, and O. Lindqvist, "Reinvestigation of the structure of tellurium," *Acta Crystallographica Section C*, vol. 45, pp. 941–942, 1989.

[2] Y. Feutelais, B. Legendre, N. Rodier, and V. Agafonov, "A study of the phases in the bismuth - tellurium system," *Materials Research Bulletin*, vol. 28, pp. 591–596, 1993.

[3] J. Martín, C. V. Manzano, O. Caballero-Calero, and M. Martín-González, "High-Aspect-Ratio and Highly Ordered 15-nm Porous Alumina Templates," *ACS Applied Materials & Interfaces*, vol. 5, pp. 72–79, 2013.

[4] J. Reguera, J. Langer, D. Jimenez de Aberasturi, and L. M. Liz-Marzan, "Anisotropic metal nanoparticles for surface enhanced raman scattering," *Chem. Soc. Rev.*, vol. 46, pp. 3866–3885, 2017.

[5] S. O. Kasap, "Principles of electronic materials and devices," *Boston McGraw-Hill*, vol. xiii, p. 874, 2006.

[6] T. Ruf, J. Serrano, M. Cardona, P. Pavone, M. Pabst, M. Krisch, M. D'Astuto, T. Suski, I. Grzegory, and M. Leszczynski, "Phonon Dispersion Curves in Wurtzite-Structure GaN Determined by Inelastic X-Ray Scattering," *Phys Rev Lett.*, vol. 86, pp. 906–909, 2001.

[7] C. M. Lieber, "One-dimensional nanostructures: Chemistry, physics & applications," *Solid State Communications*, vol. 107, pp. 607–616, 1998.

[8] A. P. Alivisatos, "Semiconductor Clusters, Nanocrystals, and Quantum Dots," *Science*, vol. 271, pp. 933–937, 1996.

[9] X. Peng, L. Manna, W. Yang, J. Wickham, E. Scher, A. Kadavanich, and A. P. Alivisatos, "Shape control of CdSe nanocrystals," *Nature*, vol. 404, p. 59, 2000.

[10] M. T. Borgström, J. Wallentin, M. Heurlin, S. Fält, P. Wickert, J. Leene, M. H. Magnusson, K. Deppert, and L. Samuelson, "Nanowires with promise for photovoltaics," *IEEE Journal on Selected Topics in Quantum Electronics*, vol. 17, pp. 1050–1061, 2011.

[11] A. I. Boukai, Y. Bunimovich, J. Tahir-Kheli, J. K. Yu, W. A. Goddard, and J. R. Heath, "Silicon nanowires as efficient thermoelectric materials," *Nature*, vol. 451, no. 7175, pp. 168–171, 2008.

[12] F. Qian, S. Gradevcak, Y. Li, C. Y. Wen, and C. M. Lieber, "Core/multishell nanowire heterostructures as multicolor, high-efficiency light-emitting diodes," *Nano Letters*, vol. 5, pp. 2287–2291, 2005.

[13] M. S. Gudiksen, J. Wang, and C. M. Lieber, "Size-dependent photoluminescence from single indium phosphide nanowires," *Journal of Physical Chemistry B*, vol. 106, pp. 4036–4039, 2002.

[14] G. Zhang, K. Tateno, H. Sanada, T. Tawara, H. Gotoh, and H. Nakano, "Synthesis of GaAs nanowires with very small diameters and their optical properties with the radial quantum-confinement effect," *Applied Physics Letters*, vol. 95, no. 12, pp. 1–4, 2009.

[15] Y. Cui, Z. Zhong, D. Wang, W. U. Wang, and C. M. Lieber, "High performance silicon nanowire field effect transistors," *Nano Letters*, vol. 3, no. 2, pp. 149–152, 2003.

[16] X. Dai, S. Zhang, Z. Wang, G. Adamo, H. Liu, Y. Huang, C. Couteau, and C. Soci, "GaAs/AlGaAs nanowire photodetector," *Nano Letters*, vol. 14, pp. 2688–2693, 2014.

[17] X. Yan, B. Li, Y. Wu, X. Zhang, and X. Ren, "A single crystalline InP nanowire photodetector," *Applied Physics Letters*, vol. 109, no. 5, 2016.

[18] M. D. Brubaker, P. T. Blanchard, J. B. Schlager, A. W. Sanders, A. Roshko, S. M. Duff, J. M. Gray, V. M. Bright, N. a. Sanford, and K. A. Bertness, "On-chip optical interconnects made with gallium nitride nanowires.," *Nano letters*, vol. 13, no. 2, pp. 374–381, 2013.

[19] H. Kind, H. Yan, B. Messer, M. Law, and P. Yang, "Nanowire Ultraviolet Photodetectors and Optical Switches," *Adv. Mater.*, vol. 14, no. 2, pp. 158–160, 2002.

[20] P. Krogstrup, H. I. Jørgensen, M. Heiss, O. Demichel, J. V. Holm, M. Aagesen, J. Nygard, and A. Fontcuberta I Morral, "Single-nanowire solar cells beyond the Shockley-Queisser limit," *Nature Photonics*, vol. 7, no. 4, pp. 306–310, 2013.

[21] J. V. Holm, H. I. Jørgensen, P. Krogstrup, J. Nygård, H. Liu, and M. Aagesen, "Surface-passivated GaAsP single-nanowire solar cells exceeding 10% efficiency grown on silicon," *Nature Communications*, vol. 4, pp. 1–5, 2013.

[22] A. I. Hochbaum, R. Chen, R. D. Delgado, W. Liang, E. C. Garnett, M. Najarian, A. Majumdar, and P. Yang, "Enhanced thermoelectric performance of rough silicon nanowires," *Nature*, vol. 451, pp. 163–167, 2008.

[23] L. Shi, D. Yao, G. Zhang, and B. Li, "Large thermoelectric figure of merit in $Si_{1-x}Ge_x$ nanowires," *Applied Physics Letters*, vol. 96, p. 173108, 2010.

[24] N. Mingo, "Thermoelectric figure of merit of II-VI semiconductor nanowires," *Applied Physics Letters*, vol. 85, pp. 5986–5988, 2004.

[25] I. Zardo, S. Conesa-Boj, F. Peiro, J. R. Morante, J. Arbiol, E. Uccelli, G. Abstreiter, and A. Fontcuberta i Morral, "Raman spectroscopy of wurtzite and zinc-blende GaAs nanowires: Polarization dependence, selection rules, and strain effects," *Phys. Rev. B*, vol. 80, p. 245324, 2009.

[26] M. Möller, M. M. De Lima, A. Cantarero, T. Chiaramonte, M. A. Cotta, and F. Iikawa, "Optical emission of InAs nanowires," *Nanotechnology*, vol. 23, no. 37, 2012.

[27] A. Cantarero, *Optical Techniques for Nanostructure Characterization*, pp. 1969–1981.
In: Bhushan B. (eds) Encyclopedia of Nanotechnology. Springer, Dordrecht, 2012.

[28] A. Cantarero, "Review on Raman scattering in semiconductor nanowires: I. theory," *Journal of Nanophotonics*, vol. 7, pp. 7–29, 2013.

[29] M. Cardona and P. Yu, *Fundamentals of Semiconductors*, pp. XXII, 778.
No. 4, Springer Science & Business Media, 2010.

[30] K. A. Dick, "A review of nanowire growth promoted by alloys and non-alloying elements with emphasis on Au-assisted III-V nanowires," *Progress in Crystal Growth and Characterization of Materials*, vol. 54, pp. 138–173, 2008.

[31] J. jing Feng, W. Zhu, and Y. Deng, "An overview of thermoelectric films: Fabrication techniques, classification, and regulation methods," *Chinese Physics B*, vol. 27, p. 047210, 2018.

[32] F. Nasirpouri, *Electrodeposition of Nanostructured Materials*, ch. Template Electrodeposition of Nanowires Arrays, pp. 187–259.
Springer International Publishing, 2017.

[33] H. He and N. J. Tao, *Electrochemical fabrication of metal nanowires*, vol. 10, ch. Encyclopedia of nanoscience and nanotechnology, pp. 1–18.
American Scientific Publishers: New York, 2003.

[34] H. Chaouni, J. Bessiéres, A. Modaressi, and J. Heizmann, "Texture prediction of Bi_2Te_3 electroplated layers using Hartman's theory of crystal growth," *Journal of Applied Electrochemistry*, vol. 30, pp. 419–427, 2000.

[35] P. Magri, C. Boulanger, and J.-M. Lecuire, "Synthesis, properties and performances of electrodeposited bismuth telluride films," *J. Mater. Chem.*, vol. 6, pp. 773–779, 1996.

[36] C. V. Manzano, A. A. Rojas, M. Decepida, B. Abad, Y. Feliz, O. Caballero-Calero, D.-A. Borca-Tasciuc, and M. Martin-Gonzalez, "Thermoelectric properties of Bi_2Te_3 films by constant and pulsed electrodeposition," *Journal of Solid State Electrochemistry*, vol. 17, no. 7, pp. 2071–2078, 2013.

[37] W. Schwarzacher, O. Kasyutich, P. Evans, M. Darbyshire, G. Yi, V. Fedosyuk, F. Rousseaux, E. Cambril, and D. Decanini, "Metal nanostructures prepared by template electrodeposition," *Journal of Magnetism and Magnetic Materials*, vol. 198, pp. 185 – 190, 1999.

[38] A. Huczko, "Template-based synthesis of nanomaterials," *Applied Physics A*, vol. 70, pp. 365–376, 2000.

[39] R. S. Wagner and W. C. Ellis, "Vapor-liquid-solid mechanism of single crystal growth," *Applied Physics Letters*, vol. 4, pp. 89–90, 1964.

[40] M. F. Ashby and D. R. Jones, *Engineering Materials 2 (Fourth Edition), Butterworth-Heinemann*, ch. 4-Phase Diagrams 2, pp. 63–87.
2013.

[41] H. W. Kim, H. G. Na, J. Bae, J. C. Yang, S. S. Kim, H. Cheong, and D. Y. Kim, "Synthesis and Characterization of Orthorhombic Sb_2O_4 Nanowire Prepared by Heating Sb_2S_3 Powder," *Electrochemical and Solid-State Letters*, vol. 15, pp. 49–52, 2012.

[42] N. U. Saidin, K. Ying, Y. Khuan, N.I., Y. Tanaka, and S. Noda, "Electrodeposition: Principles, Applications and Methods," *Nuclear Technical Convention (Malaysia)*, 2011.

[43] R. D. Reeves, L. A. Crosser, G. E. Chester, and J. J. Hill, "Thermoelectric property enhancement via pore confinement in template grown bismuth telluride nanowire arrays," *Nanotechnology*, vol. 28, p. 505401, 2017.

[44] W. T. Tsang, "Chemical beam epitaxy of InP and GaAs," *Applied Physics Letters*, vol. 45, pp. 1234–1236, 1984.

[45] Y.-M. Houng, "Chemical beam epitaxy," *Critical Reviews in Solid State and Materials Sciences*, vol. 17, pp. 277–306, 1992.

[46] C. V. Raman and K. S. Krishnan, "A new type of secondary radiation," *Nature*, vol. 121, pp. 501–502, 1928.

[47] G. Landsberg and L. Mandelstam, "Über die lichtzerstreuung in kristallen," *Zeitschrift für Physik*, vol. 50, no. 11, pp. 769–780, 1928.

[48] A. Smekal, "Zur Quantentheorie der Dispersion," *Naturwissenschaften*, vol. 11, pp. 873–875, 1923.

[49] V. I. Belitsky, A. Cantarero, S. T. Pavlov, M. Gurioli, F. Bogani, A. Vinattieri, and M. Colocci, "Elastic light scattering from semiconductor structures: Localized versus propagating intermediate electronic excitations," *Phys. Rev. B*, vol. 52, pp. 16665–16675, 1995.

[50] M. Gurioli, F. Bogani, A. Vinattieri, M. Colocci, V. Belitsky, A. Cantarero, and S. Pavlov, "Resonant rayleigh scattering in quantum well structures," *Solid State Communications*, vol. 97, pp. 389–394, 1996.

[51] R. Loudon, "The raman effect in crystals," *Advances in Physics*, vol. 13, pp. 423–482, 1964.

[52] W. Richter, *Solid-State Physics*, vol. 78, ch. Resonant Raman scattering in semiconductors, pp. 121–272.
Springer Berlin Heidelberg, 1976.

[53] P. F. Bernath, *Spectra of atoms and molecules*.
Second edition. Oxford ; New York : Oxford University Press, 2005.

[54] M. Möller, M. M. de Lima, A. Cantarero, L. C. O. Dacal, J. R. Madureira, F. Iikawa, T. Chiaramonte, and M. A. Cotta, "Polarized and resonant Raman spectroscopy on single InAs nanowires," *Phys. Rev. B*, vol. 84, pp. 085318–085326, 2011.

[55] R. Tanta, *Raman Spectroscopy of InAs Based Nanowires and Electronic Characterization of Heterostructure InAs/GaInAs Nanowires*.
PhD thesis, 2015.

[56] M. Möller, M. M. de Lima, A. Cantarero, L. C. O. Dacal, J. R. Madureira, F. Iikawa, T. Chiaramonte, and M. A. Cotta, "Polarized and resonant Raman spectroscopy on single InAs nanowires," *Phys. Rev. B*, vol. 84, p. 085318, 2011.

[57] A. Otto, I. Mrozek, H. Grabhorn, and W. Akemann, "Surface-enhanced Raman scattering," *Journal of Physics: Condensed Matter*, vol. 4, p. 1143, 1992.

[58] K. Kneipp, H. Kneipp, I. Itzkan, R. R. Dasari, and M. S. Feld, "Surface-enhanced Raman scattering and biophysics," *J. Phys. Condens. Matter*, vol. 14, pp. 597–624, 2002.

[59] A. Campion and P. Kambhampati, "Surface-enhanced raman scattering," *Chem. Soc. Rev.*, vol. 27, pp. 241–250, 1998.

[60] S. Burany, "Scanning Electron Microscopy and X-Ray Microanalysis. J. Goldstein, D. Newbury, D. Joy, C, Lyman, P. Echlin, E. Lifshin, L. Sawyer, and J. Michael. Kluwer Academic," *Microscopy and Microanalysis*, vol. 9, p. 688, 2003.

[61] L. Reimer, "Scanning electron microscopy," *Springer Berlin*, vol. 45, p. 3, 1998.

[62] S. Yadav, C. Rodríguez-Fernández, M. M. De Lima, A. Cantarero, and S. Dhar, "Structural and luminescence properties of GaN nanowires grown using cobalt phthalocyanine as catalyst," *Journal of Applied Physics*, vol. 118, no. 22, 2015.

[63] C. Rodríguez-Fernández, C. V. , A. H. Romero, J. Martín, M. Martín-González, M. Morais de Lima Jr, and A. Cantarero, "The fingerprint of Te-rich and stoichiometric Bi_2Te_3 nanowires by Raman spectroscopy," *Nanotechnology*, vol. 27, p. 075706, 2016.

[64] H. Matsubara, S. Yoshimoto, H. Saito, Y. Jianglin, Y. Tanaka, and S. Noda, "GaN Photonic-Crystal Surface-Emitting Laser at Blue-Violet Wavelengths," *Science*, vol. 319, pp. 445–447, 2008.

[65] D. A. Steigerwald, J. C. Bhat, D. Collins, R. M. Fletcher, M. O. Holcomb, M. J. Ludowise, P. S. Martin, and S. L. Rudaz, "Illumination with solid state lighting technology," *IEEE Journal of Selected Topics in Quantum Electronics*, vol. 8, pp. 310–320, 2002.

[66] J. C. Johnson, H.-J. Choi, K. P. Knutsen, R. D. Schaller, P. Yang, and R. J. Saykally, "Single gallium nitride nanowire lasers," *Nature Materials*, vol. 1, p. 106, 2002.

[67] L. Rigutti, M. Tchernycheva, A. De Luna Bugallo, G. Jacopin, F. H. Julien, L. F. Zagonel, K. March, O. Stephan, M. Kociak, and R. Songmuang, "Ultraviolet Photodetector Based on GaN/AlN Quantum Disks in a Single Nanowire," *Nano Letters*, vol. 10, pp. 2939–2943, 2010.

[68] M. den Hertog, R. Songmuang, F. Gonzalez-Posada, and E. Monroy, "Single GaN-Based Nanowires for Photodetection and Sensing Applications, journal=Japanese Journal of Applied Physics, volume=52, pages=1101, year=2013,"

[69] R. Koester, D. Sager, W.-A. Quitsch, O. Pfingsten, A. Poloczek, S. Blumenthal, G. Keller, W. Prost, G. Bacher, and F.-J. Tegude, "High-Speed GaN/GaInN Nanowire Array Light-Emitting Diode on Silicon(111)," *Nano Letters*, vol. 15, pp. 2318–2323, 2015.

[70] M. Tchernycheva, P. Lavenus, H. Zhang, A. V. Babichev, G. Jacopin, M. Shahmohammadi, F. H. Julien, R. Ciechonski, G. Vescovi, and O. Kryliouk, "InGaN/GaN Core-Shell Single Nanowire Light Emitting Diodes with Graphene-Based P-Contact," *Nano Letters*, vol. 14, pp. 2456–2465, 2014.

[71] Y. Li, J. Xiang, F. Qian, S. Grade/ak, Y. Wu, H. Yan, D. A. Blom, and C. M. Lieber, "Dopant-Free GaN/AlN/AlGaN Radial Nanowire Heterostructures as High Electron Mobility Transistors," *Nano Letters*, vol. 6, pp. 1468–1473, 2006.

[72] Q. N. Abdullah, F. K. Yam, Z. Hassan, and M. Bououdina, "Hydrogen gas sensing performance of gan nanowires-based sensor at low operating temperature," *Sensors and Actuators, B: Chemical*, vol. 204, pp. 497–506, 2014.

[73] B. Poudel, Q. Hao, Y. Ma, Y. Lan, A. Minnich, B. Yu, X. Yan, D. Wang, A. Muto, D. Vashaee, X. Chen, J. Liu, M. S. Dresselhaus, G. Chen, and Z. Ren, "High-Thermoelectric Performance of Nanostructured Bismuth Antimony Telluride Bulk Alloys," *Science*, vol. 320, pp. 634–638, 2008.

[74] R. Venkatasubramanian, E. Siivola, T. Colpitts, and B. O'Quinn, "Thin-film thermoelectric devices with high room-temperature figures of merit," *Nature*, vol. 413, p. 597, 2001.

[75] S. Bäβler, T. Böhnert, J. Gooth, C. Schumacher, E. Pippel, and K. Nielsch, "Thermoelectric power factor of ternary single-crystalline Sb_2Te_3 - and Bi_2Te_3 - based nanowires," *Nanotechnology*, vol. 24, p. 495402, 2013.

[76] J. Lee, S. Farhangfar, J. Lee, L. Cagnon, R. Scholz, U. Gösele, and K. Nielsch, "Tuning the crystallinity of thermoelectric Bi_2Te_3 nanowire arrays grown by pulsed electrodeposition," *Nanotechnology*, vol. 19, p. 365701, 2008.

[77] R. J. Mehta, C. Karthik, B. Singh, R. Teki, T. Borca-Tasciuc, and G. Ramanath, "Seebeck Tuning in Chalcogenide Nanoplate Assemblies by Nanoscale Heterostructuring," *ACS Nano*, vol. 4, pp. 5055–5060, 2010.

[78] A. Soni, Z. Yanyuan, Y. Ligen, M. K. K. Aik, M. S. Dresselhaus, and Q. Xiong, "Enhanced thermoelectric properties of solut $bi_2te_{3-x}se_x$ nanoplatelet composites," *Nano Lett.*, vol. 12, pp. 1203–1209, 2012.

[79] G. Zhang, H. Fang, H. Yang, L. A. Jauregui, Y. P. Chen, and Y. Wu, "Design Principle of Telluride-Based Nanowire Heterostructures for Potential Thermoelectric Applications," *Nano Lett.*, vol. 12, pp. 3627–3633, 2012.

[80] Y. L. Chen, J. G. Analytis, J.-H. Chu, Z. K. Liu, S.-K. Mo, X. L. Qi, H. J. Zhang, D. H. Lu, X. Dai, Z. Fang, S. C. Zhang, I. R. Fisher, Z. Hussain, and Z.-X. Shen, "Experimental Realization of a Three-Dimensional Topological Insulator, Bi_2Te_3," *Science*, vol. 325, pp. 178–181, 2009.

[81] M. Z. Hasan and C. L. Kane, "Colloquium: Topological insulators," *Rev. Mod. Phys.*, vol. 82, pp. 3045–3067, 2010.

[82] J. Wang, H. Li, C. Chang, K. He, J. S. Lee, H. Lu, Y. Sun, X. Ma, N. Samarth, S. Shen, Q. Xue, M. Xie, and M. H. W. Chan, "Anomalous anisotropic magnetoresistance in topological insulator films," *Nano Research*, vol. 5, pp. 739–746, 2012.

[83] Y. Ando, "Topological insulator materials," *Journal of the Physical Society of Japan*, vol. 82, p. 102001, 2013.

[84] X. Weng, R. A. Burke, and J. M. Redwing, "The nature of catalyst particles and growth mechanisms of GaN nanowires grown by Ni-assisted metal-organic chemical vapor deposition," *Nanotechnology*, vol. 20, p. 085610, 2009.

[85] C. Chèze, L. Geelhaar, O. Brandt, W. M. Weber, H. Riechert, S. Münch, R. Rothemund, S. Reitzenstein, A. Forchel, T. Kehagias, P. Komninou, G. P. Dimitrakopulos, and T. Karakostas, "Direct comparison of catalyst-free and catalyst-induced GaN nanowires," *Nano Research*, vol. 3, pp. 528–536, 2010.

[86] C.-C. Chen and C.-C. Yeh, "Large-Scale Catalytic Synthesis of Crystalline Gallium Nitride Nanowires," *Advanced Materials*, vol. 12, no. 10, pp. 738–741, 2000.

[87] C.-C. Chen, C.-C. Yeh, C.-H. Chen, M.-Y. Yu, H.-L. Liu, J.-J. Wu, K.-H. Chen, L.-C. Chen, J.-Y. Peng, and Y.-F. Chen, "Catalytic growth and characterization of gallium nitride nanowires," *Journal of the American Chemical Society*.

[88] M. A. Reshchikov and H. Morko, "Luminescence properties of defects in GaN," *Journal of Applied Physics*, vol. 97, 2005.

[89] E. Kroumova, M. Aroyo, J. Perez-Mato, A. Kirov, C. Capillas, S. Ivantchev, and H. Wondratschek, "Bilbao Crystallographic Server : Useful Databases and Tools for Phase-Transition Studies," *Phase Transitions*, vol. 76, pp. 155–170, 2003.

[90] P. Sahoo, S. Dhara, S. Dash, A. K. Tyagi, B. Raj, C. R. Das, P. Chandramohan, and M. P. Srinivasan, "Surface optical modes in GaN nanowires," *International Journal of Nanotechnology*, vol. 7, pp. 823–832, 2010.

[91] V. Yu Davydov, Y. Kitaev, I. N. Goncharuk, A. N. Smirnov, J. Graul, O. Semchinova, D. Uffmann, M. Smirnov, A. P. Mirgorodsky, and R. Evarestov, "Phonon Dispersion and Raman Scattering in Hexagonal GaN and AlN," *Physical Review B*, vol. 58, pp. 12899–12907, 1998.

[92] S. Dhara, P. Sahoo, A. Tyagi, and B. Raj, "Surface Optical Mode in Semiconductor Nanowires," *Surface Optical Modes in Semiconductor Nanowires, Nanowires - Implementations and Applications, Dr. Abbass Hashim (Ed.), InTech*, 2011.

[93] I. Gorczyca, N. E. Christensen, E. L. Peltzer y Blancá, and C. O. Rodriguez, "Optical phonon modes in GaN and AlN," *Phys. Rev. B*, vol. 51, pp. 11936–11939, 1995.

[94] C.-L. Hsiao, L.-W. Tu, T.-W. Chi, M. Chen, T.-F. Young, C.-T. Chia, and Y.-M. Chang, "Micro-Raman spectroscopy of a single freestanding GaN nanorod grown by molecular beam epitaxy," *Applied Physics Letters*, vol. 90, pp. 043102–043102, 2007.

[95] L. Bergman, M. Dutta, C. Balkas, R. F. Davis, J. A. Christman, D. Alexson, and R. Nemanich, "Raman analysis of the E1 and A1 quasi-longitudinal optical and quasi-transverse optical modes in wurtzite AIN," *Journal of Applied Physics*, vol. 85, pp. 3535–3539, 1999.

[96] J. Wang, F. Demangeot, R. Péchou, C. Bayon, A. Mlayah, and B. Daudin, "Size and shape effects in the Raman scattering by single GaN nanowires," *Journal of Applied Physics*, vol. 114, p. 223506, 2013.

[97] K. Jeganathan, R. K. Debnath, R. Meijers, T. Stoica, R. Calarco, D. Grützmacher, and H. Lüth, "Raman scattering of phonon-plasmon coupled modes in self-assembled gan nanowires," *Journal of Applied Physics*, vol. 105, pp. 1–6, 2009.

[98] D. Spirkoska, G. Abstreiter, and A. Fontcuberta I Morral, "Size and environment dependence of surface phonon modes of gallium arsenide nanowires as measured by Raman spectroscopy," *Nanotechnology*, vol. 19, no. 43, 2008.

[99] R. Gupta, Q. Xiong, G. D. Mahan, and P. C. Eklund, "Surface Optical Phonons in Gallium Phosphide Nanowires," *Nano Letters*, vol. 3, no. 12, pp. 1745–1750, 2003.

[100] N. Begum, A. S. Bhatti, F. Jabeen, S. Rubini, and F. Martelli, "Lineshape analysis of Raman scattering from LO and so phonons in III-V nanowires," *Journal of Applied Physics*, vol. 106, no. 11, pp. 1–6, 2009.

[101] S. Bhattacharya, A. Datta, S. Dhara, and D. Chakravorty, "Surface optical Raman modes in GaN nanoribbons," *Journal of Raman Spectroscopy*, vol. 42, no. 3, pp. 429–433.

[102] S.-E. Wu, S. Dhara, T.-H. Hsueh, Y.-F. Lai, C.-Y. Wang, and C.-P. Liu, "Surface optical phonon modes in ternary aligned crystalline ingan/gan multi-quantum-well nanopillar arrays," *Journal of Raman Spectroscopy*, vol. 40, pp. 2044 – 2049, 12 2009.

[103] I. Tiginyanu, A. Sarua, G. Irmer, J. Monecke, S. Hubbard, D. Pavlidis, and V. Valiaev, "Fröhlich modes in GaN columnar nanostructures," *Phys. Rev. B*, vol. 64, p. 33317, 11 2001.

[104] M. E. Levinshtein, S. L. Rumyantsev, and M. Shur, "Properties of advanced semiconductor materials : GaN, AlN, InN, BN, SiC, SiGe," *New York : Wiley*, 2001.

[105] C. Manzano, J. Martín, and M. Martín-González, "Ultra-narrow 12nm pore diameter self-ordered anodic alumina templates," *Microporous and Mesoporous Materials*, vol. 184, pp. 177–183, 2014.

[106] M. Eddrief, P. Atkinson, V. Etgens, and B. Jusserand, "Low-temperature Raman fingerprints for few-quintuple layer topological insulator Bi_2Se_3 films epitaxied on GaAs," *Nanotechnology*, vol. 25, p. 245701 (8pp), 2014.

[107] A. Cantarero, J. Martinez-Pastor, A. Segura, and A. Chevy, "Transport properties of bismuth sulfide single crystals," *Phys. Rev. B*, vol. 35, pp. 9586–9590, 1987.

[108] Y. Liang, W. Wang, B. Zeng, G. Zhang, J. Huang, J. Li, T. Li, Y. Song, and X. Zhang, "Raman scattering investigation of Bi_2Te_3 hexagonal nanoplates prepared by a solvothermal process in the absence of NaOH," *Journal of Alloys and Compounds*, vol. 509, pp. 5147–5151, 2011.

[109] H. Xu, Y. Song, Q. Gong, W. Pan, X. Wu, and S. Wang, "Raman spectroscopy of epitaxial topological insulator Bi_2Te_3 thin films on GaN substrates," *Modern Physics Letters B*, vol. 29, p. 1550075, 2015.

[110] R. He, Z. Wang, R. L. J. Qiu, C. Delaney, B. Beck, T. E. Kidd, C. C. Chancey, and X. P. A. Gao, "Observation of infrared-active modes in Raman scattering from topological insulator nanoplates," *Nanotechnology*, vol. 23, p. 455703, 2012.

[111] L. Ren, X. Qi, Y. Liu, G. Hao, Z. Huang, X. Zou, L. Yang, J. Li, and J. Zhong, "Large-scale production of ultrathin topological insulator bismuth telluride nanosheets by a hydrothermal intercalation and exfoliation route," *J. Mater. Chem.*, vol. 22, pp. 4921–4926, 2012.

[112] C.-L. Hsin, M. Wingert, C.-W. Huang, H. Guo, T.-J. Shih, J. Suh, K. Wang, J. Wu, W.-W. Wu, and R. Chen, "Phase transformation and thermoelectric properties of bismuth-telluride nanowires," *Nanoscale*, vol. 5, pp. 4669–4672, 2013.

[113] H. Peng, K. Lai, D. Kong, S. Meister, Y. Chen, X.-L. Qi, S.-C. Zhang, Z.-X. Shen, and Y. Cui, "Aharonov-Bohm interference in topological insulator nanoribbons," *Nature Materials*, vol. 9, pp. 225–229, 2009.

[114] D. Olguín, A. Rubio-Ponce, and A. Cantarero, "Ab initio electronic band structure study of III-VI layered semiconductors," *The European Physical Journal B*.

[115] G. Han, Z.-G. Chen, C. Sun, L. Yang, L. Cheng, Z. Li, W. Lu, Z. M. Gibbs, G. J. Snyder, K. Jack, J. Drennan, and J. Zou, "A new crystal: layer-structured rhombohedral In_3Se_4," *CrystEngComm*, vol. 16, pp. 393–398, 2014.

[116] C. L. Choi, J. Feng, Y. Li, J. Wu, A. Zak, R. Tenne, and H. Dai, "WS_2 nanoflakes from nanotubes for electrocatalysis," *Nano Research*, vol. 6, pp. 921–928, 2013.

[117] Q. Zhang, Z. Zhang, Z. Zhu, U. Schwingenschlögl, and Y. Cui, "Exotic Topological Insulator States and Topological Phase Transitions in Sb_2Se_3 and Bi_2Se_3 Heterostructures," *ACS Nano*, vol. 6, no. 3, pp. 2345–2352, 2012.

[118] E. Anastassakis, A. Cantarero, and M. Cardona, "Piezo-Raman measurements and anharmonic parameters in silicon and diamond," *Phys. Rev. B*, vol. 41, pp. 7529–7535, 1990.

[119] Y. Zhao, R. W. Hughes, Z. Su, W. Zhou, and D. H. Gregory, "One-Step Synthesis of Bismuth Telluride Nanosheets of a Few Quintuple Layers in Thickness," *Angewandte Chemie International Edition*, vol. 50, pp. 10397–10401.

[120] G. Mi, L. Li, Y. Zhang, and G. Zheng, "Sn-doped bismuth telluride nanowires with high conductivity," *Nanoscale*, vol. 4, pp. 6276–6278, 2012.

[121] W. Richter and C. R. Becker, "A Raman and far-infrared investigation of phonons in the rhombohedral V_2VI_3 compounds Bi_2Te_3, Bi_2Se_3, Sb_2Te_3 and

$Bi_2(Te_{1-x}Se_x)_3$ (0 < x < 1), $Bi_{1-y}Sb_{1-y})_2Te_3$ (0 < y < 1)," *physica status solidi (b)*, vol. 84, pp. 619–628, 1977.

[122] C. Wang, X. Zhu, L. Nilsson, J. Wen, G. Wang, X. Shan, Q. Zhang, S. Zhang, J. Jia, and Q. Xue, "In situ Raman spectroscopy of topological insulator Bi_2Te_3 films with varying thickness," *Nano Research*, vol. 6, pp. 688–692, 2013.

[123] K. M. F. Shahil, M. Z. Hossain, D. Teweldebrhan, and A. A. Balandin, "Crystal symmetry breaking in few-quintuple Bi_2Te_3 films: Applications in nanometrology of topological insulators," *Applied Physics Letters*, vol. 96, p. 153103, 2010.

[124] C. Rischau, B. Leridon, B. Fauqué, V. Metayer, and C. van der Beek, "Doping of Bi_2Te_3 using electron irradiation," *Physical Review B*, vol. 88, pp. 1–10, 2013.

[125] C. V. Manzano, B. Abad, M. Muñoz Rojo, Y. R. Koh, S. L. Hodson, A. M. Lopez Martinez, X. Xu, A. Shakouri, T. D. Sands, T. Borca-Tasciuc, and M. Martin-Gonzalez, "Anisotropic Effects on the Thermoelectric Properties of Highly Oriented Electrodeposited Bi2Te3 Films," *Scientific Reports*, vol. 6, p. 19129, 2016.

[126] C. Rodríguez-Fernández, M. Almokhtar, W. Ibarra-Hernández, M. M. de Lima, A. H. Romero, H. Asahi, and A. Cantarero, "Isotopic Heft on the B1l Silent Mode in Ultra-Narrow Gallium Nitride Nanowires," *Nano Letters*, vol. 18, pp. 5091–5097, 2018.

[127] R. Nelson, T. Berlijn, J. Moreno, M. Jarrell, and W. Ku, "What is the Valence of Mn in $Ga_{1-x}Mn_xN$?," *Phys. Rev. Lett.*, vol. 115, p. 197203, 2015.

[128] U. Wahl, L. M. Amorim, V. Augustyns, A. Costa, E. David-Bosne, T. A. L. Lima, G. Lippertz, J. G. Correia, M. R. da Silva, M. J. Kappers, K. Temst, A. Vantomme, and L. M. C. Pereira, "Lattice Location of Mg in GaN: A Fresh Look at Doping Limitations," *Phys. Rev. Lett.*, vol. 118, p. 095501, 2017.

[129] A. Bhattacharya, M. Z. Baten, I. Iorsh, T. Frost, A. Kavokin, and P. Bhattacharya, "Room-Temperature Spin Polariton Diode Laser," *Phys. Rev. Lett.*, vol. 119, p. 067701, 2017.

[130] "Efficiency Drop in Green InGaN/gan light emitting diodes: The role of random alloy fluctuations,"

[131] W. Tian, H. Lu, and L. Li, "Nanoscale ultraviolet photodetectors based on one-dimensional metal oxide nanostructures," *Nano Res.*, vol. 8, pp. 382–405, 2015.

[132] T. T. Tran, H. Yu, J. M. Rondinelli, K. R. Poeppelmeier, and P. S. Halasyamani, "Deep Ultraviolet Nonlinear Optical Materials," *Chem. Mater.*, vol. 28, pp. 5238–5258, 2016.

[133] J. Watson and G. Castro, "A review of high-temperature electronics technology and applications," *J. Mater. Sci. - Mater. Electron.*, vol. 26, pp. 9226–9235, 2015.

[134] F. Tuomisto, V. Prozheeva, I. Makkonen, T. H. Myers, M. Bockowski, and H. Teisseyre, "Amphoteric Be in GaN: Experimental Evidence for Switching between Substitutional and Interstitial Lattice Sites," *Phys. Rev. Lett.*, vol. 119, p. 196404, 2017.

[135] G. M. Dalpian and J. R. Chelikowsky, "Self-Purification in Semiconductor Nanocrystals," *Phys. Rev. Lett.*, vol. 96, p. 226802 (pp4), 2006.

[136] M. Hugues, P. A. Shields, F. Sacconi, M. Mexis, M. A. D. Maur, M. Cooke, M. Dineen, A. Di Carlo, D. W. E. Allsopp, and J. Zúñiga Pérez, "Strain evolution in GaN nanowires: From free-surface objects to coalesced templates," *J. Appl. Phys.*, vol. 114, p. 084307, 2013.

[137] R. Trommer and M. Cardona, "Resonant Raman scattering in GaAs," *Phys. Rev. B*, vol. 17, pp. 1865–1876, 1978.

[138] C. Trallero-Giner, A. Cantarero, and M. Cardona, "One-phonon resonant Raman scattering: Fröhlich exciton-phonon interaction," *Phys. Rev. B*, vol. 40, pp. 4030–4036, 1989.

[139] T. Ruf, R. T. Phillips, A. Cantarero, G. Ambrazevicius, M. Cardona, J. Schmitz, and U. Rössler, "Resonant Raman scattering and piezomodulated reflectivity of InP in high magnetic fields," *Phys. Rev. B*, vol. 39, pp. 13378–13388, 1989.

[140] C. Trallero-Giner, A. Cantarero, M. Cardona, and M. Mora *Phys. Rev. B*, vol. 45, p. 6601, 1992.

[141] I. Tiginyanu, A. Sarua, G. Irmer, J. Monecke, S. Hubbard, D. Pavlidis, and V. Valiaev, "Frohlich modes in GaN columnar nanostructures," *Phys. Rev. B*, vol. 64, pp. 233317–233320, 2001.

[142] S. Prasana, S. Dhara, S. Dash, a. K. Tyagi, and B. Raj, "Surface optical modes in GaN nanowires," *Int. J. Nanotechnology*, vol. 9-12, pp. 823–832, 2010.

[143] F. Demangeot, J. Gleize, J. Frandon, M. A. Renucci, M. Kuball, D. Peyrade, L. Manin-Ferlazzo, Y. Chen, and N. Grandjean, "Raman scattering in GaN pillar arrays," *J. Appl. Phys.*, vol. 91, p. 2866, 2002.

[144] L. Filippidis, H. Siegle, a. Hoffmann, and C. Thomsen, "Hyper-Raman scattering on GaN and CdS," *Phys. Stat. Sol. (b)*, vol. 212, pp. R1–R2, Mar. 1999.

[145] A. Hushur, M. H. Manghnani, and J. Narayan, "Raman studies of GaN/sapphire thin film heterostructures," *J. Appl. Phys.*, vol. 106, p. 054317, 2009.

[146] W. Limmer, W. Ritter, R. Sauer, B. Mensching, C. Liu, and B. Rauschenbach, "Raman scattering in ion-implanted GaN," *Appl. Phys. Lett.*, vol. 72, p. 2589, 1998.

[147] H. Harima, "Properties of GaN and related compounds studied by means of Raman scattering," *J. Phys.: Condens. Matter*, vol. 14, pp. R967–R993, 2002.

[148] V. Y. Davydov, Y. E. Kitaev, I. N. Goncharuk, A. N. Smirnov, J. Graul, O. Semchinova, D. Uffmann, M. B. Smirnov, A. P. Mirgorodsky, and R. A. Evarestov, "Phonon dispersion and Raman scattering in hexagonal GaN and AlN," *Phys. Rev. B*, vol. 58, pp. 12899–12907, 1998.

[149] N. Wieser, O. Ambacher, H. Angerer, R. Dimitrov, M. Stuttzmann, B. Stritzker, and J. K. N. Lindner, "Disorder-Activated Scattering and Two-Mode Behavior in Raman Spectra of Isotopic GaN and AlGaN," *Phys. Stat. Sol. (b)*, vol. 216, pp. 807–811, 1999.

[150] M. Katsikini, K. Papagelis, E. C. Paloura, and S. Ves, "Raman study of Mg, Si, O, and N implanted GaN," *J. Appl. Phys.*, vol. 94, p. 4389, 2003.

[151] L. S. Wang, S. Tripathy, W. H. Sun, and S. J. Hua, "Micro-Raman spectroscopy of Si-, C-, Mg- and Be-implanted GaN layers," *J. Raman Spectrosc.*, vol. 35, p. 73, 2004.

[152] R. Cuscó, L. Artús, D. Pastor, F. B. Naranjo, and E. Calleja, "Local vibrational modes of H complexes in Mg-doped GaN grown by molecular beam epitaxy," *Appl. Phys. Lett.*, vol. 84, no. 6, p. 897, 2004.

[153] M. Almokhtar, S. Emura, A. Koide, T. Fujikawa, and H. Asahi, "Photoluminescence related to Gd3+:N-vacancy complex in GaN:Gd multi-quantum wells," *J. Alloys Compd.*, vol. 628, pp. 401–406, 2015.

[154] M. Almokhtar, S. Emura, Y. K. Zhou, S. Hasegawa, and H. Asahi, "Photoluminescence from exciton-polarons in GaGdN/AlGaN multiquantum wells," *J. Phys.: Condens. Matter*, vol. 23, no. 23, pp. 325802–4, 2011.

[155] M. Almokhtar, S. Emura, Y. K. Zhou, S. Hasegawa, and H. Asahi, "Structural, magnetic and optical studies of ultrathin GaGdN/AlGaN multiquantum well structure," *Phys. Stat. Sol. (c)*, vol. 9, pp. 737–740, 2012.

[156] M. Almokhtar, S. Emura, H. Tambo, S. Hasegawa, and H. Asahi, "Structural and Optical Characterization of GaN/AlGaN Single Quantum Disk Nanorods," *Acta. Phys. Pol. A*, vol. 123, pp. 473–475, 2013.

[157] P. Hohenberg and W. Kohn, "Inhomogeneous electron gas," *Phys. Rev.*, vol. 136, pp. B864–B871, 1964.

[158] W. Kohn and L. J. Sham, "Self-consistent equations including exchange and correlation effects," *Phys. Rev.*, vol. 140, pp. A1133–A1138, 1965.

[159] X. Gonze, "Adiabatic density-functional perturbation theory," *Phys. Rev. A*, vol. 52, pp. 1096–1114, 1995.

[160] X. Gonze, F. Jollet, F. A. Araujo, D. Adams, B. Amadon, T. Applencourt, C. Audouze, J.-M. Beuken, J. Bieder, A. Bokhanchuk, E. Bousquet, F. Bruneval, D. Caliste, M. Cote, F. Dahm, F. D. Pieve, M. Delaveau, M. D. Gennar, B. Dorado, C. Espejo, G. Geneste, L. Genovese, A. Gerossier, M. Giantomassi, Y. Gillet, D. R. Hamann, L. He, G. Jomard, J. L. Janssen, S. L. Roux, A. Levitt, A. Lherbier, F. Liu, I. Lukacevic, A. Martin, C. Martins, M. J. T. Oliveira, S. Ponce, Y. Pouillon, T. Rangel, G.-M. Rignanese, A. H. Romero, B. Rousseau, O. Rubel, A. A. Shukri, M. Stankovski, M. Torrent, M. J. V. Setten, B. V. Troeye, M. J. Verstraete, D. Waroquier, J. Wiktor, B. Xue, A. Zhou, and J. W. Zwanziger, "Recent developments in the ABINIT software package," *Comp. Phys. Commun.*, vol. 205, p. 106, 2016.

[161] X. Gonze, B. Amadon, P.-M. Anglade, J.-M. Beuken, F. Bottin, P. Boulanger, F. Bruneval, D. Caliste, R. Caracas, M. Côté, T. Deutsch, L. Genovese,

P. Ghosez, M. Giantomassi, S. Goedecker, D. R. Hamann, P. Hermet, F. Jollet, G. Jomard, S. Leroux, M. Mancini, S. Mazevet, M. J. T. Oliveira, G. Onida, Y. Pouillon, T. Rangel, G.-M. Rignanese, D. Sangalli, R. Shaltaf, M. Torrent, M. J. Verstraete, G. Zerah, and J. W. Zwanziger, "ABINIT: First-principles approach to material and nanosystem properties," *Comp. Phys. Commun.*, vol. 180, pp. 2582–2615, 2009.

[162] X. Gonze, G. Rignanese, M. Verstraete, J. Betiken, Y. Pouillon, R. Caracas, F. Jollet, M. Torrent, G. Zerah, M. Mikami, P. Ghosez, M. Veithen, J.-Y. Raty, V. Olevano, F. Bruneval, L. Reining, R. Godby, G. Onida, D. Hamann, and D. Allan, "A brief introduction to the ABINIT software package," *Zeitschrift Kristallog.(Special issue on Computational Crystallography)*, vol. 220, pp. 558–562, 2005.

[163] J. P. Perdew, K. Burke, and M. Ernzerhof, "Generalized gradient approximation made simple," *Phys. Rev. Lett.*, vol. 77, pp. 3865–3868, 1996.

[164] J. P. Perdew, K. Burke, and M. Ernzerhof, "Generalized gradient approximation made simple," *Phys. Rev. Lett.*, vol. 78, pp. 1396–1396, 1997.

[165] D. Olguin, A. Cantarero, and M. Cardona, "Electron-phonon effects on the direct band gap in semiconductors: LCAO calculations," *Sol. State Commun.*, vol. 122, pp. 575–589, 2002.

[166] J. M. Zhang, M. Giehler, A. Göbel, T. Ruf, M. Cardona, E. E. Haller, and K. Itoh, "Optical phonons in isotopic Ge studied by Raman scattering," *Phys. Rev. B*, vol. 57, p. 1348, 1998.

[167] H. Yamashita, K. Fukui, S. Misawa, and S. Yoshida, "Optical properties of aln epitaxial thin films in the vacuum ultraviolet region," *Journal of Applied Physics*, vol. 50, pp. 896–898, 1979.

[168] Y. Taniyasu, M. Kasu, and T. Makimoto, "An aluminium nitride light-emitting diode with a wavelength of 210 nanometres," *Nature*, vol. 441, p. 325, 2006.

[169] T. Shiosaki, T. Yamamoto, T. Oda, and A. Kawabata, "Low-temperature growth of piezoelectric AlN film by rf reactive planar magnetron sputtering," *Applied Physics Letters*, vol. 36, pp. 643–645, 1980.

[170] K. M. Lakin, J. K. Liu, and K. L. Wang, "Growth morphology and surface-acoustic-wave measurements of AlN films on sapphire," *Journal of Vacuum Science and Technology*, vol. 13, pp. 37–38, 1976.

[171] P. Kuo, G. Auner, and Z. Wu, "Microstructure and thermal conductivity of epitaxial AlN thin films," *Thin Solid Films*, vol. 253, pp. 223 – 227, 1994.

[172] O. Landré, V. Fellmann, P. Jaffrennou, C. Bougerol, H. Renevier, A. Cros, and B. Daudin, "Molecular beam epitaxy growth and optical properties of AlN nanowires," *Applied Physics Letters*, vol. 96, p. 061912, 2010.

[173] Q. Wang, H. P. T. Nguyen, K. Cui, and Z. Mi, "High efficiency ultraviolet emission from $Al_xGa_{1-x}N$ core-shell nanowire heterostructures grown on Si (111) by molecular beam epitaxy," *Applied Physics Letters*, vol. 101, p. 043115, 2012.

[174] J. M. Hayes, M. Kuball, Y. Shi, and J. H. Edgar, "Temperature Dependence of the Phonons of Bulk AlN," *Japanese Journal of Applied Physics*, vol. 39, p. L710, 2000.

[175] S. Nie and S. R. Emory, "Probing Single Molecules and Single Nanoparticles by Surface-Enhanced Raman Scattering," *Science*, vol. 275, pp. 1102–1106, 1997.

[176] A. Pescaglini, E. Secco, A. Martin, D. Cammi, C. Ronning, A. Cantarero, N. Garro, and D. Lacopino, "Non-resonant Raman spectroscopy of individual ZnO nanowires via Au nanorod surface plasmons," *J. Mater. Chem. C*, vol. 4, pp. 1651–1657, 2016.

[177] C. Y. Liu, M. M. Dvoynenko, M. Y. Lai, T. H. Chan, Y. R. Lee, J.-K. Wang, and Y. L. Wang, "Anomalously enhanced Raman scattering from longitudinal optical phonons on Ag-nanoparticle-covered GaN and ZnO," *Appl. Phys. Lett.*, vol. 96, p. 033109, 2010.

[178] H. Wang and N. Halas, "Mesoscopic Au Meatball Particles," *Adv. Mater.*, vol. 20, pp. 820–825, 2008.

[179] C. E. Talley, J. B. Jackson, C. Oubre, N. K. Grady, C. W. Hollars, S. M. Lane, T. R. Huser, P. Nordlander, and N. J. Halas, "Surface-Enhanced Raman Scattering from Individual Au Nanoparticles and Nanoparticle Dimer Substrates," *Nano Lett.*, vol. 5, pp. 1569–1574, 2005.

[180] J. B. Jackson, S. L. Westcott, L. R. Hirsch, J. L. West, and N. J. Halas, "Controlling the surface enhanced raman effect via the nanoshell geometry," *Appl. Phys. Lett.*, vol. 82, pp. 257–259, 2003.

[181] R. Bardhan, S. Mukherjee, N. A. Mirin, S. D. Levit, P. Nordlander, and N. J. Halas, "Nanosphere-in-a-Nanoshell: A Simple Nanomatryushka," *J. Phys. Chem. C*, vol. 114, pp. 7378–7383, 2010.

[182] F. Hao, C. L. Nehl, J. H. Hafner, and P. Nordlander, "Plasmon Resonances of a Gold Nanostar," *Nano Lett.*, vol. 7, pp. 729–732, 2007.

[183] L. Rodríguez-Lorenzo, R. A. Álvarez-Puebla, I. Pastoriza-Santos, S. Mazzucco, O. Stéphan, M. Kociak, L. M. Liz-Marzán, and F. J. García de Abajo, "Zeptomol Detection Through Controlled Ultrasensitive Surface-Enhanced Raman Scattering," *J. Am. Chem. Soc*, vol. 131, pp. 4616–4618, 2009.

[184] J. Wu, W. Walukiewicz, W. Shan, K. M. Yu, J. W. Ager, E. E. Haller, H. Lu, and W. J. Schaff, "Effects of the narrow band gap on the properties of InN," *Phys. Rev. B*, vol. 66, p. 201403, 2002.

[185] A. G. Bhuiyan, A. Hashimoto, and A. Yamamoto, "Indium nitride (InN): A review on growth, characterization, and properties," *Journal of Applied Physics*, vol. 94, no. 5, pp. 2779–2808, 2003.

[186] P. Rinke, M. Scheffler, A. Qteish, M. Winkelnkemper, D. Bimberg, and J. Neugebauer, "Band gap and band parameters of InN and GaN from quasiparticle energy calculations based on exact-exchange density-functional theory," *Applied Physics Letters*, vol. 89, p. 161919, 2006.

[187] A. Cavalli, J. Wang, I. Esmaeil Zadeh, M. E. Reimer, M. A. Verheijen, M. Soini, S. R. Plissard, V. Zwiller, J. E. M. Haverkort, and E. P. A. M. Bakkers, "High-Yield Growth and Characterization of <100> InP p-n Diode Nanowires," *Nano Lett.*, vol. 16, pp. 3071–3077, 2016.

[188] Z. Wang, B. Tian, M. Pantouvaki, W. Guo, P. Absil, J. Van Campenhout, C. Merckling, and D. Van Thourhout, "Room-temperature InP distributed feedback laser array directly grown on silicon," *Nat. Photonics*, vol. 9, pp. 837–842, 2015.

[189] J. Wallentin, N. Anttu, D. Asoli, M. Huffman, I. Åberg, M. H. Magnusson, G. Siefer, P. Fuss-Kailuweit, F. Dimroth, B. Witzigmann, H. Q. Xu, L. Samuelson, K. Deppert, and M. T. Borgström, "InP Nanowire Array Solar Cells Achieving 13.8% Efficiency by Exceeding the Ray Optics Limit," *Science*, vol. 339, pp. 1057–1060, 2013.

[190] X. Yan, B. Li, Y. Wu, X. Zhang, and X. Ren, "A single crystalline InP nanowire photodetector," *Appl. Phys. Lett.*, vol. 109, p. 053109, 2016.

[191] Y. Ding, J. Motohisa, B. Hua, S. Hara, and T. Fukui, "Observation of Microcavity Modes and Waveguides in InP Nanowires Fabricated by Selective-Area Metalorganic Vapor-Phase Epitaxy," *Nano Lett.*, vol. 7, pp. 3598–3602, 2007.

[192] A. T. Hui, F. Wang, N. Han, S. Yip, F. Xiu, J. J. Hou, Y.-T. Yen, T. Hung, Y.-L. Chueh, and J. C. Ho, "High-performance indium phosphide nanowires synthesized on amorphous substrates: from formation mechanism to optical and electrical transport measurements," *J. Mater. Chem.*, vol. 22, pp. 10704–10708, 2012.

[193] S. De Franceschi, J. A. van Dam, E. P. A. M. Bakkers, L. F. Feiner, L. Gurevich, and L. P. Kouwenhoven, "Single-electron tunneling in InP nanowires," *Appl. Phys. Lett.*, vol. 83, pp. 344–346, 2003.

[194] S. Mukherjee, N. Nateghi, R. M. Jacobberger, E. Bouthillier, M. de la Mata, J. Arbiol, T. Coenen, D. Cardinal, P. Levesque, P. Desjardins, R. Martel, M. S. Arnold, and O. Moutanabbir, "Growth and Luminescence of Polytypic InP on Epitaxial Graphene," *Adv. Funct. Mater.*, vol. 28, p. 1705592, 2018.

[195] N. E. E. and H. W. A. R., "Surface-enhanced Raman scattering spectroscopy via gold nanostars," *Journal of Raman Spectroscopy*, vol. 40, pp. 86–91.

[196] S. Pedireddy, A. Li, M. Bosman, I. Y. Phang, S. Li, and X. Y. Ling, "Synthesis of spiky ag-au octahedral nanoparticles and their tunable optical properties," *The Journal of Physical Chemistry C*, vol. 117, pp. 16640–16649, 2013.

[197] T. K. Sau and C. J. Murphy, "Room Temperature, High-Yield Synthesis of Multiple Shapes of Gold Nanoparticles in Aqueous Solution," *Journal of the American Chemical Society*, vol. 126, pp. 8648–8649, 2004.

[198] S. Tamil Selvan, "Novel nanostructures of gold-polypyrrole composites," *Chem. Commun.*, pp. 351–352, 1998.

[199] X. Xu, J. Jia, X. Yang, and S. Dong, "A Templateless, Surfactantless, Simple Electrochemical Route to a Dendritic Gold Nanostructure and Its Application to Oxygen Reduction," *Langmuir*, vol. 26, pp. 7627–7631, 2010.

[200] X.-L. Tang, P. Jiang, G.-L. Ge, M. Tsuji, S.-S. Xie, and Y.-J. Guo, "Poly(N-vinyl-2-pyrrolidone) (PVP)-Capped Dendritic Gold Nanoparticles by a One-Step Hydrothermal Route and Their High SERS Effect," *Langmuir*, vol. 24, pp. 1763–1768, 2008.

[201] O. M. Bakr, B. H. Wunsch, and F. Stellacci, "High-Yield Synthesis of Multi-Branched Urchin-Like Gold Nanoparticles," *Chemistry of Materials*, vol. 18, pp. 3297–3301, 2006.

[202] H. Yuan, C. Khoury, H. Hwang, and T. Vo-Dinh, "Gold nanostars: surfactant-free synthesis, 3D modelling, and two-photon photoluminescence imaging," *Nanotechnology*, vol. 23, 2012.

[203] M. J. R. Carretero, *Characterization of Magnetic-Plasmonic Compounds by means of Raman Spectroscopy*.
PhD dissertation, University of Valencia, 2017.

[204] A. J. Lohn, T. Onishi, and N. P. Kobayashi, "Optical properties of indium phosphide nanowire ensembles at various temperatures," *Nanotechnology*, vol. 21, p. 355702, 2010.

[205] M. T. Bjork, B. J. Ohlsson, T. Sass, A. I. Persson, C. Thelander, M. H. Magnusson, K. Deppert, L. R. Wallenberg, and L. Samuelson, "One-dimensional steeplechase for electrons realized," *Nano Lett.*, vol. 2, pp. 87–89, 2002.

[206] M. Koguchi, H. Kakibayashi, M. Yazawa, K. Hiruma, and T. Katsuyama, "Crystal Structure Change of GaAs and InAs Whiskers from Zinc-Blende to Wurtzite Type," *Jpn. J. Appl. Phys*, vol. 31, p. 2061, 1992.

[207] K. Pemasiri, M. Montazeri, R. Gass, L. M. Smith, H. E. Jackson, J. Yarrison-Rice, S. Paiman, Q. Gao, H. H. Tan, C. Jagadish, X. Zhang, and J. Zou, "Carrier Dynamics and Quantum Confinement in type II ZB-WZ InP Nanowire Homostructures," *Nano Lett.*, vol. 9, pp. 648–654, 2009.

[208] E. G. Gadret, M. M. De Lima, J. R. Madureira, T. Chiaramonte, M. A. Cotta, F. Iikawa, and A. Cantarero, "Optical phonon modes of wurtzite InP," *Appl. Phys. Lett.*, vol. 102, pp. 1–5, 2013.

[209] I. D. Mayergoyz, *Plasmon Resonances in Nanoparticles*. World Scientific Series in Nanoscience and Nanotechnology, 2013.

[210] S. Vaddiraju, A. Mohite, A. Chin, M. Meyyappan, G. Sumanasekera, B. W. Alphenaar, and M. K. Sunkara, "Mechanisms of 1D Crystal Growth in Reactive Vapor Transport: Indium Nitride Nanowires," *Nano Letters*, vol. 5, pp. 1625–1631, 2005.

[211] K. Andreas, A. Rolf, C. Volker, K. Lutz, B. Martina, L. Crenguta-Columbina, L. Vadim, W. Jan, W. Markus, and W. Joachim, "Transport characteristics of indium nitride (InN) films grown by plasma assisted molecular beam epitaxy (PAMBE)," *physica status solidi c*, vol. 6, pp. 1480–1483, 2009.

[212] K. A. Rickert, A. B. Ellis, F. J. Himpsel, H. Lu, W. Schaff, J. M. Redwing, F. Dwikusuma, and T. F. Kuech, "X-ray photoemission spectroscopic investigation of surface treatments, metal deposition, and electron accumulation on InN," *Applied Physics Letters*, vol. 82, pp. 3254–3256, 2003.

[213] S. Sahoo, M. S. Hu, C. W. Hsu, C. T. Wu, K. H. Chen, L. C. Chen, A. K. Arora, and S. Dhara, "Surface optical Raman modes in InN nanostructures," *Applied Physics Letters*, vol. 93, p. 233116, 2008.

[214] V. Y. Davydov, V. V. Emtsev, I. N. Goncharuk, A. N. Smirnov, V. D. Petrikov, V. V. Mamutin, V. A. Vekshin, S. V. Ivanov, M. B. Smirnov, and T. Inushima, "Experimental and theoretical studies of phonons in hexagonal InN," *Applied Physics Letters*, vol. 75, pp. 3297–3299, 1999.

[215] A. A. K., R. M., R. T. R., and S. V., "Raman spectroscopy of optical phonon confinement in nanostructured materials," *Journal of Raman Spectroscopy*, vol. 38, pp. 604–617, 2007.

[216] R. S. Chen, H. Y. Tsai, C. H. Chan, Y. S. Huang, Y. T. Chen, K. H. Chen, and L. C. Chen, "Comparison of CVD- and MBE-grown GaN Nanowires : Crystallinity , Photoluminescence , and Photoconductivity," vol. 44, pp. 21–24, 2015.

[217] M. Kuball, J. Pomeroy, M. Wintrebert-Fouquet, K. Butcher, H. Lu, and W. Schaff, "A Raman spectroscopy study of InN," *Journal of Crystal Growth*, vol. 269, pp. 59–65, 2004.

[218] B. Tian, X. Zheng, T. J. Kempa, Y. Fang, N. Yu, G. Yu, J. Huang, and C. M. Lieber, "Coaxial silicon nanowires as solar cells and nanoelectronic power sources," *Nature*, vol. 449, p. 885, 2007.

[219] M. Law, L. E. Greene, J. C. Johnson, R. Saykally, and P. Yang, "Nanowire dye-sensitized solar cells," *Nature Materials*, vol. 4, p. 455, 2005.

[220] W. U. Huynh, J. J. Dittmer, and A. P. Alivisatos, "Hybrid Nanorod-Polymer Solar Cells," *Science*, vol. 295, pp. 2425–2427, 2002.

[221] T. Martensson, C. P. T. Svensson, B. A. Wacaser, M. W. Larsson, W. Seifert, K. Deppert, A. Gustafsson, L. R. Wallenberg, and L. Samuelson, "Epitaxial III-V Nanowires on Silicon," *Nano Letters*, vol. 4, pp. 1987–1990, 2004.

[222] D. C. Look, J. W. Hemsky, and J. R. Sizelove, "Residual native shallow donor in zno," *Phys. Rev. Lett.*, vol. 82, pp. 2552–2555, 1999.

[223] S. M. Sze, *Semiconductor devices, physics and technology*. Hoboken, N.J. : John Wiley, 2nd ed ed., 2002.

[224] U. Özgür, Y. I. Alivov, C. Liu, A. Teke, M. A. Reshchikov, S. Doğan, V. Avrutin, S.-J. Cho, and H. Morkoç, "A comprehensive review of ZnO materials and devices," *Journal of Applied Physics*, vol. 98, p. 041301, 2005.

[225] R. Dingle, "Luminescent Transitions Associated With Divalent Copper Impurities and the Green Emission from Semiconducting Zinc Oxide," *Phys. Rev. Lett.*, vol. 23, pp. 579–581, 1969.

[226] X. L. Wu, G. G. Siu, C. L. Fu, and H. C. Ong, "Photoluminescence and cathodoluminescence studies of stoichiometric and oxygen-deficient ZnO films," *Applied Physics Letters*, vol. 78, pp. 2285–2287, 2001.

[227] D. Hou, T. Voss, C. Ronning, A. Menzel, and M. Zacharias, "Deep-level emission in ZnO nanowires and bulk crystals: Excitation-intensity dependence versus crystalline quality," *Journal of Applied Physics*, vol. 115, p. 233516, 2014.

[228] X. Yu, X. Shen, X. Mu, J. Zhang, B. Sun, L. Zeng, L. Yang, Y. Wu, H. He, and D. Yang, "High Efficiency Organic/Silicon-Nanowire Hybrid Solar Cells: Significance of Strong Inversion Layer," *Scientific Reports*, vol. 5, p. 17371, 2015.

[229] H.-J. Syu, S.-C. Shiu, and C.-F. Lin, "Silicon nanowire/organic hybrid solar cell with efficiency of 8.40%," *Solar Energy Materials and Solar Cells*, vol. 98, pp. 267–272, 2012.

[230] R. Liu, J. Wang, T. Sun, M. Wang, C. Wu, H. Zou, T. Song, X. Zhang, S.-T. Lee, Z. L. Wang, and B. Sun, "Silicon Nanowire/Polymer Hybrid Solar Cell-Supercapacitor: A Self-Charging Power Unit with a Total Efficiency of 10.5%," *Nano Letters*, vol. 17, pp. 4240–4247, 2017.

[231] M. Culebras, C. M. Gómez, and A. Cantarero, "Enhanced thermoelectric performance of PEDOT with different counter-ions optimized by chemical reduction," *J. Mater. Chem. A*, vol. 2, pp. 10109–10115, 2014.

[232] P. E. Blöchl, "Projector augmented-wave method," *Phys. Rev. B*, vol. 50, pp. 17953–17979, 1994.

[233] G. Kresse and D. Joubert, "From ultrasoft pseudopotentials to the projector augmented-wave method," *Phys. Rev. B*, vol. 59, pp. 1758–1775, 1999.

[234] G. Kresse and J. Hafner, "Ab initio molecular-dynamics simulation of the liquid-metalamorphous-semiconductor transition in germanium," *Phys. Rev. B*, vol. 49, pp. 14251–14269, 1994.

[235] G. Kresse and J. Furthmueller, "Efficiency of ab-initio total energy calculations for metals and semiconductors using a plane-wave basis set," *Computational Materials Science*, vol. 6, pp. 15 – 50, 1996.

[236] H. J. Monkhorst and J. D. Pack, "Special points for Brillouin-zone integrations," *Phys. Rev. B*, vol. 13, pp. 5188–5192, 1976.

[237] M. Dion, H. Rydberg, E. Schröder, D. C. Langreth, and B. I. Lundqvist, "Van der Waals Density Functional for General Geometries," *Phys. Rev. Lett.*, vol. 92, p. 246401, 2004.

[238] J. Klimeš, D. R. Bowler, and A. Michaelides, "Chemical accuracy for the van der Waals density functional," *Journal of Physics: Condensed Matter*, vol. 22, p. 022201, 2009.

[239] A. Togo, F. Oba, and I. Tanaka, "First-principles calculations of the ferroelastic transition between rutile-type and $CaCl_2$-type SiO_2 at high pressures," *Phys. Rev. B*, vol. 78, p. 134106, 2008.

[240] P. Giannozzi, S. Baroni, N. Bonini, M. Calandra, R. Car, C. Cavazzoni, D. Ceresoli, G. L. Chiarotti, M. Cococcioni, I. Dabo, A. D. Corso, S. de Gironcoli, S. Fabris, G. Fratesi, R. Gebauer, U. Gerstmann, C. Gougoussis, A. Kokalj, M. Lazzeri, L. Martin-Samos, N. Marzari, F. Mauri, R. Mazzarello, S. Paolini, A. Pasquarello, L. Paulatto, C. Sbraccia, S. Scandolo, G. Sclauzero, A. P. Seitsonen, A. Smogunov, P. Umari, and R. M. Wentzcovitch, "QUANTUM ESPRESSO: a modular and open-source software project for quantum simulations of materials," *Journal of Physics: Condensed Matter*, vol. 21, p. 395502 (19pp), 2009.

[241] G. Kresse and J. Hafner, "Ab initio molecular dynamics for liquid metals.," *Phys. Rev. B*, vol. 47, pp. 558–561, 1993.

[242] G. Kresse and J. Furthmueller, "Efficient iterative schemes for ab initio total-energy calculations using a plane-wave basis set," *Phys. Rev. B*, vol. 54, pp. 11169–11186, 1996.

[243] R. E. Tallman, T. M. Ritter, B. A. Weinstein, A. Cantarero, J. Serrano, R. Lauck, and M. Cardona, "Pressure measurements of TO-phonon anharmonicity in isotopic ZnS, journal = Phys. Stat. Sol. (b)," vol. 241, pp. 491–494, 2004.

[244] S. Barbosa, A. Agrawal, L. Rodríguez-Lorenzo, I. Pastoriza-Santos, R. A. Alvarez-Puebla, A. Kornowski, H. Weller, and L. M. Liz-Marzán, "Tuning size and sensing properties in colloidal gold nanostars," *Langmuir*, vol. 26, pp. 14943–14950, 2010.

[245] R. Rodríguez-Oliveros and J. A. Sánchez-Gil, "Gold nanostars as thermoplasmonic nanoparticles for optical heating," *Opt. Express*, no. 1, pp. 621–626, 2012.